ISSN 1068-3755, Surface Engineering and Applied Electrochemistry, 2014, Vol. 50, No. 1, pp. 1–8. © Allerton Press, Inc., 2014.
Original Russian Text © N.I. Anyakin, M. Nayebi, V.S. Kovalenko, V.V. Kremenitskii, R.O. Zhuk, A.N. Stepura, P.V. Kondrashev, 2014, published in Elektronnaya Obrabotka Materialov, 2014, No. 1, pp. 1–7.

Technology of Dimensional Laser Processing of Intractable Materials

N. I. Anyakin[a], M. Nayebi[a], V. S. Kovalenko[a], V. V. Kremenitskii[b], R. O. Zhuk[a], A. N. Stepura[a], and P. V. Kondrashev[a]

[a] *National Technical University of Ukraine, Laser Technology Research Institute, pr. Pobedy 37, Kiev, 03056 Ukraine*
e-mail: anyakin@ukr.net; v.kovalenko@kpi.ua

[b] *Technical Center, National Academy of Ukraine, ul. Pokrovskaya 13, Kiev, 04070 Ukraine*
e-mail: krem@nasu.kiev.ua

Received December 6, 2012; in final form, February 28, 2013

Abstract—The technological process of laser milling using the Q-switched mode is studied in this work. It is shown that the results of the laser action (the roughness of the surface and its chemical composition, the thickness of the removed layer) considerably depend on the processing conditions and the thermal and physical properties of the workpiece. The quality is also influenced by the amount of the liquid phase appearing in the case of laser heating and the fracture mode.

Keywords: laser technology, laser dimensional processing, laser milling, intractable materials

DOI: 10.3103/S1068375514010025

INTRODUCTION

Focused laser radiation used as a milling tool makes it possible to develop a general-purpose process of machining nearly any materials [1–5] (ceramics, synthetic or natural diamonds, hard alloy metals, steels, etc.). With laser milling (LM), as in the case of conventional high-velocity cutting and electrospark machining, there is realized the following:

—the process of the layer-by-layer removal of the stock;

—the permanent penetration of the tool (in our case, it is a focused laser radiation flow limited by a conditional caustic surface; spatially a conoid with a "small" working section) into the workpiece body;

—no passage of the tool body (not the working section) through the surface of the workpiece;

—the dependence of the stock removal rate on the workpiece properties.

Yttrium-aluminum garnet (YAG) Q-switched lasers (the emission wavelength of 1.06 μm, the average laser power P_m up to 100 W, the pulse recurrence frequency ν up to 50 kHz) are usually used for LM [1–5]. LM has some peculiar feature. Thus, a single pulse (with length τ_p of 100–500 ns, power P_p up to 5 kV) makes (through evaporation) a dimple with diameter of 10–200 μm and a depth from 1 to 100 μm in the work material. As it is noted in [3, 4], the work material undergoes structural and phase transformations in the course of heating. Under the action of plasma vapors and shock waves, a part of the generated liquid phase is thrown out of the dimple and deposits on the neighboring section distorting not only the surface under processing but also the machined section, which needs additional treatment. The LM peculiarities for different materials are studied in this work.

EXPERIMENTAL EQUIPMENT AND RESEARCH PROCEDURE

There were used YAG Q-switched lasers (average power P_m with single-mode operation in the range from 3 to 50 W) with service devices to carry out the experiments [5]. The two-coordinate scanning system RAZORSCAN-15 with interchangeable lenses helped to move the focused radiation on the surface of the specimens. Work pieces of WC8 alloy, 65G steel, borazon, and constructive silicon-carbide ceramics were used as specimens. The scanning rate *Vs*, the track spacing *StepOX*, and the pulse recurrence frequency ν (Fig. 1) were varied in the course of the investigations. Obviously, with *Vs* and ν being varied, it changed both the spacing *StepOX* between the separate spots of the radius r_p and the overlapping coefficient. The tests were threefold repeated at every experimental point. The action of the focused laser radiation on the materials (the processing depth *H* and microroughness height *Rz* (Fig.1)) was measured with the help of a BMI-1Ts toolroom microscope and an MIS-11 Linnik double microscope. The chemical composition of the surface of the specimen was determined using a

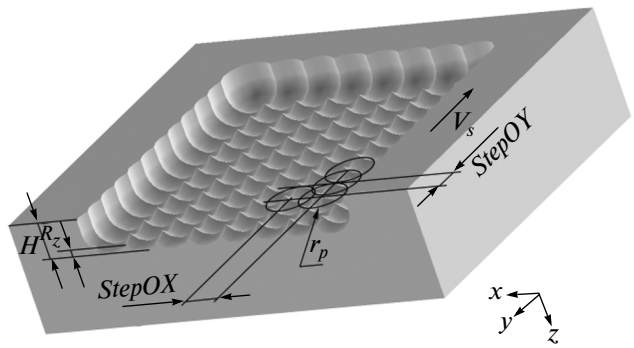

Fig. 1. Pattern of the workpiece machining.

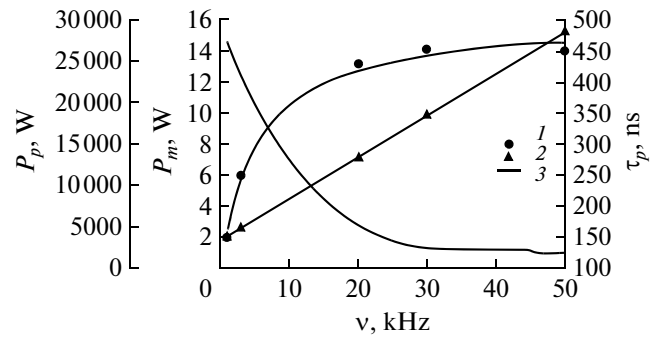

Fig. 2. Dependences of the laser radiation energy parameters on the modulation frequency: (*1*) the measured dependence of the average radiation power on the modulation frequency; (*2*) the measured dependence of the pulse duration on the modulation frequency; (*3*) the computed peak power of the pulse.

JSM-6490 scanning electron microscope (JEOL Ltd., Japan) fitted with an energy-dispersive spectrometer and wavelength spectrometers. The measurements were performed on each specimen at 6 random points with three of them on the unprocessed section of the surface and three on the area processed with the focused laser radiation. The laser radiation parameters were measured with the help of IMO-2 power meters, and the pulse time parameters were determined by FD-7 photodiodes in the photodiode mode; the signals were recorded by S1-74, S1-55, and S1-122A oscillographs or were received at the input of the analog–digital converters.

The preliminary studies of the process were carried out with the help of computing experiments. The process was simulated through the multidimensional nonlinear unsteady-state heat equation with a nonlinear scheme for accounting for phase transformations (1)–(5) being substituted by the finite-difference analog and solved by the sweep method [6]. The solution results (temperature patterns, dimensions of the melting and evaporation zones at different moments of time, thermal histories) under different processing conditions and for different materials were displayed:

$$c(T)\rho(T)\frac{\partial T}{\partial t} = \frac{\partial}{\partial x}\left(\lambda(T)\frac{\partial T}{\partial x}\right) + \frac{\partial}{\partial y}\left(\lambda(T)\frac{\partial T}{\partial y}\right) + \frac{\partial}{\partial z}\left(\lambda(T)\frac{\partial T}{\partial z}\right) + Q_{\text{HEAT}}(x, y, z, t, T), \quad (1)$$

$$c_v(T) = c_v(T) + \delta Q_f(T - T_f), \quad (2)$$

$$T_{\text{Start}} = 25°\text{C}, \quad (3)$$

$$\left.\frac{\partial T}{\partial x}\right|_{\substack{x=0\\x=HX}} = 0, \left.\frac{\partial T}{\partial y}\right|_{\substack{y=0\\y=HY}} = 0, \left.\frac{\partial T}{\partial z}\right|_{\substack{z=0\\z=HZ}} = 0, \quad (4)$$

$$Q_{\text{HEAT}}(x, y, z, t, T) = (1 - R(T))W_p(x, y, t)\exp(-\alpha(T)z), \quad (5)$$

where $c(T)$, $\rho(T)$, $\lambda(T)$ are the dependences of the heat capacity, density, and heat conduction of the workpiece on the temperature T; $Q_{HEAT}(x, y, z, t, T)$ is the heating source; x, y, z, t are the spatial and temporal coordinates; $c_v(T)$ is the volumetric heat capacity being $c_v(T) = c(T)\rho(T)$; δ–δ is the Dirac function; Q_f is the latent heat; T_{Start} is the initial temperature of the workpiece; HX, HY, HZ are the dimensions of the workpiece; and $R(T)$, $\alpha(T)$ are the dependences of the coefficients of the reflection and absorption of the laser radiation on the temperature T.

When describing the dependence of the power density of the focused laser radiation $W_P(x, y, t)$ on the spatial coordinates x, y, we used the predicted distribution of the flux rate (TEM_{00} mode), which is presented by the following equation:

$$W_P(x, y, t) = \frac{2P(t)}{\pi r_P^2}\exp\left(-\frac{2*((x - x_c)^2 + (y - y_c)^2)}{r_P^2}\right), \quad (6)$$

where $P(t)$ is the time dependence of the radiation power; r_P is the focusing spot radius on the level of $\exp^2$; and x_c, y_c are the moving coordinates of the focused laser beam axis.

EXPERIMENTAL RESULTS AND DISCUSSION

Let us consider the process of the interaction of the Q-switched focused laser radiation and the test materials. Note that, with the pulse recurrence frequency ν increasing, in spite of the growth of the average radiation power P_m, it simultaneously raises the length τ_p of the laser pulses causing the decrease of their peak power P_p (Fig. 2).

Undoubtedly, with the other processing conditions (Vs, r_p, $StepOX$) remaining the same, this phenomenon tells about the dimensions of the evaporated layer, the

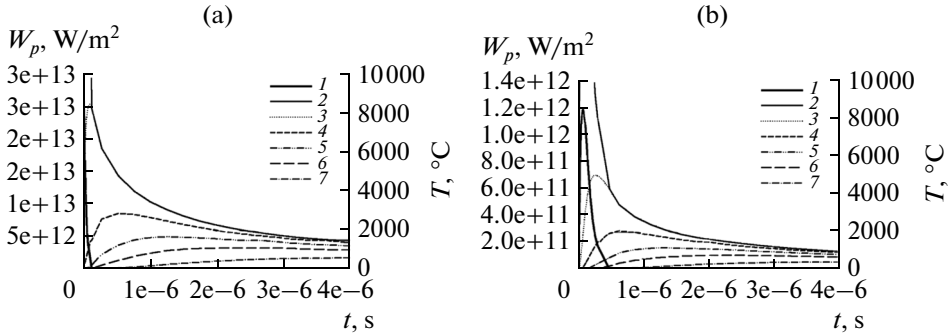

Fig. 3. Time dependences of the laser power radiation density and the WC8 specimen temperature under different conditions of processing (r_p = 0.025 mm, Vs = 50 mm/s): (a) $P_p = 2.45 \times 10^4$ W, τ_p = 150 ns; (b) $P_p = 1.17 \times 10^4$ W, τ_p = 480 ns; (*1*) $Wp(t)$ characteristic; (*2*) $T(z, t)$ when $z = 0$ μm; (*3*) $T(z, t)$ when $z = 4$ μm; $z = 8$ μm; (*4*) $T(z, t)$ when $z = 16$ μm; (*5*) $T(z, t)$ when $z = 24$ μm; (*6*) $T(z, t)$ when $z = 36$ μm; (*8*) $T(z, t)$ when $z = 44$ μm.

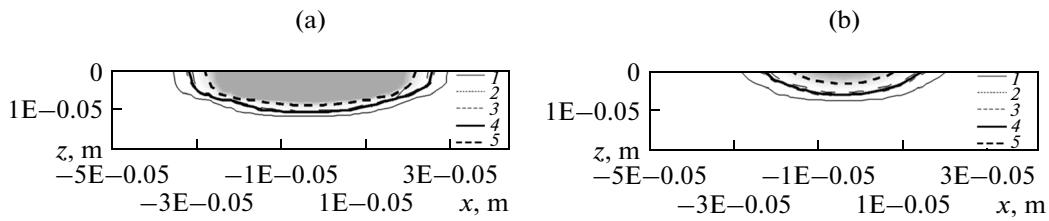

Fig. 4. Temperature distribution in the WC8 specimen in the case of processing with laser pulses (r_p = 0.025 mm, Vs = 50 mm/s): (a) $P_p = 2.45 \times 10^4$ W, τ_p = 150 ns, recurrence frequency ν = 3 kHz; (b) $P_p = 1.17 \times 10^4$ W, τ_p = 480 ns, ν = 50 kHz; (*1*) Co melting isotherm; (*2*) WC dissociation isotherm; (*3*) W melting isotherm; (*4*) Co evaporation isotherm; (*5*) W evaporation isotherm.

liquid bath, and so on. Let us consider as an example the result of the laser radiation action on the workpiece (Figs. 3–5) for the cases of the modulation frequencies of 3 and 50 kHz. At that, the single pulse power amounts to 2.45×10^4 W and 1.17×10^3 W and its length is 150 and 480 ns, respectively (Fig. 2). Thus, in Fig. 3 there are presented the calculated dependences of the power density of the laser radiation $Wp(t)$ with the temperature $T(z, t)$ on the time t that appear in the specimen of the WC8 hard alloy in the case of processing by the Q-switched focused laser radiation focused into a spot with r_p = 0.025 mm and moving at a speed of Vs = 50 mm/s with different modulation frequencies; in Fig. 4, there are depicted the temperature distributions in the specimen (for the given conditions of processing) at the moment of the laser pulse action.

As expected, with P_p decreasing, the dimensions of the evaporation zone reduce. Besides, for both cases of processing, the evaporation of the surface goes on after the action of a pulse is over. As such, when processing with a high pulse recurrence frequency (ν = 50 kHz), in spite of the high heat conduction of the work material, the temperature of the work surface section continuously grows due to the little time between the pulses (2×10^{-5} s). Obviously, the pulses with higher P_p

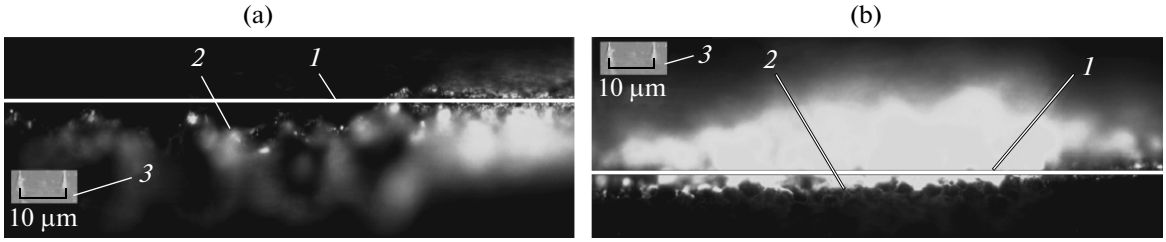

Fig. 5. Profile of the processed surface of the WC8 alloy under different conditions (r_p = 0.025 mm, Vs = 50 mm/s, $StepOX$ = 0.02 mm): (a) $P_p = 2.45 \times 10^4$ W, τ_p = 150 ns, recurrence frequency ν = 3 kHz; (b) $P_p = 1.17 \times 10^4$ W, τ_p = 480 ns, ν = 50 kHz; (*1*) unprocessed section; (*2*) processed section; (*3*) scale.

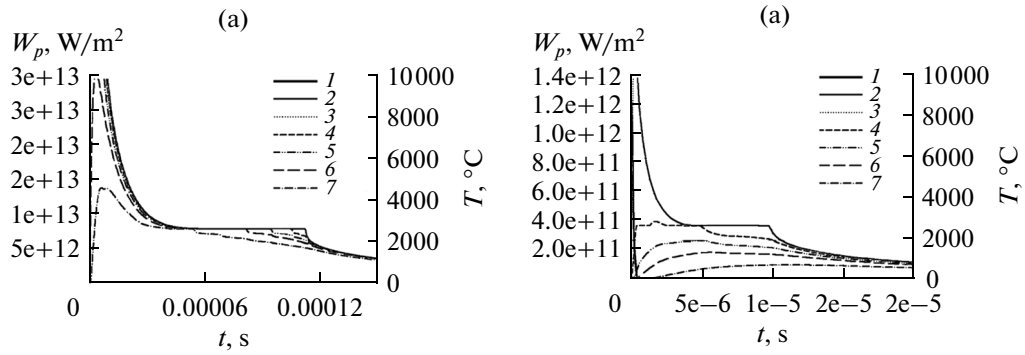

Fig. 6. Time dependences of the power density of the laser radiation and the temperature of the borazon specimen under different conditions of processing (r_p = 0.025 mm, Vs = 50 mm/s): (a) $P_p = 2.45 \times 10^4$ W, τ_p = 150 ns; (b) $P_p = 1.17 \times 10^4$ W, τ_p = 480 ns; (*1*) $Wp(t)$ characteristic; (*2*) $T(z, t)$ when z = 0 mm; (*3*) $T(z, t)$ when z = 4 μm, 8 μm; (*4*) $T(z, t)$ when z = 16 μm; (*5*) $T(z, t)$ when z = 24 μm; (*6*) $T(z, t)$ when z = 36 μm; (*7*) $T(z, t)$ when z = 44 μm.

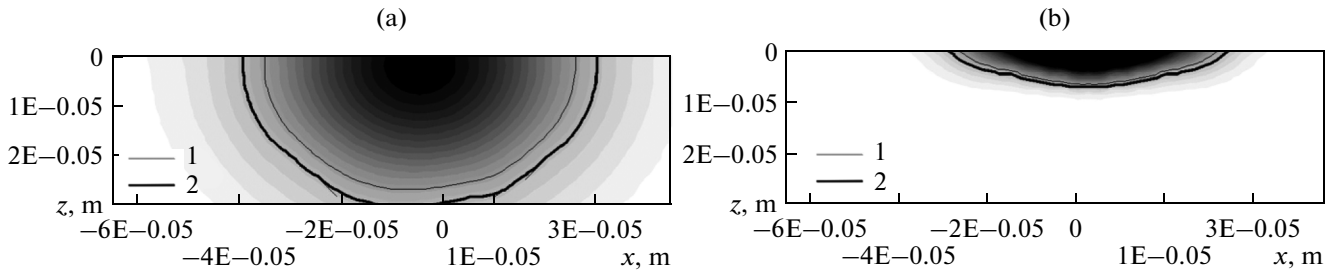

Fig. 7. Temperature distribution in the borazon specimen in the case of processing with laser pulses (r_p = 0.025 mm, Vs = 50 mm/s): (a) $P_p = 2.45 \times 10^4$ W, τ_p = 150 ns, recurrence frequency ν = 3 kHz; (b) $P_p = 1.17 \times 10^4$ W, τ_p = 480 ns, ν = 50 kHz; (*1*) NB dissociation isotherm; (*2*) B melting isotherm.

(at a low recurrence frequency) evaporate a larger volume of the work material (Fig. 4a) thus ensuring the high capacity of the process. Despite the short pulse duration and high density of the focused laser radiation power in the focusing spot, there is generated a considerable amount of liquid phase (Figs. 4, 5) that is expelled from a single dimple by the erosive plasma vapors. Then, depositing on the surface of the work, the set melt deforms the group scribe profile, thus deteriorating the surface finish (Fig. 5).

Note that some transformations take place in the course of the laser heating of the WC8 alloy. Thus, at a temperature of 1494°C, the (Co) binding substance melts; later on, at a temperature of 2720°C, there occurs melting and dissociation of the WC. Then, as the amount of the incoming energy grows (and the temperature as well), W melts and Co evaporates and finally wolfram itself evaporates too. Considering the high temperatures of the phase transformations and the high enthalpy of the phase transitions [7, 8], the process of laser processing of this material demands a significant energy input.

As was mentioned above, the liquid phase, hardened at random on the processed section of some intractable material (metal), distorts its profile (Fig. 5). At that, the size of the microroughnesses formed by the set melt may be commensurable with the dimensions of the evaporated layer (Fig. 5a). In the case when n increases, i.e., P_p decreases and the evaporated layer volume and liquid phase amount (Figs. 3b, 4b) also reduce, the treatment quality is improved (the surface roughness becomes smaller). However, the amount of the removed stock (the evaporated layer depth) is considerably less than in the case of processing with a smaller frequency.

Unlike the WC8 hard alloy with the melting–evaporation phase transitions in the case of laser processing with nanosecond pulses, the heating of some superhard tool materials based on borazon at atmospheric pressure and the ambient air temperature has a number of peculiarities. Thus, according to [8, 9], the slow oxidation of borazon begins at a temperature above 2000°C and its transition into hexagonal boron nitride happens at a temperature of 2500°C and is possible at pressures above 4053 MPa. Under ordinary conditions in the case of heating (at temperatures of 2700–3000°C), borazon dissolves into hexagonal boron nitride (powder), which in turn, at further heating,

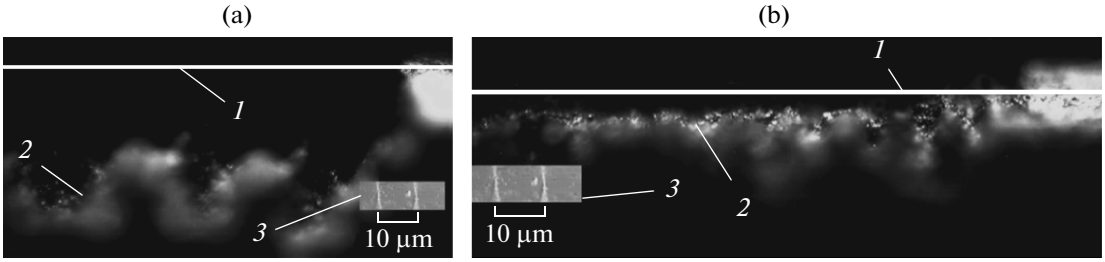

Fig. 8. Profile of the processed borazon surface under different conditions (r_p = 0.025 mm, *Vs* = 50 mm/s, *StepOX* = 0.02 mm): (a) $P_p = 2.45 \times 10^4$ W, τ_p = 150 ns, recurrence frequency ν = 3 kHz; (b) $P_p = 1.17 \times 10^4$ W, τ_p = 480 ns, ν = 50 kHz; (*1*) unprocessed section; (*2*) processed section; (*3*) scale.

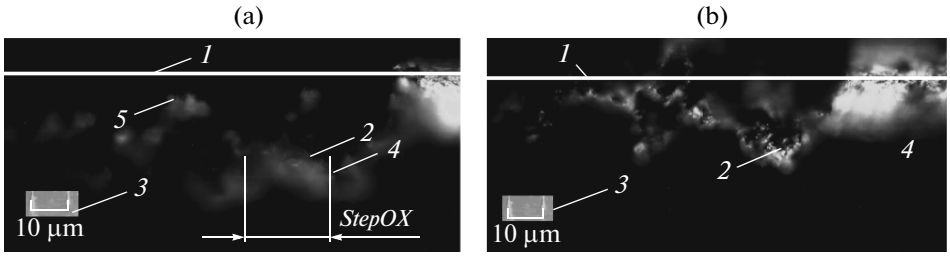

Fig. 9. Profiles of the processed surface of structural ceramics (a) and 65G steel (b) in the case of r_p = 0.025 mm, *Vs* = 50 mm/s, *StepOX* = 0.02 mm; $P_p = 2.45 \times 10^4$ W, τ_p = 150 ns, recurrence frequency ν = 3 kHz,: (*1*) unprocessed section; (*2*) processed section; (*3*) scale; (*4*) the track "bottom"; (*5*) the "top" between the tracks.

dissolves into boron and nitrogen; thus, its laser processing becomes significantly simpler. The calculated results for the process of borazon heating by focused laser radiation with different parameters are presented in Figs. 6–7.

As in the previous case (Figs. 3, 4), the process of the fracturing of the work material continues after the laser radiation action is over (Figs. 5, 6). Moreover, due to the lower (than of WC8) density and heat capacity (at nearly the same heat conduction) and in spite of the higher dissociation heat, the process is more efficient.

The absence of the liquid phase, which is generated in the course of the fracture of the borazon-based tool material, affects the processed surface profile (Fig. 8). Thus, under the same conditions, the surface of the borazon workpiece after processing has a "regular" form, unlike the processed surface of the WC8 alloy (Fig. 5), and it follows the motion path of the focused laser beam (Fig. 8). At that, with the spacing between the tracks *StepOX* decreasing (unlike for the WC8 alloy), the size of the microroughnesses reduces. Comparing the calculation results (Figs. 3, 4, 6, 7) and the experimental testing of them (Figs. 5, 8), we note that the efficiency of LM of the synthetic borazon-based super-hard materials is three times as that of LM of the intractable super-hard materials based on tungsten carbide.

The mentioned differences in the profile and microroughness of the processed surface are the same as for the other materials with different fracture modes. For example, the regular character of the microroughnesses on the processed surface, which follow the motion path of the focused laser radiation, is observed in the case of the materials whose fracturing happens without the generation of a liquid phase or when its amount is minimal (natural and synthetic diamonds [2, 5], structural ceramics based on silicon carbide (Fig. 9a)). In the case of machining metals and structural (Fig. 9b) tool and stainless steels, while undergoing an ordinary thermal cycle (heating—melting—evaporation—vapor deposition—cooling) at laser heating, as well as processing intractable materials, there is also observed an uncontrolled surface roughness, the value of which may be more than the depth of the stock removal through a separate track.

Note that, at LM of the WC8 alloy, besides the dependence of the stock removal depth and the microroughness value on the machining modes, one observes the change of the chemical composition of the processed surface. Thus, if before machining the surface of a WC8 plate contains about 10% C, 0.8% Co, and 91% W (Fig. 10a), after it, the chemical composition of the surface changes (Table 1). In the case of processing with a low pulse recurrence frequency (when

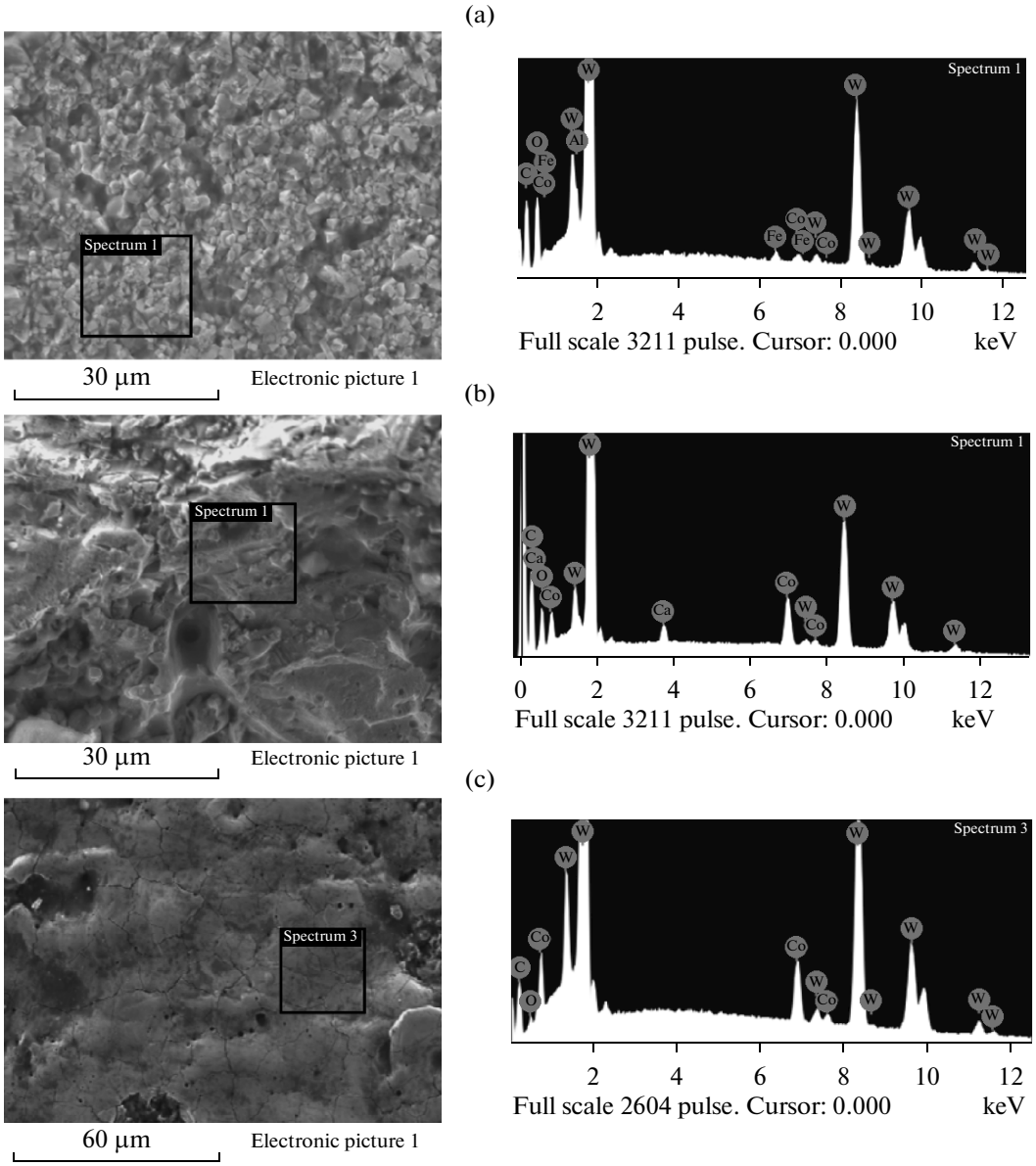

Fig. 10. Surface fragments of the WC8 specimen and spectrograms of its chemical composition: (a) unprocessed fragment; (b, c) processed fragments at $r_p = 0.025$ mm, $Vs = 50$ mm/s, $StepOX = 0.02$ mm: (b) $P_p = 2.45 \times 10^4$ W, $\tau_p = 150$ ns, recurrence frequency $\nu = 3$ kHz; (c) $P_p = 1.17 \times 10^4$ W, $\tau_p = 480$ ns, $\nu = 50$ kHz.

there is generated a lot of liquid phase (Figs. 3a, 4a)), the surface contains a greater C percentage, indicating the possible growth of the amount of carbides that form when the melt interacts with the atmosphere; the growth of the Co percentage (in both cases) is evidently associated with the deposition of the cooled metal vapors on the processed section.

The analysis of the chemical composition of the processed borazon surface did not demonstrate any changes in comparison with the basic one.

As for the structural ceramics based on silicon carbide, there are found some differences in the element percentage on the "bottom" (Fig. 9a) and "tops" of the tracks formed in the course of the processing (Table 2).

It should be noted that, when the concentrations of the chemical elements are measured using the X-ray microanalysis method, the total concentration differs from 100% as the surface of the specimens under investigation (before and after laser processing) was

Table 1. Microanalysis data for the surface of the hard alloy WC8 specimen

Sl.No.	Unprocessed surface		Surface after processing with ν = 3 kHz		Surface after processing with ν = 50 kHz	
	element	weight percent	element	weight percent	element	weight percent
1	C	10.265	C	16.47	C	7.59
2	O	3.288333	O	3.236	O	0.328889
3	Al	0.123333	Al			
4	Fe	0.158333				
5			Ca	0.39		
6	Co	0.805	Co	6.358	Co	6.986667
7	W	90.92	W	64.044	W	101.0789
		105.56		90.498		115.9844

Table 2. Microanalysis data for the surface of the specimen of structural ceramics on SiC

Sl.No.	Unprocessed surface (position 1, Fig. 3)		Processed surface (“cavity”)		Processed surface (“top”)	
	element	weight percent	element	weight percent	element	weight percent
1	Fe	0.11	Fe	0.054333	Fe	0.01
2	Si	75.395	Si	74.97	Si	21.64
3	C	53.445	C	39.94	C	52.04
4	O	3.19	O	4.91	O	2.99
5	Ca	0.38	Ca	0.166667	Ca	0.02
		132.52		120.041		76.7

not polished, which is necessary in the case of microanalysis.

The appearance of Ca in the processed specimen is most likely caused by the fact that the distribution of Ca on the surface of both the initial specimen and the processed one is nonuniform, and the regions of the concentration measurement are different for the initial and processed specimens.

CONCLUSIONS

Thus, analyzing the results, we note the following:

The efficiency of the Q-switched laser milling of synthetic super-hard borazon-based materials is three times more than that of the intractable super-hard materials based on tungsten carbide; this is explained not only by the difference of their thermophysical properties but primarily by the difference in the modes of their fracturing.

The worst quality of the processed surface is observed in the case of the intractable materials that undergo, in the course of laser heating, solid–liquid–vapor phase transitions with the following uncontrolled deposition of the fracture products on the processed surface section.

The minimization of the pulse duration with the simultaneous increase of its power results in the growth of the depth of processing, which with the equipment used (YAG Q-switched lasers) is possible when the pulse recurrence frequency is reduced. The application of this phenomenon in the case of the laser

milling of intractable materials will make it possible to improve the efficiency of the process; however, some further investigations should be carried out with the purpose to preserve the high quality of the surface processed with the focused laser radiation.

REFERENCES

1. Kuhl, M., From macro to micro—the development of laser ablation, *Proc. 21st Int. Congress on Applications of Lasers and Electrooptics*, Scottsdale, Arizona, 2002.
2. Cao, F. and Huang, J., Technique of precise laser machining for the diamond wire drawing dies, *Proc. Int. Symp. on Electromachining "ISEM-XI"*, Lausanne, 1995, pp. 629–637.
3. Vasco, J.C. and Bartolo, P.J., Processing conditions of laser micro-milling, *Proc. 15th Int. Symp. on Electromachining*, Pittsburgh, Pennsylvania, 2000, pp. 427–432.
4. Leong, K., Drilling with laser, *Ind. Laser Solut. Manuf.*, 2000, vol. 15, no. 9, pp. 39–45.
5. Anyakin, N.I., Naebi, M., and Kovalenko, V.S., Processing of irregularly shaped holes with the help of the focused laser radiation, *Surf. Eng. Appl. Electrochem.*, 2012, vol. 48, no. 1, pp. 22–27.
6. Samarskii, A.A. and Vabishchevich, P.N., *Additivnye skhemy dlya zadach matematicheskoi fiziki* (Additive Patterns for Problems of Mathematical Physics), Moscow: Nauka, 2001.
7. Samsonov, G.V. and Vinitskii, I.M., *Tugoplavkie soedineniya*, (High-Melting Compounds), Moscow: Metallurgiya, 1976.
8. Shackelford, J. and Alexander, W., *Material Science and Engineering Handbook*, New York: CRC Press, 1969.
9. Beiss, P., Ruthardt, R., and Warlimont, H., *Powder Metallurgy Data. Refractory, Hard and Intermetallic Materials*, Berlin-Heidelberg: Springer, 2002.

Translated by M. Myshkina

ISSN 1068-3755, Surface Engineering and Applied Electrochemistry, 2014, Vol. 50, No. 1, pp. 9–17. © Allerton Press, Inc., 2014.
Original Russian Text © A.I. Shul'man, S.S. Belevskii, S.P. Yushchenko, A.I. Dikusar, 2014, published in Elektronnaya Obrabotka Materialov, 2014, No. 1, pp. 8–16.

Role of Complexation in Forming Composition of Co–W Coatings Electrodeposited from Gluconate Electrolyte

A. I. Shul'man[a], S. S. Belevskii[b], S. P. Yushchenko[a, b], and A. I. Dikusar[a, b]

[a]*Shevchenko State University of Pridnestrovie, 25 Oktyabrya St. 128, Tiraspol, Republic of Moldova*
[b]*Institute of Applied Physics, Academy of Sciences of Moldova, Academiei St. 5, Chisinau, MD-2028 Republic of Moldova*
e-mail: dikusar@phys.asm.md

Received July 1, 2013; in final form, August 13, 2013

Abstract—The purpose of the given research has been to specify the route of formation of Co–W coatings. To this end, the gel-chromatographic separation of gluconate electrolyte has been used, as well as the photocolorimetric determination of the composition of the separation products, and the evaluation of the electrochemical activity of these complexes in the pH range of 4.0 to 8.0. As a result, it has been found out that the composition of the Co–W coatings thus formed is defined by the relation of the rates of the reduction of those heterometallic complexes (with the Co–W ratio 1 : 1) and Co complexes in solution, as well as the reaction of hydrogen reduction, dependent on both the electrolyte pH and hydrodynamic conditions.

Keywords: nanocrystal coatings, heterometallic complexes, gel-chromatographic separation, Co–W electrolytic coatings, induced codeposition, cyclic voltammetry

DOI: 10.3103/S106837551401013X

INTRODUCTION

The study and development of methods for obtaining and controlling properties (mechanical, magnetic, catalytical, etc.) of the deposited alloys on the base of iron group and refractory metals, Co–W alloys in particular, are among the priority areas in modern electrochemical materials science [1, 2]. This is due to both application issues (e.g., the development of methods, as alternatives to chroming, for manufacturing wear and corrosion resistant coatings [2–5]) and the theoretical ones, since electrodeposition of those alloys can be treated as anomalous [1]. The reason for the latter is accounted for by the composition of those coatings (and, hence, their properties) that cannot be predicted according to the electrochemical characteristics of the processes of the reduction of individual components. Among anomalous processes of electrodeposition is the so-called induced codeposition [2, 6, 7], in particular, the process of manufacturing electrolytic coatings of iron group metals with refractory metals: W-, Mo- and Re-based alloys. Tungsten, for example, cannot be electrodeposited from an aqueous solution, but introducing compounds of the iron group metals into the electrolyte makes it possible to obtain alloys containing tungsten [1–6].

It is obvious that the control of the composition, structure and properties of those coatings should be determined by the mechanism of electrodeposition. However, today there is no generally recognized mechanism of the induced codeposition of the alloys of the iron group metals with refractory ones.

Some authors, starting from the time of publication of [6], consider that the formation of the alloy results from the complexation in solution, and the respective complex (e.g., Co–W) is formed in the electrolyte. The latter is in fact a precursor in the electrochemical synthesis of the alloy [1, 6, 8]. The complex formation in the electrolyte is also determined by the following: as a rule, during the induced electrodeposition ions of ligands (citrate, gluconate, tartrate, succinate, etc.) are introduced into the solution. Other authors are of the opinion that the composition of the complex in the electrolyte is not of primary importance as electrodeposition occurs from an intermediate, formed on the surface of the electrode, i.e., owing to the electrochemical process itself [7, 9, 10] (see also review in [2]).

There are numerous investigations on complexation in electrolyte solutions, however, the induced electrodeposition of the iron group metals with refractory metals in gluconate solutions has been out of the scope of research so far (see on this point, e.g., [2]). A possibility of electrodeposition from the respective composite compounds is usually viewed basing on indirect data, such as the effect of the composition of the solution on the composition of the formed coatings (in [1] it refers to the production of Ni–W coatings). Or it may be the change in the absorption spectra after the change in the composition of solution during electrodeposition of Co–W coatings from gluconate solutions [8].

In [11], to obtain Co–W coatings, gel-chromatographic separation into the components with various

Table 1. Composition and concentration of electrolytes

Components of electrolytes	Electrolyte						
	1	2	3	4	5	6	7
$CoSO_4$ (M)	0.053	–	–	–	–	–	0.053
Na_2WO_4 (M)	0.05	0.05	0.05	0.05	0.05	0.05	–
H_3BO_3 (M)	0.65	–	–	0.65	0.65	0.65	0.65
NaCl (M)	0.51	–	0.51	–	0.51	0.51	0.51
Sodium gluconate (M)	0.55	–	–	–	–	0.55	055

molecular masses of a citric electrolyte is used and the elctrodeposition of such coatings is shown to result from the formation of multinuclear heterometallic complexes in the solution whose composition depends on the solution pH and the near-electrode layer.

The given paper uses the method of gel-chromatographic separation for gluconate electrolyte, which was earlier applied for manufacturing nanocrystalline Co–W coatings [3, 4, 8]. However, since the existence of the complex in the solution does not imply its reduction to a metal state (for example, compare the reduction of a ferricyanide complex of iron on platinum, or obtaining silver from a dicyanoargentate complex of silver), the research into the complexation in solution should be combined with the analysis of electrochemical activity of complex compounds, this is why a variant of cyclic voltammetry (CVA) was used in the given work.

EXPERIMENTAL

Electrolytes and Their Preparation

Table 1 lists the compositions of electrolytes used for the gel-chromatographic separation and the examination of their electrochemical activity.

The basis for all solutions used in the given study was electrolyte 1 described in [3, 4, 8]. It included not only sodium wolframate, cobalt salt, and a ligand (sodium gluconate) but also sodium chloride with a concentration of ~0.5 M. Its presence is necessary in order to increase the electroconductivity, since this electrolyte is diluted with respect to the main components. Boric acid was used as a buffer reagent. The preparation of the electrolyte started with the dissolution of the cobalt salt, gluconate, and sodium chloride, which was followed by adding boric acid and dissolving sodium wolframate in this solution. The pH values of all the electrolytes (during the gel-chromatographic separation and the CVA measurements of the electrochemical activity) were fixed (4.0, 5.35, 6.5, and 8.0). Sodium hydroxide or sulphuric acid was added to bring the pH to the required level. Thus, we used 28 solutions in this study: seven of which, with four pH values, are shown in Table 1.

Gel-Chromatographic Separation and Estimation of Cobalt and Tungsten Content in Separation Products

Chromatographic studies were carried out using a 1086-mm-long column, 9.9 mm in diameter, with a full volume of 83.6 cm^3; BioGel P-2 (50–150 mash) was the bulking agent. This sorbent is characterized by inertness and it separates the solution components according to their molecular masses [12]. The free bulk of the column was defined according to the BSA and was found to be 28 mL. Cyanocobalamin (Vitamin B_{12}, whose molecular mass is 1356 g/mol) was used as a reference compound for estimating the molecular mass. The rate of the eluent flow was ~0.75 mL/min; it was controlled by a P-3 peristaltic pump during each experiment run and the chromatogram was recalculated according to the particular value of the flow rate. A Specord M40 spectrophotometer with a 2-mm flow ditch was used as a yield sensor of the separation products. The measurements of the optical density were performed at a wave length of 230 nm. The preparative separation (the volume of each sample ~1.5 mL) was carried out to determine the ratio of Co and W in the products.

The content of cobalt and tungsten was specified by photocolorimetric measurement of the optical density of the solutions of the complex of cobalt with nitroso-R-salt [13, p. 677], and that of tungsten, by the rhodanide method [13, p. 600], after its reduction by Sn(II) and Ti(III), with the formation of a respective dyed complex. In both cases, the calibration curves were plotted using solutions that contained not only Co^{2+} and WO_4^{2-} but also all components of the electrolyte solution.

Cyclic Voltammetry of the Solutions (CVA)

The analysis of the electrochemical activity of the solutions (with the view of electrodeposition of the alloy or its components) was performed using different pH values in the following CVA variants. In the solution under study, the cycling was carried out on a platinum wire electrode (the surface area was 0.159 cm^2) from the stationary potential (OCP) in the cathodic direction at a rate of 10 mV/s up to –1.45 V and then in the anodic direction up to the potential of +0.9 V.

After that, the cycle was repeated. Before the beginning of each experiment, we performed the anode–cathode purification of the platinum electrode in nitric acid (~30%) at a potential of +1 V up to a maximal decrease of the current followed by the surface reduction at –0.2 V in the same medium. Purification was not carried out in between separate cycles. A saturated silver-chloride electrode was used as a reference electrode. Typical voltammograms are shown in Fig. 1.

The degree of electrochemical activity was determined, according to the current density in the cathodic direction in the first cycle, to be in the range of potentials from +0.2 to –0.5 V, any anodic peaks were absent, whereas, after the reduction in the cathodic region, during cycling in the anodic direction, anodic peaks emerged (Fig. 1), which can be classified as the peaks of the anodic dissolution for the following reasons: (1) except for some particular case, they were reproduced from cycle to cycle (Fig. 1a), which indirectly indicated that the anodic dissolution of the product (that was reduced in the cathodic cycle) resulted from the anodic process; (2) visual products on the platinum electrode after the anodic cycle were absent, unlike the state of the surface after the cathodic cycle.

Taking into account that the electrochemical equivalents of Co(II) and W(VI) with an error of less than 2% coincide, the area of the peak of the anodic dissolution (C/cm^2) shows what amount of the substance is deposited during the cathodic cycle irrespective of the composition of the deposit obtained. The absence of a peak of the anodic dissolution showed that the process of reduction of the complex is not accompanied by its reduction to a metal state.

In [14, 15], the anodic peaks in the system of Co–gluconate are described that are specified not by the anodic dissolution but rather by the anodic electrodeposition of cobalt oxide in a strongly alkaline medium. However, their behavior during cycling, described in the works cited above, differed substantially from that in our study. First, those peaks were observed only in a strongly alkaline medium, then, during the cycling, the growth of both the anodic and cathodic peaks occurred from cycle to cycle, because the product obtained was not dissolved during the anodic cycle.

As a rule, the cycles that were successively registered (the anodic dissolution, above all) coincided (Fig. 1a). However, in some cases, the current densities in the successive anodic cycles differed substantially from each other (Fig. 1b). In that latter case, we analyzed the curves of the anodic dissolution reproducible from cycle to cycle. Several measurements were performed in a non-agitated solution. In order to verify the impact of hydrodynamics on the rate of deposition–dissolution, cycling was performed while stirring the solution with a magnetic agitator. The measurements were carried out at temperature 22 ± 2°C.

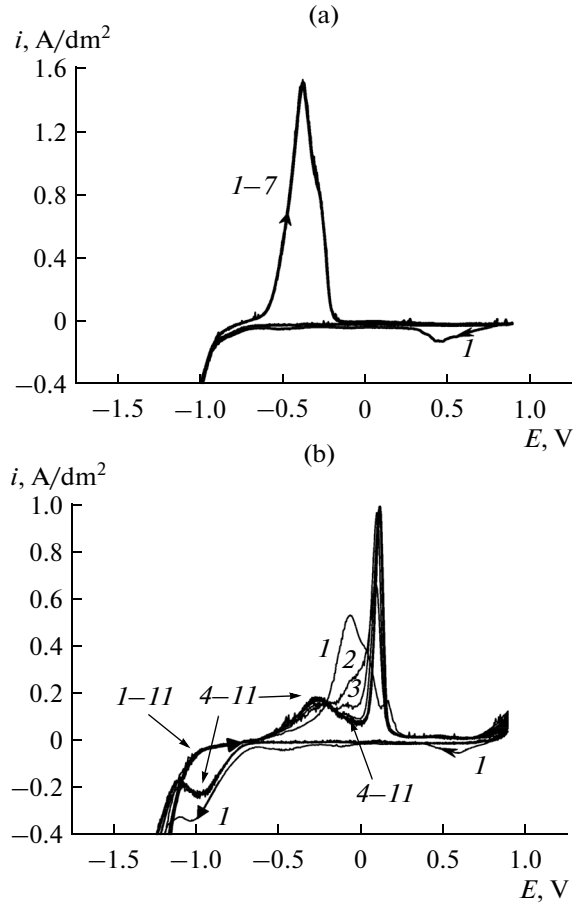

Fig. 1. Cyclic voltammograms of electrolytes 1 (a) and 7 (b) at pH 8. The figures on voltammograms correspond to the numbers of successive cycles. The peak of the reduction of the first cycle (1) is not repeated in successive cycles.

RESULTS AND DISCUSSION

Compounds of Sodium Wolframate

The chromatograms in Fig. 2 show that the sodium wolframate solution is an associate (a set of associates) with a very high molecular mass (Fig. 2a). The broadened peaks of the sodium wolframate chromatograms testify to the existence of several products and correspond to the molecular masses in the range of 1200–1400 g/mol, which is close to the molecular mass of vitamin B_{12}. The change in the pH of the solution (i.e., the change in the ionic force) modifies the composition of the associates; it can break them into pieces and liberate the compounds with lower molecular masses (compare curves *1*, *2*, and *3* in Fig. 2a). The most crucial changes (according to the measurements of the optical density) take place during the transition to alkaline solutions (Fig. 2a, pH 8).

Precise values of molecular masses were not determined, since there was no linear dependence between the position of the peak on a chromatogram and the markers with a known molecular mass used for this

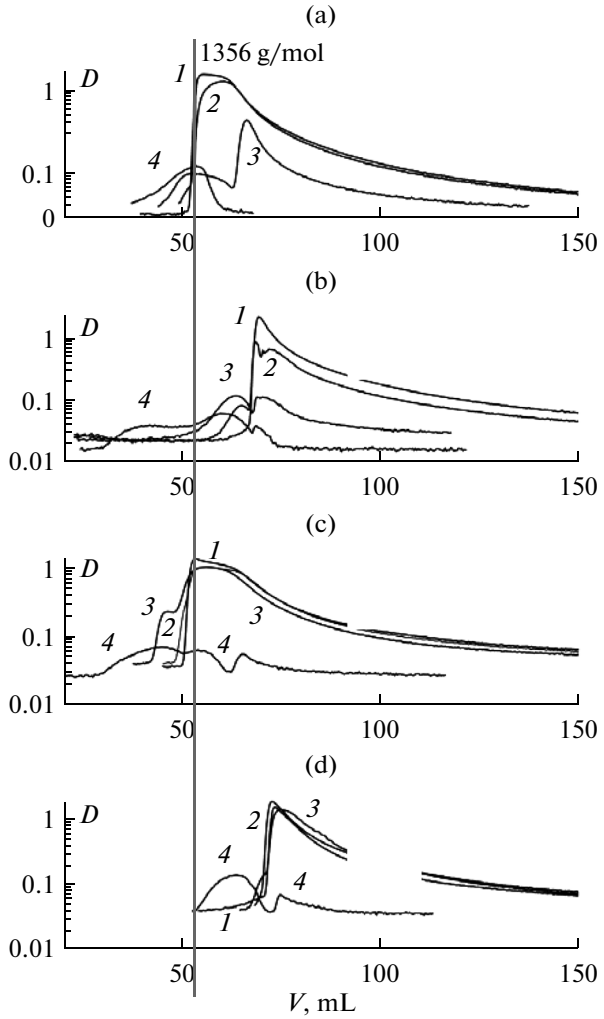

Fig. 2. Gel-chromatograms of electrolytes 2(a), 3(b), 4(c), and 5(d). Figures on chromatograms correspond to values of pH of solutions: 4.0 (*1*); 5.4 (*2*); 6.5 (*3*); 8.0 (*4*). The vertical line corresponds to the volume of the yield of vitamin B_{12} (1356 g/mol).

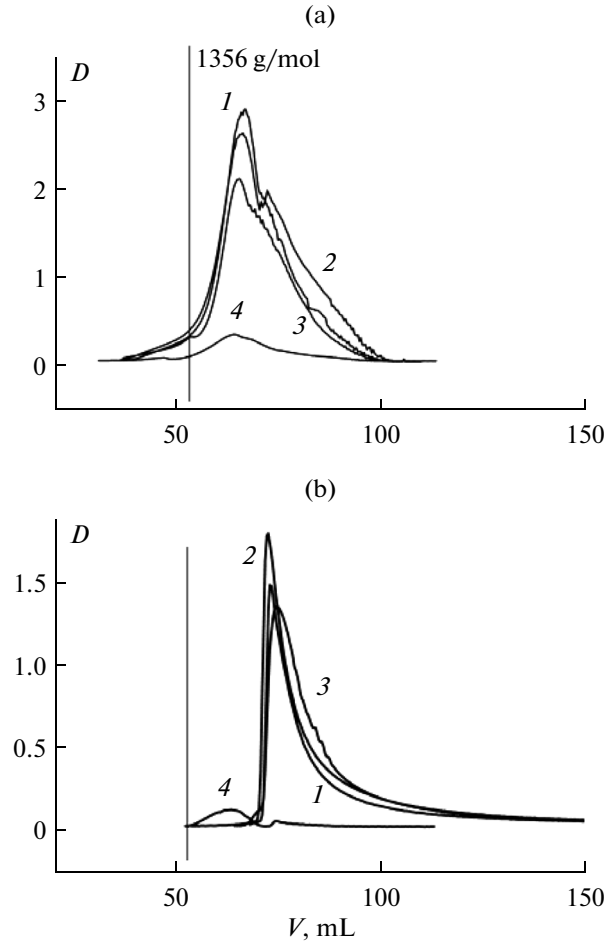

Fig. 3. Gel-chromatograms of electrolytes 6(a), 5(b), and 4(c). Figures on chromatograms correspond to values of pH of solutions: 4.0 (*1*); 5.4 (*2*); 6.5 (*3*); 8.0 (*4*). The vertical line corresponds to the volume of the yield of vitamin B_{12} (1356 g/mol).

purpose. However, it is known that at pH of ~5–8 tungsten takes the form of various associates such as $HW_{12}O_{41}^{10-}$ and $HW_6O_{21}^{5-}$, i.e., with the molecular mass of the complex in the associate of the order of 1450–3000 g/mol [2] (see also [16, 17]). Taking into account that both the composition of the complexes and the composition of the associates strongly depend on the concentration of wolframate, we can consider that the results we have obtained (which are close in the order of magnitude to the values of molecular masses) are in agreement with the available experimental data.

The introduction of sodium chloride into the solution resulted in a sharp decrease in the molecular mass (Fig. 2b). This decrease refers to all of the solutions used regardless of their pH. The maximum decrease in the optical density can be observed during the transition to the electrolyte with pH 8 (Fig. 2b).

By adding boric acid to sodium wolframate (electrolyte no. 4) some complexes are formed including those whose molecular mass is higher than that of vitamin B_{12} (Fig. 2c); while the presence of chloride ions in the solution causes fragmentation and formation of compounds with lower molecular masses (Fig. 2d).

The addition of sodium gluconate to this solution (Table 1, electrolyte no. 6) facilitates formation of gluconate complexes with a higher molecular mass. Their composition obviously depends on pH, since, with varying pH the optical density of the solution changes substantially (Fig. 3). The comparison of the gel-chromatograms (Fig. 3) shows that the addition of sodium gluconate into electrolyte no. 5 (a) increases the optical density and (b) increases the molecular mass of the tungsten complexes being formed.

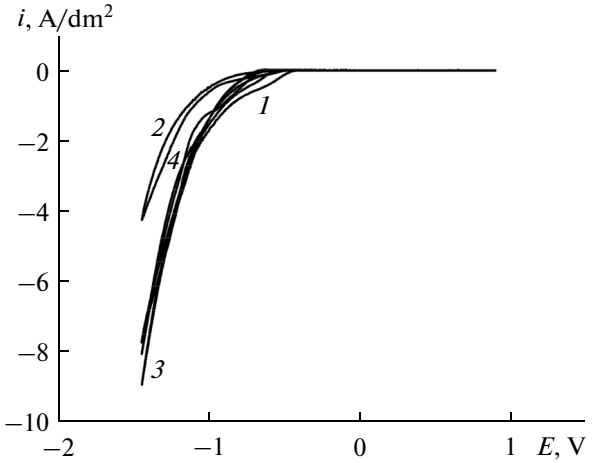

Fig. 4. Cyclic voltammograms of electrolyte 6 at pH 4.0 (*1*); 5.4 (*2*); 6.5 (*3*); 8.0 (*4*).

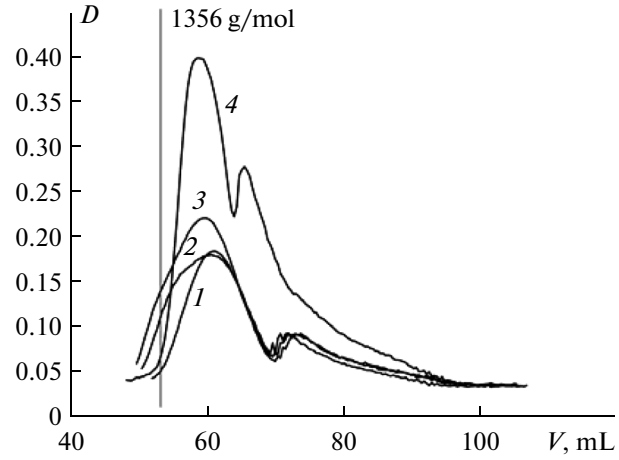

Fig. 5. Gel-chromatograms of electrolyte 7 at pH 4.0 (*1*); 5.4 (*2*); 6.5 (*3*); 8.0 (*4*). The vertical line corresponds to the volume of the yield of vitamin B_{12} (1356 g/mol).

However, none of the tungsten-containing gluconate complexes (obtained at different pH) reduces to a metal state, and no voltammogram in Fig. 4 shows peaks that indicate anodic dissolution, though reduction in the cathode region is found to occur. It is obvious that either this process results only from hydrogen reduction, or the intraspheric reduction of the complex takes place without the formation of a metal on the surface of the electrode.

Cobalt Complexes

Gluconate complexes of cobalt with sufficiently high molecular mass are formed as well. According to Fig. 5, the respective complexes: (a) consist, at least, of two products with sufficiently high molecular masses, and (b) their composition varies with the change in the pH of the solution. It is worth noting here that the peaks of the chromatograms reveal that the gluconate complexes of cobalt formed in those solutions differ greatly from the complexes described in literature [18] since their molecular mass is, at least, twice as much as the molecular mass of the known gluconate complexes of cobalt. However, unlike complexes that contain only tungsten, among the compounds under study, we observe reduction with the formation of cobalt on the surface (Fig. 6).

The rate of reduction of the complexes that are formed greatly depends on pH (Fig. 6), increasing with a decrease in the pH of the electrolyte. The amount of the metal yielded, which is determined with respect to the area of the peak of the anodic dissolution, also grows with a decrease of pH (Fig. 7), which is confirmed by the detected increase in the rate of reduction of cobalt-containing complexes with a decrease of pH. Moreover, during reduction in an alkaline medium (pH 8), at least, two forms of cobalt are deposited (perhaps, α and β cobalt), since at the curves of the anodic dissolution at pH 8 two peaks are detected (Fig. 6).

Complexes Co(II) are known to be oxidized in an alkaline medium to Co(III). The comparison of curves *4* and *5* shows that one peak at the curves of the anodic dissolution is increased after the air is blown through the electrolyte (for oxidizing the cobalt complex) for a few hours. Obviously, one form of cobalt that is being formed is connected with the reduction of the oxidized complex (Fig. 6).

The amount of the deposited metal sharply increases at agitation (Fig. 7). The area of the peak of the anodic dissolution grows by ~3.5 times during agi-

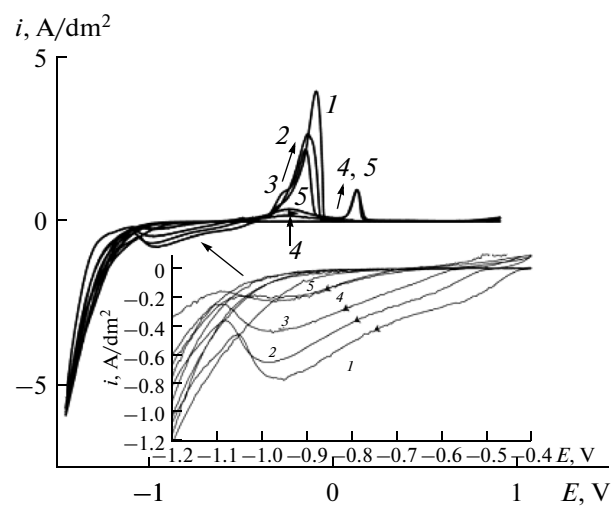

Fig. 6. Cyclic voltammograms of electrolyte 7 at pH 4.0 (*1*); 5.4 (*2*); 6.5 (*3*); 8.0 (*4*). Voltammogram 5 was obtained at pH 8.0 after air bubbling. The insert shows the cathodic cycles of voltammograms.

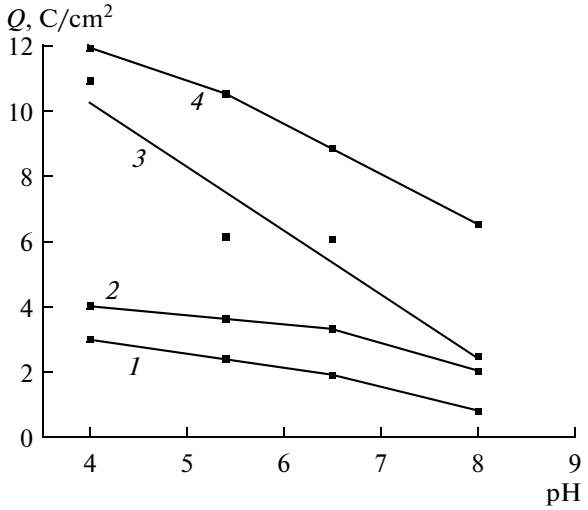

Fig. 7. Dependence of the charge values spent for anodic dissolution during cycling of electrolytes 7 (*1*, *3*) and 1 (*2*, *4*) without agitation (*1*, *2*) and with it (*3*, *4*).

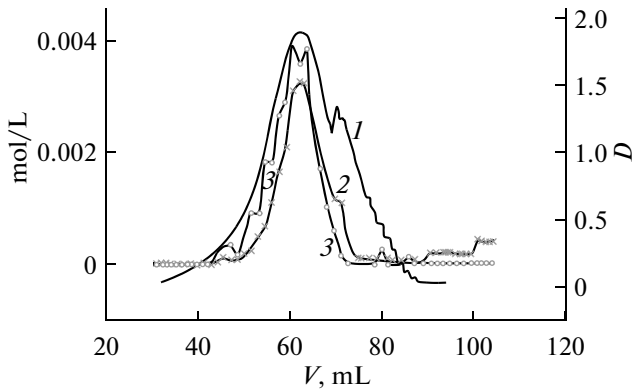

Fig. 8. Gel-chromatogram (*1*) and the concentrations of cobalt (*2*) and tungsten (*3*) in respective fractions of electrolyte 1 at pH 5.4.

tation at pH 4, and, to a lesser degree, at pH 8 (Fig. 7). The effect of hydrodynamics on the deposition (dissolution) rate is in support of the hypothesis that the process of cobalt reduction from its complexes (different at various pH) is either controlled by diffusion (ion mass transfer) or hydrodynamics affects the pH of the near-electrode layer, and, as a consequence, the nature of the reduced complex changes (see also, e.g., [19]).

Cobalt-Tungsten Complexes

The combination of the preparative gel-chromatographic separation and photocolorimetric determination of cobalt and tungsten in the products of separation shows that the main component of the solution is a heterometallic cobalt–tungsten-containing gluconate complex with a ratio of metals in the complex close to 1 : 1 and a molecular mass of the order of 1000 g/mol (Fig. 8). In addition, the second peak of the chromatogram, with a lower molecular mass, (see also the second peak in Fig. 5) is obviously connected with the presence of a pure cobalt complex in the solution, as the cobalt concentration in those products of separation substantially exceeds the tungsten concentration (compare curves *2* and *3* in Fig. 8).

Table 2 demonstrates that not all cobalt is registered in the acidic medium (~77% at pH 4 and 90% at pH 5.4) and the concentration of cobalt determined in the separation products with a lower molecular mass grows (Fig. 8). Obviously, in an acidic medium, cobalt can exist not only as a complex compound but also as a hydrated cobalt (II) ion, whereas, in an alkaline medium, the share of the high molecular complexes of cobalt is increased (Table 2). Unlike cobalt (II) ions, almost all amount of tungsten is in the complexes with a higher molecular mass, and it can easily be detected in the separation products (Table 3).

With increasing pH, the formation of cobalt complex with a very high molecular mass (above 1360 g/mol) is noticed (Fig. 9). Here, the heterometallic cobalt–tungsten-containing gluconate complex also exists with the cobalt–tungsten ratio being close to unity (Fig. 9). However, in this case (both at pH 6.5 and pH 8), the maxima of the peaks of the compounds

Table 2. Cobalt content (in metal, mg) in studied fractions of electrolyte

	pH 4.0	pH 5.4	pH 6.5	pH 8.0
Number of samples	50	50	40	40
Introduced into a column (mg)	~2.95			
Found (mg)	~2.26	~2.66	~2.60	~2.82
Found (%)	76.6	90.1	88.1	95.6

Table 3. Tungsten content (in metal, mg) in studied fractions of electrolyte

	pH 4.0	pH 5.4	pH 6.5	pH 8.0
Number of samples	50	50	40	40
Introduced into a column (mg)	~ 9.22			
Found (mg)	~8.78	~8.81	~9.2	~9.2
Found (%)	95.5	95.8	100	100

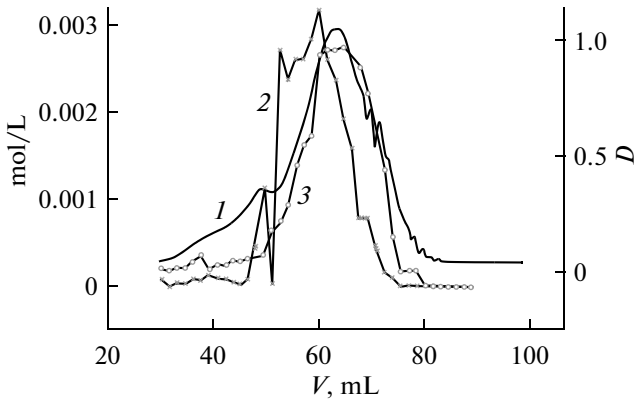

Fig. 9. Gel-chromatogram (*1*) and concentrations of cobalt (*2*) and tungsten (*3*) in respective fractions of electrolyte 1 at pH 6.5.

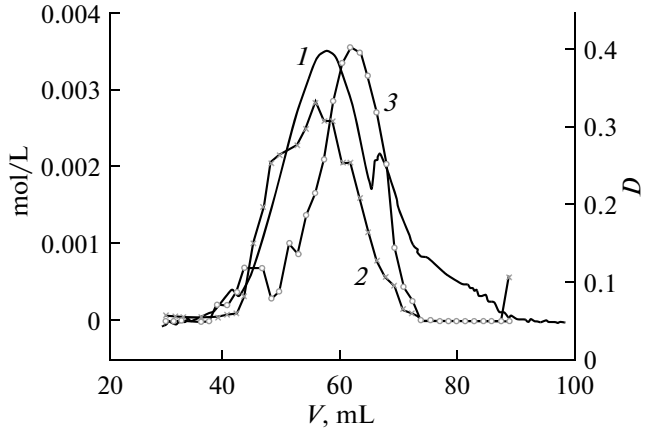

Fig. 10. Gel-chromatogram (*1*) and concentrations of cobalt (*2*) and tungsten (*3*) in respective fractions of electrolyte 1 at pH 8.0.

with tungsten and cobalt are somewhat different in the separation products (Figs. 9, 10). The reasons for this discrepancy are yet to be studied.

As a result of electrodeposition, the alloy deposit is formed in those complexes and the amount of electricity consumed for the dissolution increases (Fig. 7). In this case, the rate of electrodeposition grows at agitation. In addition, the amount of the deposited metal decreases with an increase of pH at a similar analytical concentration of cobalt and tungsten in solution (Fig. 7). The formation of various products of electrodeposition is also registered, depending on pH (Fig. 11).

It is clear that, in all of the cases the formation of the deposit occurs on the electrode but with a different content of tungsten in the alloy. It can be estimated by both taking into account the shift of the potential of the anodic dissolution towards the cathodic region compared with cobalt (see the curves of the anodic dissolution in Figs. 6 and 11) and considering the increase in the quantity of electricity consumed for the anodic dissolution of the deposit (coating) (Fig. 7, curves *1* and *2*).

Changes, depending on pH, in the peaks of the anodic dissolution, whether qualitative (Fig. 11) or quantitative (Fig. 7), are by no means strong evidence of the changes in the composition of the alloy and, hence, of the influence of the complex formation on the composition of the coating, since the applied method makes it impossible to measure the composition of the coating (after cycling, the deposit is entirely dissolved). However, firstly, the qualitative difference in the peaks of the anodic dissolution attests to the fact that different products of reduction are dissolved in the anodic region. Then, specially performed measurements (not described in detail in this article but will be discussed in a separate work), showed that the composition of the coating changes under conditions of galvanostatic electrodeposition from electrolyte no. 1 at 2 A/dm^2 and at various pH.

Thus, the concentration of tungsten (at %) in the coating changes as follows: 15 (5), 23 (6), 20 (7), and 16 (8) (the respective pH value of electrolyte no. 1 is shown in brackets). Thus, a change in the composition of the coating after electrodeposition from the electrolyte with various pH values and, hence, in various complexes can be considered well-grounded.

Agitation increases the rate of electrodeposition not only of cobalt but also of its alloy (Fig. 7).

The Role of Complexation in Forming the Composition of the Coating

The results obtained allow us to infer that in gluconate electrolyte for manufacturing Co–W coatings,

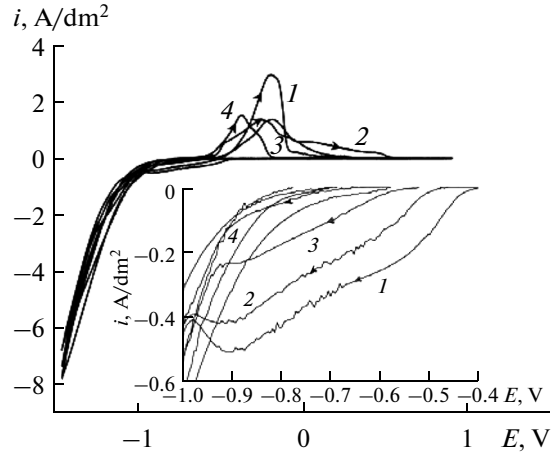

Fig. 11. Cyclic voltammograms of electrolyte 1 at pH 4.0 (*1*); 5.4 (*2*); 6.5 (*3*); 8.0 (*4*). Voltammogram 5 was obtained at pH 8.0 after air bubbling. The insert shows cathodic cycles of voltammograms.

both mixed heterometallic cobalt–tungsten gluconate complexes and pure cobalt and tungsten compounds are formed. However, tungsten cannot be reduced to a metal from the tungsten complexes but it can be from those of cobalt and cobalt–tungsten. The ratio of cobalt and tungsten is 1 : 1 in a mixed complex but in a coating this ratio differs from that observed in the mixed heterometallic compound, with a tendency towards an increase of the cobalt content in the alloy (see the above data which demonstrate that the content of cobalt in the coating formed at the current density of 1 A/dm^2 was in the range of 77–85 at % and varied with respect to pH). In addition, according to [8], in the coatings from electrolyte no. 1, depending on the current density, the concentration of cobalt varied from 74 to 84 at % possibly because there is the reduction not only of the mixed complex but also of the gluconate complex of cobalt. The ratio of the rates of those two processes and of the hydrogen reduction process, which is accompanied by alkalization of the solution, determines the composition of the alloy to be obtained.

This role of complexation in forming the composition (and properties) of a coating is not new. As a hypothesis, such a route of forming the composition of a coating during electrochemical deposition was offered, for example, in [1]. However, that idea is not totally confirmed by the results of the given work, which show that the gluconate complexes formed, both mixed and those of cobalt or tungsten, are complexes of a different nature, with a very high molecular mass, and their compositions, as well as the deposition rates, do strongly depend on the pH of solution. One of the principally important results of our analysis is the confirmation of the fact that the ratio of cobalt and tungsten is 1 : 1 in the mixed cobalt–tungsten complex. The known data on the composition of the coatings from this electrolyte, combined with those on the composition of the cobalt–tungsten complex in solution, can be considered as an indirect confirmation of the hypothesis in [1]. Unfortunately, the applied method of fixation of complexes in solution could not be used to determine their composition.

CONCLUSIONS

The results of this study give an incomplete explanation on the nature of the "anomalous" electrodeposition of alloys that was observed during the induced electrodeposition of Co–W coatings from the gluconate electrolyte. It can be accounted for by the formation of gluconate complexes in solution, with electrodeposition taking place both in the mixed heterometallic cobalt–tungsten complex with a ratio of Co–W 1 : 1 and in the cobalt complex. The ratio of the rates of the reduction of those complexes, which depends on the pH of the solution (and which affects the pH of the near-electrode layer of the process of hydrogen reduction), determines the composition of the coating. It is also clear that the finite composition of the alloy should be specified by the processes on the surface of the electrode, which were out of the scope of the given paper However, no doubt, the precursors for obtaining the alloys as coatings are cobalt and mixed cobalt–tungsten complexes formed in solution.

ACKNOWLEDGMENTS

The authors thank professor H. Cesiulis for fruitful discussions of the results of the study.

This investigation was performed in the framework of the following projects: "Electrochemical Methods for Manufacturing and Treatment of New Materials and Coatings with Improved Functional Properties" no. 11. 817. 05. 05A, financed by the Academy of Sciences of Moldova; the project of Shevchenko State University of Pridnestrovie, as well as FP7 IRSES, TEMADEP, no. 05-104-7540.

REFERENCES

1. Eliaz, N. and Gileadi, E., Codeposition of alloys of tungsten, molybdenum and rhenium with transition metals, *Modern Aspects of Electrochem.,* 2008, vol. 42, pp. 191–301.
2. Tsyntsaru, N., Cesiulis, H., Donten, M., Sort, J., Pelliccer, E., and Podlaha-Murphy, E.J., Modern trends in tungsten alloys electrodeposition with iron group metals, *Surf. Eng. Appl. Electrochem.*, 2012, vol. 48, no. 6, pp.491–520.
3. Weston, D.P., Shipway, P.H., Harris, S.J., and Cheng, M.K., Friction and sliding wear behavior of electrodeposited cobalt and cobalt-tungsten alloy coatings for replacement of electrodeposited chromium, *Wear*, 2009, vol. 267, pp. 934–943.
4. Weston, D.P., Harris, S.J., Capel, H., Ahmed, N., Shipway, P.H., and Yellup, J.M., Nanostructured Co–W coatings produced by electrodeposition to replace hard Cr on aerospace components, *Trans. Inst. Met. Finish.*, 2010, vol. 88, no. 1, pp. 47–56.
5. Tsyntsaru, N., Belevsky, S., Dikusar, A.I., and Celis, J.-P., Tribological behavior of electrodeposited cobalt-tungsten coatings. Dependence on current parameters, *Trans. Inst. Met. Finish.,* 2008, vol. 86, no., 6, pp. 301–307.
6. Brenner, A., *Electrodeposition of Alloys*, New York: Academic Press Inc, 1963.
7. Podlaha, E.J. and Landolt, D., Induced codeposition. I. An experimental investigation of Ni-Mo alloys, *J. Electrochem. Soc.*, 1996, vol. 143, no. 3, pp. 885–892.
8. Weston, D.P., Harris, S.J., Shipway, P.H., Weston, N.J., and Yap, G.N., Establishing relationships between bath chemistry, electrodeposition and microstructure of Co–W Alloy coatings produced from a gluconate bath, *Electrochim. Acta*, 2010, vol. 55., no. 20, pp. 5695–5708.
9. Podlaha, E.J. and Landolt, D., Induced codeposition. II. A mathematical model describing the electrodeposi-

tion of Ni-Mo alloys, *J. Electrochem. Soc.*, 1996, vol. 43, pp. 893–899.

10. Podlaha, E.J. and Landolt, D., Induced codeposition. III. Molybdenum alloys with nickel, cobalt and iron, *J. Electrochem. Soc.*, 1997, vol. 144, no. 5, pp. 1672–1680.
11. Belevskii, S.S., Yushchenko, S.P., and Dikusar, A.I., Anomalous electrodeposition of Co–W coatings from a citrate electrolyte due to the formation of multinuclear heterometallic complexes in the solution, *Surf. Eng. Appl. Electrochem.*, 2012, vol. 48, no. 1, pp. 97–98.
12. Osterman, L.A., *Khromatographiya belkov i nukleinovykh kislot* (Chromatography of albumens and nucleinic acids), Moscow: Nauka, 1985.
13. Sharlo, G., *Metody analiticheskoi khimii. Kolichestvennyi analiz neorganicheskikh soedinenii* (Methods of analytical chemistry. Quantitative analysis of inorganic compounds), vol. 2, Moscow: Khimiya, 1996.
14. Casela, I.G. and Di Frozo, D.A., Anodic electrodeposition of cobalt oxides from alkaline bath, containing gluconate complexes on glassy carbon, *Electrochim. Acta*, 2011, vol. 56, pp. 7536–7540.
15. Casela, I.G. and Contrusi, M., Cobalt oxide electrodeposition on various electrode substrates from alkaline medium containing Co-gluconate complexes: a comparative voltammetric study, *J. Solid State Electrochem.*, 2012, vol. 16, no. 12, pp. 3739–3746.
16. Ashton, J.F. and Pickering, W.F., Cobalt (II)-gluconate complexes., *Australian J. Chem.*, 1970, vol. 23, pp. 1367–1373.
17. Aveston, J., Hydrolysis of tungsten (YI): ultracentrifugation, acidity measurements, and Raman spectra of polytungstates, *Inorg. Chem.*, 1964, vol. 3, pp. 981–986.
18. Kortly, S. and Sucha, L., *Handbook of Chemical Equilibria in Analytical Chemistry*, Eds. Chalmers, R.A. and Masson, M.N.Y.: Wiley, 1985.
19. Belevskii, S.S., Cesiulis, H., Tsyntsaru, N.I., and Dikusar, A.I., The role of mass transfer in the formation of the composition and structure of Co–W coatings electrodeposited from citrate solutions, *Surf. Eng. Appl. Electrochem.*, 2010, vol. 46, no. 6, pp. 570–578.

Translated by M. Baznat

ISSN 1068-3755, Surface Engineering and Applied Electrochemistry, 2014, Vol. 50, No. 1, pp. 28–32. © Allerton Press, Inc., 2014.

Low-Reflective Surface Texturing for Large Area Multicrystalline Silicon Using NaOH–NaClO Solution[1]

Jing Dong and Shi-Hua Huang

Physics Department, Zhejiang Normal University, Zhejiang 321004, China

e-mail: huangshihua@zjnu.cn

Received April 24, 2013; in final form, November 06, 2013

Abstract—Multicrystalline silicon surface texturing using the mixed etching solution of the sodium hydroxide (NaOH) and of the sodium hypochlorite (NaClO) has been investigated. The reaction rate during the texturing process is easier to control due to the presence of NaOCl as an oxidizing agent in NaOH solution. The advantage of this etching is that the uniform mc-Si surface texturing with a low step height and less grain boundary delineation can be obtained. The Mc-Si surface after NaOH–NaOCl mixed etching with the 1 : 4 ratio in the case of 20% NaOH has the optimum light trapping effect. In the case of the optimum etching condition, the average reflectivity for the textured surface of a large area (156 × 156 mm^2) mc-Si can be reduced to less than 10%.

Keywords: multicrystalline silicon, NaOH–NaOCl texturing, reflectivity

DOI: 10.3103/S1068375514010050

INTRODUCTION

Surface texturing plays a critical role in the silicon solar cell performance, affecting both reflectance and light trapping. Numerous techniques for texturing monocrystalline or multicrystalline silicon have been examined in the past decades. For monocrystalline silicon, an isotropic etching by alkaline solution such as sodium hydroxide (NaOH) or potassium hydroxide (KOH) results in the surface covered by pyramids, which can collect the reflected light and trap the light inside the cells by repeated reflections. As opposed to multicrystalline silicon (mc-Si), which is today the dominant technology for solar cells fabrication, this alkali texturing has little usefulness and cannot generate sufficient effect due to its inherently randomly oriented grains. Nowa-days the industry-standard solution is an isotropic etching with hydrofluoric acid (HF) and nitric acid (HNO_3). This etching process simultaneously removes some saw damage and forms a scalloped surface texture, and is fast enough to be performed with an inline tool. However, its main drawback is that both cell voltage and current do not simultaneously maximize. The reason is that the typical isotropic etching process still leaves residual saw damage in the wafer, because a deeper etching would result in a non-textured surface.

A new method has been developed recently for mc-Si texturing [1], and isotropic etchants such as NaOH and sodium hypochlorite (NaClO) solution have been adopted. NaOH–NaClO texturing can generate low mc-Si grain boundaries and thus has an excellent isotropic etch characteristics to enhance related solar cell parameters [2]. For the industrial production of mc-Si solar cells, the NaOH–NaClO texturing can provide a convenient and low-cost alternative [3]. In addition, sodium chloride (NaCl) is the main reaction product formed during etching, so there is no special requirement for the disposal of the reaction product. However, NaOH–NaClO tex-turing is also having its inherent problems in the photovoltaic application due to its polishing effect [4].

The present paper reports the investigation of the surface morphology and the reflectance of mc-Si etched by NaOH–NaClO texturing method. Using the optimum etching conditions of the NaOH–NaOCl solution, the average reflectivity in the wavelength range of 350–800 nm for the textured surface of a large area (156 × 156 mm^2) mc-Si can be reduced to less than 10%.

EXPERIMENTAL DETAILS

Boron-doped *p*-type mc-Si wafers with the resistivity of 1.0~3.0 Ω/cm and the size of 156 × 156 mm^2 were used in the present study. The etchant solution

[1] The article is published in the original.

was heated with a temperature-controlled hot plate. While texturing with the NaOH–NaOCl solution, the concentration of NaOH solution as well as the ratio of NaOH and NaOCl (AR, 10.5%) varied. The key parameters as studied here in the process steps of texturing with the solution of NaOH–NaCl can be described as follows: the ratio of NaOH and NaClO, the concentration of NaOH, the etching time, and the temperature. The temperature of mc-Si etching is an important technology parameter, and it is maintained on 80°C during the entire etching process. When the etching temperature is lower than 80°C, the etch rate reduces substantially. However, if the etching temperature is higher than 80°C, the self-decomposition rate of NaOH–NaOCl to O_2 and NaCl increases greatly [5]. The concentration of NaOH in the solution varied from 5% to 40%, the ratio of NaOH : NaClO from 1 : 1 to 1 : 6, and the etching time from 5 to 20 min. After finishing the texturing process, all Si wafers were analyzed with an optical microscope, and also the etched-off thickness was calculated from the standard gravitometry. The surface morphology was observed by scanning electron microscope (SEM) and the surface reflectance was measured using a spectrophotometer.

RESULTS AND DISCUSSION

NaOH is a well-known anisotropic etchant widely used for crystalline Si solar cell texturing and in Micro-Electro-Mechanical Systems (MEMS) application, and NaOCl is a strong oxidizing agent [4, 6]. The strong oxidation is equally effective for all crystallographic directions. It has been assumed that the mechanism of silicon dissolution is shifted from the orientation-dependent process to the isotropic "layer-by-layer" removal. The appropriate ratio of NaOCl and NaOH in the etching solution, therefore, makes the change of the behavior of etching from anisotropic towards isotropic [7]. The conventional alkali (NaOH or KOH) etching of as-cut mc-Si wafers results in high steps between successive grains, which may result in tailing off or breaking of the metal lines in the metallization stage. Smaller steps along the grain boundaries were obtained using NaOCl–NaOH etching, because lower anisotropy leads to a lower etch rate difference between the differently oriented grains.

The etching process of NaOH–NaClO texturing mc-Si is composed of two parts: oxidation and dissolution. Firstly, NaClO is a strong oxidizing agent that controls the oxidation rate, and SiO_2 is produced on the surface.

$$NaClO = Na^+ + ClO^-,$$

$$ClO - H_2O = HClO + OH^-,$$

$$Si + ClO- = SiO_2 + 2Cl^-.$$

Secondly, NaOH controls the etching of the oxide layer formed during the etching process. Namely, the SiO_2 layer can prevent NaOH rapid anisotropic corrosion.

$$NaOH = Na^+ + OH^-,$$

$$SiO_2 + 2OH^- = SiO_3^{2-} + H_2O.$$

The increase of the concentration of NaOH in NaOH–NaOCl solution can enhance the etching rate of the formed silicon oxide layer after the dissociation of NaOCl in the solution. However, too high concentration of NaOH solution will result in the polishing of mc-Si surface due to the rapid etching of the produced oxide layer. In order to minimize the impact of grain boundaries on the surface texturing, the mount of NaOH in NaOH–NaOCl mixed solution should be maintained at a reasonable value, which does not hinder the etching of the oxide layer produced by NaOH. A large proportion of NaClO in the mixed etchant will results in a large amount of the saw damage marks in the surface of the mc-Si wafers. It takes a long time to remove the damage marks, which ultimately affects the rate of industrial production. If the proportion of NaClO in NaOH–NaOCl mixed etchant is lower than a specific value, then NaOH plays the role of the rapid polishing rather than texturing. The etching time is one of the parameters that affects mc-Si surface morphology. When the etching time increases from 5 to 15 min in the case of texturing with NaOH (concentration varied from 5% to 40%) with different ratios of NaOH : NaOCl (from 1 : 1 to 1 : 6), the observation with an optical microscope indicates that the surface structures are not yet satisfactory. The etched-off thickness in almost all samples was not more than 10 μm after 15-min etching. A layer with the thickness of at least 10 μm should be removed before subjecting the silicon wafers to cell processing for proper cleaning and saw damage marks removal from the Si surface [8]. Therefore, in the present study, the etching time was fixed for 20 min for NaOH–NaOCl etching at different experimental conditions.

Figure 1 shows SEM micrographs of the textured mc-Si surfaces etched in NaOH : NaOCl = 1 : 1 solution with various NaOH concentrations (5%, 10%, 15%, 20%, 25% and 40%). When NaOH concentration is low, the etching of the mc-Si surface is not very sufficient, as shown in Figs. 1a–1c. With the increase of NaOH concentration, the etching rate of NaOH on the oxide layer formed after the dissociation of NaOCl enhances rapidly. However, too high concentration of NaOH in NaOH–NaOCl solution can cause the polishing effect on the Si wafer, as shown in Figs. 1e and 1f, which results in the flattening of the mc-Si texturing surface. The surface morphology shown in Fig. 1d indicates that 20% concentration of NaOH in the etching solution of NaOH–NaOCl with the ratio of 1 : 1 is suitable. When the ratio of NaOH : NaOCl var-

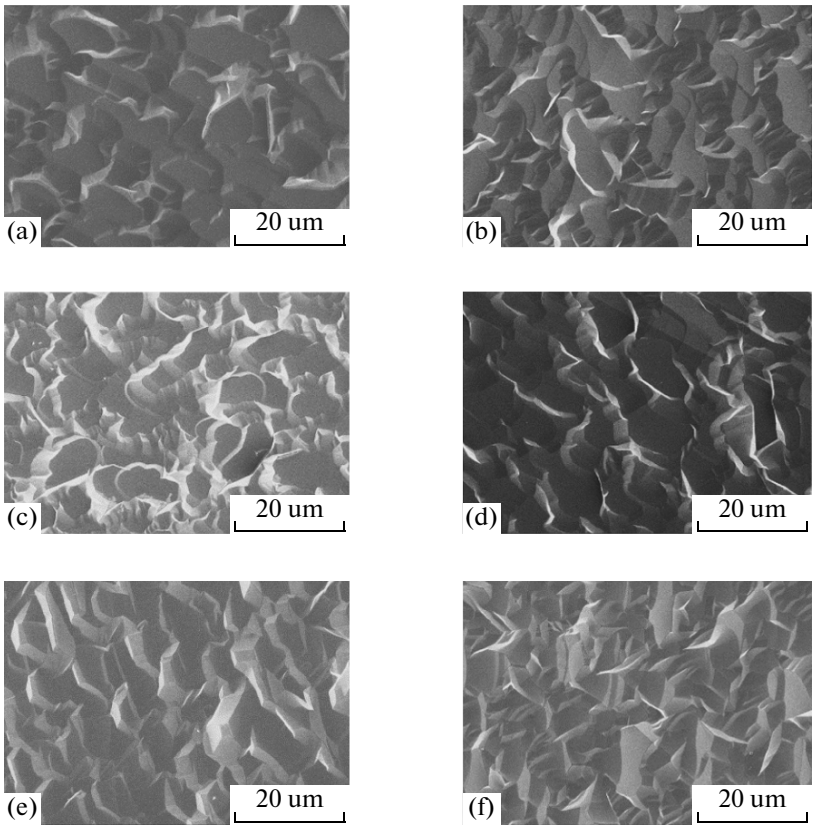

Fig. 1. SEM micrographs of textured mc-Si surfaces after etching in NaOH:NaOCl = 1 : 1 solution with NaOH concentrations of (a) 5%; (b) 10%; (c) 15%; (d) 20%; (e) 25%, and (f) 40%.

ies from 1 : 2 to 1 : 6, the changing trend of the texturing surface morphology is the same as that of 1 : 1 with the increase of concentration of NaOH. Figure 2 shows SEM micrographs of the textured mc-Si surfaces etched in NaOH : NaOCl solution, with the different ratio (1 : 1, 1 : 2, 1 : 3, 1 : 4, 1 : 5, and 1 : 6) and the 20% concent-ration of NaOH. When the NaClO ratio is small, the polishing effect of NaOH is stronger than its texturing effect, which leads to the flattening surface, as shown in Figs. 2a–2c. A too high ratio of NaClO can cause a large amount of the saw damage marks in the surface of the mc-Si wafers, which means that the texturing effect of NaOH: NaOCl etching solution becomes weak within the same etching time, as shown in Figs. 2e and 2f. Therefore, in order to obtain a uniform mc-Si surface texturing with a low step height and less grain boundary delineation, the most appropriate is NaOH–NaOCl mixed etching solution with 1 : 4 ratio and the 20% NaOH.

To compare the light-trapping effect on the surfaces of mc-Si wafers etched with different approaches, the surface reflectance was measured after each etching. Figure 3 gives the reflectivity of the textured mc-Si surfaces etched in NaOH : NaOCl = 1 : 1 solution, with NaOH concentrations of 5%, 10%, 15%, 20%, 25% and 40%. With the increase of NaOH concentration, the reflectivity of the texturing surface first increases and then decreases. When NaOH concentration is 20% in the case of NaOH : NaOCl = 1 : 1, the reflectivity is minimal and its average value in the range of 350–800 nm is 13.1%. Figure 4 shows the reflectivity of the textured mc-Si surfaces etched in NaOH:NaOCl solution, with different ratio (1 : 1, 1 : 2, 1 : 3, 1 : 4, 1 : 5, and 1 : 6) and the 20% concentration of NaOH. With the increase of the ratio of NaOH: NaOCl, the reflectivity of the texturing surface first increases and then decreases. When the ratio of NaOH:NaOCl is 1 : 4, the reflectivity is minimal and its average value in the range of 350–800 nm is 9.5%. These results of reflectivity measurements are consistent with SEM results. The reduction observed in the reflectivity could be explained by a higher roughness of the surface. The higher the roughness, the higher the scattering and the lower the reflectance. The polished surface tends to a higher reflectance due to its lower light scattering. Mc-Si surface after NaOH–NaOCl mixed etching with the 1 : 4 ratio in the case of 20% NaOH has the optimum light trapping effect, and is suitable for achieving higher efficiency of solar cells compared to that with other etching condition.

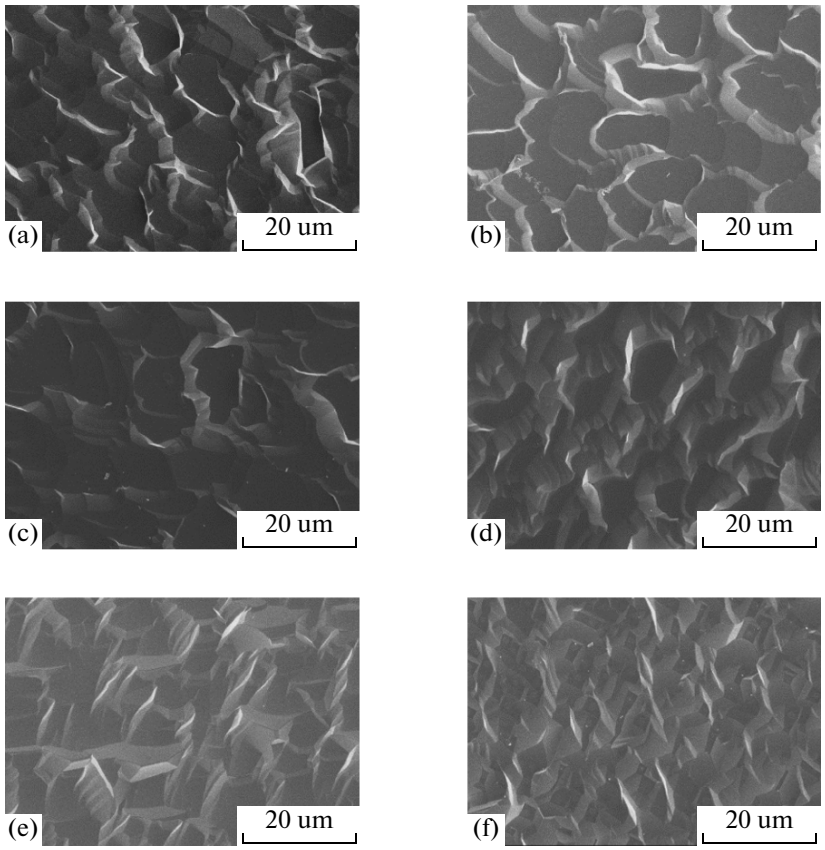

Fig. 2. SEM micrographs of textured mc-Si surfaces after etching, with 20% NaOH concentration and NaOH:NaOCl ratio of (a) 1 : 1; (b) 1 : 2; (c) 1 : 3; (d) 1 : 4; (e) 1 : 5, and (f) 1 : 6.

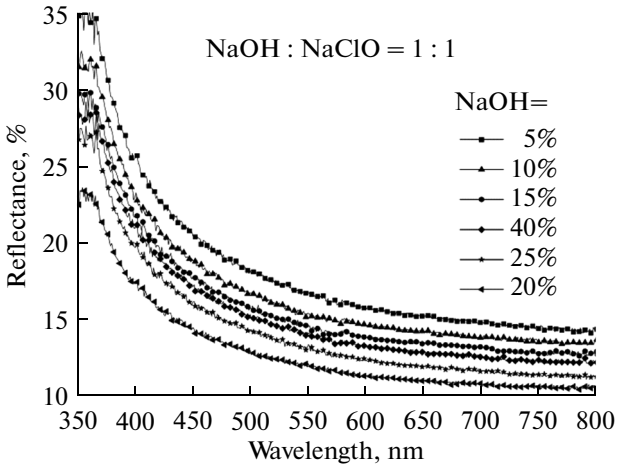

Fig. 3. Reflectance of textured mc-Si surfaces using NaOH : NaOCl = 1 : 1 etching solution with NaOH concentration of (a) 5%; (b) 10%; (c) 15%; (d) 20%; (e) 25%, and (f) 40%.

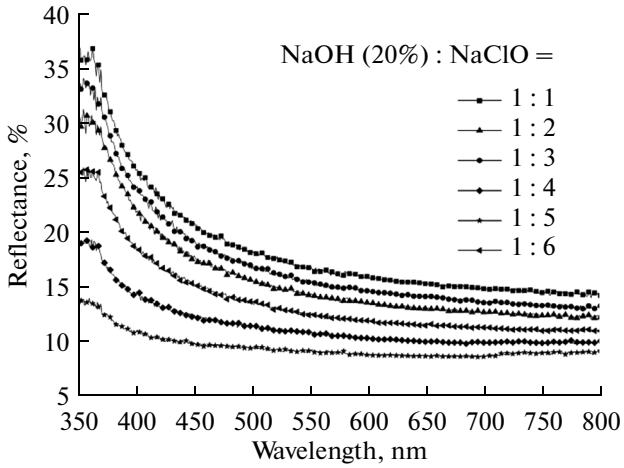

Fig. 4. Reflectance of textured mc-Si surfaces after etching with 20% NaOH concentration and NaOH:NaOCl ratio of (a) 1 : 1; (b) 1 : 2; (c) 1 : 3; (d) 1 : 4; (e) 1 : 5, and (f) 1 : 6.

CONCLUSIONS

In this work, multi-crystalline silicon surface texturing using NaOH–NaOCl mixed etching solution was investigated for solar cells fabrication of a very large area (156 × 156 mm^2). Compared with the traditional acid etching of HF–HNO_3, the reaction rate during NaOH–NaOCl texturing process is easier to control due to the presence of NaOCl as an oxidizing agent in NaOH solution. NaOH–NaOCl etching can generate the uniform mc-Si surface texturing with a low step height and less grain boundary delineation. Mc-Si surface after NaOH–NaOCl mixed etching with 1 : 4 ratio in the case of 20% NaOH has the optimum light trapping effect. In the case of the optimum etching condition, the average reflectivity in wavelength range of 350–800 nm for the textured surface of a large area (156 × 156 mm^2) mc-Si can be reduced to less than 10%. Using NaOH–NaOCl etching solution, the procedure of HCl disposal can be omitted, and the production environment is greatly improved.

ACKNOWLEDGMENTS

The authors are expressing their gratitude to the National Natural Science Foundation of China (no. 61076055), Jinhua Science and Technology Project (2009-1-141), to the Open Project Program of Surface Physics Laboratory (National Key Laboratory) of Fudan University (no. FDS-KL2011-04), to the Zhejiang Provincial Science and Technology Key Innovation Team (no. 2011R 50012) and to the Zhejiang Provincial Key Laboratory (no. 2013E10022) for their overall support of the present research.

REFERENCES

1. Gangopadhyay, U., Dhungel, S.K., Kim, K., Manna, U., Basu, P.K., Kim, H.J., Karungaran, B., Leo, K.S., Yow, J.S., and Yi, J., Novel low cost chemical texturing for very large area industrial multi-crystalline silicon solar cells, *Semicondr. Sci. Tech.*, 2005, vol. 20, no. 9, pp. 938–946.
2. Macdonald, D.H., Cuevas, A., Kerr, M.J., Samundsett, C., Ruby, D., Winderbaum, S., and Leo, A., Texturing industrial multicrystalline silicon solar cells, *Sol. Energy*, 2004, vol. 76, nos. 1–3, pp. 277–283.
3. Geetha, M., Kumar, P.S., Govindan, R., Ramu, P., Arivuselvam, L., and Anbarasan, P.M., Design of microlens focused V-groove textured silicon solar cell with different aspect ratio using ZEMAX, *Recent Research in Science and Technology*, 2010, vol. 2, no. 10, pp. 5–8.
4. Vazsonyi, E., Clercq, K.D., Einhaus, R., Kerschaver, E.V., Said, K., Poortmans, J., Szlufcik, J., and Nijs, J., Improved anisotropic etching pocess for industrial texturing of silicon solar cells, *Sol. Energ. Mat. Sol. C*, 1999, vol. 57, no. 2, pp. 179–188.
5. Hua, X.S., Zhang, Y.J., and Wang, H.W., The effect of texture unit shape on silicon surface on the absorption properties, *Sol. Energ. Mat. Sol. C,* 2010, vol. 94, no. 2, pp. 258–262.
6. Manshanden, P., Burgers, A.R., Nositschka, W.A., Voige, O., and Weeber, A.W., Silicon solar cells textured by low damage RIE with natural lithography, *Proceedings of the 29th IEEE Photovoltaic Specialists Conference (New Orleans)*, 2002, pp. 324–327.
7. Kendall, D.L., Vertical etching of silicon at very high aspect ratios, *Annual Review of Materials Research,* 1979, vol. 9, pp. 373–403.
8. Park, S.W., Kim, J., Lee, S.H., Application of acid texturing to multi-crystalline silicon wafers, *Journal of the Korean Physical Society*, 2003, vol. 43, no. 3, pp. 423–426.
9. Tyagi, R.K., Theoretical analysis of silicon surface roughness induced by plasma etching, *Surf. Eng. Appl. Electrochem.*, 2013, vol. 49, no. 1, pp. 78–82.

ISSN 1068-3755, Surface Engineering and Applied Electrochemistry, 2014, Vol. 50, No. 1, pp. 33–37. © Allerton Press, Inc., 2014.
Original Russian Text © N.I. Globa, V.D. Prisyazhnyi, A.V. Potapenko, 2014, published in Elektronnaya Obrabotka Materialov, 2014, No. 1, pp. 30–34.

Electrochemical Characteristics of $LiMn_2O_4$ in Electrolytes Based on Tetraethylene Glycol Dimethyl Ether–LiBOB Mixtures

N. I. Globa, V. D. Prisyazhnyi, and A. V. Potapenko

Inter-Agency Department of Electrochemical Energy Systems, National Academy of Sciences of Ukraine, bul'v. Vernadskogo 38a, Kiev, 03680 Ukraine

e-mail: gnl-n@ukr.net

Received July 31, 2012; in final form, November 7, 2012

Abstract—Results of the examination of the electrochemical characteristics of a lithium–manganese spinel in LiBOB–tetraethylene glycol dimethyl ether (tetraglyme) electrolytes as a function of the LiBOB concentration and the cycling and storage temperatures are described. According to the results, the lithium–manganese spinel in electrolytes based on LiBOB–tetraglyme mixtures exhibits a high specific capacity and ability for stable cycling over a wide temperature range. The conductivity of the solutions is governed by the salt concentration, and its temperature dependence is linear in the coordinates of the Vogel–Tamman–Fulcher equation in the temperature range of 10–100°C. The studies were conducted using a lithium anode in 2016 disc cells.

Keywords: salt–solvate electrolytes, conductivity, electrochemical stability

DOI: 10.3103/S1068375514010062

INTRODUCTION

Lithium-ion batteries (LIBs) are among the most intensively developed autonomous energy sources because they have a number of significant advantages over other electrochemical systems. However, the problems of improving the safety and performance and reducing the cost of LIBs remain fairly relevant. Special emphasis is placed on the development of electrolytes that can satisfy the following requirements: stability over a wide range of temperatures and electrochemical stability potentials, electric conductivity, and a high charge conservation of LIBs. Close attention is paid to the thermal and electrochemical stability and the maintenance of an appropriate level of electric conductivity and the high charge conservation of the batteries. An important role is played by the price of the environmental safety of the components that constitute the electrolyte. Typically, electrolytes in modern power supplies are aprotic solvents consisting of a mixture of cyclic and linear carbonates or esters comprising one of the lithium salts, i.e., $LiPF_6$, $LiN(CF_3SO_2)_2$, $LiBF_4$, and $LiClO_4$ [1–3]. However, these electrolytes do not meet modern requirements in many instances, because they do not provide the required level of safety and high electrochemical characteristics of lithium-ion power supplies over a wide range of operating temperatures. Therefore, studies of new solutions of electrolytes with cathode materials exhibiting high anodic potentials of their charge (e.g., $LiMn_2O_4$, $LiCoO_2$, and $LiMnPO_4$) are highly relevant.

Electrolytes based on aprotic solvents that are used in LIBs contain a lithium salt in a concentration close to 1 M. This concentration of the salt provides for the maximum conductivity. A considerable disadvantage of these electrolytes is the relatively low temperatures of the operation and storage of the LIBs, which generally do not exceed 60°C. Unlike dilute solutions, electrolytes that comprise a significant concentration of a lithium salt and form disolvates or monosolvates in a mixture with an aprotic solvent are chemically and electrochemically stable over a fairly wide temperature range.

It has been previously shown [4] that electrolytes based on tetraglyme–lithium salt mixtures exhibit high thermal stability: their electric conductivity, dynamic viscosity, and thermal stability are determined by the nature of the anion of the lithium salt and its concentration in the solution [5, 6]. It has been shown [6] that, under the galvanostatic cycling of $LiMn_2O_4$, the most consistent results are obtained in a lithium bis(oxalate)borate (LiBOB)–tetraglyme electrolyte.

A disadvantage of salt–solvate electrolytes is their relatively low conductivity, in particular, at low temperatures. This is attributed to the fact that the specific capacity and charge–discharge potentials significantly depend on the resistance of the electrolyte in the porous structure of the electrode, the interelectrode space, and at the interface. A decrease in the salt concentration leads to an increase in the conductivity; at the same time, it is accompanied by the narrowing of

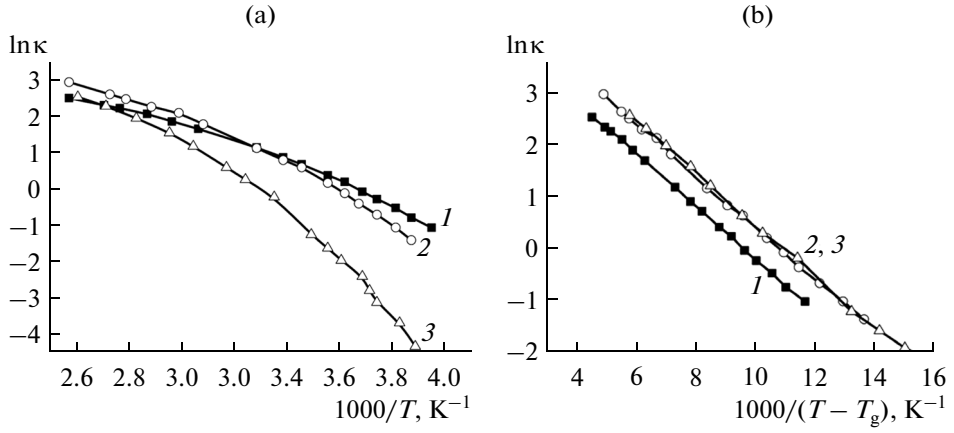

Fig. 1. Temperature dependence of the conductivity of LiBOB–tetraglyme electrolytes in accordance with (a) the Arrhenius equation and (b) the Vogel–Fulcher–Tamman equation: (*1*) 0.8, (*2*) 1.4, and (*3*) 2.3 M LiBOB.

the range of the electrochemical stability potentials and the region of high operating temperatures. Therefore, the determination of the stability of the specific characteristics of $LiMn_2O_4$ as a function of the lithium salt concentration in the electrolyte is of high priority.

This study describes some physicochemical characteristics of LiBOB–tetraglyme electrolytes and the electrochemical characteristics of $LiMn_2O_4$ as a function of the salt concentration, temperature, and discharge current density.

EXPERIMENTAL

The electrolyte solutions were prepared using the following lithium salts: bis(trifluoromethanesulfonimide) ($LiN(CF_3SO_2)_2$) with a purity of 99.9% (Aldrich) and tetraglyme with a purity of 99.9% (Aldrich). Lithium bis(oxalato)borate ($LiB(C_2O_4)_2$) was synthesized by the technique proposed in [7]. The technique consists in the microwave processing of a solid-phase mixture of oxalic and boric acids with a lithium compound. The solutions were prepared by the direct dissolution of a calculated amount of the lithium salt in an appropriate amount of tetraglyme at a temperature of 50–60°C. The electric conductivity was determined by measuring the ohmic resistance of a two-electrode cell with platinum electrodes using a Z2000 impedancemeter (Russia). The electrolytes and cells were prepared in a dry glove box. The studies were conducted at a fixed temperature in a cryostat equipped with a temperature controller and a mercury thermometer.

The electrochemical studies were carried out in cells with three (working, auxiliary, and reference) electrodes. In addition, disc cells of 2016 dimensions were used.

The cathode was prepared by mixing $LiMn_2O_4$ powder with a conductive additive (carbon black) and a Teflon binder (F42L) in a ratio of 80 : 10 : 10 (wt %). The resulting cathode mixture was deposited on a stainless steel grid acting as a current lead. After drying at a temperature of 120–125°C for 5–6 h, the cathode block was placed in a dry argon box. The cathode and anode compartments were separated using a polypropylene separator (UFIM, Russia).

The lithium anode was pressed on the cover of the 2016 cell.

The ranges of the electrochemical stability potentials of the electrolytes were determined in cells with a platinum working electrode and lithium reference and auxiliary electrodes using a P-30 potentiostat (Russia).

The galvanostatic cycling of the breadboard models was conducted using UZR 0.03–10 modules (Russia).

RESULTS AND DISCUSSION

The dependence of the conductivity on the concentration and temperature plotted in the coordinates of the Arrhenius equation for the LiBOB–tetraglyme electrolytes is shown in Fig. 1. The length of the linear portion of the $\ln\kappa - 1/T$ dependence is determined by the LiBOB concentration and corresponds to a relatively small range of the salt concentration in the electrolyte (Fig. 1a). The dependence plotted in accordance with the Vogel–Fulcher–Tamman equation (Fig. 1b) is linear over a wide range of temperatures and LiBOB concentrations, which is characteristic of electrolytes with a quasi-crystalline structure.

The electrolytes with an LiBOB concentration of about 1.0 M exhibited the maximum values of the conductivity κ: 2.8 mS/cm at 25°C, 7.87 mS/cm at 60°C, and 14.5 mS/cm at 100°C. As the temperature increases, the maximum conductivity is shifted to higher salt concentrations in the electrolyte. At 60°C, the maximum value of κ (8.25 mS/cm) corresponds to a salt concentration of 1.25 M; at 100°C, the conductivity is the maximum (16.56 mS/cm) at an LiBOB concentration of 1.7 M. These values provide the nec-

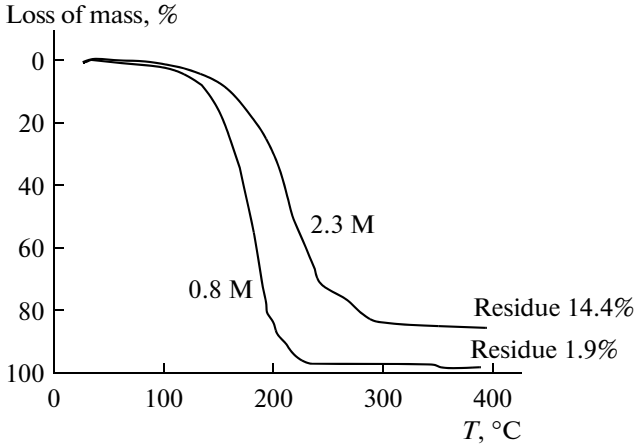

Fig. 2. Thermogravimetric characteristics of LiBOB–tetraglyme electrolytes at a heating rate of 1.5°C/min. The LiBOB concentration: (*1*) 0.8 M and (*2*) 2.3 M.

essary level of conductivity of the electrolytes, as well as their chemical and thermal resistance, at relatively high temperatures.

Tetraglyme is a solvent with a high boiling point (275°C at a pressure of 760 mmHg) [8], and the decomposition temperature of LiBOB is 302°C [9]. Therefore, it should be expected that electrolytes based on an LiBOB–tetraglyme mixture will provide high operating temperatures of LIBs with cathodes based on $LiMn_2O_4$. This is confirmed not only by the derived temperature dependences of the conductivity but also by the conducted thermogravimetric studies (Fig. 2). At a salt concentration of 1 M, the kink of the TG curve occurs at a temperature of 120–130°C. At an LiBOB concentration of 2.3 M (0.4 mole fraction), the kink of the TG curve occurs at 220–230°C. This suggests that an increase in the salt concentration leads to an increase in the thermal stability of the electrolytes.

Figure 3 shows the current–voltage dependences of the electrochemical stability of the electrolytes. The potentials of the anodic decomposition of the electrolytes in concentrated solutions are higher than in diluted solutions. This is characteristic of both room temperature and high temperatures. The potentials of the onset of the decomposition of the electrolytes are fairly high to provide for the operation of some electrode materials such as $LiMn_2O_4$, the charge voltage of which is in the potential range of 4.0–4.5 V.

It is known [10] that $LiMn_2O_4$ exhibits a significant capacity loss during cycling and storage even at relatively low temperatures (above 35°C). The capacity loss is mostly attributed to the disproportionation reaction that occurs in accordance with the equation

$$2LiMn_2O_4 \leftrightarrow Li[Li_xMn_{2-x}]]O_4 + Mn^{2+}.$$

Therefore, the content of trivalent and tetravalent manganese in the spinel composition decreases, which leads to the loss of the specific capacity of $LiMn_2O_4$.

To enhance the stability of $LiMn_2O_4$ during cycling, minor amounts of LiBOB are introduced into electrolytes containing lithium salts, such as $LiPF_6$, $LiN(CF_3SO_2)_2$, and $LiClO_4$; this makes it possible to expand the range of operating and storage temperatures of $LiMn_2O_4$ [11]. Typically, these electrolytes are composed of two or more aprotic solvents comprising a mixture of cyclic carbonates and nonlinear esters. However, the range of stable operation of the spinel in these electrolytes is limited to a temperature of 60°C [12].

The derived dependences of the specific capacity Q on the current density at temperatures of 25 and 60°C are shown in Fig. 4. At a temperature of 25°C and a current density of 100 μA/cm^2, the Q value is determined by the conductivity of the electrolyte. A decrease in the conductivity with the increasing salt concentration leads to a decrease in Q. Accordingly, the specific capacity of $LiMn_2O_4$ in a 0.8 M LiBOB solution is higher than in 1.4 and 2.3 M solutions. As the current density increases to 500 μA/cm^2, the max-

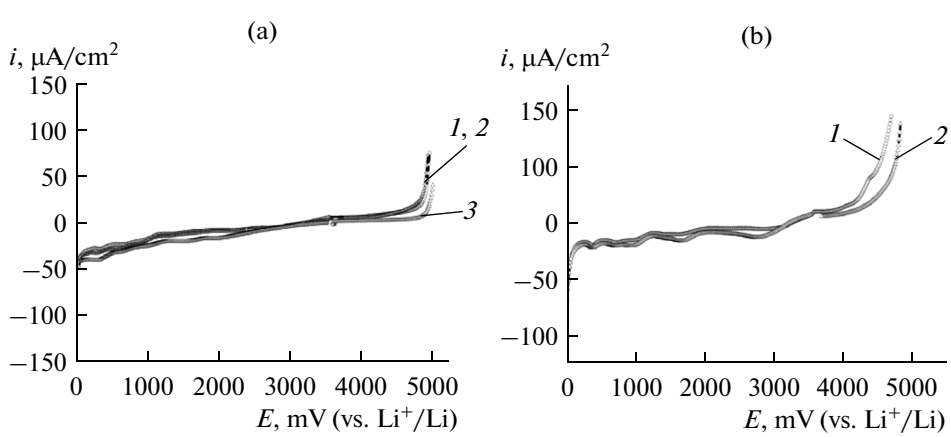

Fig. 3. Current–voltage characteristics measured using a Pt electrode in LiBOB–tetraglyme electrolytes (a) at room temperature and (b) at 60°C. The LiBOB concentration: (*1*) 0.8, (*2*) 1.4, and (*3*) 2.3 M.

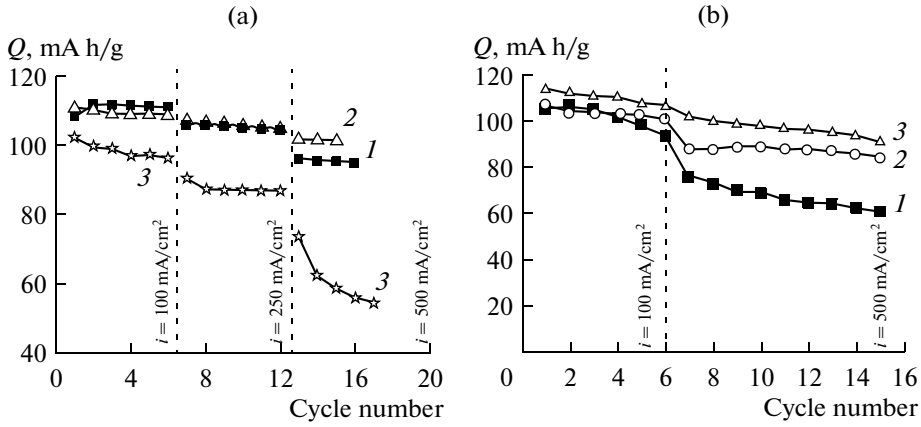

Fig. 4. Dependence of the specific capacity of $LiMn_2O_4$ on the cycle number and current density (a) at room temperature and (b) at 60°C. The LiBOB concentration: (*1*) 0.8, (*2*) 1.4, and (*3*) 2.3 M.

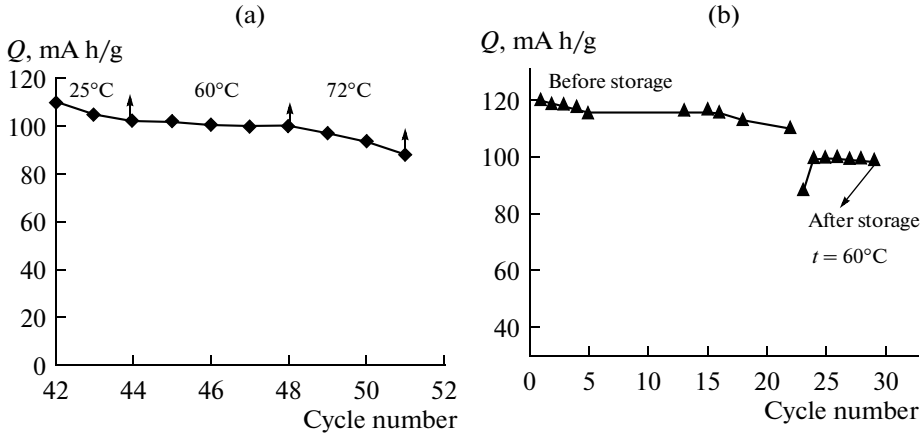

Fig. 5. (a) Effect of the temperature on the specific characteristics of $LiMn_2O_4$ during cycling and (b) the dependence of the charge conservation of $LiMn_2O_4$ at a temperature of 60°C; a 2.3 M LiBOB–tetraglyme electrolyte; a charge–discharge current of 100 μA/cm^2.

imum specific capacity is observed in the electrolyte with a salt concentration of 1.4 M. We attribute this fact to the resistance of a solid electrolyte film that is formed on the surface of the electrode. The nature and thickness of this film depend on the properties of the solvent and the lithium salt concentration, in this case, on the concentration of LiBOB. However, the proof of this assumption requires further studies and is not considered here. At a temperature of 60°C (Fig. 4b), the specific capacity value and its stability during cycling increase with the increasing salt concentration. In the electrolyte with a salt concentration of 2.3 M, the maximum specific capacity is observed. As the temperature increases to 72°C (Fig. 5), the specific capacity of the spinel slightly decreases. A decrease in Q was also observed after the storage of the cell in a charged state at a temperature of 60°C (Fig. 5b). However, during cycling, the capacity increases, although it does not achieve its initial value. It should be noted that the 2016 cell prototypes were charged at a temperature of 60°C. Under these cycling conditions, the specific capacity's value may also depend on changes undergone by the surface of the lithium electrode associated with the known electrolyte decomposition and dendrite formation processes. Tests involving cells containing a reference electrode have shown that the lithium electrode remains stable during the cycling of the Li|LiBOB–TG|$LiMn_2O_4$ electrode system even at high temperatures.

CONCLUSIONS

(1) The dependence of the conductivity of tetraglyme–LiBOB solutions in a wide range of concentrations and temperatures has been studied. It has been shown that the temperature dependence of the conductivity is linear in the coordinates of the Vogel–Fulcher–Tamman equation. The maximum conductivity value varies in the range of 10^{-3} to 10^{-2} S/cm, depends on the temperature, and is shifted from a 1 M

solution at a temperature of 25°C to a 1.7 M solution at 100°C.

(2) The thermal stability of the electrolytes increases with the increasing salt concentration; at a LiBOB concentration of 2.3 M, the electrolyte decomposition temperature approaches the decomposition temperature of the salt.

(3) The potentials of the electrochemical stability of the electrolytes in the anode region exceed 4.5 V and increase with the increasing salt concentration.

(4) It has been shown that cathodes based on $LiMn_2O_4$ are capable of stable cycling in LiBOB–tetraglyme electrolytes in wide ranges of salt concentrations and temperatures even at temperatures above 70°C.

ACKNOWLEDGMENTS

This work was supported by the National Academy of Sciences of Ukraine.

REFERENCES

1. Moumouzias, G., Ritzoulis, G., Siapkas, D., and Terzidis, D., Comparative study of $LiBF_4$, $LiAsF_6$, $LiPF_6$, and $LiClO_4$ as electrolytes in propylene carbonate–dimethyl carbonate solutions for Li/$LiMn_2O_4$ cells, *J. Power Sources*, 2003, vol. 122, no. 1, pp. 57–66.
2. Xu, K., Nonaqueous liquid electrolytes for lithium-based rechargeable batteries, *Chem. Rev.*, 2004, vol. 104, pp. 4303–4417.
3. Aurbach, D., Marovsky, B., Salitra, G., Markevich, E., Talyossef, Y., Koltypin, M., Nazar, L., Ellis, B., and Kovacheva, D., Review on electrode–electrolyte interactions related to cathode materials for Li-ion batteries, *J. Power Sources*, 2007, vol. 165, pp. 491–499.
4. Globa, N.I., Prisyazhnyi, V.D., Potapenko, A.V., and Diamant, V.A., Electrochemical behavior of a $LiMn_2O_4$ cathode in electrolyte systems based on linear ether–lithium salt solvates, *Ukr. Khim. Zh.,* 2010, vol. 76, no. 6, pp. 101–104.
5. Potapenko, A.V., Globa, N.I., Prisyazhnyi, V.D., and Davidenko, V.V., Salt–solvate electrolytes based on "tetraglyme–lithium salt" mixtures for LIBs, *Vopr. Khim. Khim. Tekhnol.*, 2011, vol. 2, no. 4, pp. 142–144.
6. Globa, N.I., Prisyazhnyi, V.D., Diamant, V.A., and Potapenko, A.V., Electrochemical characteristics of electrode materials in solvate and salt–solvate electrolytes, *Materialy XI Mezhdunarodnoi konferentsii* (Proc. XI Int. Conf.), Novocherkassk, 2010, pp. 261–262.
7. Globa, N.I., Prisyazhnyi, V.D., Diamant, V.A., and Potapenko, A.V., UA Patent 90234, 2012.
8. Tobishima, S., Morimoto, H., Aoki, M., Saito, Y., Inose, T., Fakumoto, T., and Kuryu, T., Glyme-based nonaqueous electrolytes for rechargeable lithium cell, *Electrochim. Acta*, 2004, vol. 49, pp. 979–987.
9. Larush-Asraf, L., Biton, M., Teller, H., Zinigrad, E., and Aurbuch, D., On the electrochemical and thermal behavior of lithium bis(oxalate)borate (LiBOB) solutions, *J. Power Sources*, 2007, vol. 74, pp. 400–407.
10. Yamane, H., Saitoh, M., Sano, M., Fujita, M., Sakata, M., Takada, M., Nishibori, E., and Tanaka, N., Cycle performance in each state-of-charge in $LiMn_2O_4$, *J. Electrochem. Soc.*, 2002, vol. 149, issue 12, pp. A1514–A1520.
11. Wang, S., Qiu, W., Li, T., Yu, B., and Zhao, H., Properties of lithium bis(oxalate)borate (LiBOB) as a lithium salt and cycle performance in $LiMn_2O_4$ half cell, *Int. J. Electrochem. Sci.,* 2006, vol. 1, pp. 250–257.
12. Zang, S.S., Xu, K., and Low, T.R., LiBOB-based gel electrolyte Li-ion battery for high temperature operation, *J. Power Sources*, 2006, vol. 154, pp. 276–280.

Translated by M. Timoshinina

ISSN 1068-3755, Surface Engineering and Applied Electrochemistry, 2014, Vol. 50, No. 1, pp. 38–42. © Allerton Press, Inc., 2014.

Effect of Gamma Radiation on Oxidation of Electroless Ni–P Deposited on Stainless Steel st. 304[1]

M. Y. Hashemi, A. A. Garibov, and T. N. Agayev*

Institute of Radiation Problems, of Azerbaijan National Academy of Sciences,
9 B. Vahabzade, str., AZ1143, Baku, Azerbaijan
**e-mail: agayevteymur@rambler.ru*

Received December 07, 2012; in final form, March 25, 2013

Abstract—The given work deals with the effect of gamma-irradiation on the oxidation process of the Ni–P che-mical deposition on the surface of the stainless steel marked 304. The methods used are scanning electron microscopy and X-ray analysis. As a result, it has been found out that after gamma-irradiation the surface of the Ni–P layer is completely covered with cracks, and on the surface of this layer a high content of oxygen and phosphor has been detected because of formation of the P_2O_5 oxide.

Keywords: Ni–P layer, surface morphology, gamma-radiation, structure

DOI: 10.3103/S1068375514010074

INTRODUCTION

Electroless plating is carried out via the redox reaction of an oxidizer and a reductant in an electrolyte solution. It is an autocatalytic process widely used for the production of uniform, less porous, adherent deposit for many industrial applications [1]. Electroless plating is a chemical reduction process that depends upon the catalytic reduction of a metallic ion in an aqueous solution containing a reducing agent and the subsequent deposition of a metal without the use of electrical energy [2]. Electroless nickel coatings have gained popularity due to their inherent properties like excellent resistance to corrosion, wear and abrasion [3]. In particular, electroless nickel—phosphorus plating has been used as a functional coating due to the advantage of corrosion [4]. Electroless nickel, as an engineering coating, is used in many industrial applications, for instance, nuclear engineering, aerospace, automotive, oil petrochemicals, textiles, etc. Nuclear reactor parts are coated with electroless nickel, as an engineering coating, so as to improve their corrosion and wear resistance [2]. The radiolysis of the primary coolant water by gamma radiation in the water-cooled nuclear reactors is often related to corrosion problems. The interaction of gamma radiation with aqueous solutions produces a host of transient radicals, ion and stable molecular species. In addition to unstable radicals, hydrogen peroxide is the most stable molecular species generated by water radiolysis [5, 6]. Various studies have been done on the effect of H_2O_2 induced change on the surface characterization of stainless steels extensively used in the water-cooled nuclear reactors [7–9]. So far, there is no reported study on the effect of gamma radiation on the surface characteristics of electroless Ni–P deposition. From scientific and technological points of view, surface characterization of coatings has of great importance because in any application it is the surface of the material that is in contact with the surroundings [10]. In the given paper we have investigated the effect of gamma radiation induced change on the surface morphology of electroless Ni–P deposited on stainless steel st. 304. The methods used are: Scanning electron microscopy (SEM) equipped with energy-dispersive X-ray analysis (EDX) system and Atomic Force Microscopy (AFM). Chemical characterization of the surface was performed by the X-ray photoelectron spectroscopy (XPS).

EXPERIMENTAL PROCEDURE

Electroless Ni–P coatings were deposited on specimens made of stainless steel st. 304 with dimensions of 15 mm × 10 mm × 0.35 mm. Prior to the coating deposition, the surfaces of the specimens were ground with abrasive paper of 400–1200 grit. After that the specimens were cleaned with alkaline solution at 60–80°C for 10–20 min and then rinsed with water. Subsequently the specimens were immersed for 2 min in 37% HCl at 30°C and then washed in cold running water and in distilled water. Next, the specimens were activated for 2–3 s in the 10% HCl and 90% H_2SO_4

[1] The article is published in the original.

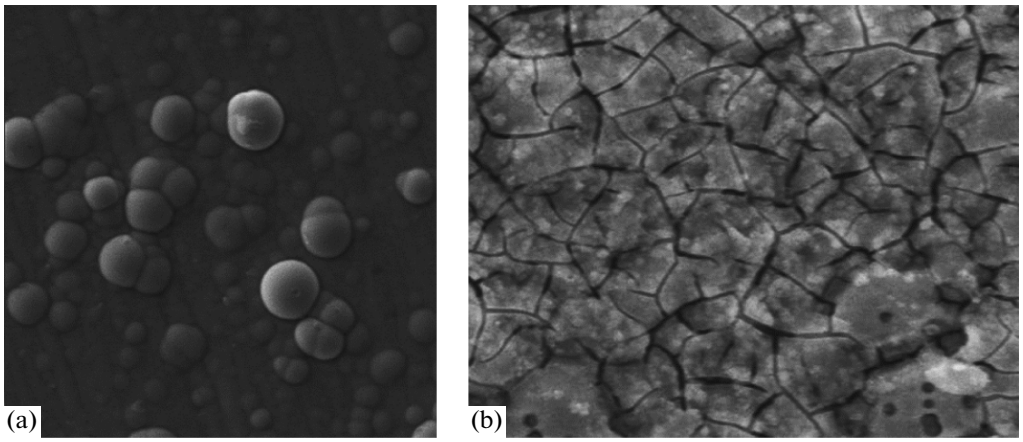

Fig. 1. SEM surface morphology of electroless Ni–P deposit: (a) before and (b) after radiation.

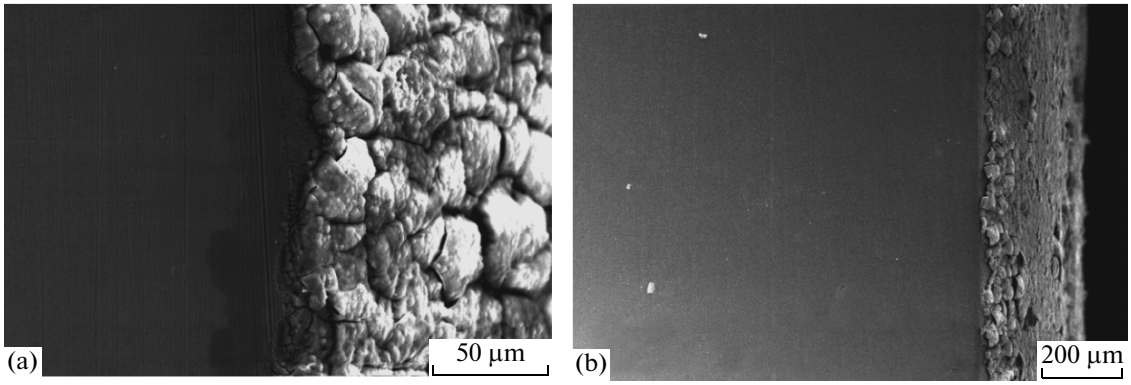

Fig. 2. Cross sectional SEM micrograph of Ni–P deposit to gamma radiation influence: (a) 500×, and (b) 85× magnifications.

solution, washed with distilled water and immediately subjected to the electroless nickel-phosphorus deposition process. The contents of chemicals for the electroless plating baths were nickel sulfate (21.2 g/L), sodium hypophosphite (24 g/L), lactic acid (23 mL/L), and propionic acid (1.8 mL/L). The pH value of the plating bath was fixed at 4.2 and adjusted with 20 vol % H_2SO_4 and 50 vol % NH_4OH solutions. The Ni–P deposits were irradiated in the 30% H_2O_2 environment with a ^{60}Co gamma source at a dose rate of 0.48 Gy/s at ambient temperature. The microstructure and chemical composition of the surface layer were characterized with SEM (Model SSI, CSEM) equipped with EDX. XPS was used to study the structure of the surface after gamma radiation. In order to analyze the surface topography of the deposits, AFM measurements were carried out at room temperature to obtain surface topological images of the samples within the scale of 10 μm × 10 μm.

RESULTS AND CONCLUSION

Figures 1a and 1b show the SEM surface morphology of the electroless Ni–P deposit before and after radiation. The surface morphology of the Ni–P deposit shows the hemispherical nodular structure, which indicates a typical amorphous structure of the deposit. The diameter of the biggest nodule size on the surface reached about 100 nm. No micro crack was observed at the surface of the deposit. After radiation, the surface morphology of the Ni–P deposit showed a completely cracked structure; no hemispheres were found on the surface.

Figures 2a and 2b display the cross sectional SEM micrographs of the Ni–P deposit to gamma radiation influence. As seen, the Ni–P deposit is completely fragmented. Fragments near the surface have been detached from the surface most probably due to a polishing process.

Chemical composition of the electroless Ni–P deposit before and after gamma radiation

Element	Before radiation (wt %)	After radiation (wt %)
Ni	87.4	48.6
P	12.6	11.8
O	–	38.6

The chemical composition of the electroless Ni–P deposit before and after gamma radiation is presented in table. The Ni–P deposit contains 12.6 wt % phosphorus and 87.4 wt % nickel, which indicates the amorphous structure of the Ni–P deposit. The P content in the Ni–P layer is very important because it allows to easily control the properties of the Ni–P alloy [11]. In general, the electroless Ni–P deposits can be classified as low (1–5 wt % P), medium (5–8 wt % P) and high (9 wt % P and more) phosphorus deposits, based on their phosphorus contents. It has been shown that a low phosphorus content in coatings is crystalline whereas the coatings with a higher phosphorus content are amorphous [12]. After gamma radiation the surface of the Ni–P deposit showed a considerable oxygen concentration (38.6 wt %). Also the Ni content decreased from 87.4 wt % to 48.6 wt % after radiation.

The EDX spectra of the electroless Ni–P deposit before and after gamma radiation are shown in Figs. 3a and 3b.

High oxygen content of the Ni–P deposit after gamma radiation most likely originated from the oxidation of the Ni–P deposit in the H_2O_2 environment. The XPS full scan spectra of the Ni–P deposit and narrow scan spectra of oxygen on the Ni–P surface after gamma irradiation are depicted in Figs. 4a and 4b. As is seen, the surface of the Ni–P deposit after gamma irradiation contained elements of oxygen and carbon (Fig. 4a), with the main peak from C(1*s*) at 284.2 eV as a reference and a peak from O(1*s*) at 532.2 eV energy (Fig. 4b), which is related to the (O–P) formation visible in the XPS spectra [12]. There were not any peaks from Ni (2*p*3/2) in Ni, Ni–P, NiO, and $Ni(OH)_2$ in the XPS spectra, respectively (Fig. 4a).

This fact indicates a preferential segregation of P to the surface, which could be due to its low heat of evaporation or due to the strain energy. The heat of evaporation of P is 2.97 Kcal/g-atom, while that of Ni is 91 Kcal/g-atom [13]. That might be the cause for the predominant formation of (O–P) on the surface of the deposit after gamma irradiation in the H_2O_2 environment.

Three dimensional AFM images of the Ni–P deposit before and after gamma radiation are shown in Fig. 5. As is seen, the surface of the Ni–P deposit before radiation (Fig. 5a) is relatively regular and consists of typical hemispherical nodules distributed over the scanned area. After radiation the surface of the Ni–P deposit shows a clustered structure. Each cluster consists of small nodules agglomerated together. Breaking off of positions was observed between the clusters that illuminate the cracked structure of the surface, as shown by arrows.

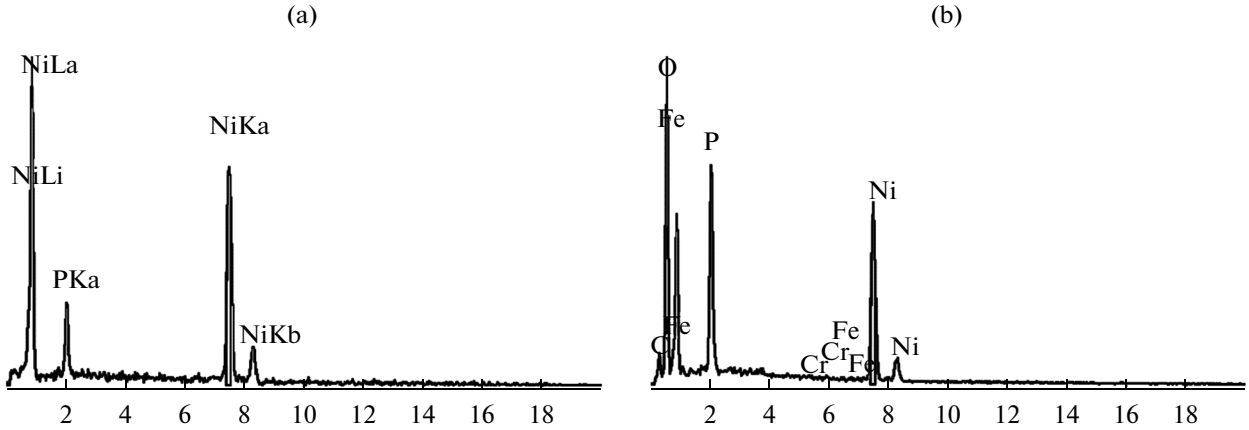

Fig. 3. EDX pattern of the electroless Ni–P deposit before and after gamma radiation.

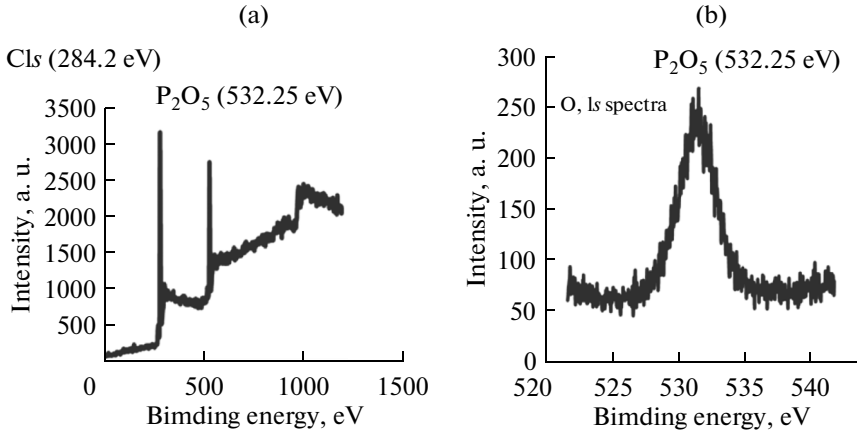

Fig. 4. XPS spectra: (a) full scan spectra of the surface of Ni–P film, and (b) narrow scan analysis of the surface element of O after gamma radiation.

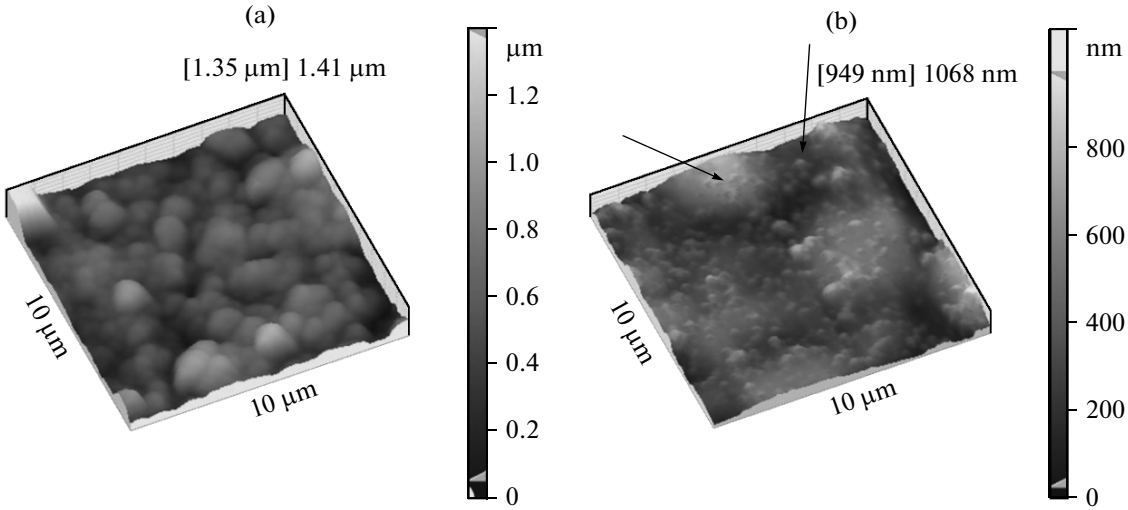

Fig. 5. Three dimensional AFM images of Ni–P deposit: (a): before and (b) after gamma radiation.

CONCLUSIONS

This investigation has found out that gamma radiation has a considerable effect on the electroless Ni–P deposit. Gamma radiation of electroless Ni–P deposits in the 30% H_2O_2 environment caused a complete fragmentation of the Ni–P deposit. This most probably was due to the oxidation of the Ni–P deposit in the H_2O_2 environment during gamma radiation. Expansion of the Ni–P deposit followed by the preferential formation of P_2O_5 oxide during gamma radiation resulted in the formation of an intensive residual stress in the structure of the Ni–P deposit, thus leading to the fragmentation of this deposit after gamma radiation. The preferential segregation of P to the surface, probably due to its low heat of evaporation or due to the strain energy, caused the preferential formation of the P_2O_5 oxide on the surface of the deposit. There were not observed any compositions from Ni (2*p*3/2) in Ni, Ni–P, NiO, and $Ni(OH)_2$ in the XPS spectra of the Ni–P deposit.

REFERENCES

1. Balaraju, J.N., Anandan, C., and Rajam, K.S., Influence of codeposition of copper on the structure and morphology of electroless Nix2013; Wx2013; P alloys from sulphate- and chloride-based baths, *Surf. Coat. Tech.*, 2006, vol. 200, pp. 3675–3681.
2. Hari Krishnan, K., John, S., Srinivasan, K.N., Praveen, J., Ganesan, M., and Avimani, P.M., An overall aspect of electroless Ni–P depositions—a review

article, *Metall. Mater. Trans. A*, 2006, vol. 37, pp. 1917–1926.

3. Balaraju, J.N., Ezhil Selvi, V., William Grips, V.K., and Rajam, K.S., Electrochemical studies on electroless ternary and quaternary Nix20P based alloys, *Electrochim Acta*, 2006, vol. 52, pp. 1064–1074.
4. Yi-Ying Tsai, Fan-Bean Wu, Yung-I Chen, Pei-Jun Peng, Jenq-Gong Duh, and Su-Yueh Tsai, Thermal stability and mechanical properties of Ni–W–P electrolessdeposits, *Surf. Coat. Tech.*, 2001, no. 1, pp. 502–507.
5. Pastina, B., Isabey, J., and Hickel, B., The influence of water chemistry on the radiolysis of the primary coolant water in pressurized water reactors, *J. Nucl. Mater.*, 1999, vol. 264, pp. 309–318.
6. Xin Lou, Ruitang, Chongsheng Long, Zhimiao, Qian Peng, and Cong, Corrosion behavior of austenitic and ferritic steels in supercritical water, *Nucl. Eng. Techn.,* 2007, vol. 40, no. 2, pp. 141–145.
7. Junichi Sugama, Shunsuke Uchida, Naoya Yamashiro, Yusuke Morishima, Tatsuya Hirose, Takahiro Miyazawa, Tomonori Satoh, Yoshiyuki Satoh, Koichi Iinuma, Yoichi Wada, and Masahiko Tachibana, Effects of hydrogen peroxide on corrosion of stainless steel (II), *J. Nucl. Sci. Techn.*, 2004, vol. 41, no. 9, pp. 880–889.
8. Genn Saji, Radiation-induced "long-cell" (macrocell) corrosion in light water reactors, *Nucl. Eng. Design.*, 2010, vol. 240, pp. 1340–1354.
9. Tan, E., Alacakir, A., Uzun, C., and Goven, O., Investigation of the radiation induced changes on the surface topology of PVC films by atomic force microscopy, *Radiat. Phys. Chem.*, 1995, vol. 46, nos. 4–6, pp. 897–900.
10. Jeong-Won Yoon, Jong-Hyun Park, Chang-Chae Shur, and Seung-Boo Jung, Characteristic evaluation of electroless nickel–phosphorus deposits with different phosphorus contents, *Microelectron. Eng.*, 2007, vol. 84, pp. 2552–2557.
11. Farber, B., Cadel, E., Menand, A., Schmitz, G., and Kirchheim, R., Phosphorus segregation in nanocrystalline Ni-3.6 at.% P alloy investigated with the tomographic atom probe (TAP), *Acta Mater.*, 2000, vol. 48, pp. 789–796.
12. Zuqiang Qi and Weiming Lee, XPS study of CMP mechanisms of NiP coating for hard disk drive substrates, *Tribol. Int.*, 2010, vol. 43, pp. 810–814.
13. Rajam, K.S. and Rajagapalan, S.R., Characterization of electroless nickel by Esca, *Mater. Chem. Phys.*, 1991, vol. 27, pp. 141–154.

ISSN 1068-3755, Surface Engineering and Applied Electrochemistry, 2014, Vol. 50, No. 1, pp. 43–49. © Allerton Press, Inc., 2014.
Original Russian Text © E.B. Khobotova, L.M. Egorova, V.I. Larin, O.A. Beshentseva, 2014, published in Elektronnaya Obrabotka Materialov, 2014, No. 1, pp. 39–44.

Regularities of Electrochemical Dissolution of Cu 62 Zn Alloy in Chloride Solutions

E. B. Khobotova[a], L. M. Egorova[a], V. I. Larin[b], and O. A. Beshentseva[a]

[a] *Kharkov National Automobile and Highway University, ul. Petrovskogo 25, Kharkov, 61002 Ukraine*
e-mail: chemistry@khadi.kharkov.ua

[b] *Scientific Research Institute of Chemistry, Karazin National University, ul. Svobody 4, Kharkov, 61022 Ukraine*
e-mail: vasili.i.Larin@univer.kharkov.ua

Received November 26, 2012; in final form, June 2, 2013

Abstract—The pattern of the electrochemical ionization and passivation of Cu 62 Zn brass in chloride solutions with different compositions is studied. The electrochemical dissolution of Cu 62 Zn alloy is shown to be controlled by ionization of the copper component in the alloy. The dissolution selectivity of the brass Cu 62 Zn components and the modification of the surface of the alloy during electrochemical etching in chloride solutions are studied. The uniform electrochemical dissolution of α-brass in an acid medium was found to occur in the presence of chlorine ions and an Fe^{3+} oxidizing agent.

Keywords: brass, ionization, etching solution, dissolution selectivity

DOI: 10.3103/S1068375514010098

INTRODUCTION

The progressive application of microelectronic components in electronic engineering expands the spectrum of printed circuits used. Among them are the standard printing boards for output components, plates for surface-mounted assemblies, modem boards for personal computers, multichip modules, high frequency boards, plates with an optical interface, etc. [1–5]. In the technologies for their manufacture, anodic processes with application of a metal, namely, copper and its alloys, are of importance. It is necessary to study the mechanisms of the processes of chemical and electrochemical dissolution of copper and its alloys in order to control the kinetics, the selectivity of the etching processes, and increasing their efficiency.

The mechanism of anodic dissolution of α-brass in chloride media was described in [4–6]. The authors described the initial dissolution selectivity of zinc, which created a surface layer enriched with copper with nonequilibrium vacancies. The anodic dissolution both of pure copper and that on the surface of brass was found to occur with the formation of strong complexes of $CuCl_n^{1-n}$ [7]. Ions of Cu^+, which result from their dissociation, enter into a balanced reaction with copper,

$$Cu^+ + e \leftrightarrow Cu,$$

and determine its potential. In the case of brass, the potential-determining reaction is different:

$$Cu^+ + e \leftrightarrow Cu^* \text{ (alloy)},$$

where Cu* (alloy) are hyperactive copper atoms in the brass surface layer, which were formed as a result of the dissolution selectivity of zinc.

Owing to the increased activity of Cu* (alloy), the stationary potential of brass is more negative than the stationary potential of copper in its own phase at the same ion concentration of the latter. In this case, Cu* ions that were formed during the anode oxidation of brass are reduced to their own phase. During the reduction, the concentration of Cu* ions decreases in the near-electrode layer of the solution; therefore, the stationary potential of the brass must shift towards the negative side, which allows us to infer the presence of dezincing of brasses [7].

It is shown [8] that, at alternating current polarization of α-brass in a chloride media, the first anodic half-period of dissolution of the alloy is controlled by the diffusion of $CuCl_2^+$ complexes from the electrode to the solution. Thus, the controlling stage of the anodic dissolution of α-brass is the dissolution of the precious component.

THEORETICAL ANALYSIS

Each of the components of the alloys during the dissolution displays its electrochemical properties. The experimental studies of electrochemical ionization of brasses [9] created a foundation for the modern image of the anodic dissolution of intermetallic phases. A.V. Vedenskii showed [10, 11] that the state of the nonequilibrium layer that is formed during the dis-

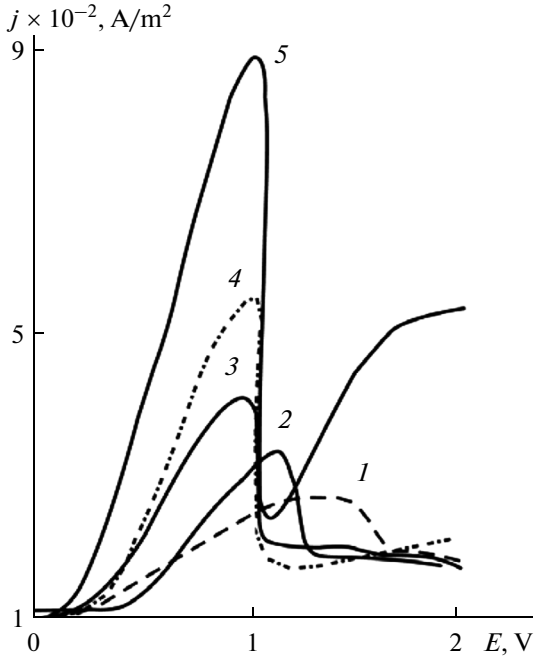

Fig. 1. Anodic polarization curves for the Cu 62 Zn alloy in NaCl solutions with the following concentrations, mol/L: (*1*) 0.1, (*2*) 0.25, (*3*) 0.5, (*4*) 1.0, and (*5*) 2.0 at $V = 2 \times 10^{-2}$ V/s and $\omega = 0$ rot/s.

solution selectivity of a homogeneous system determines the peculiarities of the ionization, the electrochemical properties of the alloy, and the change of the electrocatalytic activity of the alloys.

At present, despite the great variety of literary data, there has not yet been developed a unified theory on the chemical and electrochemical dissolution of metals. The study of the processes of electrochemical dissolution of copper and its alloys is very important for the creation of a unified theory to connect the processes that occur in the liquid phase and on the surface of the "metal–solution" for the development of the theory on passivation and for solving a number of application problems of size etching of metals and alloys.

The aim of this work is to study the regularities of the electrochemical dissolution of Cu 62 Zn brass in chloride solutions and the topography of the surface of the alloy.

EXPERIMENTAL

The electrochemical polarization measurements were carried out using a PI-50-1.1 potentiostat with a PR-8 programmer. The cyclic voltammograms (CVA) were obtained during the dissolution of Cu 62 Zn alloy in solutions of NaCl, HCl, and $FeCl_3$ with various concentrations in the potential range of $E = -0.2$–2.0 V with a potential sweep of $V = 2 \times 10^{-2}$ V/s. The reference electrode used was a silver-chloride electrode, and a platinum plate served as the auxiliary electrode. The auxiliary Pt electrode was kept for ten minutes in concentrated nitric acid prior to the measurements, after which it was rinsed thoroughly. A standard initial treatment of the surface of the disk electrode was selected that included mechanical peeling and polishing, degreasing, and chemical polishing in an H_3PO_4 solution. All the E values in this work are presented with respect to the hydrogen electrode. The accuracy of the maintenance of the potential is $\pm 3 \times 10^{-3}$ V. The error of setting the polarizing current is $\pm 2\%$. The error of a B7-21 voltmeter at the boundary of the measuring is 1 V $\pm$ 0.7%.

The measurements were performed at 25 $\pm$ 0.1°C. Thermostating was carried out using a YT-15 Y 42 thermostat. The working cell was equipped with a casing through which distilled water from the thermostat was constantly pumped. The tests were conducted with the lid closed, which was equipped with holders for the electrodes. The Luggin–Haber capillary was brought to the very surface of the working electrode. The area of the brass surface of the electrode was 6.4×10^{-5} m^2.

The concentrations of Cu(II) and Zn(II) ions in the etching solutions were determined by an atomic-absorption method using a "Saturn" spectrophotometer with wave lengths of 213.9 nm for Zn and 324.8 nm for Cu.

The morphologic peculiarities of the surface of the electrode were studied by the method of electron-probe microanalysis (EPMA) on a JSM-6390 LV electron microscope with an INCA system of X-ray microanalysis. An NT-206 scanning probe microscope equipped with a CSC-37 probe cantilever was used to examine the roughness of the electrodes and the difference in the nanosize peculiarities of the morphology of the electrode samples.

The mineralogical composition of the sediments with low solubility compounds, which are formed in the waste etching solutions, was determined using X-ray analysis on a Siemens D500 powder diffractometer in copper radiation with a graphite monochromator [12]. The initial search of the phases was performed using a PDF-1 card file [13] followed by the calculation of the X-ray diffraction patterns verified using the Ritveld method according to the FullProf program [14].

RESULTS AND DISCUSSION

The Effect of the Composition of the Electrolyte on the Electrochemical Dissolution of the Cu 62 Zn Alloy

The effect of chloride ions on the electrochemical dissolution of the Cu 62 Zn alloy was studied. Figure 1 shows the anodic polarization curves for the Cu 62 Zn alloy in NaCl solutions of various concentrations. With the shift of the potential towards the anodic area,

the current density increases, and the slope of $dj/dE > 0$ (Fig. 1, curves *1–5*). The active dissolution of brass in NaCl solutions of 0.5–2.0 mol/L (Fig. 1, curves *3–5*) is observed in the range of potentials of 0–0.8 V.

For the diluted solutions (Fig. 1, curves *1*, *2*), the Tafel fractions of the curves have a longer range of potentials. The medium of the NaCl solutions is neutral; therefore, there is an increase in the angle of the *j* slope; the *E*-curves result only from the activating effect of the chlorine ions. A similar effect of anions on the electrochemical dissolution of metals is described in [15], namely, the increasing concentrations of Cl^-, Br^-, and I^- ions in the solution is accompanied by an increase in the rate of the process of dissolution of the metal phase. The observed maximum of the current density *j* is indicative of the onset of the passivation of the surface of the alloy. The maximum of *j* increases with an increase in C^-_{Cl}. Thus, the activating effect of chlorine ions manifests itself.

In the inactive region, the rate of dissolution of the alloy is almost independent of the potential (Fig. 1, curves *1–4*), which is connected with an increase in the amount of the inactive compounds on its surface. The potential of the passivation E_p is in the range of 0.8–0.9 V (Fig.1, curves *3–5*), at which the transition of the metal from an active to a passive state starts. For curves *1* and *2*, the passivation starts at higher values of the anodic potential. The occurrence of passivation at lower E_p with a growth in the concentration of the chlorine ions can be explained by the easier deposition of CuCl from the near-electrode layer due to the parallel process of the chemical dissolution of copper. However, the range of passivation in the area of high C^-_{Cl} is short (Fig. 1, curve *5*), and the inactive state of the metal or the alloy is disturbed either partially or entirely owing to the introduction of Cl^-, Br^-, and I^- anions into the solution [15]. A new increase in *j* with the growth of the potential is observed in a 2.0 M solution of sodium chloride. The process of the disturbance of the passivity near the potential of complete passivation E_{cp} is considered by the authors [16] as resulting from the appearance in unsound sites of an inactive layer with zones of rapid dissolution, which then turn into pittings. A crucial factor for the appearance of the pittings is the rivalry between the passive action of the water and the activating action of the chlorine anions.

The shape of the *j* and *E*-curves is affected by a number of factors, one of which is the pH of the medium [16]. In the region of low pH, where the concentration of OH^- ions is low and the share of the surface occupied is insignificant, Cl^- anions can be adsorbed on a vacant surface. Under these conditions, the rate of dissolution increases with an increase in the overall concentration of anions [17]. In order to reveal the effect of the acidity of the solution on the electrochemical dissolution of the alloy, we obtained the

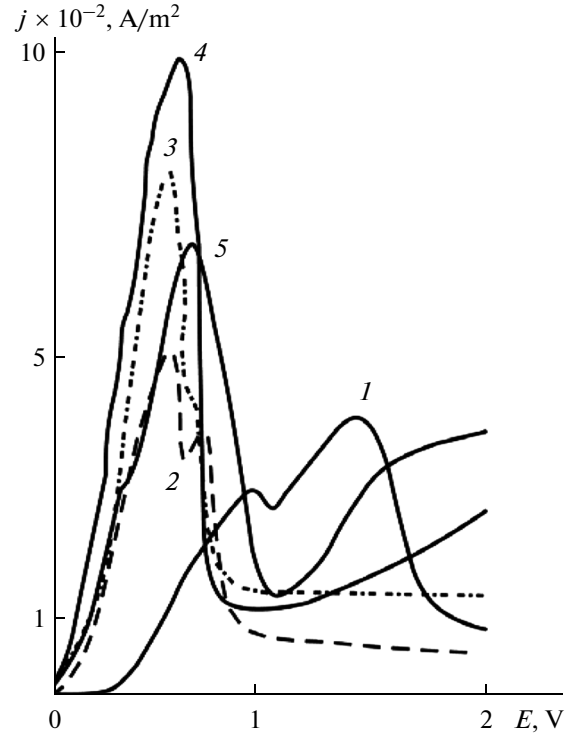

Fig. 2. Anodic polarization curves for the Cu 62 Zn alloy in HCl solutions with the following concentrations, mol/L: (*1*) 0.1, (*2*) 0.25, (*3*) 0.5, (*4*) 1.0, and (*5*) 2.0 at $V = 2 \times 10^{-2}$ V/s and $\omega = 0$ rot/s.

anodic polarization curves for Cu 62 Zn in HCl solutions with various concentrations. For curves *1–5* (Fig. 2), a large angle of slope is observed for the fraction of the active dissolution of the alloy and an increase in the *j* maxima compared to the NaCl solutions, which can be associated not only with the effect of the chlorine ions on the electrochemical dissolution of the alloy but also with the effect of the H^+ ions. In an acidic medium, the chemical dissolution of the Zn component of the alloy occurs more easily.

Two *j* extreme points were registered on curves *1–3* (Fig. 2). In [18], the appearance of two peaks on the Cu polarization curves was shown to be connected with the change in the structure of the passive layer of CuCl from spongy to dense-packed as the anode potential grows.

At high concentrations of chlorine ions, the second peak of the anodic dissolution of copper disappeared owing to the formation of the spongy surface phase of CuCl. As the concentration of the HCl solutions grew, a second maximum of the current during the brass dissolution is produced to a lesser degree, and, at curve *3*, it is in the shape of a bend of the curve. The reason for this is that both the passivation of the Cu 62 Zn alloy and the disturbance of the passivity by Cl^- ions can occur in the region of potentials of $E \geq E_p$. Note that, with an increase in the concentration of HCl in the solution, the second process predominates.

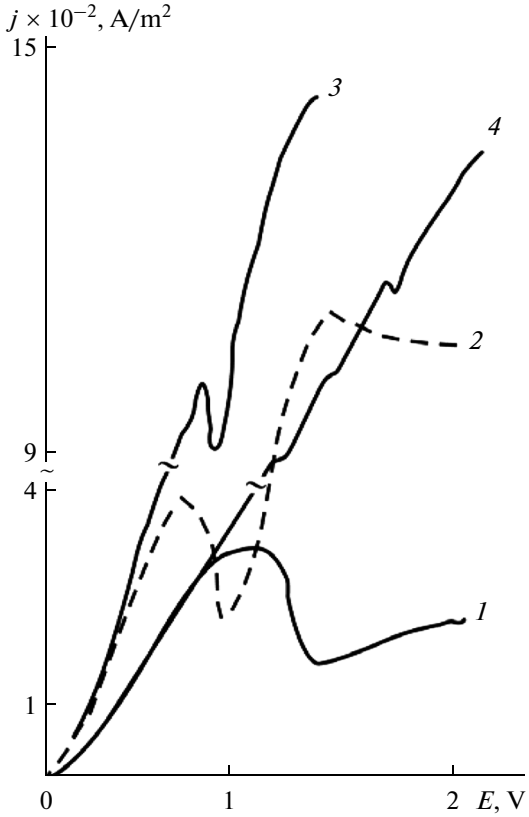

Fig. 3. Anodic polarization curves for Cu 62 Zn alloy in $FeCl_3$ solutions with the following concentrations, mol/L: (*1*) 0.1, (*2*) 0.25, (*3*) 0.5, and (*4*) 2.0 at $V = 2 \times 10^{-2}$ V/s and $\omega = 0$ rot/s.

The passivation of brass can take place not only due to the anodic polarization but also during the introduction of an oxidizing component into the solution. In [15], the intensity of the pitting corrosion of metals is found to increase in the presence of dissolved oxygen and Fe^{3+} ions. The introduction of iron(III) ions into the chloride solution caused a shift of the potential of the metal up to a critical value and to the formation of pittings [15]. The activity of the oxidizing agent is determined by the nature of the metal, the pH value, the nature and concentration of the corrosion-active anion, and the temperature and rate of mixing of the solution.

Table 1. Quantitative indices of the selectivity of the ionization of the Cu 62 Zn alloy during electrochemical dissolution in a potentiostatic mode for 120 min in chloride electrolytes with various compositions

Solution concentration, mol/L	E, V	Concentration of ions, mol/L		Selectivity coefficients	
		Cu^{2+}	Zn^{2+}	Z_{Cu}	Z_{Zn}
0.5 HCl	1.1	4×10^{-3}	6.5×10^{-3}	0.39	2.66
0.5 NaCl	0.9	1.5×10^{-3}	0.27×10^{-3}	3.5	0.3
0.1 $FeCl_3$	1.2	4.9×10^{-3}	4.2×10^{-3}	0.73	1.4

To study the influence of ions of the oxidizing agent on the shape of j of the E-curve, we obtained the anodic polarization curves using the Cu 62 Zn alloy in solutions of ferric(III) chloride with various concentrations (Fig. 3). For a 0.1 M $FeCl_3$ solution, the anodic polarization curve is characterized by a region of active dissolution of the alloy (Fig. 3, curve *1*) and the preservation of the passivation of the brass electrode.

The extremum of j is observed at $E_p = +1.1$ V. As E increases, the passive region passes to the region of repassivation. With an increase in the $FeCl_3$ concentration, the slope of the activation branch grows (Fig. 3, curves *2*, *3*). On j of the E-curves, a second j-maximum is also observed, which disappears with an increase in the concentrations of the solutions (Fig. 3, curve *4*).

The anodic j of the E-curves for the Cu 62 Zn alloy in the solutions of ferric(III) chloride are similar to those for copper. It was shown in [18] that the formation of a CuCl compound with low solubility on the surface of copper corresponds to the region of the minimum of the current, while, in the region of high anodic polarizations, CuO is found to form.

With a further increase of the potential, a new rise in the current is observed, which corresponds to the dissolution of the manufactured layer and the formation of Cu^{2+} and $CuCl^{+}$ ions and a $CuCl_2$ compound. The copper dissolution continues up to the beginning of a new passivation by copper(II) compounds.

Selectivity of the Electrochemical Dissolution of the Cu 62 Zn Alloy Components

The dissolution selectivity of the Cu 62 Zn alloy components (elemental composition, mass %: Cu—61.3, Zn—37, Al—0.24, Si—0.19) was estimated according to the values of the coefficients Z of the dissolution selectivity. The results are listed in Table 1. For example, Z_{Zn} was calculated using the formula

$$Z_{Zn} = \frac{(Zn/Cu)_{solution}}{(Zn/Cu)_{alloy}},$$

where the concentrations of Zn^{2+} and Cu^{2+} in the solution were determined by the method of atomic-absorption spectrometry, and $(Zn/Cu)_{alloy}$ is the ratio of the components in the alloy.

In a 0.5 M NaCl solution, the dissolution selectivity of the copper component of the alloy is exhibited; Zn_{Cu} exceeds Z_{Zn} by 11.7 times. In HCl solutions, Z_{Zn} exceeds Z_{Cu} by 6.8 times. This can be explained by the fact that the main factor of dissolution for zinc is the acidity of the solution (Table 1).

The data of Table 1 are supported by the results of the electron-probe microanalysis of the surface of the brass electrode after etching in chloride solutions (Table 2). After etching, in the surface layer of the brass, the Cu/Zn ratio changed as compared to that in the initial alloy: 61, 63/37, 94 = 1.62. The copper enrichment of the surface attests to the dissolution selectivity of zinc, which is more evident after the etching in $FeCl_3$ and HCl acid solutions.

In iron (III) chloride solutions, Z_{Zn} is found to exceed Z_{Cu} by 1.9 times only (Table 1); i.e., in iron(III) chloride solutions, the process of the dissolution of the alloy turns to be more uniform. Thus, it can be inferred that the presence of chlorine ions, an oxidizing agent, and the acid medium of the solution facilitates the uniformity of the electrochemical dissolution of α-brass.

The surface morphology of the Cu 62 Zn alloy after the electrochemical etching in chloride solutions was studied during the electrochemical etching of NaCl, $FeCl_3$, and HCl solutions in a potentiostatic mode for 120 min. The concentrations of the solutions were selected according to the smallest j_p value using the anodic polarization curves that were obtained in a potentiodynamic mode (Figs. 1–3).

The studies of the nanostructure of the surfaces of the electrodes was performed in fields of 2.5 × 2.5 μm. The relevant 2D and 3D maps of the surface of the etched brass electrode are shown in Figs. 4–6. The topography of the surface of the Cu 62 Zn alloy that was exposed to the anodic polarization at the potential $E_p = +0.9$ V in 0.5 M Na Cl is shown in Fig. 4.

When analyzing the topography of the brass electrode, the sufficient uniformity of the major surface can be noted. The depth of the etching is in the range of 1.86–2.1 nm.

Table 2. Fractions of the total mass and the ratios of copper and zinc in the surface layer of the Cu 62 Zn alloy

Electrolyte, mol/L	Fraction of the total mass of a component in the surface layer of the alloy, %		Ratio between the Cu : Zn components in the surface layer of the alloy
	Cu	Zn	
0.5 NaCl	18.21	44.44	0.5
0.5 HCl	54.86	29.14	1.88
0.1 $FeCl_3$	63.25	21.4	2.95

On the surface, elliptical structures of 100–200 nm crystallites are formed. These crystallites form larger structures with arbitrary forms, which reproduce the microrelief of the substrate.

The peculiarities of the topography of the surface of the Cu 62 Zn alloy that was exposed to the anodic polarization at a potential of $E_p = +1.2$ V in 0.1 M $FeCl_3$ are shown in Fig. 5.

The major part of the surface of the sample is 1200–1600 nm high, and the range is narrower than that during the etching in an NaCl solution. The typical sizes of the crystallites are 80–180 nm. The crystallites form a dense film on the surface of the electrode, which reproduces the microrelief of the substrate. Deep punctures are found on the surface of the sample resulting evidently from the conditions of the formation of the film. The topography of the surface of the brass sample after etching in 0.5 M HCl (Fig. 6) is of interest. A distinguishing feature of the surface of the

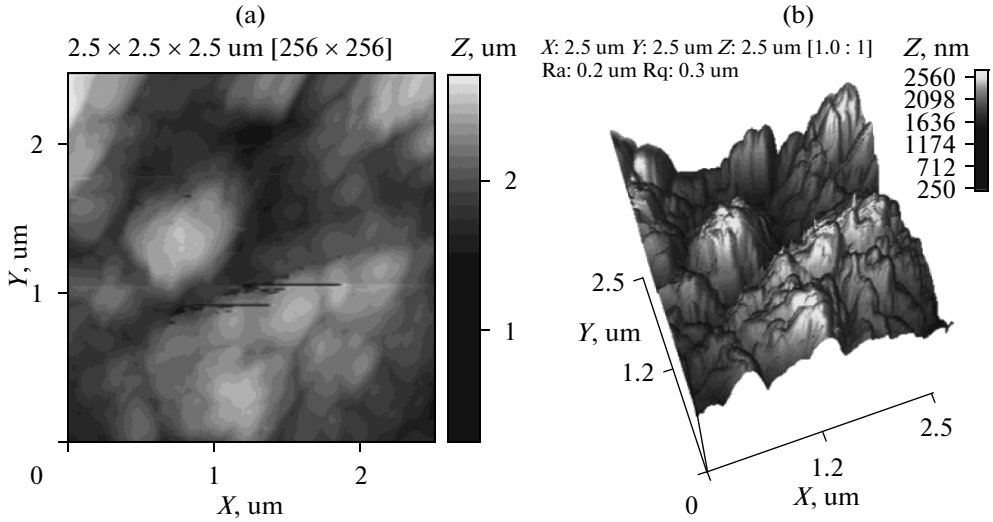

Fig. 4. Surface map of the sample of Cu 62 Zn alloy after the electrochemical etching in 0.5 M NaCl for 120 min: (a) 2D-; (b) 3D map.

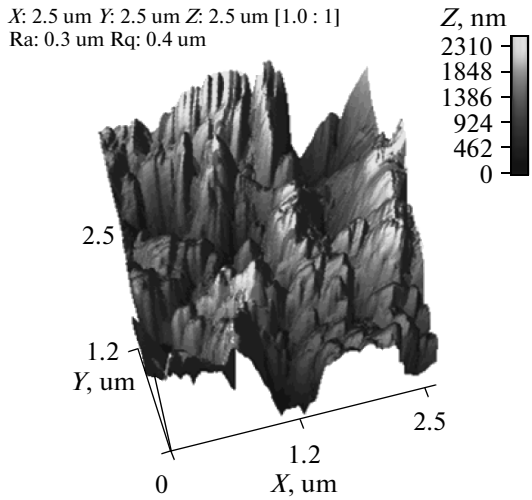

Fig. 5. Surface 3D map of the sample of Cu 62 Zn alloy after the electrochemical etching in 0.1 M $FeCl_3$.

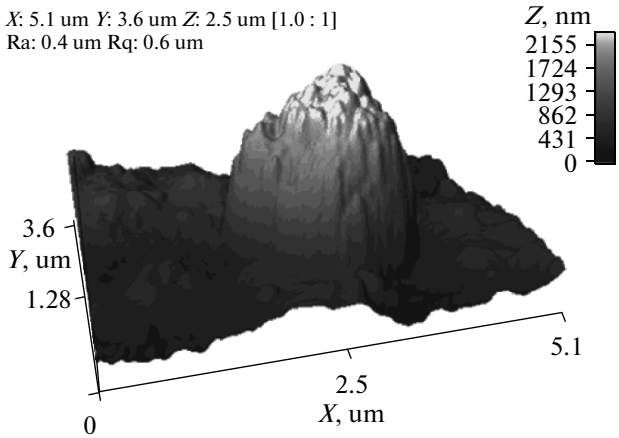

Fig. 6. Surface 3D map of the sample of Cu 62 Zn alloy after the electrochemical etching in 0.5 M HCl.

brass is the presence of large grains in the form of peaks with a thinner substructure. Those agglomerates are in a random order on the surface of the sample. Their presence results from dezincing of the Cu 62 Zn alloy in an acid medium.

CONCLUSIONS

Thus, the dependence of the pattern of the electrochemical dissolution of the Cu 62 Zn alloy on the composition of the electrolyte, the anion concentration, the acidity, and the presence of an oxidizing agent was justified. Chlorine ions in the region of high concentrations were shown to activate the process of the electrochemical dissolution of the Cu 62 Zn alloy and disturb the passivation of its surface.

The activation of the dissolution of brass in an acid medium occurs due to the easier dissolution of zinc, which is supported by the comparison of the quantitative indices of the selectivity of the ionization of the components of the Cu 62 Zn alloy in chloride solutions of various compositions. The introduction of ions of an Fe^{3+} oxidizer into the chloride solution intensifies the active dissolution of brass with the passivation being preserved.

By the method of atomic-force microscopy, we estimated the quality of the surface treatment and the uniformity of the dissolution of the Cu 62 Zn alloy with respect to the experimental conditions. The conditions of the uniform electrochemical etching of the Cu 62 Zn alloy were found, namely, an acid medium and the presence of chlorine ions and Fe(III), which is typical of $FeCl_3$ solutions.

REFERENCES

1. Cherkasov, S., Production facilities for modern printed-circuit boards. RESCO equipment and etching lines, *Elektronika: Nauka, Tekhnol., Biznes*, 2005, no. 6, pp. 66–69.
2. Flerov, V.N., *Khimicheskaya tekhnologiya v proizvodstve radioelektronnykh detalei (Chemical technology in production of radio electronic parts)*, Moscow: Radio i svyaz', 1988.
3. Evzhenko, V., Market of printed-circuit boards in the countries of Eastern Europe, *Tekhnol. Elektron. Promysh.*, 2008, no. 4, pp. 4–8.
4. Sitnikov, A.D., Pchel'nikov, A.P., Marshakov, I.K., and Losev, V.V., Dezincing of α-brasses during corrosion in chloride solutions, *Dokl. Akad. Nauk SSSR*, 1978, vol. 240, no.5, pp. 1164–1167.
5. Kondrashin, V.Yu., Bokov, G.A., and Marshakov, I.K., Initial selective dissolution α- and β-brasses and their tendency for dezincing, *Zashchita Met.*, 1994, vol. 30, no. 3, pp. 229–233.
6. Losev, V.V., Pchel'nikov, A.P., and Marshakov, A.I., Peculiarities of electrochemical behavior of selectively dissolving alloys, *Elektrokhimiya*, 1979, vol. 15, no. 6, pp. 837–842.
7. Chan Phyong Zung, Tutukina, N.M., and Marshakov, I.K., Tendency of brasses for dezincing in chloride media, *Kondensirovannye Sredy Mezhfaz. Granitsy*, 2009, vol. 11, no. 4, pp. 349–353.
8. Marshakov, I.K., Kuksina, O.Yu., and Kondrashin, V.Yu., Character of dissolution and partial electrodic processes at alternating current infra-low frequency polarization of brasses in chloride media. I. α-brass $Cu_{20}Zn$, *Phiz. khim. Poverkhn. Zashchita mater.*, 2007, vol. 43, no. 2, pp. 128–134.
9. Marshakov, I.K., Electrochemistry of intermatallic phases, *Kondensirovannye Sredy Mezhfaz. Granitsy*, 1999, vol. 1, no. 1, pp. 5–9.
10. Vvedenskii, A.V., Reorganization of the surface of the alloy after selective anodic dissolution, *Electrochim. Acta*, 1991, vol. 36, nos. 5, 6, pp. 905–910.
11. Vvedenskii, A.V. and Marshakov, I.K., Anodic dissolution of homogenous alloys at a limited power of vacancy drains, *Elektrokhimiya*, 1994, vol. 30, no. 4, pp. 459–472.

12. Bokii, G.B. and Porai-Koshits, M.A., *Rentgenostructurnyi analiz. T. 1* (X-ray analysis, vol. 1), Moscow: Mos. Gos. Univ., 1964.

13. *JCPDS PDF-1 File. Int. Committee for Diffraction Data, release*, 1994, PA, USA.

14. Rodriguez-Carvajal J. and Roisnel T., FullProf. 98 and WinPLOTR: New Windows 95/NT Applications for Diffraction. Commission for Powder Diffraction. Int. Union of Crystallography. *Newsletters*, 1998, no. 20, May-August.

15. Kolotyrkin, Ya.M., The effect of anions on kinetics of dissolution of metals, *Usp. Khim.*, 1962, vol. 31, no. 3, p. 322.

16. Freiman, L.I., Makarov, V.A., and Bryksin, I.E., *Potentsiostaticheskie metody v korrosionnykh issledovaniyakh i elektrokhimicheskoi zashchite* (Potentiostatic methods in corrosion investigations and electrochemical protection), Leningrad: Khimiya, 1972.

17. Antropov, L.I., *Teoreticheskaya elektrokhimiya* (Theoretical electrochemistry), Moscow: Vyssh. shkola, 1984.

18. Larin, V.I., Khobotov, E.B., Datsenko, V.V., Egorova, L.M., and Dobriyan, M.A., *Elektrokhimicheskoe rastvorenie medi i ee splavov v rastvorakh razlichnogo sostava i sozdanie tekhnologicheskikh protsessov regeneratsii otrabotannykh travil'nykh rastvorov* (Electrochemical dissolution of copper and its alloys in solutions with various compositions and creation of technological processes of regeneration of waste etching solutions), Kharkov: Kharkov Karazin Natl. Univ., 2009.

Translated by M. Baznat

ISSN 1068-3755, Surface Engineering and Applied Electrochemistry, 2014, Vol. 50, No. 1, pp. 50–56. © Allerton Press, Inc., 2014.

Effects of TiO_2 Particles Size and Heat Treatment on Friction Coefficient and Corrosion Performance of Electroless Ni–P/TiO_2 Composite Coatings[1]

Elina Esmaeel Nad and Maryam Ehteshamzadeh*

Department of Materials Science and Engineering, Faculty of Engineering, P. O. Box 76175-133, Shahid Bahonar University of Kerman, Jomhoori Blvd., Kerman, Iran

**e-mail: ehtesham@uk.ac.ir*

Received December 20, 2012; in final form March 25, 2013

Abstract—The effects of the titanium dioxide (TiO_2) particles size on the friction coefficient and corrosion performance of the Ni–P/TiO_2 composite coatings before and after heat treatment at 400°C for 1h have been investigated. Pin-on-disc analysis results have revealed that the highest and the lowest friction coefficients belonged, respectively, to the simple Ni–P coating and the Ni–P/TiO_2 composite coating containing TiO_2 particles of the average size of 0.1 μm ($\mu \sim 0.62$ against 0.52). Eventually, a relative reduction in the corrosion resistance and the friction coefficient (as low as $\mu \sim 0.38$) have been observed after heat treatment of Ni–P and Ni–P/TiO_2 composite coatings.

Keywords: particle-reinforcement, friction, corrosion, EIS

DOI: 10.3103/S1068375514010116

INTRODUCTION

Electroless deposition, a long-used process, an autocatalytic reduction of metals and alloys, is an attractive and alternative method of producing coatings with high Ni content; it has been known to form a thin and uniform deposit on the substrate when compared to electroplating [1].

The idea of codepositing various second phase particles in electroless nickel matrix and thereby taking advantages of their inherent uniformity, harden ability, wear and corrosion resistance, has led to the development of electroless nickel composite coatings. Many composite coatings are characterized by an amorphous or crystalline nickel matrix into which oxides such as NiO, Sc_2O_3, Fe_2O_3, RuO_2, Al_2O_3 and TiO_2 are incorporated [2, 3]. Other chemical compounds can also be codeposited with the nickel matrix, e.g. SiC, BN or PTFE [4, 5].

Incorporation of nano-sized particles within Ni–P autocatalytic coatings has greatly improved their properties thus imparting new functional features to the coating performance, which finally has widened their application in different fields. One of those particles, TiO_2, has attracted tremendous interest in the research community due to its wide application in engineering [6]. This material is widely used because of its high refractive index [7]. However, so far little attention has been paid to the incorporation of TiO_2 nanoparticles in the Ni matrix [8]. Composite coatings of the Ni matrix with a stable inorganic TiO_2 oxide offer the synergistic advantage of the metal matrix that is conductive and corrosion resistant and the oxide, which may enhance the corrosion and wear resistance or catalytic properties of the system [9]. In composite materials, the TiO_2 phase, with its high strength and high hardness, can serve as an effective reinforcement to strengthen the composite and increase its hardness and wear resistance. The Ni–P plates containing TiO_2 composite have improved physical-chemical characteristics [10].The right configuration of the size, morphology and structure of the TiO_2 nanoparticles should be specified for every particular application.

The given paper considers a very important effect of adding second-phase particles into simple electroless coatings and partially fills the gap in the insufficient number of investigations on the effect of the second-phase particle size and of heat treatment on wear and corrosion performance of composite coatings.

EXPERIMENTAL DETAILS

Preparation of Substrate

Mild steel specimens ($5 \times 2 \times 0.5$ cm^3) were used as substrates of electroless Ni–P coatings. The samples were polished by successive emery papers (grit numbers: 120, 500, 1000 and 2400). Having been cleaned by distilled water and ethanol for removing any pollution, the specimens were soaked in acetone for 30 min.

[1] The article is published in the original.

The procedure was followed by immersing the specimens in the sulfuric acid solution for 30 s in order to activate the samples surfaces. All chemicals were of the analytical grade (Merck).

Plating Bath and Coating Process

The compositions of electroless baths are given in Table 1. Magnetic stirrer was used to get uniform suspension of particles in the solution. In each case, 250 mL of suspension containing Ti particles and an optimized amount of the anionic surfactant sodium dodecyl sulfate (SDS) [11] were stirred for 12 h on a magnetic stirrer to improve wettability of the particles. The TiO_2 powder was added to the composite coating bath, separately, in three average sizes: 20 nm, 0.1 μm and 0.3 μm, which, respectively, leaded to the composite coatings with symbols D1, D2 and D3 thereafter. As to D, it showed a simple Ni–P coating.

Table 1. Simple and composite coating bath composition and operating conditions for electroless coating

Composition	Simple Ni-P bath	Ni-P/TiO_2 bath
$NiSO_4 \cdot 6H_2O$, g/L	21	21
$NaH_2PO_2 \cdot H_2O$, g/L	25	25
Lactic acid, mL	24	24
Propionic acid, mL	3	3
TiO_2, g/L	–	2
Pb acetate, g/L	0.004	0.004
Thio urea, g/L	0.002	0.002
Surfactant, g/L	–	0.2 (SDS)
Temperature	89 ± 2°C	89 ± 2°C
pH	4.6 ± 0.2	4.6 ± 0.2
Duration, min	40	40

Heat Treatment

To study the effect of heat treatment on the properties and structure of the composite coatings, the samples were subjected to the annealing heat treatment. This was carried out in an argon atmosphere furnace at 400°C for 1h. The samples were allowed to cool in the furnace after the heat treatment.

Equipment

Scanning electron microscope (SEM) CamScan MV2300 was employed to study surface morphologies. Also, the deposits compositions were analyzed by the energy dispersive X-ray (EDX) analyzer. The X-ray diffraction (XRD) analyzer equipment (Philips, Xpert, CuK_α radiation) with X'pert Highscore 1.0d software was used for detecting the phases. Microhardness of the Ni–P based coatings was measured using a microhardness equipment (Struers Duramin, Denmark), with a diamond pyramid as an indenter and 50 *g* load, 15 s loading duration and five trials per each sample.

Electrochemical measurements were done using an EG and G Potentiostat/Galvanostat Model 263A accompanied with a frequency response analyzer Model 1025. A classical cell of three-electrodes was employed: a platinum electrode was a counter electrode, a saturated calomel electrode (SCE) was a reference electrode and the samples with an exposed area of 1 cm^2 were working electrodes. The potentiodynamic polarization curves were recorded in the range of –0.4 to 0.4 vs. an open circuit potential with the scan rate of 1 mV s^{-1}. Electrochemical impedance spectroscopy (EIS) measurements were done in the frequency range of 100 KHz–10 mHz and the perturbation amplitude was 5 mV. Aqueous solution of 3.5% NaCl was used as the corrosive media in electrochemical tests.

Friction and wear performance were studied using pin-on-disc equipment interfaced with a data acquisition system. For all tests, the sliding velocity was fixed at 0.024 m/s and the sliding distance was 100 m. The load applied was 10 N. No lubricant was used during the test. The pins were made of steel with hardness of 62 RC.

RESULTS AND DISCUSSION

Morphology and Microstructure

Figures 1a–1d exhibits the SEM images of the composite coatings containing TiO_2 particles in different sizes. It can be seen that there are many spherical protrusions over the surface. It was observed that when increasing the size of TiO_2 particles, the coatings sur-

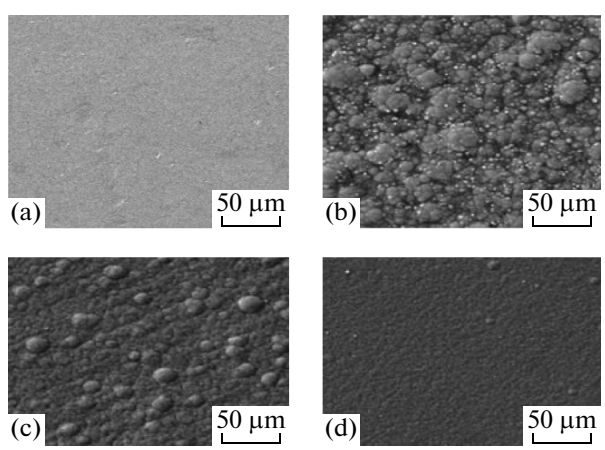

Fig. 1. SEM micrographs of electroless Ni–P and Ni–P/TiO_2 composite coatings; (a) D, Ni–P coating; (b) D1, Ni–P/TiO_2 in average size 20 nm; (c) D2, Ni–P/TiO_2 of average size 0.1 μm; (d) D3, Ni–P/TiO_2 in average size 0.3 μm.

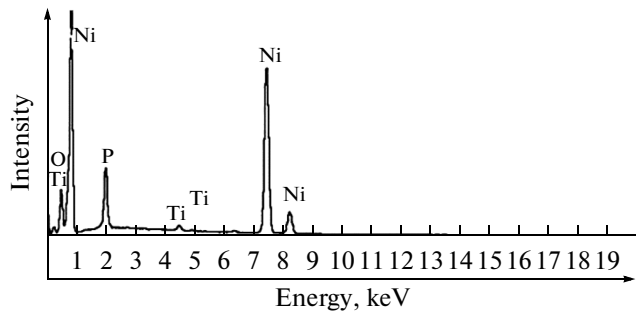

Fig. 2. Typical energy dispersive X-ray analysis of electroless Ni–P/TiO_2 composite coating containing TiO_2 particles of average size 0.1 μm.

faces became softer and smoother. This can be interpreted by a higher agglomeration of small TiO_2 particles in D1 and D2 composite coatings, which led to a rougher surface.

Figure 2 shows a typical EDX spectrum of the composite coating D2. Similar results were observed for the composite coatings D1 and D3. Chemical compositions of the composite coatings are listed in Table 2. Incorporated TiO_2 particles in the Ni–P matrix for the composite coatings D1, D2 and D3 were found to be 2.9, 3.4 and 2.2 wt %, respectively. It is obvious that the most incorporated amount of the TiO_2 particles was in the composite coating D2. In general, the incorporation of second phase particles in electroless Ni–P matrix depends on two factors: particles impingement on the electrode surface and the remaining time of the particles on the electrode surface [12]. Lower incorporation of the averagely sized—20 nm and 0.3 μm, TiO_2 particles in composite coatings D1 and D3, respectively, can be ascribed to either a relatively small or very large size of the particles, which are believed to be swept away from the surface, as compared to the particles in the averagely sized (0.1 μm) D2. Despite the presence of the surfactant *SDS*, another inevitable fact is agglomeration of nano-sized particles, which most probably occurs in the composite coating containing TiO_2 particles of the average size 20 nm, as is D1.

XRD patterns of the electroless Ni–P and Ni–P/TiO_2 composite coatings, before and after heat treatment, are shown in Fig. 3. The amorphous nature of the electroless Ni–P matrix was evidenced in which

Table 2. Composition of electroless Ni–P and Ni–P/TiO_2 composite coatings

Type of coating	TiO_2 particles average size	Ni, wt %	P, wt %	TiO_2, wt %
(D) Ni-P	–	89.1	10.9	–
(D1) Ni-P/TiO_2	20 nm	86.9	10.2	2.9
(D2) Ni-P/TiO_2	0.1 μm	87.0	9.6	3.4
(D3) Ni-P/TiO_2	0.3 μm	87.6	9.5	2.2

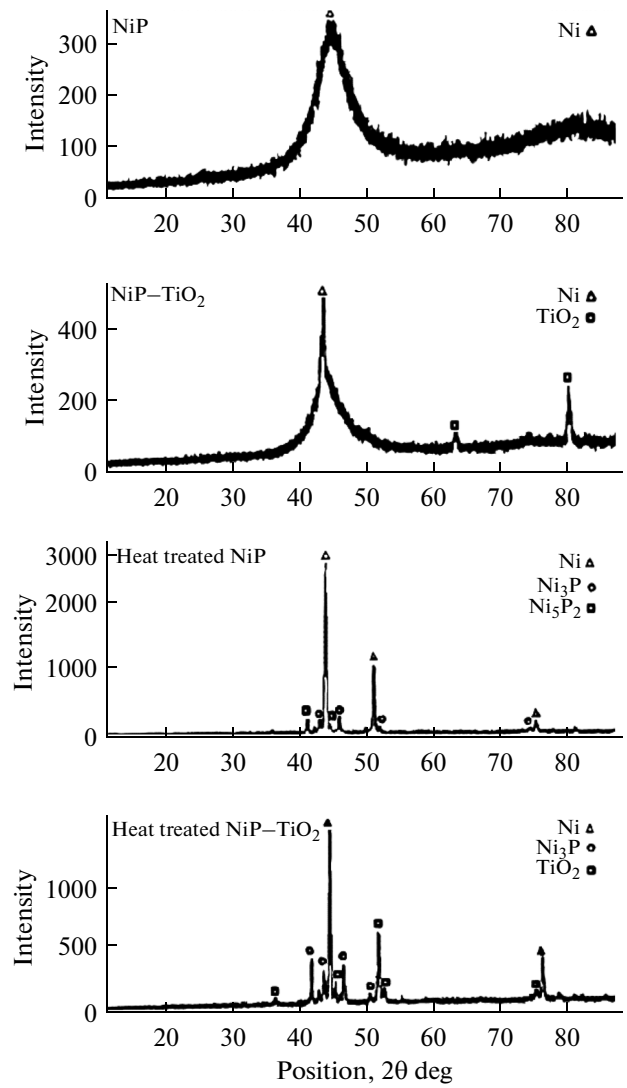

Fig. 3. XRD patterns of as-plated and heat treated Ni–P and typical Ni–P/TiO_2 composite coating containing TiO_2 particles of average size 0.1 μm.

crystalline TiO_2 particles are embedded. In the composite coatings, apart from a single broad peak corresponding to the amorphous Ni (111) plane at 45°, there are low intensity peaks of TiO_2. After heat treatment, rapid transformation, from a disordered to an ordered arrangement, in the structure of the electroless Ni–P coatings of Ni_3P, Ni_5P_2, Ni–P_3 which resulted in several sharp peaks in the X-ray diffraction pattern.

Wear Behavior

A tribological contact of solid bodies results in two major phenomena: friction and wear. Abrasion test results of simple and composite coatings are presented in Fig. 4. The Ni–P/TiO_2 composite coa-tings showed improved wear resistance compare to a simple Ni–P

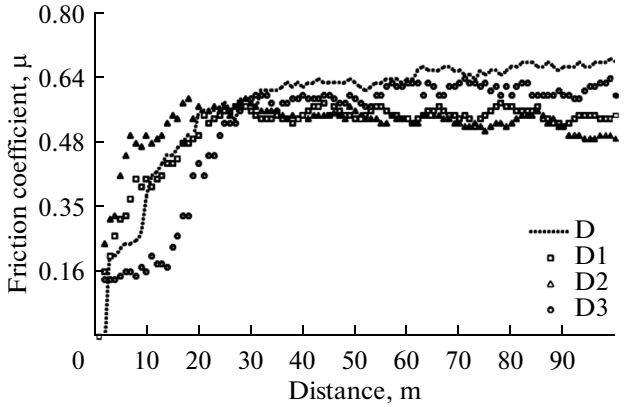

Fig. 4. Friction coefficient vs. sliding distance of electroless Ni–P and Ni–P/TiO_2 composite coatings; (D) Ni–P coating, (D1) Ni–P/TiO_2 of average size 20 nm, (D2) Ni–P/TiO_2 of average size 0.1 μm, (D3) Ni–P/TiO_2 of average size 0.3 μm.

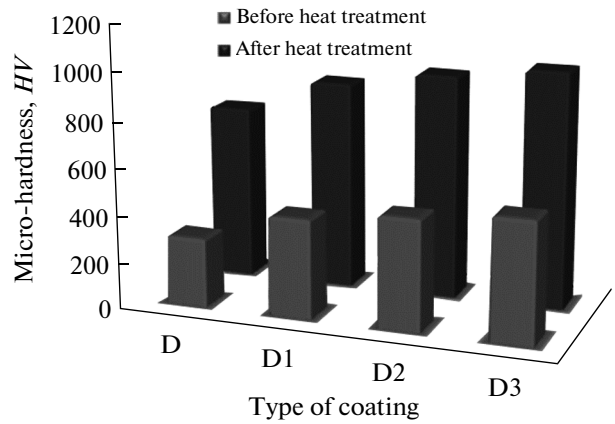

Fig. 5. Hardness profile of electroless Ni–P and Ni–P/TiO_2 composite coatings before and after heat treatment at 400°C for 1 h; (D) Ni–P coating, (D1) Ni–P/TiO_2 of average size 20 nm, (D2) Ni–P/TiO_2 of average size 0.1 μm, (D3) Ni–P/TiO_2 of average size 0.3 μm.

deposit, with a friction coefficient (μ) ~0.62. Among the composite coatings, D2 showed the lowest friction coefficient (~0.52) which led to the best abrasion resistance. This could be explained by the amount of adsorbed TiO_2 particles in the deposit (3.4 wt %), as evaluated by the EDX analysis. A higher percentage of the powder resulted in a reduced wear between the coating and the pin, thus enhancing the abrasion resistance of D2 in comparison with the other two composite coatings. The Friction Coefficients of D1 and D3 were estimated as ~0.55 and ~0.58, respectively.

Figure 5 displays Vickers microhardness values for as plated and heat treated electroless Ni–P and Ni–P/TiO_2 composite coatings. As is evident, increase in the size of TiO_2 particles led to a higher coating hardness. It can be recalled from the EDX analysis (Table 2) of the coatings that the amounts of phosphorus present in D, D1, D2 and D3 coatings, which is a crucial parameter in the electroless Ni–P plating, were 9.29, 10.2, 9.6 and 9.5 wt %, respectively. It is clear that the larger the size of Ti particles, the smaller the amount of the deposited phosphorus. Because of the fact that phosphorus phase is a type of a soft phase, it affects the surface microhardness and can lead to smaller hardness values of the deposits. When electroless coatings are heated at a suitable temperature, formation and precipitation of the intermetallic Ni_3P, Ni_5P_2, Ni–P_3 phases occur, which act as barriers for dislocations movement, thereby hardness goes on increasing. This unique property of electroless alloys led to an extremely wide exploitations of such coatings for applications requiring wear and abrasion resistance.

As it is clear from Fig. 6, heat treatment affects the coatings abrasion behavior. A relative reduction of the friction coefficient values was observed after heat treatment. This can be accounted for by the creation of hard phases, such as Ni_3P, after heat treatment, which led to higher hardness values of coa-tings and therefore wear resistance. Besides, as was the case before heat treatment, the lowest friction coefficient is that of D2, which is as low as 0.38.

Corrosion Performance

Figure 7 shows polarization curves of electroless Ni–P and Ni–P/TiO_2 composite coatings containing TiO_2 particles of different sizes in the 3.5% sodium chloride solution; Table 3 lists their polarization parameters. It can be seen that the corrosion current density (i_{corr}) for a simple electroless Ni–P coating (D) is 2.04 μA/cm^2, whereas i_{corr} values for D1, D2 and D3 coatings are 2.54, 0.36 and 1.58 μA/cm^2,

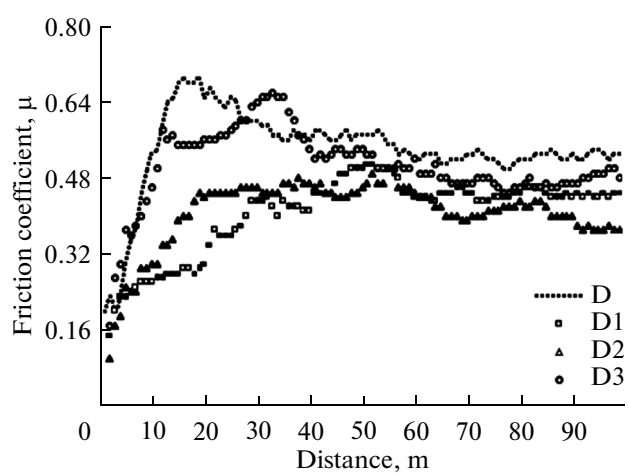

Fig. 6. Friction coefficient vs. sliding distance of electroless Ni–P and Ni–P/TiO_2 composite coatings after heat treatment at 400°C for 1 h; (D) Ni–P coating, (D1) Ni–P/TiO_2 of average size 20 nm, (D2) Ni–P/TiO_2 of average size 0.1 μm, (D3) Ni–P/TiO_2 of average size 0.3 μm.

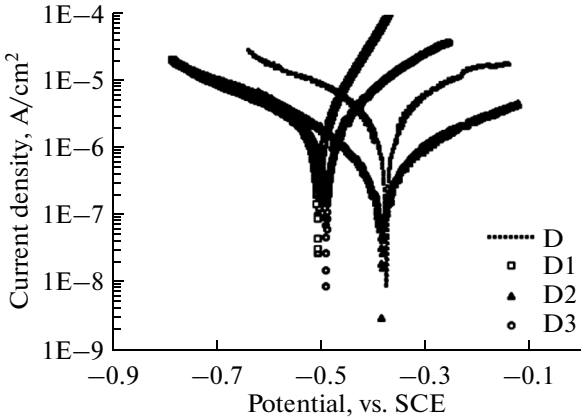

Fig. 7. Potentiodynamic polarization curves of electroless Ni–P and Ni–P/TiO_2 composite coatings in 3.5% NaCl aqueous solution; (D) Ni–P coating, (D1) Ni–P/TiO_2 of average size 20 nm, (D2) Ni–P/TiO_2 of average size 0.1 μm, (D3) Ni–P/TiO_2 of average size 0.3 μm.

respectively. Among the four composite coatings, D2 showed the highest corrosion resistance. This can be attributed to the appropriate incorporation of Ti particles and their relevant distribution in the deposit, which are much better than at the other ones. This, in turn, can be attributed to the deposition of an enhanced barrier effect caused by the presence of TiO_2 particles in the Ni–P matrix and therefore a higher corrosion resistance of the deposit.

The lowest resistance was associated with D1 coating, which can be attributed to an effective exposure of the metallic area to the corrosive media. In D1 deposit, incorporation of extremely small TiO_2 particles can result in augmenting the particles agglomeration in the electroless bath and therefore in the composite film. This can be due to a big surface energy of ultrafine TiO_2 particles, which tends to pile them up severely, despite the presence of an appropriate surfactant SDS. Hence, the probability of localized corrosion in the D1 deposit is even higher than at a simple electroless plating.

On the other hand, more particle collisions in the electroless bath in the process of making D3 coating has led a lower content of TiO_2 in the deposit, thus causing a lower corrosion resistance of the deposit unlike the process in D2.

Table 3. Polarization parameters of electroless Ni–P and Ni–P/TiO_2 composite coatings in 3.5% NaCl aqueous solution; (D) Ni–P coating, (D1) Ni–P/TiO_2 of average size 20 nm, (D2) Ni–P/TiO_2 of average size 0.1 μm, (D3) Ni–P/TiO_2 of average size 0.3 μm

Type of coating	i_{corr}, μA/cm²	E_{corr}, mV	B_a, V/dec	B_c, V/dec	R_P, $\Omega \times 10^4$
D	2.046	−385	0.164	0.192	1.375
D1	2.543	−509	0.089	0.306	0.840
D2	0.361	−380	0.106	0.170	10.69
D3	1.580	−497	0.133	0.210	2.247

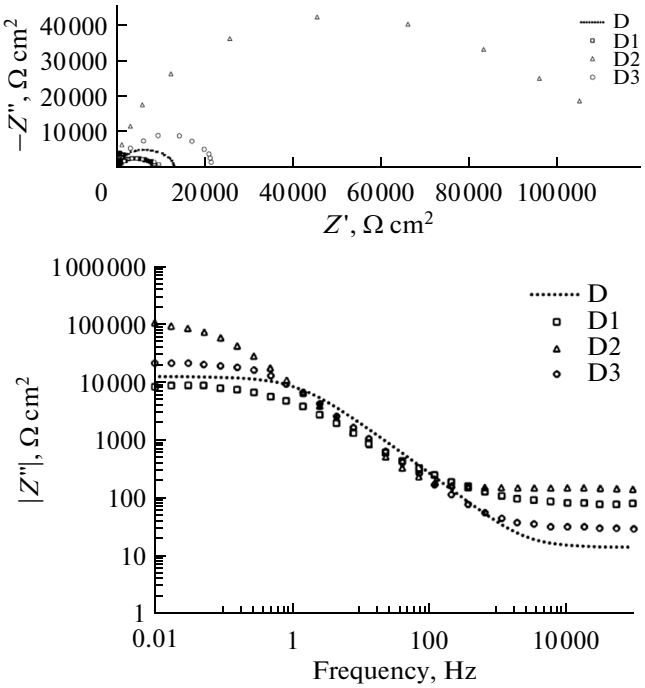

Fig. 8. EIS spectra of electroless Ni–P and Ni–P/TiO_2 composite coatings in 3.5% NaCl aqueous solution; (D) Ni–P coating, (D1) Ni–P/TiO_2 of average size 20 nm, (D2) Ni–P/TiO_2 of average size 0.1 μm, (D3) Ni–P/TiO_2 of average size 0.3 μm.

The impedance data of the coatings in the format of Nyquist and Bode plots are shown in Fig. 8. The results of the EIS studies also indicate a similar trend in the corrosion resistance like that observed in potentiodynamic polarization effects. The highest value of R_P for the D2 coating also implied that this type of a coating is more protective against corrosion, while the D1 deposit plot exhibited a low resistance in contrast with other films.

Corrosion behavior of the heat treated electroless coatings in the format of Nyquist and Bode plots are shown in Fig. 9. Extracted results of the EIS analysis are listed in Table 4. They are as follows: the highest R_P value refers to the D2 composite coating; in addition, the highest and the lowest corrosion resistance demonstrated D2 (i_{corr} = 1.419 A/cm²) and D1 (i_{corr} = 3.24 A/cm²), respectively. The heat treated electroless Ni–P and Ni–P/TiO_2 composite coatings exhibited larger i_{corr} values than the equivalent as-plated coatings. A higher corrosion resistance of as-plated coatings may be attributed to their amorphous nature. Amorphous alloys offer better resistance to corrosion attack than the equivalent polycrystalline materials because of the freedom from grain and grain boundaries [9].

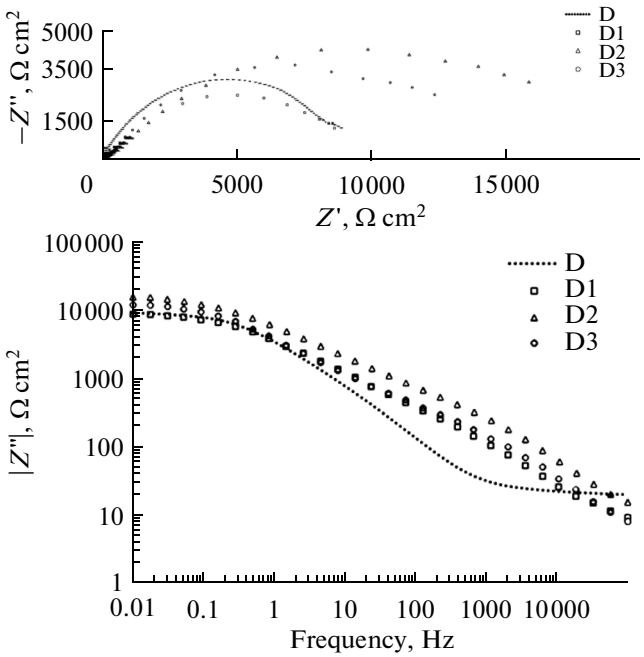

Fig. 9. EIS spectra of electroless Ni–P and Ni–P/TiO_2 composite coatings in 3.5% NaCl aqueous solution after heat treatment at 400°C for 1 h; (D) Ni–P coating, (D1) Ni–P/TiO_2 of average size 20 nm, (D2) Ni–P/TiO_2 of average size 0.1 μm, (D3) Ni–P/TiO_2 of average size 0.3 μm.

After heat treatment, a mixture of crystalline nickel and nickel phosphide is created, therefore areas of different corrosion potentials are produced. This may leads to the formation of minute active/passive corrosion cells and consequently provoke an accelerated attack by an aggressive medium. The comparison of deposits demonstrates that the composite coating with the 20 nm particle size of TiO_2 has the lowest corrosion resistance, which is even less than with a simple Ni–P coating. Figure 10 schematically compares the corrosion behavior of the coatings before and after heat treatment.

Table 4. Polarization parameters of electroless Ni–P and Ni–P/TiO_2 composite coatings in 3.5% NaCl aqueous solution after heat treatment at 400°C for 1 h; (D) Ni–P coating, (D1) Ni–P/TiO_2 of average size 20 nm, (D2) Ni–P/TiO_2 of average size 0.1 μm, (D3) Ni–P/TiO_2 of average size 0.3 μm

Type of coating	i_{cor}, μA/cm^2	E_{corr}, mV	R_P, Ωcm^2 × 10^4
D	2.793	–495.0	0.889
D1	3.249	–485.8	0.867
D2	1.419	–546.2	1.586
D3	1.780	–551.3	1.235

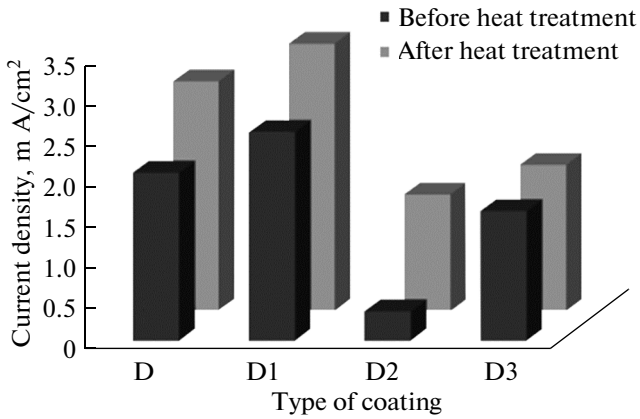

Fig. 10. Comparison in corrosion current densities of electroless Ni–P and Ni–P/TiO_2 composite coatings before and after heat treatment at 400°C for 1 h; (D) Ni–P coating, (D1) Ni–P/TiO_2 of average size 20 nm, (D2) Ni–P/TiO_2 of average size 0.1 μm, (D3) Ni–P/TiO_2 if average size 0.3 μm.

CONCLUSIONS

(1) Heavier agglomeration of TiO_2 particles was observed in the presence of 20 nm TiO_2 particles.

(2) A larger and more uniform distribution of TiO_2 particles were found in the Ni–P/TiO_2 composite coatings containing TiO_2 particles of the average size of 0.1 μm.

(3) The highest and the lowest friction coefficients were observed with the simple Ni–P and the Ni–P/TiO_2 composite coatings containing TiO_2 particles of the average size of 0.1 μm, respectively, (μ ~ 0.62 against 0.52).

(4) Heat treatment of the electroless Ni–P and Ni–P/TiO_2 at 400°C for 1h caused lowering of the friction coefficient, so that μ arrived ~0.38 in the electroless Ni–P/TiO_2 composite coatings containing TiO_2 particles of the average size of 0.1 μm.

(5) A reduction in the corrosion resistance was observed in the coatings after heat treatment.

ACKNOWLEDGMENTS

The authors would like to thank Mr. Amir Farzaneh for his technical support.

REFERENCES

1. Ranganatha, S., Venkatesha, T.V., and Vathsala, K., Development of electroless Ni–Zn–P/nano TiO_2 composite coatings and their properties, *Appl. Surf. Sci.*, 2010, vol. 256, no. 24, pp. 7377–7383.
2. Novakovic, J., Vassiliou, P., Samara, K.L., and Argyropoulos, Th., Electroless Ni–P/TiO_2 composite coat-

ings: their production and properties, *Surf. Coat. Technol.*, 2006, vol. 201, pp. 895–901.

3. Chen Wei, Gao Wei, and He Yedong, Electrodeposition of soenhanced nanostructured Ni–TiO_2 composite coatings, *Surf. Coat. Technol.*, 2010, vol. 204, pp. 2493–2498.
4. Ramalho, A. and Miranda, J.C., Friction and wear of electroless NiP and Ni–P PTFE coatings, *Wear*, 2005, vol. 259, nos. 7–12, pp. 828–834.
5. Allahkaram, S.R., Honarvar Nazari, M., Mamaghani, S., and Zarebidaki, A., Characterization and corrosion behavior of electroless Ni–P/nano-SiC coating inside the CO_2 containing media in the presence of acetic acid, *Materials and Design*, 2011, vol. 32, pp. 750–756.
6. León, O.A., Staia, M.H., and Hintermann, H.E., Wear mechanism of Ni–P-BN(h) composite autocatalytic coatings, *Surf. Coat. Technol.*, 2005, vol. 200, pp. 1825–1829.
7. Pokrant, S. and Irsen, S., Crystal structure of TiO_2 nano-particles, *Microsc. Microanal.*, 2008, vol. 14, no. 2, pp. 354–355.
8. Abdel Aal, A., Hassan Hanaa, B., and Abdel Rahim, M.A., Nanostructured Ni–P–TiO_2 composite coatings for electrocatalytic oxidation for small organic molecules, *J. Electroanal. Chem.,* 2008, vols. 619–620, pp. 17–25.
9. Ramalho, A. and Miranda, J.C., The relationship between wear and dissipated energy in sliding systems, *Wear*, 2006, vol. 260, nos. 4–5, pp. 361–367.
10. Novakovic, J. and Vassiliou, P., Vacuum thermal treated electroless NiP–TiO_2 composite coatings, *Electrochim. Acta*, 2009, vol. 54, no. 9, pp. 2499–2503.
11. Farzaneh, A., Ehteshamzadeh, M., Ghorbani, M., and Vazife Mehrabani, J., Investigation and optimization of *SDS* and key parameters effect on the nickel electroless coatings properties by taguchi method, *J. Coat. Technol. Res.*, 2010, vol. 7, pp. 547–555.
12. Balaraju, J.N., Kalavati, K.S., and Rajam, Influence of particle size on the microstructure, hardness and corrosion resistance of electroless Ni–P–Al_2O_3 composite coatings, *Surf. Coat. Technol.*, 2006, vol. 200, nos. 12–13, pp. 3933–3941.

ISSN 1068-3755, Surface Engineering and Applied Electrochemistry, 2014, Vol. 50, No. 1, pp. 57–62. © Allerton Press, Inc., 2014.

Effect of Weak and High Magnetic Fields in Longitudinal and Transverse Configurations on Magneto-Thermoelectric Properties of Quantum Bi wires[1]

A. Nikolaeva[a, b], L. Konopko[a, b], T. E. Huber[c], Gh. Para[a], and A. Tsurkan[a]

[a]*Ghitu Institute of Electronic Engineering and Nanotechnologies, ASM, Academiei, str. 3/3, MD-2028, Chisinau, Republic of Moldova*

[b]*International Laboratory of High Magnetic Fields and Low Temperatures, Wroclaw, Poland*

[c]*Department of Chemistry, Howard University, 500 College St. N.W., DC 20059 Washington, USA*

e-mail: A.Nikolaeva@nano.asm.md

Received June 7, 2013

Abstract—We report on the magneto-thermopower of single-crystal Bi nanowires with diameters 75 and 250 nm in a longitudinal and transverse magnetic fields of 0–14 T. The temperature range is 1.5–300 K. Bi nanowires in a glass capillary have been prepared by the high frequency liquid phase casting. The temperature dependence $R(T)$ shows the transition from metallic to semiconducting behavior due to quantum size effect, where the Bi-wire diameter is reduced to less than 80 nm. It is for the first time that the effect of the negative magneto-resistance in a transverse magnetic field, due to the quantum size effect on 75 nm Bi wires, has been observed. The thermopower is very sensitive to the wire diameter, up to a change in the sign from negative to positive at low temperatures, and to a significant extent in a weak longitudinal magnetic field. The field dependences of longitudinal and transverse magneto-resistance have features characteristic of the occurrence of the quantum size effect and galvanomagnetic size effect, and provide information on the parameters of the energy spectrum and charge carrier mobility. The enhancement of the thermoelectric figure of merit for Bi nanowires is discussed. We also discuss the power factor $\alpha^2\sigma$ and its dependence on the diameter, magnetic field and temperature.

Keywords: Bi nanowires, thermoelectricity, size quantization effect

DOI: 10.3103/S1068375514010128

INTRODUCTION

The electrical transport and magneto-thermoelectric properties of single crystal Bi nanowires have attracted considerable attention because of the quantum size effect (QSE). In a semimetal, the QSE causes the conduction band and the valence band to break up into subbands whose numbers correspond to discrete values of the wave vector along the "quantizing" dimension. By introducing a quantum confinement, a semimetal—semiconductor transition can be achieved [1]. Due to a long electron mean free path (m.f.p.) l_e (~100 nm at room temperature) and a very large Fermi wavelength λ (40–60 nm), material Bi is the best candidate to study the classical and quantum size effects for the object size comparable to l_e and λ [1–9].

In [10, 11] a significant increase in thermoelectric efficiency Z was predicted in quantum Bi-wires at the semimetal—semiconductor transition due to the QSE. In the thermoelectric figure of merit $ZT = \frac{\alpha^2\sigma}{\chi}T$, σ is the electrical conductivity, α is the Seebeck coefficient (thermopower), $\chi - = k_e + k_l$ is the thermal conductivity (k_e, k_l are the electron and lattice contributions, T is the absolute temperature).

An approach to increase Z is to increase the density of states near the Fermy level at the size quantized and to decrease thermal conductivity due to an additional strong phonon scattering on the surface of quantum Bi nanowire walls [1, 10, 11]. Single-crystal wires are required so as to observe the QSE.

The galvanomagnetic size effect (GMSE) was studied theoretically and experimentally in bismuth wires with $d > 200$ nm, prepared by various methods [3, 6–10]; in particular, its occurrence in $\rho(H)$, $(H \| I)$ is in fairly good agreement for both individual Bi wires and nanowire arrays.

As for the thermoelectric power, the available experimental results obtained in most cases on Bi

[1] The article is published in the original.

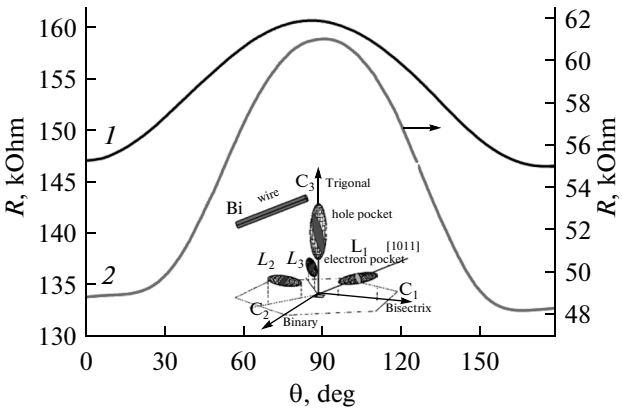

Fig. 1. Angle diagrams of transverse MR $R(\theta)$ ($H \perp T$), of Bi wires at 100 K, $H = 1$ T. *1*—$d = 75$ nm; *2*—$d = 250$ nm. Inset: Schematic drawing the three Fermy surface electron pockets L and T hole pocket. The orientation of (1011) and Bi wire is also indicated.

nanowire arrays embedded in a porous Al_2O_3 dielectric matrix are very contradictory [12–14] and differ not only quantitatively but also qualitatively. This is probably due to some variation in the diameter of nanowire arrays, filling of pores Al_2O_3 as well as to the presence of uncontrolled structural defects, especially in establishing contacts, because the length of the nanowire arrays is less than 200 μm.

The most suitable material to study the QSE and GMSE is strictly cylindrical single-crystal Bi wires, die-cast from the liquid phase in a glass envelope with a length of a few mm [6, 8, 9].

In this paper we report the dimensional features in the magneto-field dependences of resistance and thermopower in longitudinal and transverse magnetic fields up to 14 T for single crystal Bi wires with diameters of 250 and 75 nm (at the semimetal—semiconductor transition due to the QSE).

In weak magnetic fields, H_{max}, the maximum in the longitudinal magneto-resistance (LMR) $R(H)$, corresponds to the "cutoff" magnetic field of SdH oscillations at 4.2 K. With decreasing diameter of the wires ($d < 80$ nm) this maximum disappears and magneto thermopower achieves the maximum positive value at 20–30 K.

It is for the first time that the effect of the negative magneto-resistance in a transverse magnetic field (TMR) due to the QSE has been observed. The power factor $\alpha^2\sigma$ and its dependence on the diameter, magnetic field and temperature were calculated from the experimental data.

SAMPLES AND EXPERIMENT

Individual glass-coated Bi wires with the diameter <100 nm were prepared by the high frequency liquid phase casting (the improved Ulitovsky-Taylor method) [6, 8, 9].

The orientation of the wires was verified by the X-Ray diffraction. Studies on the Diffractometer Xcalibur-E reveal that the investigated wires are single crystals and have the $(10\bar{1}1)$orientation along the wire axis (Fig. 1, inset). In this orientation the wire axis makes an angle of 19.5° with the bisector axis C_1 in the bisector-trigonal plane. The trigonal axis C_3 is inclined to the wire axis at the angle of 70°, and one of the binary axes C_2 is perpendicular to it (Fig. 1, inset).

Figure 1 shows the rotation angular diagram of the transverse magneto-resistance (ADTMR) $R(\theta)$ Bi wires with $d = 75$ nm and $d = 250$ nm at 100 K. The curves qualitatively correspond to the similar ADBMR for bulk single crystal Bi samples for the case where the current is directed along the bisector axis [15]. In weak magnetic fields ADBMR curves have a simple bell-shape with a periodicity of 180°. The maximum on the $R(\theta)$ ($\theta = 90°$) corresponds to $H \| C_2$ and the minimum ($\theta = 0° = 180°$) corresponds to the situation when the wire axis, the crystallographic C_3 axis and the vector $\vec{H}$ are in one plane, and the angle $\angle HC_3 \approx 20°$.

Electrical contact in the butt-end of the wire to the copper foil was performed either by a fusible solder (58°) or by In or InGa-eutectics (low melting alloys). The type of the contact solder did not influence the results of measurements.

For investigations in the transverse magnetic field, a special device was applied, which allows rotating the sample in two directions: ⊥ and ‖ to the magnetic field. The TMR ($H \perp I$) was measured at $\theta = 0$ (Fig. 1, inset). Measurements of the LMR ($H \parallel I$) and TMR ($H \perp I$) were carried out in a superconducting solenoid field up to 14 T in the temperature range of 1.5–300 K in the International Laboratory of High Magnetic Fields and Low Temperatures (Wroclaw, Poland).

RESULTS AND DISCUSSION

The semimetalic Bi wires with a diameter of 250 nm exhibit Shubnikov de Haas (SdH) oscillations. Figure 2 (inset) shows SdH oscillations on the magneto-resistance $R(H)$ (derivative $\delta R/\delta H(H)$) in longitudinal orientations $H \parallel I \parallel C_1$ of Bi wires, with $d = 250$ nm.

The SdH oscillations are periodic in $1/H$, with a period of $\Delta(1/H) = 2\pi e\hbar/cS$, which is inversely proportional to the extreme cross-section S of the Fermy surface in the plane normal to the magnetic field H.

In the longitudinal magnetic field ($H \parallel I$), there are three different extreme cross sections S (cross-hatched in Fig. 1, inset) and three respective SdH oscillation periods: *1* —$\Delta_1 = 7 \times 10^{-5}$ Oe^{-1} from one electron ellipsoid L_1 of a smaller size S_{L1}, *2* — $\Delta_2 = 3.2 \times 10^{-5}$ Oe^{-1} from two equivalent electron ellipsoids of a larger size S_{L2}, *3*—$\Delta_3 = 0.5 \times 10^{-5}$ Oe^{-1} from the hole ellipsoid S_{T3} (Fig. 2, inset). The oscillations are in

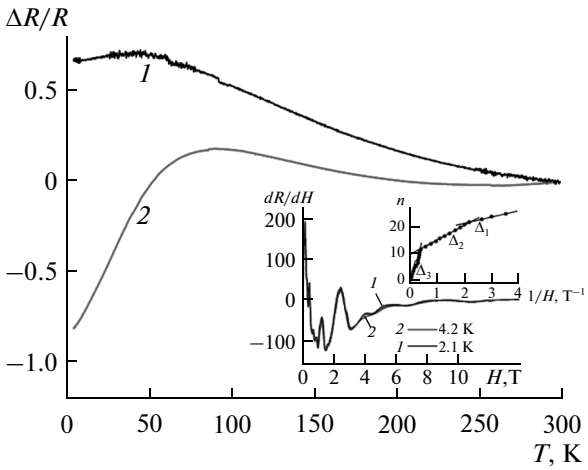

Fig. 2. Temperature dependences residual resistance $\Delta R/R(H) = (R_T - R_{300})/R_{300}(T)$ of single Bi nanowires: *1*—$d = 75$ nm; *2*—$d = 250$ nm. Inset: Field dependences of LMR derivative $\delta R/\delta H(H)$ of Bi wire ($d = 250$ nm) at $T = 2.1$ and 4.2 K and dependences of quantum number n of SdH oscillations on reverse field H^{-1}.

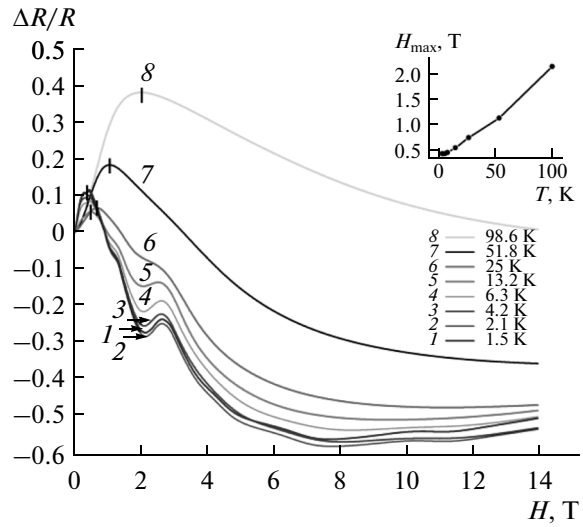

Fig. 3. Magnetic field dependences of longitudinal residual MR $\Delta R/R(H)$ for 250 nm Bi wire at different temperatures (temperatures indicated). Vertical bars indicate maximum position on $\Delta R/R(H)$. Inset: *P* peak position H_{max} as function of *T*.

good agreement with those determined from bulk single crystals [16].

The Dingle temperature was determined from the dependences of the SdH oscillation amplitude versus the magnetic field at 2.1 K. The Dingle temperature $T_D = \hbar/\kappa_B\tau$, where $\tau = l/v_F = em/\hbar\kappa_F$ is the carrier relaxation time. In our 250 nm Bi wire $T_D \approx 1$ K [6]. This suggests that the investigated single Bi wires have very high structural perfection.

Figure 2 shows temperature dependences of the residual resistance $\Delta R/R(H) = (R_T - R_{300})/R_{300}(T)$ of Bi wires with $d = 250$ nm and $d = 75$ nm. For wires with $d = 75$ nm, a semiconducting behavior of $R(T)$ is observed; it indicates the semimetal-semiconductor transition due to the QSE. The temperature dependence $\Delta R/R(T)$ for the wire with $d = 250$ nm characterizes the transition from bulk bismuth to size-dimensional wires [6, 9].

Figures 3–6 show field dependences of LMR $\Delta R/R(H)$ and longitudinal magneto-thermopower (LMTP) $\alpha(H)$ of Bi wires with $d = 250$ nm (Figs. 3, 4) and $d = 75$ nm (Figs. 5, 6) in a temperature range of 1.5–100 K. A specific feature of LMR in Bi wires is the presence of a maximum in $R(H)$ in weak magnetic fields, which depends on the wire diameter and negative magneto-resistance in strong magnetic fields. Magnetic fields change the trajectory of the carriers, which leads to a change in the electrical conductivity of metals placed in an external magnetic field. The nature of the electron motion in weak and strong magnetic fields is very different. In a weak magnetic field, the Larmor radius r_L of the electron orbit $r_L = p_\perp c/eH$ is superior to the mean free path $r_L > l$, ($p_\perp$ is the component of the Fermi momentum vector perpendicular to the magnetic field H; m.p.f. evaluated in our paper [9]) and, between the successive acts of scattering, an electron moves along a short arc trajectory. In this case, the electron motion under the influence of an applied electric field is the same as in the absence of a magnetic field. Electrons, due to the curvature of the trajectory in the magnetic field, can reach the surface and be additionally scattered on the surface. In a strong magnetic field ($\mu H \gg 1$), the electron has time to make several complete cycles of motion without scattering, and in this case $r_L < l$.

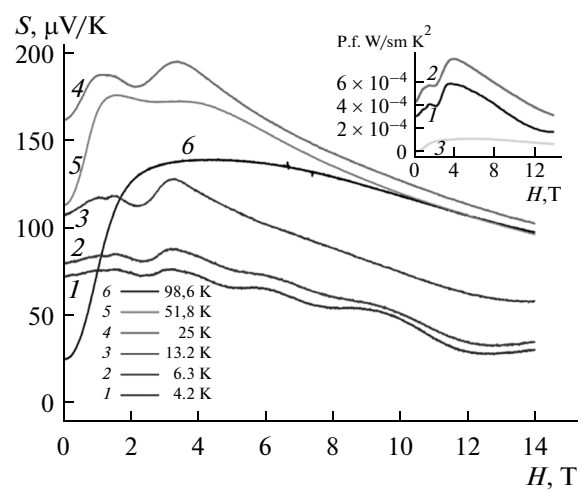

Fig. 4. Longitudinal thermopower ($H \parallel \Delta T$) as function of magnetic field at various temperatures (temperatures indicated) Bi wire, $d = 250$ nm. Inset: Magnetic field dependences ($H \parallel I$) of P.f. $= \alpha^2\sigma(H)$ for various temperatures calculated from Figs. 3, 4 of Bi wire, $d = 250$ nm. *1*—$T = 13$ K; *2*—$T = 25$ K; *3*—$T = 98$ K.

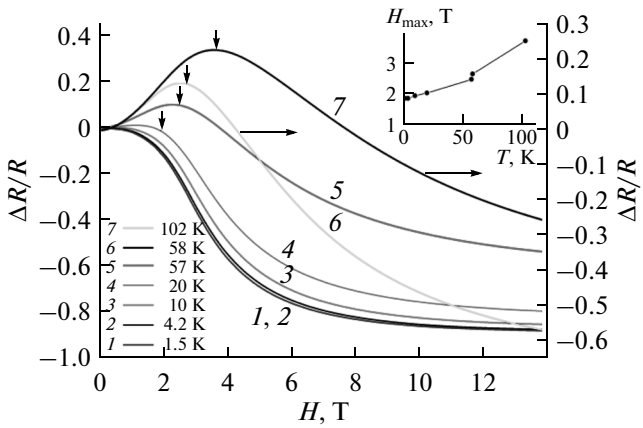

Fig. 5. Magnetic field dependences of longitudinal residual MR $\Delta R/R(H)$ Bi wire $d = 75$ nm at different temperatures (temperature indicated). Inset: Peak position H_{max} as function of temperature T.

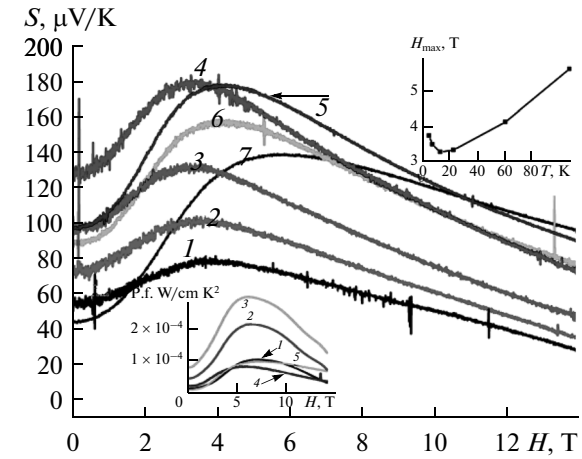

Fig. 6. Longitudinal thermopower ($H \parallel \Delta T$) as function of magnetic field at various temperatures (temperatures indicated in Fig. 5) Bi wire, $d = 75$ nm. Inset on the right: Peak positon H_{max} as function of temperature T. Inset down: Magnetic field dependences ($H \parallel \Delta T$) of P.f. = $\alpha^2\sigma$ for various temperatures calculated from Figs. 5, 6 of Bi wire $d = 75$ nm. *1*—$T = 5$ K; *2*—$T = 10$ K; *3*—$T = 20$ K; *4*—$T = 57$ K; *5*—$T = 100$ K.

As mentioned previously [3, 4, 6] in the wires with 200 nm < d < 1 μm, the dependence of $H_{max} \sim d^{-1}$. The Fermi momentum P_F was calculated from the dependence

$$H_{max} = \frac{2P_F c}{ed}, \quad (1)$$

$$P_F = \frac{deH_{max}}{2c} = 1.1 \times 10^{-21} \text{g cm/s}.$$

In the redistribution of the measurement, an error of P_F calculated from (1) coincides with the value of P_F, obtained from SdH oscillations from the two electron ellipsoids $L_{2,3}$ symmetrically arranged with respect to the wire axis (inset in Fig. 1). The presence of the maximum H_{max} in weak magnetic fields and negative magneto-resistance in strong magnetic fields testify to the occurrence of the GMSE in Bi wires. Later Dresselhaus [10] observed a similar behavior on Bi nanowire arrays.

In the wires with $d = 75$ nm, the maximum of the longitudinal magneto-resistance at 4.2 K was absent (Fig. 5, curve *1*), indicating that there is a very small contribution to the conductivity of the L carrier, or none at all, due to the absence or reduction of the overlap of L and T bands because of the QSE. However, with increasing the temperature to a certain T value, depending on the wire diameter d (in this case, $T \approx 13$ K) in weak magnetic fields, $R(H)$ exhibits the maximum, the behavior of which with a further rise in temperature T is similar to the behavior of $H_{max}(T)$ in the Bi wires with $d = 250$ nm. At $T > 40$ K, H_{max} is shifted towards higher temperatures according to the law close to linear (inset in Fig. 5). Apparently, an increase in temperature results in the diminishing of the forbidden band for semiconductors or of a band overlapping for semimetal proportionally kT, promoting the appearance of L carriers and increasing their contribution to the conductivity.

As shown in [2] and subsequently widely used in [17], especially at high temperatures, in order to explain the anomalous peak of the LMR in wires and films at higher temperatures, the following expression should be used:

$$H_{max} = \frac{2P_F}{e\sqrt{dl}}, \quad (2)$$

where l is m.p.f., i.e. in the maximum m.f.p. $l = d$. In this case, the temperature dependence of H_{max} at $R(H)$ ($H \parallel I$) becomes clear. In fact, it represents the temperature of a carrier mobility μ in Bi wires, and the maximum of $R(H)$ separates strong and weak magnetic fields ($\mu H < 1$ and $\mu H > 1$).

In the longitudinal configuration, the magneto-thermopower $\alpha(H)$ also exhibits its maximum in low magnetic fields (Fig. 6) and generally shows the same trends as the H_{max} on $R(H)$.

In the wires with $d < 100$ nm, the dependence of the maximum $H_{max}(T)$ on the longitudinal thermo-power $\alpha(H)$ ($H \parallel \Delta T$) is nonmonotonic (inset in Fig. 7). At $T > 20$ K, the maximum is shifted to the area of strong magnetic fields under the law close to linear, as in the wires with $d = 250$ nm.

In a transverse magnetic field $H \perp I$, ΔT, $H \parallel C_3$ ($\theta = 0$ point on curve *1* in Fig. 1) in Bi wires with $d = 75$ nm, we have been first to observe the effect of a negative magneto-resistance at $T < 5$ K associated with the quantum size effect [18, 19], which occurs only in Bi wires with $d < 80$ nm. At the same time, the field

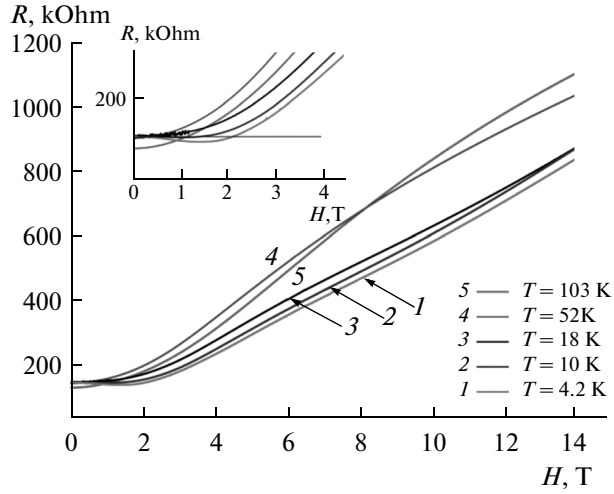

Fig. 7. Magnetic field dependences of transverse MR ($H \perp I$, $H \| C_3$) of Bi wire, $d = 75$ nm for various temperatures (temperatures indicated). Inset: Magnetic field dependences MR $R(H)$ in initial magnetic field.

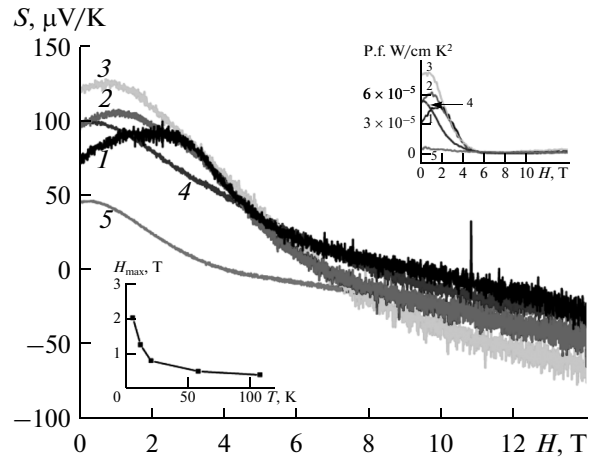

Fig. 8. Transverse magneto thermopower ($H \| \Delta T$, $H \| C_3$) as function of magnetic field at various temperatures Bi wire, $d = 75$ nm. Inset left: Peak position H_{max} as function of temperature T. Inset right: Field dependences ($H \perp I$) P.f. = $\alpha^2\sigma(H)$ calculated from Figs. 7, 8 for various temperatures (temperatures indicated in Fig. 7).

dependence of the thermoelectric power $\alpha(H)$ exhibits a maximum positive polarity, which decreases and shifts to the low magnetic field with increasing temperature (inset in Fig. 8). In strong magnetic fields, the thermoelectric power changes its sign from positive to negative and the point of the sign change is shifted in the region of weak magnetic fields according to the conclusions of the theory, taking into account the QSE [19].

Complex experimental studies of the resistance $R(H)$ and thermopower $\alpha(H)$ of Bi wires with d = 250 nm and $d = 75$ nm at different temperatures made it possible to calculate the Power factor P.f. = $\alpha^2\sigma$ and its dependence on the value and direction of the magnetic field at various temperatures.

Figures 4, 6 and 8 (insert) show the P.f. as a function of a magnetic field at various temperatures for wires with $d = 250$ nm and $d = 75$ nm. At the temperature of 100 K, the maximum value of P.f. = 1×10^{-4} W/cm K^2 at H = 2 T is achieved for Bi wires with d = 250 nm. At T = 25 K, the maximum value P.f. = 8.0×10^{-4} W/cm K^2 at $H = 5$ T is observed. In the transverse field $H \perp \Delta T$, $H \| C_3$ P.f. is almost of an order of a magnitude smaller due to a sharp rise in the positive thermopower in a transverse magnetic field.

It is known that in bulk Bi samples of trigonal orientation, in a temperature range of 100–150 K, the thermopower has a negative value and increases 2-fold in magnetic fields <1 T. The effect was used in the magneto-thermoelectric power converters.

It should be noted that in Bi wires ($d < 300$ nm), the thermopower is positive at $T < 100$ K, which is an important factor for thermoelectric applications because for the n-branches of the thermoelectric energy converter alloys, $Bi_{1-x}Sb_x$ are usually used, and the creation of p branches at low temperatures is problematic.

CONCLUSIONS

Single-crystal wires in glass cover with diameters of 250 and 75 nm have been prepared and their magneto thermoelectric properties investigated. As a result, a semimetal-semiconductor transition has been observed due to size quantization of the energy spectrum. It is shown that field dependences of the longitudinal and transverse magneto-resistance and thermopower contain singular points characterizing the expression of the GMSE and the QSE, and contain information on the parameters of the energy spectrum and on the charge carrier mobility. It is for the first time effect of the negative magneto-resistance in a transverse magnetic field, due to QSE on 75 nm Bi wires has been observed. It is also demonstrated that in quantum Bi wires the thermopower is positive, significantly increases at low temperatures and heavily depends on the wire diameter d. In addition, a significant increase in the positive thermoelectric power in the presence of a longitudinal magnetic field has been observed. The studies carried out by the authors are important not only for fundamental physics of one-dimensional structures, but also for device applications in thermoelectricity.

ACKNOWLEDGMENTS

This work was supported by the STCU grant no. 5373 and by The Ministry of Education and Science of the Russian Federation project 14.B37.21.0891, T.E.H. acknowledgment support by US NSFPRDM and by the U.S. Army Research Office.

REFERENCES

1. Hicks, L.D. and Dresselhaus, M.S., Thermoelectric figure of merit of a one-dimensional conductor. *Phys. Rev., Ser. B*, 1993, vol. 47, pp. 16631–16634.
2. Azbel, M.Ya., Prelocalization in semimetals, *Phys. Rev., Ser. B*, 1983, vol. 27, p. 3852.
3. Glocker, D.A. and Skove, M.J., Field effect and magnetoresistance in small bismuth wires, *Phys. Rev., Ser. B*, 1977, vol. 15, p. 608.
4. Mac-Donald, D.K. and Sarginson, K., Size effect variation of the electrical conductivity of metals, *Proc. Roy Soc., Ser. A* 1950, vol. 203, pp. 223–240.
5. Chambers, R.G., The conductivity of thin wires in a magnetic field, *Proc. Roy Soc., Ser. A* 1950, vol. 202, pp. 378–394.
6. Brandt, N.B., Gitsu, D.V., Nikolaeva, A.A., and Ponomarev, Ya.G., Investigation of size effects in thin cylindrical bismuth single crystals in a magnetic field, *JETP*, 1977, vol. 45, no. 6, p. 1226.
7. Gurvitch, M.J., Resistivity anomaly in thin Bi wires: possibility of a one-dimensional quantum size effect, *J. Low Temp. Phys.,* 1980, vol. 38, p. 777.
8. Gitsu, D., Konopko, L., and Nikolaeva, A., Pressure dependent thermopower of individual Bi nanowires, *J. Appl. Phys. Lett.*, 2005, vol. 86, p. 10210.
9. Nikolaeva, A., Huber, T.E., Gitsu, D., and Konopko, L., Diameter dependent thermopower of bismuth nanowires, *Phys. Rev., Ser. B*, 2008, vol. 77, p. 035422.
10. Zhang, Z., Sun, X., Dressehaus, M.S., Ying, J.Y., and Heremans, J., Electronic transport properties of single crystal bismuth nanowire arrays, *Phys. Rev., Ser. B*, 2000, vol. 61, no. 7, pp. 4850–4861.
11. Sun, X., Zhang, Z., and Dresselhaus, M.S., Theoretical modeling of thermoelectricity in Bi nanowires, *J. Appl. Phys. Lett.*, 1999, vol. 74, no. 26, pp. 4005–4007.
12. Heremans, J.P. and Trush, C.M., Thermoelectric power of bismuth nanowires, *Phys. Rev., Ser. B*, 1999, vol. 59, p. 12579.
13. Heremans, J., Trush, C.M., Zhang, Z., Sun, X., Dresselhaus, M.S., Ying, J.Y., and Morreli, D.T., Magnetoresistance of bismuth nanowire arrays: a possible transition from one-dimensional to three-dimensional localization, *Phys. Rev., Ser. B*, 1998-II, vol. 58, no. 16, pp. R10091–R10095.
14. Heremans, J.P., Trush, C.M., Morreli, D.T., and Wu, H.-C., Thermoelectric power of bismuth nanocomposites, *Phys. Rev. Lett.,* 2002, vol. 88, p. 216801.
15. Gitsu, D.V., Golban, I.M., Kantser, V.G., and Munteanu, F.M., *Transport Phenomena in Bismuth and Its Alloys*, Kishinev: Shtiintsa, 1983, p. 266.
16. Edel'man, V.S., Svoistva elektronov v vismute, *Usp. Fiz. Nauk*, 1977, vol. 123, p. 257.
17. Gaidukov, Yu.P., Elektronnye svoistva viskerov, *Usp. Fiz. Nauk*, 1984, vol. 142, p. 571.
18. Khamidullin, R.A., Brusenskaya, E., Konopko, L.A., Nikolaeva, A.A., and Tsurkan, A., Conductivity of bismuth nanowires at low temperatures in transverse magnetic field, *J. Low Temp. Phys.,* 2010, vol. 158, pp. 536–543.
19. Siniavskiy, E.P. and Solovenko, V.G., Osobennosti termo-magnitnyh yavleni' v nanostrukturah, *J. Thermoelectricity,* 2009, vol. 2, pp. 29–32.

ISSN 1068-3755, Surface Engineering and Applied Electrochemistry, 2014, Vol. 50, No. 1, pp. 63–71. © Allerton Press, Inc., 2014.

Role of Cadmium on Corrosion Resistance of Zn–Ni Alloy Coatings[1]

Vaishaka R. Rao and A. Chitharanjan Hegde

Electrochemistry Research Laboratory, Department of Chemistry, National Institute of Technology Karnataka, Surathkal Srinivasnagar, 575025, India

e-mail: hegdeac@rediffmail.com

Received November 17, 2012; in final form, February 14, 2013

Abstract—Cadmium (Cd) catalyzed Zn–Ni alloy plating has been accomplished galvanostatically on mild steel (MS) using gelatin and glycerol as additives. The effect of addition of Cd into Zn–Ni bath has been examined in terms of nickel (Ni) content and corrosion resistance of Zn–Ni–Cd ternary alloy coatings. The process and product of electrolysis under different concentrations of additives and Cd have been investigated by cyclic voltammetry (CV). The effects of current density (c.d.) on Ni content of the alloy have been studied by spectrophotometric method, supported by EDX analysis. The deposition has been carried out under different concentrations of Cd ranging from 0.004 to 0.1 M. The corrosion rates (CR) of Zn–Ni alloy coatings have been found to decrease drastically with addition of Cd. It has been also revealed that the CR of binary Zn–Ni alloy coatings decreased with the increase of Cd concentration only up to a certain optimal concentration, i.e., up to 0.02 M, and then remained unchanged. An effort to change the anomalous type of codeposition into normal one by changing the molar ratios of the metal ions, i.e. $[Cd^{2+}]/[Ni^{2+}]$ as 0.01, 0.05 and 0.25 has remained futile. CV study demonstrated an important role of Cd in mutual depositions of Zn^{2+} and Ni^{2+} ions by its preferential adsorption, thus leading to the increased Ni content of the alloy. The bath composition and operating parameters have been optimized for deposition of bright and uniform Zn–Ni–Cd alloy coatings. Changes in the surface morphology and phase structure of Zn–Ni alloy coatings due to addition of Cd has been confirmed by Scanning Electron Microscopy (SEM) and X-Ray Diffraction (XRD) study respectively. Experimental investigations so as to identify the role of Cd in codeposition Zn–Ni alloy coatings have been carried out and the results are discussed.

Keywords: Zn–Ni–Cd alloy, glycerol, corrosion study, XRD, SEM

DOI: 10.3103/S1068375514010141

INTRODUCTION

Electrodeposition of Zn-based alloys (both binary and ternary) are gaining interest in the automotive industry due to their higher corrosion resistance than pure Zn coating. Zn is a very active metal due to its low standard electrode potential [$E^0 = -0.76$V vs. Normal Hydrogen Electrode, NHE]. It is well known that proper alloying of any metal can improve its properties such as hardness, mechanical strength, wear resistance as well as corrosion resistance [1]. Zn–Ni alloy deposition is known for a peculiar anomalous type of codeposition, where the less noble Zn deposits more readily compared to the nobler Ni as explained by Brenner [2]. This unusual behavior was accounted for "*hydroxide suppression mechanism*". According to which $Zn(OH)_2$ precipitate at the cathode (due to local increase of pH) prohibits the deposition of nobler Ni [3, 4]. This phenomenon is found to be true in codepositions of all Zn–Fe group metal alloys and mutual alloys of Fe-group metals.

The Zn–Ni alloy coatings obtained by electrodeposition having higher percentage of Ni, varying between 8 and 14% by wt., was found to exhibit better corrosion protection (five to six times superior) compared to that of pure Zn coatings [5–8]. Additives are extremely important in electroplating of metals and alloys as they influence the grain size, deposition pattern and the composition of the alloy [9]. Soares et al. have studied electrodeposition of Zn–Ni alloy using gelatin [10]. They noticed that an increase in the concentration of gelatin heightened the deposition efficiency and the Ni content of the alloy. On the other hand, Pedrosa et al. used glycerol as an additive in the deposition of Zn–Ni alloy and studied the effect of glycerol content on cathode current efficiency (CCE) [11]. They declared that the CCE and corrosion stability of the coatings were found to be changed drastically with addition of more glycerol by hindering the hydrogen evolution during reduction of metal ions. Albalat et al. showed that Zn–Ni alloy coatings with even a low Ni content, but in the presence of particular addi-

[1] The article is published in the original.

Table 1. Bath composition and operating parameters for deposition of bright Zn–Ni and Zn–Ni–Cd coatings on MS

Bath ingredients, g/L	Zn–Ni	Zn–Ni–Cd
$ZnCl_2$	27.2	27.2
$NiCl_2 \cdot 6H_2O$	94.9	94.9
H_3BO_3	27.7	27.7
NH_4Cl	100	100
$CdCl_2$	–	2.2
Gelatin	5.0	5.0
Glycerol	2.5	2.5
Bath pH	4	4
Bath Temp., K	303	303

tives, can improve the surface homogeneity and corrosion stability of the coatings to a large extent [12].

The presence of high percentage of nickel in Zn–Ni alloy provides higher barrier resistance. However, these coatings with Ni content, i.e. 8–20% Ni, exhibit rough, non-uniform and unattractive finish. Hence certain brightener systems, either individually or in combination, need to be developed for bright and uniform coatings [13]. Attempts are still in progress to decrease the anomaly of codeposition observed in Zn–Ni alloys either by introducing some inert species in the deposits or by going for ternary alloy coatings [14]. The electrodeposited ternary alloys such as Zn–Ni–Co were found to exhibit higher corrosion protection compared to both binary Zn–Ni and Zn–Co alloy coatings [15–17]. Cadmium (Cd) has been widely used in aerospace, electrical and fastener industries due to its excellent corrosion resistance and other engineering attributes. But environmental concerns on its toxicity and the failure in the structure, due to hydrogen embrittlement phenomenon, made it to go for some alternative methods.

The Cd coating developed on the hard steel was found to enhance the cathodic current efficiency and retard the Zn deposition with increasing current density and temperature [18]. Addi et al. attempted to reduce the anomalous codeposition of Zn–Ni alloy using boric acid and Cd. CV study demonstrated that the presence of boric acid and Cd in sulfate bath reduced the Zn deposition by shifting the reduction peak of Ni to more negative potentials and increasing the peak height. By reducing the Zn–Ni ratio with the addition of Cd, the barrier property of the steel surface has been increased drastically. A large reduction in the corrosion current, due to increase in the Ni content of the deposit, was achieved [19–21]. The corrosion resistance of alloy was found to be dependent on the noble metal content of the deposit [22]. Kim et al. have developed an alkaline Zn–Ni–Cd bath for good coatings of high Ni content [23]. Hence in the light of the above investigations this paper considers the catalytic role of Cd in electrodeposition of Zn–Ni–Cd, in the presence of gelatin and glycerol as additives, while improving the Ni content and corrosion stability of the coatings. Comparison of binary and ternary alloy coatings in terms of surface morphology, phase structure and corrosion stability has been made and results are discussed.

MATERIALS AND METHODS

Acidic baths with $ZnCl_2$, $NiCl_2$, $CdCl_2$ (as metal salts), NH_4Cl (as conducting salt), boric acid (as buffer), gelatin + glycerol (as additives) were used. Gelatin and glycerol were used in combination in order to control the deposition rate, crystallization, leveling and brightness of the deposit. Due to a very high molecular weight of gelatin, its content in the plating baths in the present study is in concentrations that were several orders of magnitude smaller than the concentrations of metal ions. The plating solutions were freshly prepared with distilled water and filtered through Whatmann™ laboratory grade filter paper. Electroplating of mild steel (MS) plates was done at pH 4.0 and $T = 303 \pm 2$ K, for either 10 or 20 min (the former time—for corrosion study, the latter—for determination of chemical composition and CCE. The bath pH was monitored regularly and adjusted when necessary. The polished MS plates had an exposed surface area of either 7.5 or 25 cm^2 (the former—for the corrosion study) and served as a cathode. They were degreased with an alkali cleaner prior to coating. The gelatin being insoluble in cold water was dissolved in hot water and then poured into the bath. The gelatin was found to show significant effect on deposition process as proved by the CV study.

No nitrogen purging was done for electrolytic solution. The Hull cell method was used to examine the effect of additives and variation in molar concentration of Cd. The Hull cell study made it necessary to limit the applied current density (c.d.) within 1.0–4.0 A dm^{-2}, which yielded coatings with different appearance (porous/powdery/semi-bright/bright for Zn–Ni alloy and blackish/semi-bright/bright for Zn–Ni–Cd alloy). The bath composition and operating parameters of binary Zn–Ni and ternary Zn–Ni–Cd alloy baths were achieved by Hull cell method, and the data are given in Table 1. The CCE or Faradaic efficiency was calculated using the mass gained, the charge transferred and the chemical composition of the deposit:

$$\mathrm{CCE} = \frac{\text{measured mass gain}}{\text{theoretical mass gain}} \times 100$$

$$= \frac{w}{\dfrac{\mathrm{EW} \times I \times t}{F}} \times 100 = \frac{wF}{It}\sum\frac{c_i}{M_i} \times 100.$$

where w is the measured mass of the deposit in grams, t is the time of deposition, I is the current applied. EW

Table 2. Deposit characters of binary Zn–Ni alloy coatings developed from optimized bath at different c.d.'s

C.d., A dm^{-2}	Wt % of Ni	CCE, %	Hardness VHN	Nature of deposit	Thickness, μm	E_{corr}, V/vs. SCE	i_{corr}, μA cm^{-2}	CR × 10^{-2}, mm yr^{-1}
1.0	2.62	90.1	146	Porous/powdery	5.8	1.019	17.62	23.42
2.0	4.05	91.5	153	Semi-bright	10.4	1.086	13.87	18.44
3.0	7.95	92.4	202	Bright	17.8	1.105	10.88	14.46
4.0	8.07	90.5	184	Semi bright	23.2	1.162	12.53	16.66

Table 3. Deposit characters of ternary Zn–Ni–Cd alloy coatings developed from optimized bath at different c.d.'s

C.d., A dm^{-2}	Wt % of Ni	Hardness (VHN)	CCE, %	Nature of deposit	Thickness, μm	E_{corr}, V/vs. SCE	i_{corr}, μA cm^{-2}	CR × 10^{-2}, mm yr^{-1}
1.0	11.82	154	91.15	Black	7.3	1.098	2.71	3.93
2.0	6.15	169	92.10	Semi-bright	11.4	1.072	2.60	3.77
3.0	11.95	236	94.18	Bright	17.9	1.125	0.74	1.06
4.0	13.22	188	91.61	Semi-bright	21.8	1.145	2.69	3.90

is the equivalent weight of the alloy (g equiv^{-1}), c_i is the weight fraction of the element in the alloy deposit, n_i is the number of electrons transferred per atom of each metal, m_i is the atomic mass of that element and F is the Faraday constant (96485 C mol^{-1}).

All chemicals used in the present study are of Analytical Grade. Double distilled water was used for the preparation of electrolyte solutions. The effect of the additives (gelatin and glycerol) and Cd, at different molar concentrations, were studied by CV using a three-electrode cell. The deposition was carried out on a pure platinum foil as a working electrode to eliminate noise. It is confirmed that once several nanometers of coating material are deposited, the substrate no longer has any effect on the deposition process [24]. Before carrying out each experiment the electrodes were cleaned and activated by immersing in dil. HNO_3 solution for several minutes. The experiments were carried out in a still solution without disturbing. The saturated calomel electrode (SCE) was used as the reference electrode. The potential scan began at around +1.1 V in the positive direction, upto +2.7 V. Then, the scan rate reversed back in the negative direction, down to 2.5 V whereas –3.5 V, in the presence of Cd, finally reversing back in the positive direction up to +2.7 V.

The thickness of the coating was estimated by Faraday's law and verified by measuring in Digital Thickness Meter (Coatmeasure Model M&C, AA Industries/Yuyutsu Instruments). The hardness of coatings was measured using Digital Micro Hardness Tester (CLEMEX). The compositions of alloys were evaluated by the spectrophotometric method as in [25]. The corrosion behavior of the coatings, having 7.5 cm^2 active surface area, has been studied in 5% NaCl at 298 K (ACM Instruments, Gill AC Series No-1480). The electrochemical impedance spectroscopy (EIS) study was made in the frequency range of 100 kHz–10 mHz, and corresponding Nyquist plots were analyzed. The potentiodynamic polarization study has been carried out at the scan rate of 1 mV/s, in a potential ramp of ±250 mV from OCP. The corrosion resistance of coatings was evaluated by Tafel's extrapolation method [26]. The surface properties of the coatings were studied by means of SEM (Model JSM-6380 LA from JEOL, Japan) interfaced with EDX. The phase structures of alloy coatings were identified by XRD (JEOL JDX-8P), using Cu Kα (λ = 1.5406 Å) radiation in a continuous scan mode at the scan rate of 2 min^{-1}.

RESULTS AND DISCUSSION

Hull Cell Study

The Hull cell method is the most elegant approach for optimization of the operating parameters like c.d., temperature, pH and bath composition in terms of salt concentration and additives for a bright and uniform deposit [27]. The optimal bath ingredients and operating parameters of binary Zn–Ni and ternary Zn–Ni–Cd alloy baths are given in Table 1.

The deposit characters such as composition, hardness, thickness, appearance and corrosion behavior of binary Zn–Ni and ternary Zn–Ni–Cd alloy coatings deposited at different c.d.'s, from specified optimal baths are reported, respectively, in Table 2 and Table 3.

Cyclic Voltammetry Study

The CV study was carried out so as to get the preliminary information about the deposition and dissolution process of the alloy in the presence/absence of additives and Cd. Figure 1 shows the CV for deposition

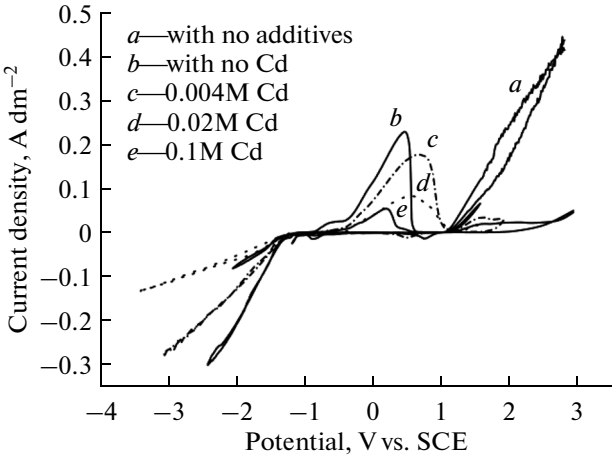

Fig. 1. Cyclic voltammetric study for deposition and dissolution of Zn–Ni alloy in presence of additives, and Cd ions at different molar concentrations at 303 K.

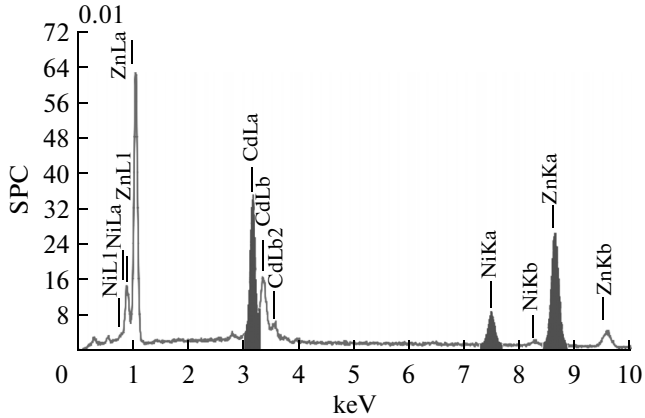

Fig. 2. EDX spectrum showing relative amount of M (Zn, Ni and Cd) in Zn–Ni–Cd coatings, deposited at 3.0 A dm^{-2} under condition of 0.02 M $CdCl_2$.

and dissolution of the alloy under various conditions mentioned therein. It may be observed that cathodic peaks are profoundly influenced by the presence of additives and of Cd at different concentrations. The preliminary CV study with only additives revealed that they are electrochemically inactive. The CV for only metal ions, the potential scan started at around 2.7 V signaled the deposition of Zn(II)-Zn(0) at −1.15 V followed by an evolution of hydrogen at still negative potential. No specific dissolution peak was observed in cyclic voltammogram corresponding to an alloy without additives (Fig. 1*a*).

However, on addition of additives, a distinct anodic peak was observed as shown in Fig. 1*b*, corresponding to the dissolution of Zn–Ni alloy having γ-Zn (411, 330), Zn (101) and Zn (103) phase structures. Further, addition of a small amount of Cd (0.004 M) into the electrolytic bath has changed the nature of CV by shifting the peak anodic potential to a more noble side as shown in Fig. 1*c*, indicating the formation of Zn–Ni–Cd alloy having different XRD patterns. This observation is supported by increased Ni content of the ternary alloy as depicted in Table 3.

Increase of Cd concentration in the bath, i.e. to 0.02 M, resulted in decrease of the anodic current corresponding to the dissolution of the alloy having 11.95 wt % Ni. However, further addition of Cd into the bath led to the coating showing lowest corrosion protection, signaled by a shorter anodic peak as shown in Fig. 1*e*. Hence, a ternary Zn–Ni–Cd alloy corresponding to 0.02 M Cd, demonstrating the least CR, was taken as optimal concentration as shown in Table 1. The CV response was found to be discouraging on further addition of Cd into the bath (Fig. 1*e*). It may be attributed to an excessive adsorption of Cd, which blocks the active sites of the cathode surface and inhibits the electrocrystallisation of Ni as well as Zn ions [19, 24]. Thus CV study revealed that addition of gelatin + glycerol has improved the homogeneity and brightness of the deposit, while Cd ions catalyzed the deposition of Zn–Ni by increasing the Ni content only at minimal concentration. Thus addition of Cd into the bath plays a specific role in improving the corrosion resistance of the ternary alloy, consequent to its Ni content.

The CV study on electrodeposition of Zn–Ni–Cd alloy revealed that depositions of Zn and Cd are mass-transfer controlled while nickel is kinetically controlled [28]. Therefore, addition of Cd into the bath has a significant effect on the nature of cyclic voltammogram represented by curves *b*, *c*, *d* and *e* in Fig. 1, in terms of anodic peak currents/potentials. This may be explained by low reduction potential of Cd compared to that of Zn, and by a low equilibrium potential (or high activation over potential) of Ni for depositing at room temperature. Hence, Cd and Ni content (in the deposit) dominates over Zn at low concentrations [24]. For the same reason, the deposition c.d. and concentrations of Cd^{2+} ions largely affect the composition of the deposit and hence its properties.

Compositional Analysis of Coatings

The composition of Zn–Ni and Zn–Ni–Cd alloy coatings deposited at different c.d's were analyzed by colorimetric method by stripping the deposit in dil. HCl [29]. This was further confirmed by Energy Dispersive X-ray analysis (EDXA) shown in Fig. 2.

Effect of Cd on Ni Content of the Ternary Alloy

Bright and uniform Zn–Ni coatings having 7.95% Ni were obtained at 3.0 A dm^{-2}. The Ni content of

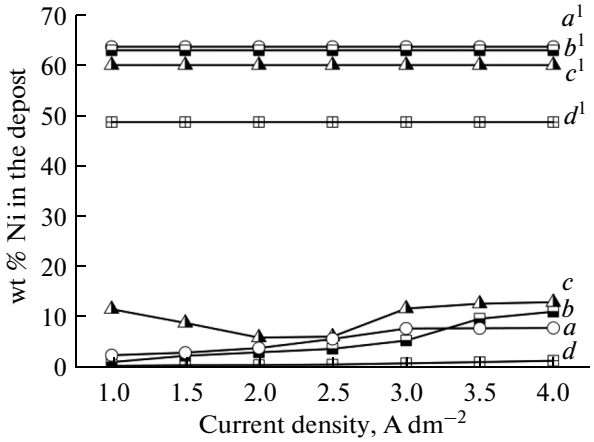

Fig. 3. Variation of Ni content at different molar concentrations of Cd: (*a*) without Cd; (*b*) 0.004 M; (*c*) 0.02 M and (*d*) 0.1 M (horizontal lines represented by a^1, b^1, c^1 and d^1 show corresponding Ni content in the bath as calculated from bath composition).

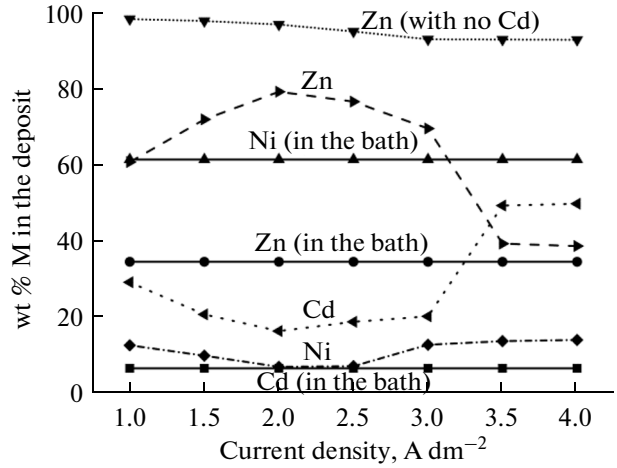

Fig. 4. Variation in metal content, M (Zn, Ni and Cd) in Zn–Ni–Cd alloy with current density under optimal bath conditions.

binary Zn–Ni alloy was found to increase with applied c.d., i.e., from 1.0 A dm^{-2} through 4.0 A dm^{-2}, showing an anomalous type of codeposition (Table 2). In addition, the Ni content of Zn–Ni–Cd coatings over a wide range of c.d. (under optimal bath condition) has been studied and results are reported in Table 3. It may be noticed that the ternary bath showed similar behavior as binary bath, except for an increase of Ni content in the deposit. It may be attributed to the codeposition of Zn and Ni catalyzed by Cd^{2+} ions.

The effect of addition of $CdCl_2$, over a range of c.d., on the composition of Zn–Ni–Cd alloy has been studied. The [$CdCl_2$] varied from 0.004 M through 0.1 M, while concentration of $ZnCl_2$ and $NiCl_2 \cdot 6H_2O$ were fixed as 27.2 and 94.9 g/L, respectively. The bath pH was maintained at 4.0, and depositions were carried out at 303 K. Variations in Ni content with Cd concentration, i.e. 0.004, 0.02 and 0.1 M $CdCl_2$ including the one without Cd, are shown in Fig. 3.

It may be noted that wt % Ni in the deposit increased with the addition of Cd only up to a certain level (0.02 M) and then decreased. Further, under no conditions of c.d.'s and $CdCl_2$ concentrations, the Ni content of the deposit has reached that in the respective baths (represented by horizontal lines) as shown in Fig. 3. Addition of a tracer amount of $CdCl_2$ increased the Ni content of the alloy at high c.d. in relation to the one without Cd as shown in Fig. 3. It can be accounted by the fact that adsorbed Cd^{2+} ions inhibited the preferential deposition of Zn, thereby suppressing the anomalous codeposition (or favoring the normal deposition).Thus Cd^{2+} ions suppressed the anomalous type of codeposition by retarding the deposition of Zn. In other words, Cd^{2+} ions catalyzed the Ni deposition.

Variation in M Content at Different Concentrations of $CdCl_2$

The concentrations of Cd^{2+} ions and applied c.d. were found to largely affect the composition, i.e., Ni content, and properties of the coatings. With this incentive, the M content (Zn, Ni and Cd) of Zn–Ni–Cd alloy over a range of c.d. has been studied, keeping $CdCl_2$ as 0.02 M. The variation of M content as a function of deposition c.d. is shown in Fig. 4. It may be noted that due to preferential adsorption of Cd^{2+} ions, even a small amount of $CdCl_2$ (2.2 g/L) decreased the Zn content of the alloy by allowing the normal codeposition (with no *hydroxide suppression mechanism*) [2]. This is evidenced by high Cd content of the alloy over the entire range of c.d., compared to that in the bath as shown in Fig. 4. This is not observed in relation to the codeposition of Ni and Cd, instead, it followed anomalous type of codeposition. Hence it may be concluded that the preferential deposition of Cd is due to inherent deposition overpotential of Ni. Thus in presence of Cd, an increase of Ni content in the deposit was observed, which increased with c.d. as shown in Fig. 4.

It may be noted that at low c.d., the wt % Zn in Zn–Ni–Cd alloy increased with c.d., while its Ni and Cd content was decreasing. This increase of Zn is due to deposition of more readily depositable metal, M (Zn). However, as c.d. increased, i.e. at 2.0 A dm^{-2}, the Zn content started decreasing indicating the onset of normal codeposition. At extremely high c.d., i.e. above 3.0 A dm^{-2}, the Zn content of the alloy was found to be less than that of Cd, leaving Ni to increase slightly, as shown in Table 3. The decrease of Zn content at very high c.d. is due to the suppression of more readily depositable Zn leading to coating having more Cd and Ni. This observation once again supports the

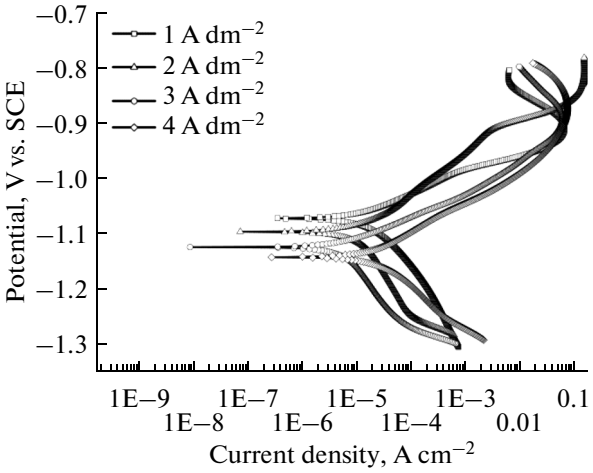

Fig. 5. Potentiodynamic polarization behavior of Zn–Ni–Cd alloy coatings at different current densities deposited from optimized bath at 303 K.

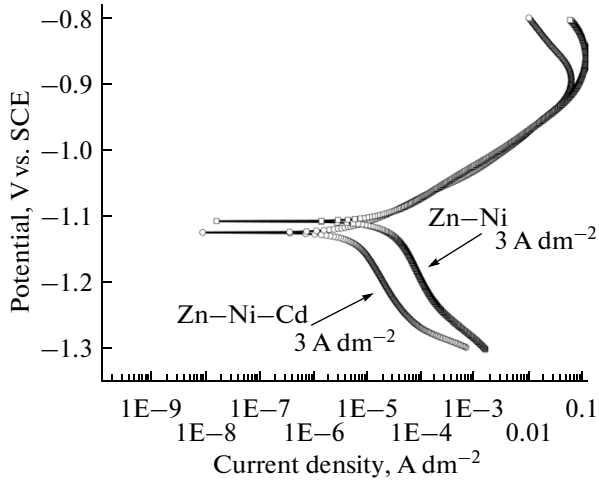

Fig. 6. Potentiodynamic polarization behavior of binary Zn–Ni and ternary Zn–Ni–Cd alloy coatings deposited from respective baths under optimal conditions.

fact that deposition of Zn and Cd are mass-transport controlled driven by the applied c.d., whereas Ni is kinetically controlled due to high activation overpotential [24]. The wt % Zn in binary alloy (deposited without Cd) was found to be much higher compared to the one with Cd as shown in Fig. 4. It shows that Cd^{2+} ions catalyze the deposition of Ni by suppressing deposition of Zn.

Thickness and Hardness of Coatings

The thickness of the coatings increased significantly with c.d. in both Zn–Ni and Zn–Ni–Cd coatings as reported in Tables 2 and 3. The thickness was found to have a linear dependency with c.d., employed for its deposition as required by Faraday's law. The appearance and composition of the coatings were found to be largely influenced by the c.d., as exhibited in other Zn–Fe group metal alloys, namely Zn–Ni, Zn–Co, Zn–Fe and less commonly in Zn–Mn. Similarly, the hardness of deposits were found to be increased with c.d. up to a certain level, and then decreased. This decrease is due to local alkylation caused by high hydrogen discharge at cathode.

CORROSION STUDY

Polarization Behavior

The electroplated coatings were subjected to the corrosion study in 5% NaCl solution. The corrosion data of Zn–Ni and Zn–Ni–Cd alloy coatings deposited at different c.d.'s, from specified baths, are reported in Tables 2 and 3, respectively. Tafel's extrapolation method was used to evaluate the corrosion rate (CR), expressed in mm yr^{-1}. The polarization behaviors of Zn–Ni–Cd alloy coatings (only representative) at different c.d.'s are shown in Fig. 5.

The CR of the coatings decreased with c.d. up to 3.0 A dm^{-2} and then increased as evidenced by corresponding i_{corr} values. The decrease in E_{corr} value with the increase in c.d. showed the corrosion protection to be anodic in nature. Thus, the Zn–Ni–Cd ternary alloy at optimal c.d., i.e., 3.0 A dm^{-2}, exhibited the least CR (1.06×10^{-2} mm yr^{-1}), which is about 14 times better than Zn–Ni binary alloy coating. The relative polarization behavior of binary Zn–Ni and ternary Zn–Ni–Cd alloy coatings deposited from respective optimal baths are shown in Fig. 6.

Electrochemical Impedance Spectroscopy Study

EIS or AC impedance method is a very popular technique to acquire the valuable information regarding electrode processes like double layer capacitance for the enhanced corrosion protection and role of inhibitors etc. EIS study considers the response of test specimen for AC signals of small amplitude. The most versatile tool is the Nyquist plot that commonly displays the data as imaginary impedance, Z_{img}, vs. real impedance, Z_{real}, with the provision to distinguish the contribution of polarization resistance (R_p) verses solution resistance (R_s) [30]. The Nyquist response of Zn–Ni–Cd coatings deposited at different c.d. is shown in Fig. 7. The impedance responses indicate that the polarization resistance, R_P increased progressively with c.d.'s, and reached maximum at 3.0 A dm^{-2} i.e., the real component of the impedance Z_{real} is more comparable to other c.d's. Comparison of impedance responses of Zn–Ni–Cd coatings developed at different c.d's reveals that coating at 3.0 A dm^{-2} is most corrosion resistant, and is shown in inset of Fig. 7.

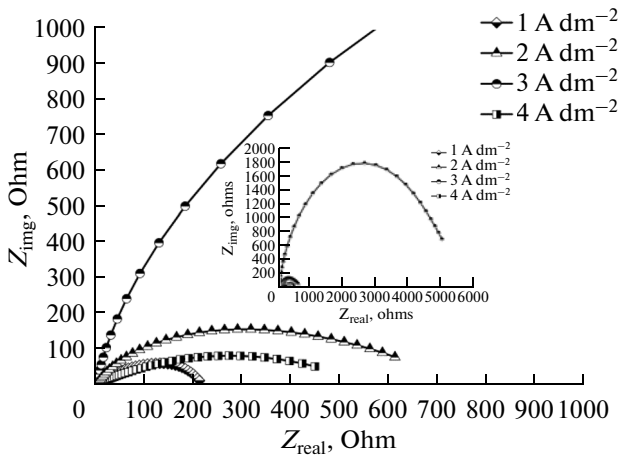

Fig. 7. Electrochemical impedance response (Real vs. Imaginary reactance values) displayed by Zn–Ni–Cd coatings at different c.d.'s from optimized bath.

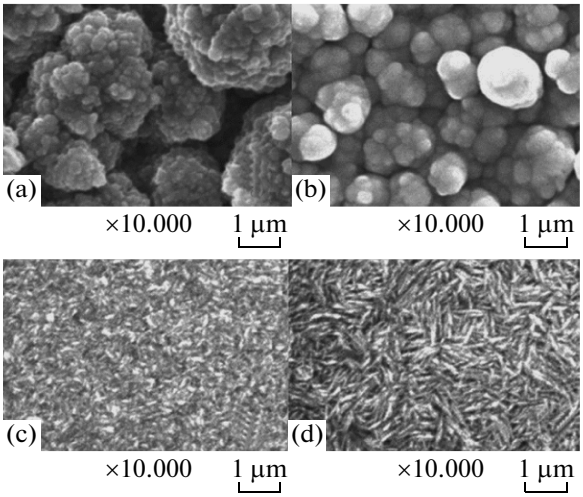

Fig. 8. SEM image of Zn–Ni–Cd coatings deposited using optimized bath at different c.d.'s: (a) 1.0 A dm^{-2}; (b) 2.0 A dm^{-2}; (c) 3.0 A dm^{-2} and (d) 4.0 A dm^{-2}.

Surface Morphology

The surface morphology of Zn–Ni–Cd at different c.d.'s deposited from the optimal bath is shown in Fig. 8.

A significant change in the surface structure of the coatings was found as c.d. was changed. The cauliflower type surface structure has changed to a well defined granular one when c.d. was changed from 1.0 to 2.0 A dm^{-2} as shown in Figs. 8a and 8b. The granular structure formed at 3.0 A dm^{-2} tends to form a needle-like structure at high c.d., i.e. 4.0 A dm^{-2}, as shown in Figs. 8c and 8d, respectively.

XRD Study

The surface morphology and XRD peaks of binary Zn–Ni and ternary Zn–Ni–Cd coatings deposited at optimal c.d., i.e., at 3.0 A dm^{-2}, is shown in Fig. 9.

The surface morphology of binary alloy coatings was changed when Cd was added into the bath. Though XRD reflection corresponding to γ-Zn (411, 300) phase was observed in both binary and ternary alloy coatings, the dominant Zn (101), Zn (103), Ni_3Zn_{22} (510) and Zn (112) peaks, observed in Zn–Ni alloy (Fig. 9a) were suppressed in ternary Zn–Ni–Cd coatings. However, addition of Cd into an electrolytic bath resulted in the coatings having distinct Cd (002), Cd (100), Ni (222), Ni_5Zn_{21} (332), Zn (102), Cd (103), Zn (600) and Ni_5Zn_{21} (631) reflections as shown in Fig. 9b. A significant difference in the surface structure of Zn–Ni alloy (having 7.95 wt % Ni) and Zn–Ni–Cd alloy (having 11.95 wt % Ni) coatings was found as shown in Figs. 9a and 9b, respectively. Thus XRD study revealed that the enhanced corrosion protection of Zn–Ni–Cd is due to unique phase structure of the coating having specific composition.

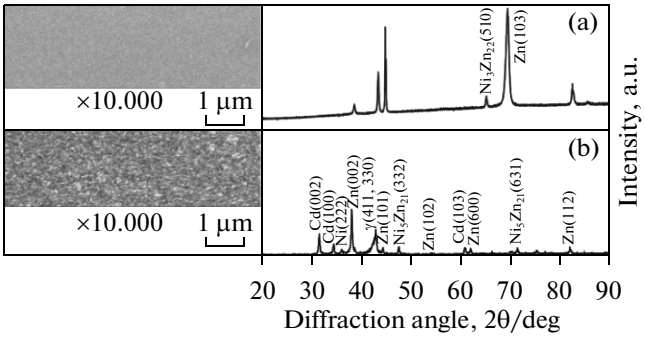

Fig. 9. Surface morphology and corresponding XRD patterns of alloy deposited from respective baths at 303 K: (a) Zn–Ni and (b) Zn–Ni–Cd.

CONCLUSIONS

Based on experimental investigations on electrodeposition of Zn–Ni alloy using Cd as a catalyst, the following observations were made as conclusions:

(1) A stable Zn–Ni–Cd bath has been proposed for electrodeposition of bright coatings on MS using gelatin and glycerol as additives.

(2) The CV study revealed that addition of gelatin and glycerol has improved the homogeneity and brightness of the deposit, while Cd ions catalyzed the deposition of Ni by suppressing the anomalous codeposition.

A small amount of Cd is good enough to bring significant increase in the Ni content, and hence corrosion resistance of the ternary alloy. The added Cd enhanced the Ni nucleation process by suppressing the anomalous codeposition.

A small amount of $CdCl_2$ decreased the Zn content of the alloy by allowing the normal codeposition. But it was not observed with referring to codeposition of Ni and Cd, due to inherent deposition overpotential of Ni.

However the effect is diminishing with the excess addition of Cd due to the adsorbed Cd that blocks the active sites of the cathode and inhibits the electrocrystallisation of Zn and Ni.

The applied cathode current density and $[Cd^{2+}]$ ions largely affect the composition, and hence the properties of the Zn–Ni–Cd alloy by decisively changing Ni content of it.

The decrease of Zn content at a very high c.d. is due to suppression of more readily depositable Zn, leading to deposition of coatings having more Cd and Ni. This observation confirms the fact that depositions of Zn and Cd are mass-transport controlled driven by the applied c.d., whereas Ni is kinetically controlled due to its high activation overpotential.

Both the SEM and XRD studies demonstrated that the peak corrosion protection of Zn–Ni–Cd coatings is due to their unique surface morphology and phase structure conditioned by the Ni and Cd content.

Zn–Ni–Cd alloy coating at optimal c.d., i.e., 3.0 A dm^{-2}, exhibited the least CR (1.06×10^{-2} mm yr^{-1}), which is about 14 times better than Zn–Ni binary alloy coating, evidenced by potentiodynamic polarization and electrochemical impedance study.

ACKNOWLEDGMENTS

Mr. Vaishaka R. Rao acknowledges the financial support of the National Institute of Technology Karnataka (NITK), Suratkal, in the form of Institute fellowship.

REFERENCES

1. Albalat, R., Gomez, E., Muller, C., Sarret, M., and Valles, E., Electrodeposition of zinc–nickel alloy coatings: Influence of a phenolic derivative, *J. Appl. Electrochem.*, 1990, vol. 20, pp. 635–639.
2. Brenner, A., *Electrodeposition of Alloys-Principles and Practice*, Vols. 1, 2, New York: Academic Press, 1963.
3. Ishihara, M., Yumoto, H., Akashi, K., and Kamei, K., Zinc–nickel alloy whiskers electrodeposited from a sulfate bath, *Mater. Sci. Eng., Ser. B*, 1996, vol. 38, pp. 150–155.
4. Zech, N., Podlaha, E.J., and Landolt, D., Anomalous codeposition of iron group metals, I: Experimental results, *J. Electrochem. Soc.*, 1999, vol. 146, pp. 2886–2891.
5. Bhat, R.S., Bhat, K.U., and Hegde, A.C., Corrosion behavior of electrodeposited Zn–Ni, Zn–Co and Zn–Ni–Co alloys, *Anal. Bioanal. Electrochem.*, 2011, vol. 3, pp. 302–315.
6. Fratesi, R. and Roventi, G., Corrosion resistance of Zn–Ni alloy coatings in industrial production, *Surf. Coat. Technol.*, 1996, vol. 82, pp. 158–164.
7. Younan, M.M., Surface microstructure and corrosion resistance of electrodeposited ternary Zn–Ni–Co alloy, *J. Appl. Electrochem.*, 2000, vol. 30, pp. 55–60.
8. Yogesha, S. and Hegde, A.C., Optimization of bright zinc–nickel alloy bath for better corrosion resistance, *T Ind. I Metals*, 2010, vol. 63, pp. 841–846.
9. Boto, K., Organic additives in Zn electroplating, *Electrodep. Surf. Treat.*, 1975, vol. 3, pp. 77–95.
10. Soares, M.E., Souza, C.A.C., and Kuri, S.E., Characteristics of a Zn–Ni electrodeposited alloy obtained from controlled electrolyte flux with gelatin, *Mater. Sci. Eng., Ser. A*, 2005, vol. 402, pp. 16–21.
11. Pedroza, G.A.G., de Souza, C.A.C., Carlos, I.A., and de Andrade Lima, L.R.P., Evaluation of the effect of deposition bath glycerol content on zinc–nickel electrodeposits on carbon steel, *Surf. Coat. Technol.*, 2012, vol. 206, pp. 2927–2932.
12. Albalat, R., Gomez, E., Muller, C., Pregonas, J., Sarret, M., and Valles, E., Zinc–nickel coatings-relationship between additives and deposit properties, *J. Appl. Electrochem.*, 1991, vol. 21, pp. 44–49.
13. Muller, C., Sarret, M., and Benballa, M., Some peculiarities in the codeposition of zinc–nickel alloys, *Electrochim. Acta,* 2001, vol. 46, pp. 2811–2817.
14. Venkatakrishna, K., Hegde, A.C., and Eliaz, N., Electro-deposition of Zn–Ni, Zn–Fe and Zn–Ni–Fe alloys, *Surf. Coat. Technol.*, 2010, vol. 205, pp. 2031–2041.
15. Younan, M.M. and Oki, T., Electrodeposition of Zn–Ni–Fe alloy in acidic chloride bath with separated anodes, *J. Appl. Electrochem.*, 1996, vol. 26, pp. 537–541.
16. Abou-Krisha, M.M., Rageh, H.M., and Matter, E.A., Electrochemical studies on the electrodeposited Zn–Ni–Co ternary alloy in different media, *Surf. Coat. Technol.*, 2008, vol. 202, pp. 3739–3746.
17. Abou-Krisha, M.M., Influence of Ni^{2+} concentration and deposition potential on the characterization of thin electrodeposited Zn–Ni–Co coatings, *Mater. Chem. Phys.*, 2011, vol. 125, pp. 621–627.
18. Abd El Rehim, S.S., Fouad, E.E., Abd El Wahaab, S.M., and Hassan, H.H., Electrodeposition of Zn–Ni–Cd ternary alloys from acetate bath, *Ind. J. Chem. Technol.*, 1998, vol. 5, pp. 387–392.
19. Addi, Y. and Khouider, A., Zinc-nickel codeposition in sulfate solution combined effect of cadmium and boric acid, *Int. J. Electrochem.*, 2011, pp. 1–7, doi: 10.4061/2011/742191.
20. Durairajan, A., Haran, B.S., White, R.E., and Popov, B.N., Development of a new electrodeposition process for plating of Zn–Ni–X (X = Cd, P) alloys, I: Corrosion characteristics of Zn–Ni–Cd ternary alloys, *J. Electrochem. Soc.*, 2000, vol. 147, no. 5, pp. 1781–1786.
21. Ganesan, P., Kumaraguru, S.P., and Popov, B.N., Development of Zn–Ni–Cd coatings by pulse electrodeposition process, *Surf. Coat. Technol.*, 2006, vol. 201, pp. 3658–3669.
22. Felloni, L., Fratesi, R., Quadrini, E., and Roventi, G., Electrodeposition of zinc-nickel alloys from chloride solution, *J. Appl. Electrochem.*, 1987, vol. 17, pp. 574–582.

23. Kim, H., Popov, B.N., and Chen, K.S., A novel electro-deposition process for plating Zn–Ni–Cd alloys, *J. Electrochem. Soc.*, 2003, vol. 150, no. 2, pp. C81–C88.

24. Eliaz, N., Venkatakrishna, K., and Hegde, A.C., Electro-plating and characterization of Zn–Ni, Zn–Co and Zn–Ni–Co alloys, *Surf. Coat. Technol.*, 2010, vol. 205, pp. 1969–1978.

25. Thangaraj, V., Udayashankar, N.K., and Hegde, A.C., Development of Zn–Co alloy coatings by pulsed current from chloride bath, *Ind. J. Chem. Technol.*, 2008, vol. 15, pp. 581–587.

26. Jones, D.A., *Principles and Prevention of Corrosion,* New York: Prentice Hall, 1996.

27. Pardhasaradhy, N.V., *Practical Electroplating Hand Book*, New Jersey: Prentice Hall Incl. Publ., 1987.

28. Ashassi-Sorkhabi, H., Hagrah, A., Parvini-Ahmadi, N., and Manzoori, J., Zinc–nickel alloy coatings electrodeposited from a chloride bath using direct and pulse current, *Surf. Coat. Technol.*, 2001, vol. 140, pp. 278–283.

29. Vogel, A.I., *Quantitative Inorganic Analysis*, 3rd ed., London: Longmans Green & Co, 1951.

30. Yuan, X., Song, C., Wang, H., and Zhang, J., *Electro-Chemical Impedance Spectroscopy in PEM Fuel Cells-Fundamentals and Applications*, London: Springer Publications, 2010.

ISSN 1068-3755, Surface Engineering and Applied Electrochemistry, 2014, Vol. 50, No. 1, pp. 72–77. © Allerton Press, Inc., 2014.
Original Russian Text © A.I. Vovchenko, V.V. Shomko, G.A. Barbashova, L.A. Kamenskaya, 2014, published in Elektronnaya Obrabotka Materialov, 2014, No. 1, pp. 66–71.

Investigation of Hydrodynamic Processes at Multi-Pulse Power Input into the Channel of an Electric Discharge in Liquid

A. I. Vovchenko, V. V. Shomko, G. A. Barbashova, and L. A. Kamenskaya

Institute of Pulse Processes and Technologies, National Academy of Sciences of Ukraine, pr. Oktyabrskii 43a, Nikolaev, 54018 Ukraine

e-mail: dpte@iipt.com.ua

Received December 12, 2012; in final form, January 18, 2013

Abstract—The method of numerical experiments has been applied to specify the conditions under which pulsation pressure pulses are realized by combined electrodischarge systems in the plasma channel and the ambient liquid. It is shown that, on the basis of a main fixed power source, it is possible to establish a series of combined power sources ensuring the generation of uniform two-pulsation pressure pulses.

Keywords: numerical experiment, pulsation pressure pulses, plasma channel, power source

DOI: 10.3103/S1068375514010153

INTRODUCTION

An electric discharge in water, which is widely used in many industries, is one of the methods to transform electric energy into mechanical energy [1, 2]. When developing processes based on an electric discharge in water through method [3] or any other, one works with the discharge characteristics (such as the discharge current and voltage in the discharge channel), which prescribe the law of the electric energy input into the channel, the pressure in it and in the ambient liquid, and the hydrodynamic load on the workpiece. Hence, it is important to produce controlled electric discharges in water.

One of the ways to produce controlled discharges is to vary the parameters of the surge-current generator (SCG) and of the length of the interelectrode gap. However, in this case, the parameters are chosen before the energy input, thus the discharge is not controlled during the process. The form of the electric power input into the channel is close to a triangular one; the compression waves propagating in the working medium most often have a steep front and a falloff near to an exponential one. Such a wave form does not meet the requirements of many discharge-pulse technological processes: for instance, there is required a wave with several peaks on the pressure–time curve with different values in each case. Multistage SCG and parametric changing of the discharge circuit (e.g., the resistance and inductance) in the course of the energy input are used in order to produce such waves in liquid.

In works [4–6], it has been shown through the numerical experiment method that, in order to realize the pulsating form of the liquid pressure on the workpiece with the multipulse energy input into the plasma channel of the electric discharge in liquid, it is necessary for a second pulse of electric power during time approximately equal to the duration of the first pulse to introduce the same or more energy than during the first one. In this case, in the second power pulse, it is necessary to introduce higher energy (3–5 times more than previously depending on the rise rate $\dot{N}_{2+}$ of the second power pulse) in order to obtain the pressure function in the channel and liquid with two pulsations with the same amplitude. The second pulsation shifts right in time with respect to the first one both due to the growth of the duration of the second power pulse $\Delta\tau_2$ and the input energy W_2, but, in the first case, it is necessary to increase W_2 in the same manner in order to obtain equal amplitudes. This energy, as a threshold one for the formation of the second pressure pulsation, can be reduced without changing of the pressure distribution owing to the growth of $\dot{N}_{2+}$ [5, 6], more truly, the growth of the relation $\dot{N}_{2+}/\dot{N}_{1+}$ ($\dot{N}_{1+}$ is the rise rate of the first power pulse).

In the works mentioned above, the start of the second power pulse input coincided with the end of the first pulse input. However, it is often necessary to repeat the electric energy input into the discharge channel at any time not only at the moment of the end of the first power pulsation [7]. The aim of this work is to ascertain the peculiarities of the hydrodynamic processes in such cases with the help of a numerical experiment.

STATEMENT OF THE PROBLEM

Assume that the discharge channel at some starting moment has the form of a quadric cylinder of some finite length; it is filled with ideal plasma and is contained in an unlimited volume of an ideal compressible liquid. In accordance with the assumptions made, the mathematical model of the process under study includes a system of two-dimensional nonlinear equations of gas dynamics [8]:

$$\begin{cases} \dfrac{\partial(r\rho)}{\partial t} + \dfrac{\partial(r\rho v_z)}{\partial z} + \dfrac{\partial(r\rho v_r)}{\partial r} = 0, \\ \dfrac{\partial(r\rho v_r)}{\partial t} + \dfrac{\partial(r\rho v_z v_r)}{\partial z} + \dfrac{\partial[r(\rho v_r^2 + p)]}{\partial r} = p, \\ \dfrac{\partial(r\rho v_z)}{\partial t} + \dfrac{\partial[r(\rho v_z^2 + p)]}{\partial z} + \dfrac{\partial(r\rho v_z v_r)}{\partial r} = 0, \\ \dfrac{\partial(re)}{\partial t} + \dfrac{\partial[r(e+p)v_z]}{\partial z} + \dfrac{\partial[r(e+p)v_r]}{\partial r} = 0. \end{cases}$$

The binomial equation of state [8]

$$s\varepsilon = [p - c_0^2(\rho - \rho_0)]/[\rho(k-1)],$$

where t is the time; r, z are the cylindrical coordinates; v_r, v_z are the radial and axial components of the liquid rate vector; p is the pressure; ρ is the water density; $e = \rho[\varepsilon + (v_r^2 + v_z^2)/2]$; ε is the specific intrinsic energy; ρ_0 is the density of the liquid at rest; c_0 is the sound velocity in the liquid at rest; and $k = 7.15$.

The condition of the energy balance in the discharge channel, as well as on its wall–plasma–water contact discontinuity (the internal boundary of the computational region) [5], is

$$\frac{1}{(\gamma-1)}\frac{d(p_a V_a)}{dt} + p_a\frac{dV_a}{dt} = N(t),$$

where p_a is the pressure in the discharge channel, V_a is the volume of the discharge channel, $\gamma = 1.26$ is the effective index of the adiabatic plasma curve, and $N(t)$ is the law of the electric energy liberation in the discharge channel.

The conditions of dynamic compatibility on the external boundary of the computational region (the shock wave) are as follows [8]:

$$[\rho]D - [\rho v_n] = 0,$$

$$[\rho v_n]D - [\rho v_n^2 + p] = 0,$$

$$[\rho(\varepsilon + v_n^2/2)]D - [\rho v(\varepsilon + v_n^2/2) + p v_n] = 0,$$

where D is the speed of the shock wave, v_n is the normal velocity of the liquid, and $[f] = f_1 - f_2, f_1, f_2$ are the values of the function to the left and to the right of the shock wave.

The initial values of the hydrodynamic characteristics are equal to those in the undisturbed medium under normal conditions.

The problem is solved through the Godunov finite-difference method [8].

The modes of the energy input into the plasma channel to determine the boundary condition on the plasma–liquid contact surface are chosen with regard for the already known conditions of the formation of pulsing pressures for the continuous model functions of the power [4, 5]. In this case, in order to take into account the conditions in [4, 5], it is assumed that the power pause time t_P between the first and the second pulses is included into the characteristic time of the energy input of the second power pulsation $\Delta\tau_{2x} = \Delta\tau_2 + t_P$. Considering two variants of the discharge modes with different values of the power pause times ($t_{P1} = 4.75$ μs and $t_{P1} = 18.75$ μs) at the fixed duration of the second power pulse of 10 μs, we obtain two values of the characteristic time of the repeated energy input $\Delta\tau_{2x}^{(2)} = 14.75$ μs and $\Delta\tau_{2x}^{(1)} = 28.75$ μs. These values of time are more than the duration of the first power pulse τ_1 by $k_\tau^{(1)} = 1.31$ and $k_\tau^{(2)} = 2.56$ times, respectively ($k_\tau^{(1,2)} = \Delta\tau_{2x}^{(1,2)}/\tau_1$). Thus, in order to form a pulsing configuration of pressure in the channel with equal amplitudes, it is necessary, in accordance with the hypothesis assumed above on the basis of the data of [4, 5], to increase the amount of the repeatedly introduced energy by (3–5) k_τ times with respect to that already introduced W_1. Please note that, if the pulsations of pressure in the channel have equal amplitudes, then, for the pressure in the liquid, it will be certainly a sufficient condition for the same situation (see [4, 5]). Thus, hereafter, we will pay special attention only to the pressure function in the channel. With regard for these estimations, we are going to form two variations of the following model modes of the discharge:

$$N(\bar{t}) = N_0\begin{cases} 0 & \text{at } \bar{t} < 0, \\ 0.281\bar{t} & \text{at } 0 \le \bar{t} \le 0.52, \\ 0.241(1.125 - \bar{t}) & \text{at } 0.52 < \bar{t} \le 1.125, \\ 0 & \text{at } 1.125 \le \bar{t} \le 1.60, \\ 0.618(\bar{t} - 1.6) & \text{at } 1.60 < \bar{t} \le 2.085, \\ 0.582(2.6 - \bar{t}) & \text{at } 2.085 < \bar{t} \le 2.6, \\ 0 & \text{at } 2.6 < \bar{t}. \end{cases} \quad (1)$$

$$N(\bar{t}) = N_0\begin{cases} 0 & \text{at } \bar{t} < 0, \\ 0.281\bar{t} & \text{at } 0 \le \bar{t} \le 0.52, \\ 0.241(1.125 - \bar{t}) & \text{at } 0.52 < \bar{t} \le 1.125, \\ 0 & \text{at } 1.125 \le \bar{t} \le 1.60, \\ 0.928(\bar{t} - 1.6) & \text{at } 1.60 < \bar{t} \le 2.085, \\ 0.874(2.6 - \bar{t}) & \text{at } 2.085 < \bar{t} \le 2.6, \\ 0 & \text{at } 2.6 < \bar{t}. \end{cases} \quad (2)$$

$$N(\bar{t}) = N_0\begin{cases} 0 & \text{at } \bar{t} < 0, \\ 0.281\bar{t} & \text{at } 0 \le \bar{t} \le 0.52, \\ 0.241(1.125 - \bar{t}) & \text{at } 0.52 < \bar{t} \le 1.125, \\ 0 & \text{at } 1.125 \le \bar{t} \le 1.60, \\ 1.236(\bar{t} - 1.6) & \text{at } 1.60 < \bar{t} \le 2.085, \\ 1.164(2.6 - \bar{t}) & \text{at } 2.085 < \bar{t} \le 2.6, \\ 0 & \text{at } 2.6 < \bar{t}. \end{cases} \quad (3)$$

$$N(\bar{t}) = N_0\begin{cases} 0 & \text{at } \bar{t} < 0, \\ 0.281\bar{t} & \text{at } 0 \le \bar{t} \le 0.52, \\ 0.241(1.125 - \bar{t}) & \text{at } 0.52 < \bar{t} \le 1.125, \\ 0 & \text{at } 1.125 \le \bar{t} \le 1.60, \\ 1.300(\bar{t} - 1.6) & \text{at } 1.60 < \bar{t} \le 2.085, \\ 1.224(2.6 - \bar{t}) & \text{at } 2.085 < \bar{t} \le 2.6, \\ 0 & \text{at } 2.6 < \bar{t}. \end{cases} \quad (3a)$$

$$N(\bar{t}) = N_0\begin{cases} 0 & \text{at } \bar{t} < 0, \\ 0.281\bar{t} & \text{at } 0 \le \bar{t} \le 0.52, \\ 0.241(1.125 - \bar{t}) & \text{at } 0.52 < \bar{t} \le 1.125, \\ 0 & \text{at } 1.125 \le \bar{t} \le 1.60, \\ 1.856(\bar{t} - 1.6) & \text{at } 1.60 < \bar{t} \le 2.085, \\ 1.748(2.6 - \bar{t}) & \text{at } 2.085 < \bar{t} \le 2.6, \\ 0 & \text{at } 2.6 < \bar{t}. \end{cases} \quad (4)$$

$$N(\bar{t}) = N_0\begin{cases} 0 & \text{at } \bar{t} < 0, \\ 0.281\bar{t} & \text{at } 0 \le \bar{t} \le 0.52, \\ 0.241(1.125 - \bar{t}) & \text{at } 0.52 < \bar{t} \le 1.125, \\ 0 & \text{at } 1.125 \le \bar{t} \le 3.0, \\ 1.949(\bar{t} - 3.0) & \text{at } 3.0 < \bar{t} \le 3.485, \\ 1.835(4.0 - \bar{t}) & \text{at } 3.485 < \bar{t} \le 4.0, \\ 0 & \text{at } 4.0 < \bar{t}. \end{cases} \quad (5)$$

$$N(\bar{t}) = N_0\begin{cases} 0 & \text{at } \bar{t} < 0, \\ 0.281\bar{t} & \text{at } 0 \le \bar{t} \le 0.52, \\ 0.241(1.125 - \bar{t}) & \text{at } 0.52 < \bar{t} \le 1.125, \\ 0 & \text{at } 1.125 \le \bar{t} \le 3.0, \\ 2.596(\bar{t} - 3.0) & \text{at } 3.0 < \bar{t} \le 3.485, \\ 2.444(4.0 - \bar{t}) & \text{at } 3.485 < \bar{t} \le 4.0, \\ 0 & \text{at } 4.0 < \bar{t}. \end{cases} \quad (6)$$

$$N(\bar{t}) = N_0\begin{cases} 0 & \text{at } \bar{t} < 0, \\ 0.281\bar{t} & \text{at } 0 \le \bar{t} \le 0.52, \\ 0.241(1.125 - \bar{t}) & \text{at } 0.52 < \bar{t} \le 1.125, \\ 0 & \text{at } 1.125 \le \bar{t} \le 3.0, \\ 3.898(\bar{t} - 3.0) & \text{at } 3.0 < \bar{t} \le 3.485, \\ 3.671(4.0 - \bar{t}) & \text{at } 3.485 < \bar{t} \le 4.0, \\ 0 & \text{at } 4.0 < \bar{t}. \end{cases} \quad (7)$$

They differ in the power pause values being 4.75 μs for modes (1)–(4) (the first variant) and 18.75 μs for modes (5)–(7) (the second variant). Here, as in [4, 5], $N_0 = 2.5$ gW is the characteristic discharge power, $\bar{t} = t/\tau_0$ is the dimensionless time, $\tau_0 = 10$ μs is the characteristic discharge time; the initial channel length was assumed to be 0.06 m. The modes were selected for each variant in such a way that there was obtained the repeatedly introduced energy necessary to form equal amplitudes of the pressure. The graphical form of the energy characteristics of model modes (1)–(7) is presented in Fig. 1. The first power pulse for all the modes remained unchanged, as this part of the electric energy is spent for the formation of only the first pulsation of pressure.

RESULTS AND DISCUSSION

There have been analyzed the results of the numerical calculation of the hydrodynamic (the time function of the pressure in the discharge channel $p_a(t)$) and energy (the time functions of the volume densities of the power $n_V(t) = N(t)/V(t)$ and energy $\varepsilon_V(t) = \int_0^t N(t)dt/V(t)$ introduced into the discharge channel) characteristics of the channel, where $V(t)$ is the current value of the volume of the discharge channel. The corresponding calculated functions are presented in Figs. 2–4.

Analyzing the change of the functions $p_a(t)$, $n_V(t)$, and $\varepsilon_V(t)$ with time, one can see that the pressure in the channel and the apparent density of the electric energy introduced in it are qualitatively similar both in the form of the curves and the degree of their dependence

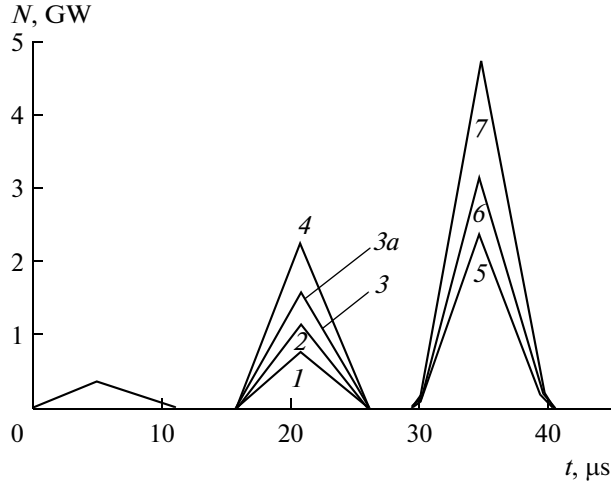

Fig. 1. Model dependences of the power on the time and energy input mode (the curves are marked in accordance with the numbers of the model presentations of the power).

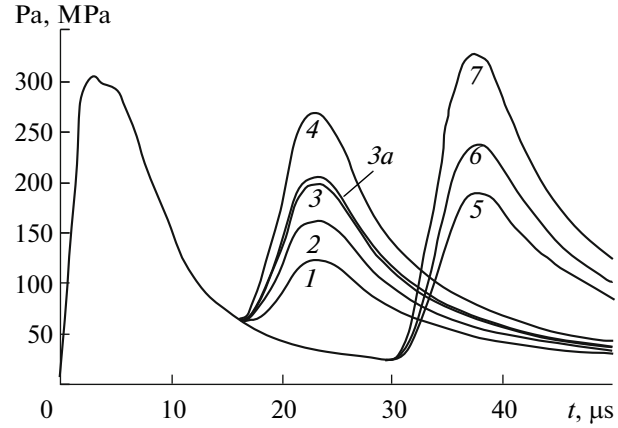

Fig. 2. Distributions of the pressure in the discharge channel.

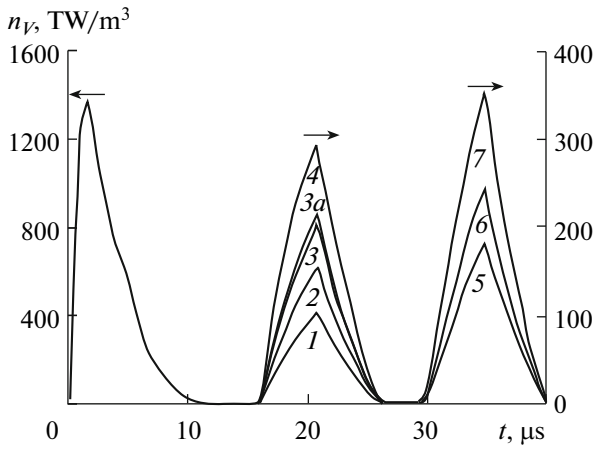

Fig. 3. Dependences of the specific spatial electric power introduced into the discharge channel on the time and discharge mode.

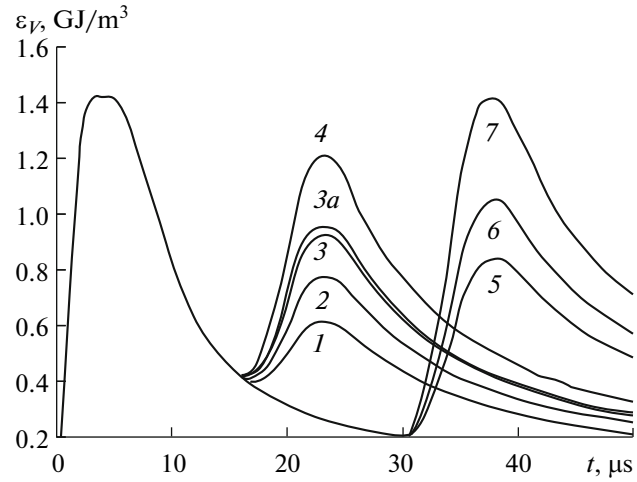

Fig. 4. Dependences of the spatial energy introduced into the discharge channel on the time and discharge mode.

on the energy liberation mode (the input energy amount W_2, the power pause time, and the power growth rate). At that, unlike the correlations of the pressure amplitudes in the channel p_{am} and the power densities n_{Vm}, the pressure amplitudes in the channel correlate with the energy density amplitudes ε_{Vm} for both the pressure pulsations and the energy densities. There is observed some quasi-linear dependence between them, which is approximated by $\delta < 4\%$ and indicated by the linear relationship of the form

$$p_{am} = 238.5(\varepsilon_{Vm} - 0.086), \quad (8)$$

where p_{am} is measured in mPa and ε_{Vm} is measured in GJ/m^3.

A similar approximation (but only for the amplitudes of the repeated pulsations) may be obtained for the function p_{am2} (n_{Vm2}):

$$p_{am2} = 0.887(n_{Vm2} + 40), \quad (9)$$

where p_{am2} is the amplitude of the second pulsation of pressure in the discharge channel, measured in mPa, and n_{Vm2} is the value of the second maximum of the power density in the discharge channel in GW/m^3.

The percentage error of the pressure calculation by formula (9) is not more than 5%. When analyzing the numerical experiment results by the dependence of the pressure in the discharge channel on the densities of the power and input energy (see Figs. 2–4 and formulas (8), (9)), no detectable influence on

Table 1. Comparison of the values of p_{am} calculated by formulas (8) and (9) with the results of the numerical experiments [3]

Variant number [5]	Initial data			Calculation by formulas		δ_{pn}, %	$\delta_{p\varepsilon}$, %
	p_{am}, mPa	n_{Vm}, TW/m^3	ε_{Vm}, gJ/m^2	(8)	(9)		
2	106	68.6	0.567	115	96	9	8
3d	111	68.6	0.588	120	96	13	8
3g	112	68.6	0.590	120	96	14	7
2b	206	210	0.986	215	222	8	4
3f	228	210	1.09	239	222	3	5
3h	231	210	1.10	242	222	4	5
1st pulsation	306	1250	1.42	318	–	–	4

these interrelations of the power pause time was found. Evidently, if this influence takes place, it is rather weak and is tacitly taken into account in the averaged coefficients in expressions (8) and (9). To clarify this situation, similar results of the numerical experiments for the model modes of the discharge without a power pause were considered [3]. The amplitude values of the quantities of interest are presented in Table 1. The analysis of these data show that formulas (8) and (9), obtained for the modes with a power pause, describe adequately (with the percentage error δp_ε being less than 8% with respect to ε_{Vm} and δ_{pn} less than 14% with respect to n_{Vm2}) the calculation data for the no-pause modes as well. Thus, within the limits of the mentioned errors, the influence of the power pause on the interrelations between the energy functions $\varepsilon_V(t)$, $n_V(t)$ and the pressure $p_a(t)$ may be neglected.

At the same time, the comparative analysis of the results presented in Figs. 1 and 2 shows that the time during which the peak of the second pressure pulsation in the channel forms depends mainly on the power pause at the fixed period of the additional energy liberation. The time interval between the pressure pulsation peaks is 1.2–1.3 times more than the corresponding time interval between the power peaks and tends to decrease as the power pause time increases. Please note that, for the discharge modes in the case of a combined energy source without a power pause (see [4, 5]), such an excess is by 1.6 times, and the time during which the second pressure peak forms is determined by the period of the additional energy liberation. Thus, when formulating the problem for the modes with a power pause, it is fully justified to include the power pause time into the characteristic time of the additional energy source liberation.

The results mentioned above (see Figs. 1–4 and formula (8)) show that, in order to obtain the two-pulsation configuration of the pressure with nearly equal amplitudes, it is necessary to realize in accordance with mode 7 the second variant (see Figs. 2, 4) or formula (8), the spatial density value of the additional energy with the same amplitude as that from the main energy source. However, it is impossible to predict the amplitude value ε_{Vm}, which depends both on the energy input law and the volume of the plasma discharge channel, which, in turn, varies with the input energy. Thus, when initially handling the parameters of the input energy (W_1 and W_2) and the times of its input (τ_1 and $\Delta\tau_2$), it is expedient to look for some connection between them and the amplitude ε_{Vm}. For this purpose, let us summarize the parameters of interest p_{am}, W_1, W_2, k_τ, $\Delta\tau_2$, $k_W = W_2/W_1$, $k^* = k_W/k_\tau$ and ε_{Vm2} (ε_{Vm2} is the value of the second peak of the energy density in the discharge channel) with respect to modes 1–7 of the present paper (PP) and the modes of works [4, 5] in Table 2.

Comparing the modes with nearly equal energy densities (they are near each other in the table in the order of ascending ε_{Vm2}), it is easy to verify that the amplitude ε_{Vm2} grows as the number k_* simultaneously increases. At that, nearly equal values of ε_{Vm2} and p_{am2} corresponded with nearly the same values of the number k_*. Thus, there exists an approximate energy criterion k_* by which it is possible to build an electrodischarge energy source capable of generating some fluctuating pressure pulses in the plasma channel and the liquid around it with equal amplitudes of the repeated pulsations. One can obtain pulsing configurations of the pressure with two initial equal amplitudes of the pulsations (see Fig. 2 and Table 2, mode 7) on the basis of a combined electrodischarge source with the energy number $k_* \geq 4.4$.

Table 2. Parameters of the pulsation activity of discharges with a power pause (nos. 5–7, 10–12, 16, and 17) and without it at W_1 = 2055 J, τ_1 = 11.25 mks, p_{am1} = 305 mPa, and ε_{Vm1} = 1.42 gJ/m^3 (p_{am1} is the amplitude of the first pulsation of pressure in the discharge channel, ε_{Vm1} is the value of the first energy density maximum in the discharge channel)

No.	Mode number (of the source)	ε_{Vm2}, gJ/m^3	p_{am2}, mPa	$\Delta\tau_2$, μs	W_2, J	k_τ	k_W	k_*
1	2 [5]	0.58	98	10	1752	0.89	0.85	0.96
2	3a [4]	0.58	96	50	5624	4.4	2.74	0.62
3	3e [5]	0.59	103	50	8760	4.4	4.26	0.96
4	3g [5]	0.59	104	80	14016	7.1	6.80	0.96
5	1 [HC]	0.61	123	14.75	3745	1.31	1.82	1.39
6	5 [HC]	0.73	189	28.75	11815	2.56	5.75	2.25
7	2 [HC]	0.78	162	14.75	5625	1.31	2.74	2.06
8	2a [4]	0.78	150	10	3747	0.89	1.82	2.04
9	3b [4]	0.87	184	50	30754	4.4	15.0	3.37
10	6 [HC]	0.91	238	28.75	15740	2.56	7.66	2.99
11	3 [HC]	0.93	199	14.75	7495	1.31	3.65	2.78
12	3a [HC]	0.96	206	14.75	7880	1.31	3.83	2.93
13	2b [4]	0.99	192	10	5626	0.89	2.74	3.08
14	3f [5]	1.09	213	50	28130	4.4	13.74	3.08
15	3h [5]	1.10	215	80	45008	7.1	21.90	3.08
16	7 [HC]	1.24	328	28.75	23630	2.56	11.15	4.36
17	4 [HC]	1.25	268	14.75	11250	1.31	5.47	4.18

CONCLUSIONS

Thus, the results of the numerical experiment demonstrate that, on the basis of the combined electrodischarge sources, say multistage SCG, it is possible to form pressure pulses with some consecutive pulsations, the number of which is the same as of the electric power. In order to form the second pressure pulsation with the amplitude nearly equal to that of the first pulsation, it is necessary to realize the spatial density of the additional energy with the amplitude of the main energy source.

On the basis of the fixed main energy source, it is possible to form a number of combined energy sources providing for the generation of uniform two-pulsation pressure pulses, including those with equal amplitudes. With this purpose, one needs to ensure the equality of the relations of the excess of the values of the repeatedly liberated energy and the liberation time over the respective parameters of the first power pulse; in this case, in order to obtain equal pressure amplitudes, it is necessary to increase the second power pulsation amplitude with respect to the first one (depending on the power pause) at least by an order of magnitude. The time interval between the pressure pulsations for each mode with a power pause is nearly 1.25 times more than the time interval between the peaks of their power, and without the pause it is 1.46 times more.

REFERENCES

1. Bologa, M.K. and Grosu, F.P., Physical aspects of electrohydrodynamic phenomena, *Electron. Obrab. Mater.*, 2006, vol. 42, no. 3, pp. 118–127.
2. Grosu, F.P. and Bologa, M.K., Thermoelectrohydrodynamic methods of energy conversion, *Surf. Eng. Appl. Electrochem.*, 2010, vol. 46, no. 6, pp. 582–588.
3. Barbashova, G.A., Restoration of the characteristics of the cavity formed upon explosion of a micro-conductor according to the specified two pulse temperature dependence of the pressure at a point in a liquid, *Surf. Eng. Appl. Electrochem.*, 2010, vol. 46, no. 1, pp. 53–56.
4. Barbashova, G.A., Vovchenko, A.I., Kamenskaya, L.A., and Shamko, V.V., Control of hydrodynamic processes at electroexplosive programmed multi-pulse input of energy, *Akust. Visn.*, 2004, vol. 7, no. 4, pp. 3–9.
5. Barbashova, G.A., Vovchenko, A.I., Kamenskaya, L.A., and Shamko, V.V., Hydrodynamic parameters of electric discharges in a liquid at two-pulse input of energy, *Electron. Obrab. Mater.,* 2006, vol. 42, no. 2, pp. 23–29.
6. Barbashova, G.A. and Shamko, V.V., Influence of cycling of electric energy input into the channel of an underwater spark discharge on the process hydrodynamics, *Electron. Obrab. Mater.*, 2007, vol. 43, no. 2, pp. 43–49.
7. Vovchenko, A.I., High-Voltage Electrodischarge Systems with Controlled Transformation of Energy, *Doct. Sci. (Eng.) Dissertation*, Kiev: Institute of Electrodynamics, NAS Ukraine, 2002.
8. *Chislennoe reshenie mnogomernykh zadach gazovoi dinamiki* (Numerical Solution of Multidimensional Problems of Gas Dynamics), Godunov, S.K, Ed., Moscow: Nauka, 1976.

Translated by M. Myshkina

ISSN 1068-3755, Surface Engineering and Applied Electrochemistry, 2014, Vol. 50, No. 1, pp. 78–83. © Allerton Press, Inc., 2014.

Action of Millimeter-Range Electromagnetic Radiation on Polypeptide Spectrum of Amylolytic Preparations from *Aspergillus Niger* 33-19 CNMN FD 02A Strain[1]

A. Ciloci[a, *], C. Bivol[a], M. Stratan[a], J. Tiurina[a], S. Clapco[a], V. Reva[b], and S. Labliuc[a]

[a] *Institute of Microbiology and Biotechnology, Academy of Sciences of Moldova, 1 Academiei str., MD 2028, Chisinau, Moldova*

[b] *State University of Moldova, Faculty of Vegetal Biology, 65A Mihail Kogălniceanu str., MD 2009, Chisinau, Moldova*

**e-mail: alexandra.ciloci@gmail.com*

Received February 07, 2013

Abstract—Micromycete *Aspergillus niger* 33-19 CNMN FD 02A standard cultivated and exposed to λ = 7.1 millimeter waves radiation has been used to obtain two enzyme preparations with the 10x degree of purity, with a 29.9% difference of the α-amylase activity in irradiated preparation but with a similar specific activity of protein of 138.3 U/mg and 141.0 U/mg. The α-amylase purification through gel filtration and ion exchange chromatography has resulted in the increase of 8.9 times of the specific activity for the control and of 8.2 times for the irradiated samples, with the yields of 25% and 17%, respectively. The SDS-PAGE of proteins isolated from initial preparations indicates the expression of new polypeptide of 45 kDa in the irradiated samples. Polypeptide spectrum of α-amylase from both preparations, purified through ion chromatography, shows two unchanged polypeptide bands of 66 and 40.5 kDa, identified as α-amylase isomorphs.

Keywords: millimeter-range electromagnetic radiation, fungi, Aspergillus niger, α-amylase purification

DOI: 10.3103/S1068375514010049

INTRODUCTION

In the past years the electromagnetic radiation (EMR) of the millimeter range has been actively used in biology, medicine, biotechnology, etc. Millimeter waves (MMW) have the wavelength of 10 to 1 mm which runs in the extremely high frequency (EHF) band. The idea that MMW can specifically influence biological structures and whole organisms was first presented by Devyatkov N.D., Golant M.B. and Gel'vich E.A. in 1964–1965 who claimed that this wave frequency can be used by living organisms to transfer information (impulse transmission) between cells [1, 2].

Currently a wide experimental material on the EMR effect of nonthermal intensity on various species of microorganisms, like model-objects of a study: yeasts, bacteria, actinobacteria, cyanobacteria, micromycetes has been gathered, which is helpful in explanation of certain action properties of MMW [3–8]. The evasive influence of the millimeter-range EMR on living cells should be noted, which depends on both frequency and strength of waves and the initial state of a biological object. It is also worth mentioning here that the influence is of a resonant character, i.e. observed in narrow frequency ranges. The main difficulty in the study of the EMR biological effect is that electromagnetic waves overlapping the cell vibrations can induce a positive as well as negative response [9].

The actual mechanism by how EMR generates biological effects is under intense study. Some hypotheses on the MMW action on organisms, which accounts for the fundamentals of their metabolisms, are proposed. It is considered that at the interaction between a millimeter-range electromagnetic radiation and the biological object, main processes take place in cell membranes, converting the electromagnetic energy into acoustic-electric waves and initiating metabolite processes inside the cell. Electromagnetic forces at the surface of a membrane could modify ligand-receptor interactions and, as result, would affect the state of the membrane molecules that control the cell secretion. The electropotential of healthy cells causes a steady flow of ions across the membrane, which is disturbed in a damaged cell. An optimal EMR can restore normal membrane potential, increasing cell activity [10–12].

Herewith, an object for the EMR is cell pre-membrane water molecules. Such water molecules are essential for biomembrane proteins hydration, switching them from a functionally passive to an active condition. Next, mechanisms that initiated biochemical reactions are activated, for which protein molecules are responsible. Thereby the permeability of membranes increases and leads to the enhancement of the

[1] The article is published in the original.

substances transport from the exterior to interior of a cell, changing its biological activity [13, 14].

Our previous studies of the MMW influence on the synthesis of extracellular hydrolases and the life cycle of fungi strains *Aspergillus niger* 33 and *Aspergillus niger* 33–19 CNMN FD 02A—producers of amylases, and *Penicillium viride* CNMN FD 04P—producer of pectinases, show the increase of 44–49% of the enzyme activity at optimal irradiation and the reduction of the growth cycle of *Aspergillus niger* 33–19 CNMN FD 02A within 48 hours. It is considered that irradiation induces structural alterations of cell membranes, causing increase of their permeability and, in turn, an easier enzymes secretion outside the cell [15].

To better understand a possible mechanism of interaction between external MMW and micromycetes—producers of hydrolases, the aim of the given work has been to assess changes in the amylolytic activity and the polypeptide spectrum of enzyme preparation obtained from the micromycete *A. niger* exposed to the millimeter-range electromagnetic irradiation.

EXPERIMENTAL

Microorganism and Culture Conditions

The object of the study, a strain of the mycelial fungi *Aspergillus niger* 33-19 CNMN FD 02A—producer of amylases, stored at the National Collection of Nonpathogenic Microorganisms at the Institute of Microbiology and Biotechnology of the Academy of Sciences of Moldova, was cultivated in Erlenmeyer flasks of 1000 mL volume, at the temperature of 28–30°C, on shakers (180–200 rpm), during 5 days. Each flask contained 200 mL of a nutrient medium of the following, chosen as optimal, composition (g/L): starch—3.0; bean flour—9.0; wheat bran—18.0; KH_2PO_4—2.0; KCl—0.5; $MgSO_4$—0.5. The initial pH of the nutrient medium was 3.0 [16].

Spore suspension of 10% v/v with the density of 3×10^6 spores/mL, obtained by washing with sterile water of the 12–14-days culture, grown on malt-agar oblique columns and irradiated for 15 min with electromagnetic radiation in the millimeter range, with the wavelength $\lambda = 7.1$ mm in a constant mode, served as the seed material [17]. As a source of a low-intensity EMR, a UEMA-3 (Moldova) instrument was used. Samples with nonirradiated inoculum were taken as the control.

Enzyme Extraction

The media of the 144-h grown control culture and the 96-h grown irradiated culture were separated from biomass by filtration and 20-min centrifugation at 4000–6000 rpm. The α-amylase was isolated from the supernatant with 96% ethanol cooled to –15°C, in the ratio 1 : 4 C_2H_5OH, with the sedimentation duration of one hour and the concentration of $CaCl_2$ 0.2%. The sediment was centrifuged for 20 minutes at 6000 rpm and dried at 20–22°C [18]. Thus obtained enzyme preparation was further investigated and purified.

Enzyme Assay

The α-amylase activity was determined according to the SKB colorimetric method by measuring the amount of the different released molecular weight dextrins at 30% hydrolysis of one gram of a soluble starch after 10 min incubation at 30°C. The reaction mixture (15 mL) contained 10 mL of buffered (0.2M acetate buffer, pH 4.7) 1% soluble starch (Sigma) solution as the substrate and 5 mL adequately diluted enzyme sample. The reaction was stopped and developed with iodine solution in the ratio of 0.5 mL reaction mixture/50 mL iodine solution (5 mg iodine and 50 mg KI in 100 mL 0.1N HCl) for 5 min [19].

Protein Assay

Total protein content was determined according to the Lowry method of taking crystalline bovine serum albumin as the standard [20].

α-Amylase Purification

Gel filtration. The dried enzyme preparation (75 mg) was washed with the 3 mL 20 mM Tris-HCl buffer (pH 7.0), then centrifuged for 10 min at 14000 rpm. The supernatant (2.5 mL) was applied to the PD-10 column (Amersham Pharmacia Biotech) equilibrated with the 20 mM TRIS-HCl buffer, pH 7.0. The column was eluted with 3 mL of the same buffer.

Ion exchange chromatography. Polled fraction was loaded onto an anion exchange HiTrap™ Q (5 mL) column at the flow rate of 1 mL/min in the FPLC System (Amersham Pharmacia). The column was equilibrated with the 20 mM Tris-HCl buffer. The bound proteins were eluted with linear gradient of 0–0.5M NaCl in the same buffer. In each eluted fraction amylolytic activity and protein was assayed.

Electrophoresis

To evaluate purity of α-amylase isolated proteins from amylolytic preparations and from amylolytic active fractions were applied to 15% SDS-PAGE electrophoresis, according to the Laemmli method [21]. The gel was stained with coomasie Brillant Blue R-250. Molecular weight markers were β-Galactosidase (116 kDa), Phosphorylase b (97.4 kDa), Bovine serum albumin (66.2 kDa), Alcohol dehydrogenase (37.6 kDa), Carbonic anhydrase (28.5 kDa).

Statistical Analysis

All experiments were performed three times and the results are presented as the simple mean of three, with the level of significance $p \leq 0.05$ [22].

Table 1. Amylolytic properties of enzyme preparations obtained from *A. niger*

Variants	Protein (%)	α-Amylase activity (U/g)	Specific activity (U/mg)
A. niger 33-19 grown under standard conditions (I)	23.5	32554.5	138.3
Irradiated with λ = 7.1 mm culture of *A. niger* (II)	30.0	42314.0	141.0

RESULTS

Enzyme complex isolation from cultural liquid of the *A. niger* standard grown (I) and irradiated with the millimeter-range electromagnetic radiation (II) allowed for obtaining two amylolytic preparations of the 10x degree of purity (Table 1). The preparation from the irradiated *A. niger* had a 29.9% higher α-amylase activity and 27.6% higher protein amount. Due to the increase of the total protein, the specific activity of both preparations was similar, i.e. 138.3 U/mg and 141.0 U/mg proteins, respectively.

The extraction of α-amylase from both enzyme preparations and their purification by gel filtration and ion exchange chromatography gave an increase of the enzyme specific activity of 8.9 times for the control and 8.2 times for the preparation obtained at *A. niger* spore suspension irradiation with MMW (Table 2). The yield of α-amylase was 25% for the control and 17% for the irradiated samples (1.5 times less), showing a greater decrease of total amylolytic activity of the irradiated preparation after purification. The protein amount of both purified preparations was identical, of 0.160–0.162 mg/mL.

In both cases, ion chromatography of protein separated from the preparations under study (Fig. 1) shows four fractions with amylolytic activity and a peak in one fraction, number 18 for the standard cultivated sample and number 14 for the irradiated sample. The general elution profile of the proteins from enzyme preparations is different. For the control sample, the peak of the α-amylase activity coincides with the peak of the protein amount. For the irradiated sample, the peak of the α-amylase activity does not coincide with the peak of protein, although the values of both amylolytic activity and protein content are practically similar in both cases. A higher protein content was observed in fraction 1 (0% NaCl gradient) and fraction 10 (32% NaCl), as 53.7% and 29.2%, respectively. Presented data are recalculated for 1.5 times dilution, used for the solution applied on ion chromatography.

SDS-PAGE electrophoresis of proteins isolated from *A. niger* enzyme preparations indicates a high heterogeneous protein content of initial complexes and some difference in polypeptide bands (Fig. 2a). A major difference is that MMW induce expression of a new polypeptide with an apparent molecular weight of 45 kDa, absent in the control sample.

The polypeptide spectrum of the determined amylolytic active fractions after ion exchange chromatography shows two polypeptide bands with apparent molecular weights of 66 kDa and 40.5 kDa after purification (Fig. 2b). The appeared polypeptides are considered as 2 isomorphs of α-amylase [23] and demonstrate that the applied λ = 7.1 millimeter-range electromagnetic radiation does not induce structural changes in α-amylase of the *A. niger* strain.

DISCUSSIONS

It is generally accepted that living organisms are not indifferent to electromagnetic radiation of millimeter range and a proper application of the EHF-radiation can be used to stimulate and regulate various

Table 2. Purification profile of α-amylase from amylolytic preparations obtained under standard conditions (I) and at irradiation with MMW λ = 7.1 of *A. niger* (II)

Purification Steps	α-Amylase activity (U/mL)		Protein (mg/mL)		Specific activity (U/mg)		Yield (%)		Purification fold	
	I	II	I	II	I	II	I	II	I	II
Amylolytic preparation solution (25 mg/mL)	813.86	1057.85	5.875	7.500	138.30	141.00	100		1	
Extract	422.88	709.12	1.908	2.487	221.63	285.13	52	67	1.6	2.0
PD-10 column gel filtration	390.12	590.38	1.173	1.725	332.45	342.25	48	56	2.4	2.4
HiTrap^{TM} Q column ion exchange chromatography	199.68	184.98	0.162	0.160	1232.61	1156.13	25	17	8.9	8.2

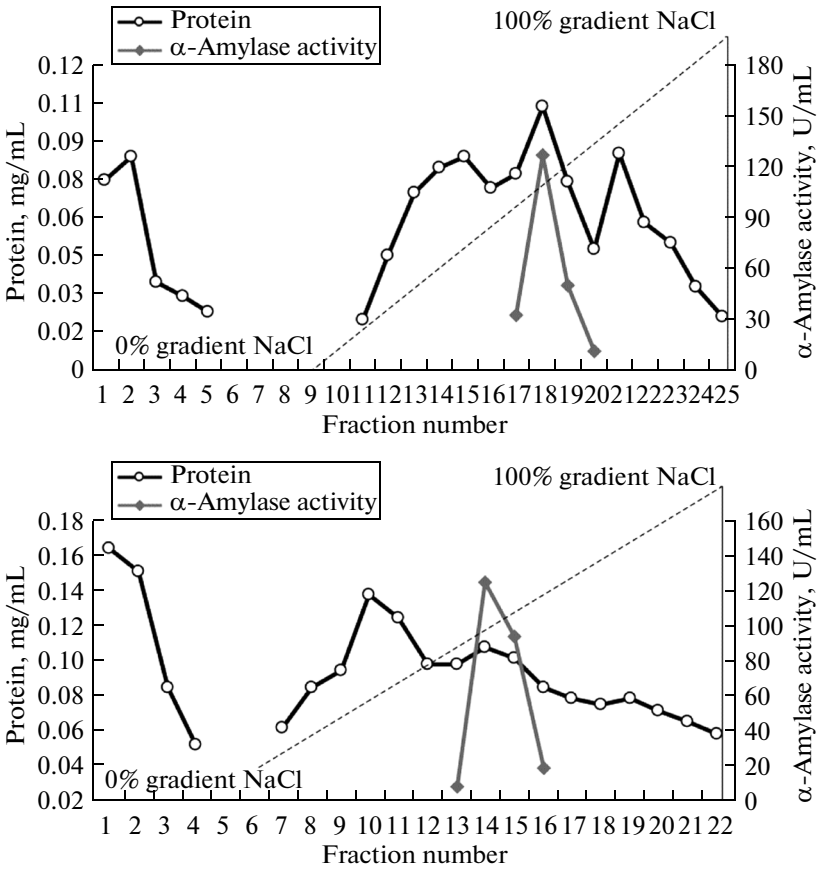

Fig. 1. Purification of α-amylase from amylolytic preparations obtained under standard conditions (I) and at irradiation with MMW λ = 7.1 of *A. niger* (II) by ion exchange chromatography. Samples: 2 ml of α-amylase preparation after gel filtration through PD-10 column. Column: HiTrap^{TM} Q (5 mL). Flow rate: 1 mL/min. Buffer A: 20 mM Tris-HCl, pH 7.0. Buffer B: A + 0.5M NaCl. Gradient: for I 0% B in 27 mL, 0%–100% B in 75 mL and for II 0% B in 15 ml, 0%–100% B in 66 mL.

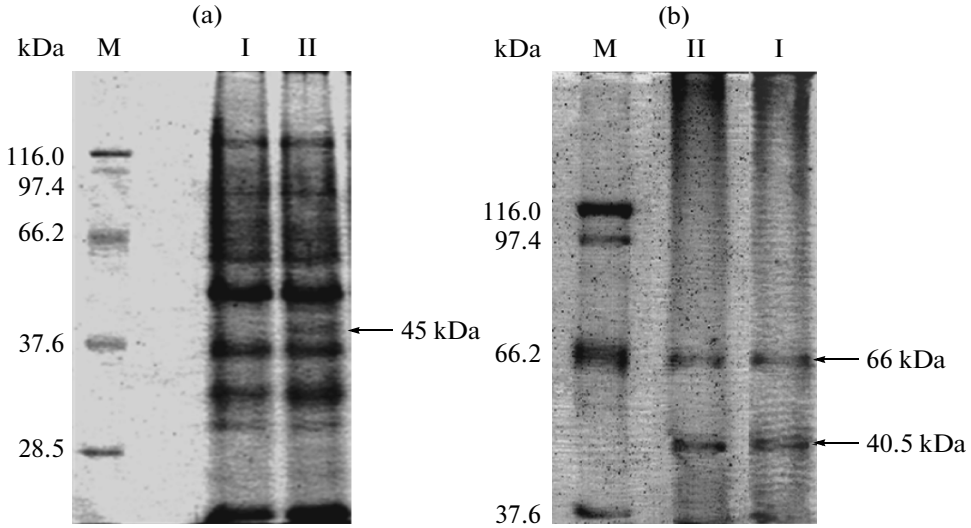

Fig. 2. SDS-PAGE of *A. niger* α-amylase purified through ethanol precipitation (a) and ion exchange chromatography (b). Lane M: Protein markers, Lane I: Sample obtained from *A. niger* cultivated under standard conditions, Lane II: Sample obtained at *A. niger* irradiation with millimeter wavelength range λ = 7.1.

cell processes. Yet the biostimulating phenomena have no comprehensive explanation just some hypotheses are discussed. It is certain that besides similarities of the millimeter-range radiation effects on various photosynthetic and non-photosynthetic organisms, some differences at fungi investigation can be identified: frequent morphological changes of cells, active wavelengths 4.9, 5.6, 5.95–7.2 mm, the intensification of a process with the simultaneous slowing down of another one, multiple MMW exposures of fungi spores (repetition factor of 10 times) so as to get a stable effect, inheritance of acquired changes by further generations [11, 15].

Although the crucial role of proteins in every biological process is known and some hypotheses of the EHF-radiation influence on proteins were proposed (increase of protein molecules hydration, magnetoreception of some ions bound with proteins etc.), studies in this field are still insufficient or completely missing when talking about mycelial fungi—producers of biotechnologically important enzymes.

The given research shows that the electromagnetic radiation of a millimeter range, chosen as a stimulator of enzyme synthesis by micromycete of *A. niger*, does not induce direct changes in the structure of α-amylase. Standard cultivated samples and the ones exposed to the optimal MMW of $\lambda = 7.1$ gave similar polypeptide bands after ion exchange purification, corresponding to the two isomorphs of α-amylase, of 66 kDa and 40.5 kDa.

MMW do not affect α-amylase, but induce other changes in the polypeptide spectrum of proteins released outside the cells in the culture medium of *A. niger*. A biological effect of the millimeter-range EMR on the irradiated preparation is demonstrated by expression of a new polypeptide band with the apparent molecular weight of 45 kDa, and, also, by differences in the elution profile of proteins from both the control and irradiated preparations, where peak of the protein content does not coincide with the peak of the α-amylase activity, as in the control sample.

How the millimeter-range EMR causes changes in the polypeptide spectrum of proteins isolated from the culture liquid of the irradiated *A. niger* still need to be discussed. According to one of the hypotheses, it is supposed that MMW increases permeability of cells membranes, leading to accumulation of a "nonspecific" protein outside the cell. This modification could change amylolytic activity of the isolated enzyme preparation that was by 29.9% higher in the non-purified irradiated preparation and, practically, similar after ion exchange chromatography, compared to the control preparation.

REFERENCES

1. Devyatkov, N.D., Golant, M.B. and Betskii, O.V., *Millimetrovye volny i ikh rol' v protsessakh zhiznedeyatel'nosti* (Millimeter Waves and Their Role in the Life Processes), Moscow: Radio i Svyaz', 1991.
2. Devyatkov, N.D., Golant, M.B. and Betskii, O.V., *Osobenosti mediko-biologicheskogo primeneniya millimetrovykh voln* (Features of Medical and Biological Applications of Millimeter Waves), Moscow: IRE RAN, 1994.
3. Luk'yanov, A.A., Effect of EHF-radiation on heterotrophic and phototrophic partners of mixed cultures of microorganisms, *Extended Abstract of Cand.Sci. (Biol.) Dissertation*, Moscow: Moscow State Univ., 2007, p. 24.
4. Gapochka, L.D., Gapochka, M.G. and Korolev, A.F., Population aspects of unicellular organisms tolerance to low intensity electromagnetic radiation influence, *Mm Volny Biol. Med.*, 2002, vol. 2, no. 26, pp. 3–9.
5. Astrakhantseva, M.N., Intensification of the metabolism of *Bacillus subtilis* and *Saccharomyces cerevisiae* under the influence of millimeter range electromagnetic radiation and chelator hydroxyethylidene diphosphonic acid, *Cand. Sci. (Eng.) Dissertation,* Kazan: Kazan Nat. Research Technol. Univ., 2006, p. 150.
6. Postolakyi, O.M. and Boortseva, S.A., MM radiation influence upon the growth and lipid formation of *Streptomycetes canosus* CNMN-Ac-02 and its variants, *Surf. Eng. Appl. Electrochem.,* 2009, vol. 45, no. 2, pp. 157–160.
7. Usatîi, A., Molodoi, E., Rotaru, A., and Moldoveanu, T., The influence of low intensity millimeter waves on the multiplication and biosynthetic activity of *Saccharomyces carlsbergensis* CNMN-Y-15 yeast, *Analele Universităţii din Oradea, Fascicula Biologie*, 2010, vol. 17, no. 2, pp. 208–212.
8. Narytnik, T.N., Vember, V.V., and Koval'chuk, V.N., Peculiarities of millimeter range electromagnetic radiation influence on the growth processes of the Micromycetes, *Proceedings of 22nd International Crimean Conference "Microwave and Telecommunication Technology"*, Crimea, 2012, pp. 958–959.
9. Reshetnyak, S.A., Shcheglov, V.A., Blagodatskikh, V.I., Gariaev, P.P., and Maslov, M.Yu., Mechanisms of interaction of electromagnetic radiation with a biosystem, *Laser Physics*, 1996, vol. 6, no. 4, pp. 621–653.
10. Kazarinov, K.D., The role of the cellular membrane systems in reception of EHF electromagnetic fields in biological objects, *Electron. Tekh., Ser. 1, SVCh-Tekh.*, 2008, vol. 1, no. 494, pp. 42–55.
11. Tambiev, A.Kh. and Skalny, A.V., Electromagnetic radiation and life: Bioelementological point of view, in *Biophysics*, Rijeka: In-Tech, 2012, pp. 193–220.
12. Pirogova, E., Vojisavljevic, V., and Cosic, I., Biological effects of electromagnetic radiation, in *Biomedical Engineering*, Vukovar: In-Tech, 2009, pp. 87–106.
13. Borisenko, G.G., Polnikov, I.G. and Kazarinov, K.D., Biological membranes—the primary receptors of electromagnetic fields in the biomedical experiment, *Electron. Tekh., Ser. 1, SVCh-Tekh.*, 2007, vol. 4, no. 492, pp. 25–27.
14. Shckorbatov, Y.G., Shakhbazov, V.G., Gorobets, N.N., Kiyko, V.I., Zhuravleva, L.A., and Navrotskaya, V.V., The influence of electromagnetic radiation of millimeter and centimeter range on human epithelial cells, *Proceedings of 10th International Crimean Conference*

"Microwave and Telecommunication Technology", Crimea, 2000, pp. 557–558.

15. Chilochi, A.A., Tyurina, Zh.P., Klapko, S.F., Stratan, M.V., Lablyuk, S.V., Dvornina, E.G., and Kondruk, V.F., Effect of millimeter-range electromagnetic radiation on the biosynthesis of extracellular hydrolytic enzymes in *Aspergillus* and *Penicillium* micromycetes, *Surf. Eng. Appl. Electrochem.,* 2011, vol. 47, no. 6, pp. 558–564.
16. MD 3943 G2 2009.07.31, Deseatnic, A., Stratan, M., Coropceanu, E., Bologa, O., Rija, A., Clapco, S., Tiurin, J., Labliuc, S., Rudic, V., and Bulhac, I., Mediu nutritiv pentru cultivarea tulpinii de fungi *Aspergillus niger 33-19 CNMN FD 02.*
17. Bilai, V.I., *Metody eksperimental'noi mikologii* (Methods of Experimental Mycology), Kyiv: Naukova Dumka, 1973.
18. Stratan, M., *Biotehnologii de cultivare a tulpinii Aspergillus niger 33-19 CNMN FD 02A—producă tor de amilaze*, Autoref. tez. doct. biologie, Chişinău, 2011.
19. Gracheva, I.M., Grachev, Yu.P. and Mosichev, M.S., *Laboratornyi praktikum po tekhnologii fermentnykh preparatov* (Laboratory Course on the Technology of Enzymatic Drugs), Moscow: Legkaya i Pishchevaya Promyshlennost', 1982, pp. 57–62.
20. Lowry, O.H., Rosebrough, N.J., Faar, A.L., and Randall, R.J., Protein measurement with the folin-phenol reagents, *Biol. Chem.,* 1951, vol. 48, pp. 17–25.
21. Laemmli, U.K., Cleavage of structural proteins during the assembly of the head of bacteriophage T4, *Nature,* 1970, vol. 227, no. 5259, pp. 680–685.
22. Maksimov, V.N., *Mnogofaktornyi eksperiment v biologii* (Multifactorial experiment in biology), Moscow: Mosk. Gos. Univ., 1980.
23. Ciloci, A., Bivol, C., Stratan, M., Reva, V., Clapco, S., Tiurin, S., and Labliuc, S., Production and purification of α-amylase from *Aspergillus niger* 33-19 CNMN FD 02a mutant form, *Analele Universită ţii din Oradea, Fascicula Biologie*, 2012, vol. 19, no. 1, pp. 74–79.

ISSN 1068-3755, Surface Engineering and Applied Electrochemistry, 2014, Vol. 50, No. 1, pp. 84–94. © Allerton Press, Inc., 2014.

Electrical Conductivity of 1 : 1 and 2 : 1 Clay Minerals[1]

A. Kriaa[a], *, M. Hajji[b], F. Jamoussi[b], and A. H. Hamzaoui[b]

[a]*Ecole supérieure des Sciences et Techniques de Tunis, Département de Physique Chimie, 5 avenue Taha Hussein, 1008 Montfleury, Tunis, Tunisia*

[b]*Centre National de Recherches en sciences des Matériaux, Laboratoire de Valorisation des Matériaux Utiles, Borj Cedria, BP 95, 2050, Hammam lif, Tunis*

*e-mail: *Kriaa1993@Yahoo.fr*

Received October 10, 2012; in final form November 30, 2012

Abstract—The A.C. impedance plots were used as tools to analyze the electrical response of two varieties of Tunisian halloysite 1 : 1 and illitic samples 2 : 1 as a function of frequency at different temperatures (80–800°C). The real and imaginary parts of the complex impedance trace semicircles in the complex plane. Except for the illite, It-1, the second sample analyzed in this study, these plots give evidence for the presence of both bulk and grain boundary effect, above 600°C onwards. The bulk resistance of the materials decreases with the rise in temperature. Impedance Spectroscopy data reveal a non-Debye type of dielectric relaxation. The Nyquist plots show the negative temperature coefficient of resistance of both pure Tunisian illite and halloysite samples. The results of bulk electrical conductivity and its activation energy are presented for the two mineral clay samples. For illite It-1, the activation energy values estimated from the *AC* conductivity pattern and modulus pattern are very similar and suggest a possibility of a long-range mobility of charge carriers (ions) via hopping mechanism of electrical transport processes at higher temperature. On the other hand, for the halloysite sample provided from kasserine, (Ha-Kass), the modulus analysis admit that the electrical transport processes of the material are very likely of electronic nature. Relaxation frequencies follow an Arrhenius behavior with the activation energy values not comparable to those found for the electrical conductivity.

Keywords: kaolinite, illite, hopping mechanism, impedance analysis, electrical conductivity

DOI: 10.3103/S1068375514010104

INTRODUCTION

The electrical conductivity and dielectric permittivity (commonly named as dielectric constant ε), of the constituent minerals are the main controlling factors of the electrical properties of soils. The dielectric permittivity of a material is a measure of the relative ability to store a charge (electrical energy) for a given applied electric field while dielectric loss is a measure of the proportion of the charge transferred in conduction and stored in polarization. The dielectric constant e is a complex number and is a function frequency. The relative dielectric constant $\varepsilon^*(\omega)$ is the ratio of the complex dielectric constant ε to dielectric constant of free space ε_0. The real part of the dielectric constant of soils particles is between 3 and 6 whereas that of water is 80 at 20°C [1, 2]. Thus the dielectric constant of soil-water mixture is between 4 and 8 depending on the proportion of each. Clay minerals are an important constituent of many mineral soils. The influence they may have on the dielectric behavior of a moist soil is therefore of great importance [3].

Ionic conductivity is known to occur in clay minerals and to be an important contributor to dielectric dispersion. The amount of conduction is related to the surface density of charge and the surface area. In general, the halloysite 1 : 1 clay mineral has a relatively small surface area and low ion-exchange capacity and would be expected to be associated with a low ionic conductivity, while the interlayers of the 2 : 1 clay minerals provide space into which cations can be adsorbed. In illite clays the interlayer contains potassium which fixes the structure rigidly. On the other hand, a large surface area of the smectite compared with other clay minerals, its capacity to swell and its ability to adsorb ions means it should create a reasonably electrically conductive material. It should be pointed out that the electrical properties of clays are still unknown at large in literature. In fact these materials are difficult to handle and experimental data are very limited. There are some literature data concerning electrical properties of clay and sandstone [4], clay or mixtures of sand/clay [5–6], conductivity measurements of dry clay minerals conducted at different temperatures in the range from 80 to 800°C have not been widely studied so far. Most of the articles published on the *AC* conductivity of rocks investigate the effect of water or oil content [7, 8] but no studies report on the characterization of the microstructure of clays as

[1] The article is published in the original.

ceramic materials by analyzing their electrical conductivities in the range of temperatures cited above. Obviously this study could be useful for Na-conducting materials.

Meanwhile, Impedance Spectroscopy (IS) is a relatively mature, cheap, and simple technique for non-destructive testing, which has been widely used to characterize the electrical properties of the materials and relate the changes in these electrical properties to microstructural changes occurring in the materials. Recently, growing interest has been developed in employing IS to characterize the microstructure of ceramic materials [9–11] particularly for studying the microstructure evolution in cement during hydration and hardening [12–14]. There are many ways *IS* data may be plotted. In the IS field, where capacitive rather than inductive effects dominate, conventionally one plots—$\mathrm{Im}(Z) \equiv -Z''$ on the y-axis vs. $\mathrm{Re}(Z) \equiv Z'$ on the x-axis to give a complex-plane impedance plot. Such graphs have been usually termed Nyquist plots. They have the disadvantage of not indicating frequency response directly, but may nevertheless be very helpful in identifying conduction processes present. Another approach, the Bode diagram, is to plot log $[|Z|]$ and $\Phi \sim$ vs. log$[f]$. Alternatively, one can plot Z' (or any I') or $-Z''$ (or $-I''$), or the logs of these quantities vs. log $[f]$ [15, 16].

In this paper, we report details concerning the physico-chemical characterization study of two Tunisan kaolinite (Ka.Kass) and illite (It-1) clays mineral providing from north and south west of Tunisia, respectively. The main goal is to present We present also a complete analysis about electrical properties of these two clay mineral samples using impedance spectroscopy technique at different temperatures ranging from 80 to 800°C. The characterization of the microstructure of Na-conducting ceramics is probably useful by this electrochemical technique. In the case of many mineral complex solid, the analysis of *IS* data, when depicted in a complex plane plot, appears generally in the form of a succession of semicircles representing the contributions to the electrical properties due to the bulk material, grain boundary effects and interfacial polarization phenomena if any. Taking into account these properties, the analysis of electric modulus enables us to separate the effects due to each component (bulk, grain boundary, and electrode polarization effects) in a solid sample very easily.

MATERIALS AND METHODS

Clays

Sample of specimen halloysite 1 : 1 clay used in this study provided from Touila, in Kasserine (Ha-Kass) situated at the north west of Tunisia. It is important to notice that this solid sample is on natural pure state, of white color and with no impurities. Whereas, the other clay sample chosen in this study, is the It-1 illite 2 : 1 clay, a pure Tunisian illite (light green) from the south west. For the two samples particles with diameter <45 μm were obtained by sedimentation and saturated with Na^+ by 7 washing cycles (successive centrifugal treatments) with 1M NaCl. After each centrifugation of the suspension, the supernatant was discarded and replaced with fresh solution of NaCl. After that, the samples were dialysed through a specific membrane, oven dried to a constant mass at 80°C and finally stored in an air-tight container prior to use.

Sample Clay Characterisation
X-ray Diffraction (XRD)

X-ray diffractograms were recorded using a "PANalytical X'Pert HighScore Plus" diffractometer with the radiation $K\alpha_1$ of copper. Two types of diffractograms are studied: diffractograms with disorientated powder where all the lines (h, k, l) appear, and diffractograms of oriented plate obtained by sedimentation. This makes it possible to follow the periodicity of the stratification of the layers, with the reflection (001) on which the identification is based.

Cation Exchange Capacities (CEC)
and Specific Surface Areas (SSA)

CEC was determined by the method of copper ethylendiamine $(EDA)_2\ CuCl_2$ complex analogous to that described by Bergaya and Vayer [17]. A known volume (2 to 5 mL) of the 0.05M Cu $(EDA)_2^{2+}$ solution (prepared firstly by mixing 1 M $CuCl_2$ with an excess 1 M EDA) is diluted with water to 25 mL and added to the clay (0.4 g) in the centrifuge tube and the pH of suspension is determined. The suspension is shaken or stirred for 30 min to ensure complete exchange, centrifuged and the pH is determined once more. The concentration of the Cu $(EDA)_2^{2+}$ remaining in the solution was determined by atomic absorption spectroscopy (AAS) or iodometry. The CEC of the sample can be obtained by the difference in Cu concentration in the initial and final solutions as determined by AAS or iodometry and the CEC calculated from the quantity of absorbed Cu $(EDA)_2^{2+}$ (amount initially added to the clay minus amount remaining).

A specific surface area BET was determined by nitrogen gas adsorption at 77 K, using a "Quan-tachrom-Autosorb1" sorptiometer.

X-Ray Patterns

The specimens after different treatments were studied by using X-ray diffraction technique. In these methods, oriented specimen is prepared on glass microscope slides. The samples were successively sub-

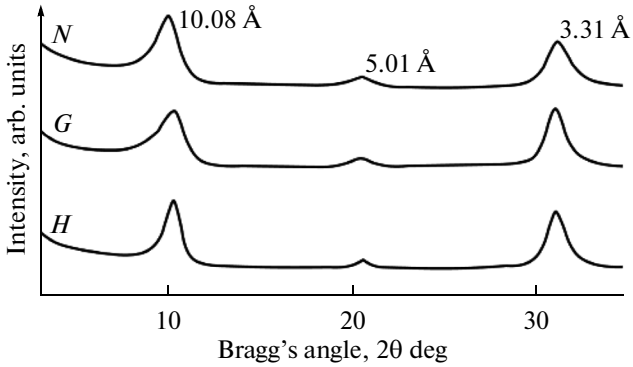

Fig. 1. XRD patterns of oriented purified clay plate illite It-1 (N: Normal, H: Heated 550°C, G: saturated by ethylene glycol).

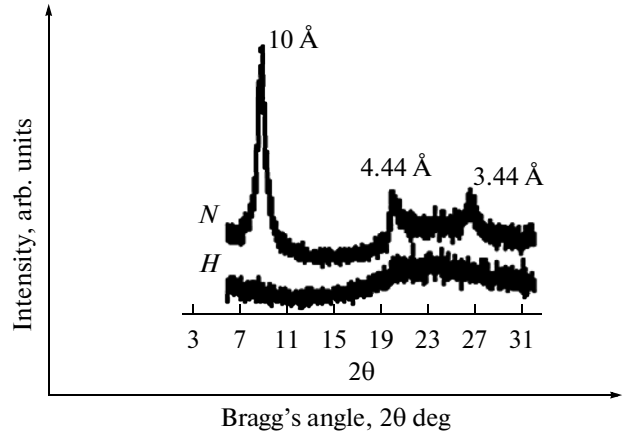

Fig. 2. XRD of purified Ha-Kass and heated at 500°C.

jected to different treatments not only to characterize the clay specimens but to identify the presence of interstratified or mixed other clay minerals:

(i) Normal at ambient temperature (N);

(ii) Saturated with ethylene glycol (EG-treatment) (G);

(iii) Heating at 550°C (H).

The diffractogram of the illite It-1 sample is shown on the Fig. 1. In the patterns of the air-dried oriented mount of pure It-1(N), the basal reflections of illite appear along with an irrational series of reflections: d(001) reflection at 10.08 Å, the $d_{(002)}$ at 5.01 Å and the $d_{(003)}$ at 3.31 Å. The *XRD* patterns of the EG-treated (G) and heated specimens (H) at 550°C were included in the Fig. 1 in order to detect minimal changes. One can observe that these peaks are not affected by treatments, i.e., the illite basal reflections do not show significant changes.

The XRD pattern of the Kasserine clay (Ha-Kass) (Fig. 2) shows sharp peaks at d = 10.01 Å, 4.40 Å, 3.34 Å and 2.58 Å attributed to the halloysite $4H_2O$ clay mineral that belongs to kaolin group [18]. When heated at 550°C, these peaks disappear.

The cation ion-exchange capacity (CEC) and the Specific Surface Area (SSA) of the clay samples are reported in Table 1.

Chemical Analyses and Structural Formulas

The clay samples were attacked by a mixture of three acids (HCl, H_2SO_4, HNO_3). All the elements pass in solution, except the silica (SiO_2) which is determined by gravimetry. Other elements, such as Al, Fe, Mg, Ca, Na and K are assayed by an Atomic Absorption Spectrophotometer (*AAS*).

Table 1. C.E.C and S.S.A for two studied clay samples

Specimen	CEC, meq/100 g	SSA, m^2/g
It-1	27	45
Ha-Kass	39.84	24.57

The chemical analysis of clay mineral samples is given in Table 2. The loss on ignition value of the Ka-Kass clay is relatively very important (28.96%); it can be due to the presence of a supplementary water layer.

It follows from these analyses that the average structural formulas are:

$$\text{It-1: } K_{1.64}Ca_{0.01}Na_{0.32}\,[Si_{6.89}Al_{1.11}]^{IV}$$

$$[Al_{2.82}Fe_{0.57}Mg_{0.44}]^{VI}\,O_{20}(OH)_4.$$

$$\text{Ha-Kass: } Na_{0.17}K_{0.02}Ca_{0.11}\,[Si_{6.49}Al_{1.51}]^{IV}$$

$$[Al_{4.239}Fe_{0.024}Mg_{0.07}]^{VI}O_{22}.$$

It reveals that the studied samples presented two significant substitutions in the octahedral and tetrahedral layers. For illite It-1the potassium (K) and metal (M) ions are present to satisfy the negative charge and will not be used in the calculation of negative charge. Thus net layer charge of illite It-1 per unit cell is 1.97 charge/cell whereas for Ha-Kass is 0.3 charge/cell.

For electrical conductivities studies, the finely ground samples were pressed into cylindrical pellets of 10–13 mm diameter and 1mm thickness using a hydraulic press at a pressure of 6000 Kg/cm^2. The pellets were mounted between two flat silver electrodes in an evacuated conductivity setup and annealed at 100°C for 24 h to avoid adsorbed water. The *AC* impedance data, the modulus of impedance $|Z|$ and phase angle were obtained in the frequency range 1 Hz to 13 MHz using HP4192A controlled frequency response analyzer over the temperature range 80–800°C. Before measurements, an input *AC* signal of voltage amplitude ~10 mV was applied across the sample cell followed by thermal stabilization for half an hour. The temperature of the sample was controlled by means of a temperature controller (West Model 6100) with an accuracy of ±1°C. A computer with serial

Table 2. Chemical analyses of fractions of purified mineral clays

Weight %	SiO_2	Al_2O_3	Fe_2O_3	MgO	Na_2O	K_2O	CaO	Ignition loss
It-1	50.24	24.38	5.58	2.13	1.21	9.39	0.05	7.53
Ha.Kass	39.40	29.91	0.19	0.27	0.52	0.1	0.65	28.96

cable RS232 and software Labview 4.0 have been used for data acquisition.

RESULTS AND DISCUSSION

Impedance Studies

A polycrystalline material usually gives grain boundary properties with different time constants leads to two successive semi-circles. The electrical properties of a material are often represented in terms of some complex electrical parameters like complex permittivity ε*, electric modulus M^* and dielectric loss tan δ. They are related to each other as follows:

Complex impedance,

$$Z^* = Z' - jZ' = R_s - 1/j\omega C_s. \quad (1)$$

Complex permittivity,

$$\varepsilon^* = \varepsilon' - j\varepsilon'', \tan\delta = \varepsilon''/\varepsilon'. \quad (2)$$

Complex modulus,

$$M^* = M' + jM'' = j\omega C_0 Z^*. \quad (3)$$

Where R_s is the series resistance, $\omega = 2\pi f_r$ (f_r = resonance frequency), C_s the capacitance in series, $j = (-1)^{1/2}$ the imaginary factor and C_0 is the vacuum capacitance of the circuit elements. Above four expressions give a wide scope for graphical representation.

On the other hand, the peak of the high frequency semi-circular arc in the impedance spectrum enables us to evaluate the relaxation frequency (ω_{max}) of the bulk material in accordance with the relation

$$\omega_{max}\tau = R_b C_b = 1 \text{ or } 2\pi f_{max} R_b C_b = 1 \geq f_{max} = 1/2\pi R_b C_b \quad (4)$$

and

$$\tau = 1/2\pi f_{max} \ (5) \quad (5)$$

where R_b and C_b refer to bulk resistance and capacitance, respectively, τ represents relaxation time and $\omega = 2\pi f$ is the angular frequency. Besides, the bulk conductivity (σ) of the material is a thermally activated process obeying Arrhenius behavior. It is calculated in accordance with the relation

$$\sigma = (\sigma_0/T)\exp(-Ea/kT). \quad (6)$$

From expression (2), the complex permittivity

$$\varepsilon^* = \varepsilon' - i\varepsilon''$$

where ε' is the real or relative permittivity or dielectric constant and; ε", the imaginary or dielectric loss, ε* can be represented as [19].

$$\varepsilon^* = 1/j\omega C_0 Z^* \quad (7)$$

where C_0 is the capacitance of free space. The ε' real and ε" imaginary parts of dielectric permittivity were calculated from impedance data of illite IMt-1 and kaolinite Ka-kass clay minerals, measured over a range 1 Hz to 13 MHz at different temperatures using

$$\varepsilon' = (t/A\omega\varepsilon_0)[Z''/(Z'^2 + Z''^2)], \quad (8)$$

$$\varepsilon'' = (t/A\omega\varepsilon_0)[Z'/(Z'^2 + Z''^2)]. \quad (9)$$

It must be noticed that ε' and ε" represent, respectively, the dielectric constant and the dielectric loss of the material.

From expression (3), the complex electric modulus M^* is the reciprocal of the complex permittivity ε*

$$M^* = 1/\varepsilon^* \quad (10)$$

where

$$M' = (A/t)\omega\varepsilon_0 Z'' \text{ and } M'' = (A/t)\omega\varepsilon_0 Z'. \quad (11)$$

The σ_{AC} was calculated using the measured impedance data of studied clay samples over a frequency range of 1 Hz to 13 MHz at different selected temperatures using

$$\sigma_{AC} = (t/A)[Z'/(Z'^2 + Z''^2)] \quad (12)$$

where t is the thickness and A the area of the sample pellet.

Impedance Spectrum Analysis

First, it must be pointed out that the impedance spectra measured at temperatures above 400°C are reproducible. But at temperatures below 400°C, several factors could affect impedance measurements, e.g. incomplete contact between sample and electrode, short circuit through a less resistive path in clay, and the presence of moisture in clay.

The electrical behavior of the system has been studied over a range of frequency and temperature using *AC* technique of *IS*. The plot of $-Z''$ versus Z' (so called Nyquist plot) of It-1 at different temperatures (400–800°C) is shown in Figs. 3a–3c.

One can observe that the effect of temperature on impedance behavior of the material sample becomes clearly visible with rise in temperature (Figs. 3a–3c). The impedance spectrum is characterized by the appear-

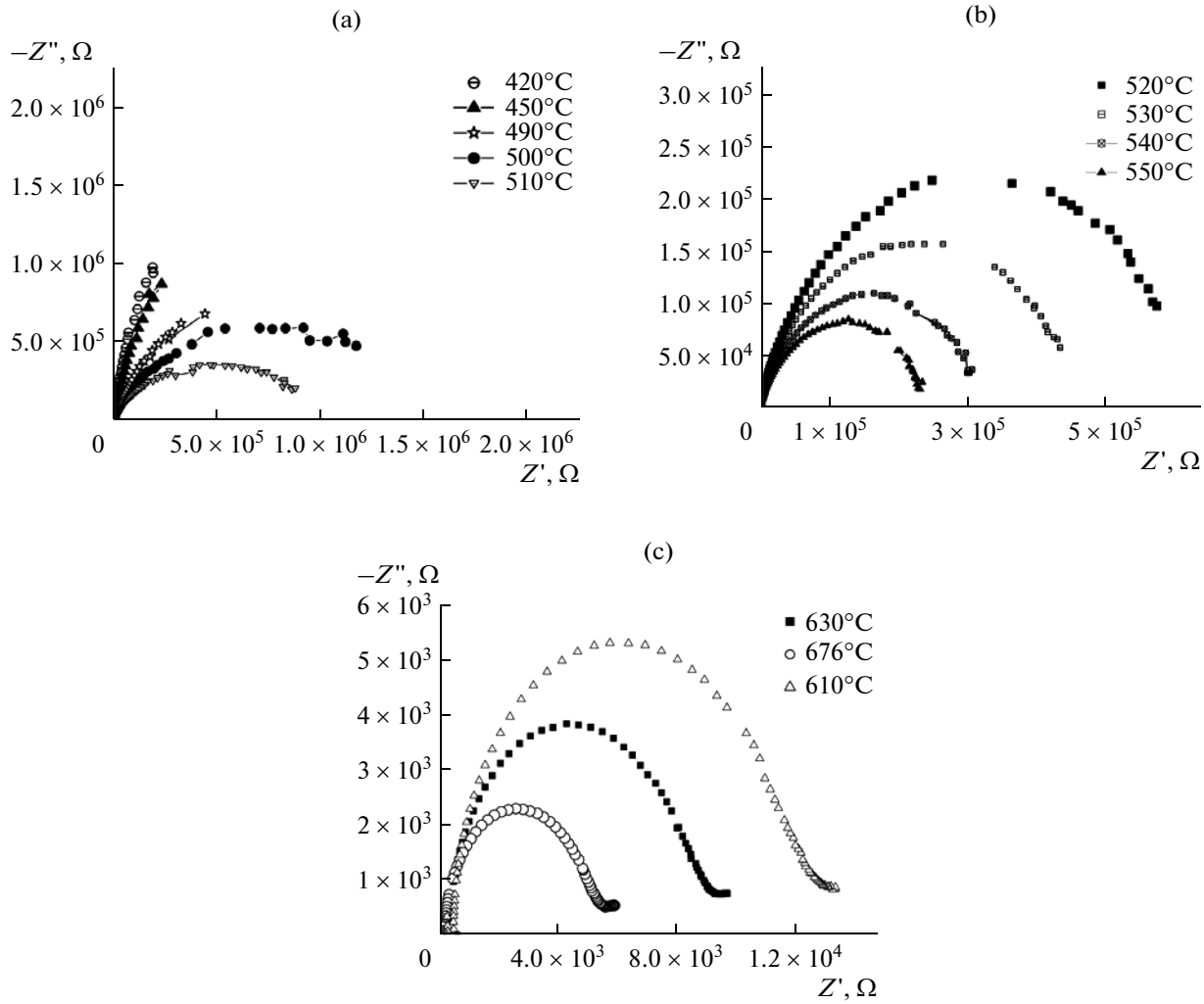

Fig. 3. Impedance spectra as a function of temperature for illite It-1 sample.

ance of single semicircular arc whose pattern of evolution changes with rise in temperature (Figs. 3a–3b). Each semicircular arc in the impedance pattern can be attributed to a parallel combination of resistance and capacitance. The center of the semicircular arc shifts towards the origin on increasing temperature which indicates that the conductivity of the illite It-1 increases with increase in temperature. With further rise in temperature, appearance of another semicircular arc in the impedance spectrum has been noticed on and after 600°C. The pattern is displayed in Fig. 3c. The presence of a single semicircular arc up to 595°C indicates that the electrical processes in the material arise basically due to the contribution from bulk material (grain interior) [20–22] and can be modeled as an equivalent electrical circuit comprising of a parallel combination of bulk resistance (R_b) and bulk capacitance (C_b). The electrical process at these temperatures may be attributed to intragrain phenomena.

Appearance of additional semicircular arcs in the impedance pattern with increasing in temperature ($T \geq 600$°C) indicates the beginning of intergranular activities within the clay sample with definite contributions from both bulk (grain interior) and grain boundary effects (Figs. 3b–3c). This type of electrical phenomena in the material can appropriately be modeled in terms of an equivalent electrical circuit, according to brick layer model [23], comprising of a series combination of two parallel R–C circuits attributed to both the grain interior (bulk) and grain boundary effects in agreement with Brahma et al [22].

Figures 4a–4c show the loss spectrum i.e. variation of the imaginary part of the impedance (Z" with frequency at different temperatures).

We must emphasis that when temperature is between $200 \leq t \leq 450$°C, a monotonous decrease in (Z") without any peak in the frequency range (ii) appearance of peaks in the loss spectrum (iii) typ-

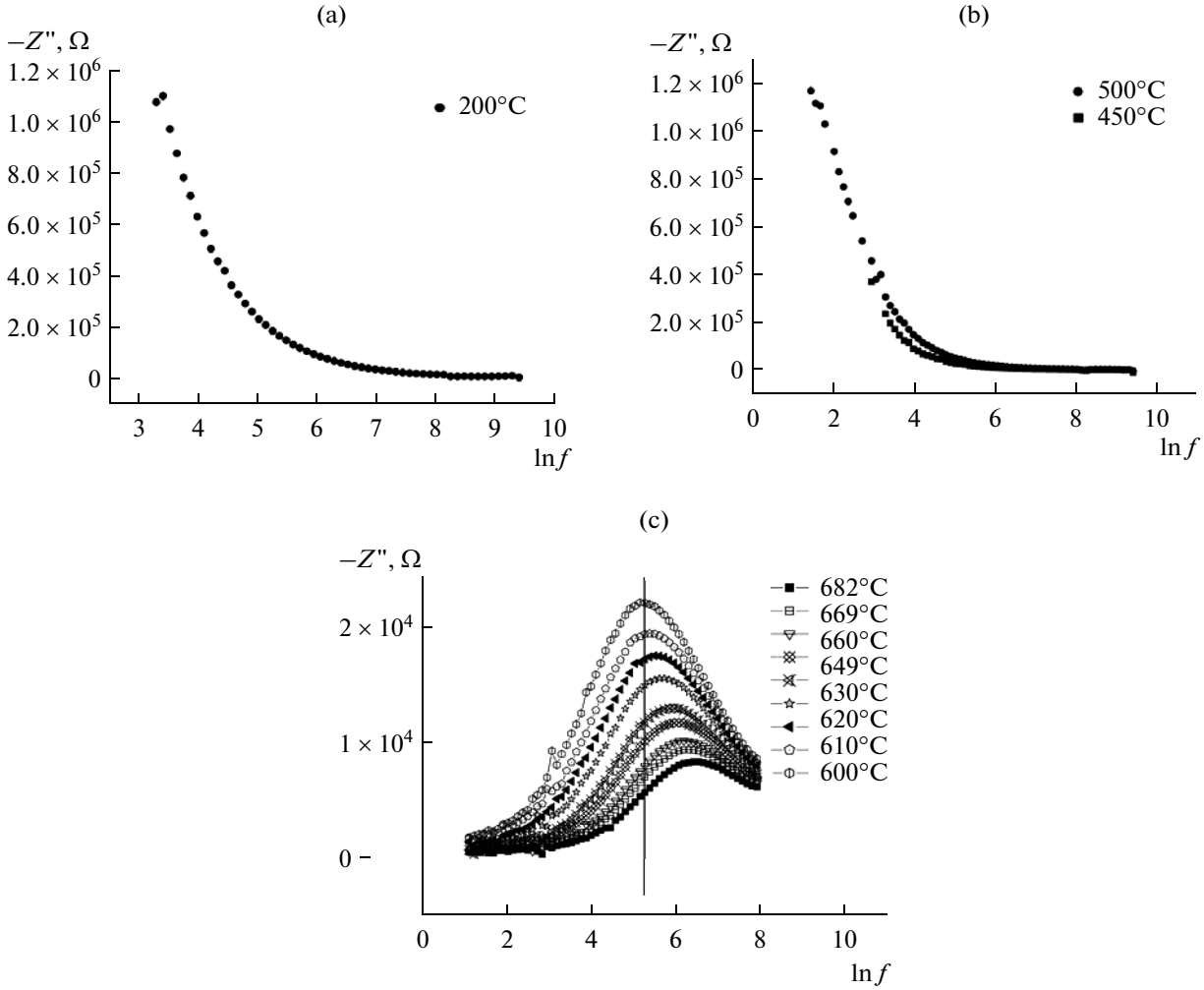

Fig. 4. Variation of imaginary part of impedance (Z'') as a function of frequency for illite It-1.

ical peak broadening with increase in temperature and (iv) asymmetric peak broadening. The absence of peaks up to a temperature 450°C in the pattern indicates negligible or absence of current dispersion in this temperature region. Figure 4c shows peaks at unique frequency that describes the type and strength of electrical relaxation phenomenon in the material [22, 24]. A significant broadening of the peaks with increasing in temperature suggests the presence of electrical processes in the material [25]. In addition, the coincidence of the impedance Z values at higher frequencies at all the temperatures indicates a possible release of space charge.

Figures 5a–5c show the variations of real part of impedance (Z' i.e. bulk resistance) with frequency at different temperatures.

As we can observe, at relatively low temperature (up to 500°C), the curve Z' vs. $\ln f$ shows a monotonic de crease in the value of Z' with temperature. The impedance value is typically higher at lower temperatures in the low–frequency region and decreases gradually with increasing frequency (Fig. 5b). As the temperature increases, the pattern of variation of Z' as a function of frequency assumes a sigmoidal variation in the low–frequency region follow by a plateau region at higher frequency. This behavior has been observed to be almost similar at temperatures on and above 530°C (Figs. 5c and 5d). In addition the magnitude of Z' a (bulk resistance) decreases with increasing temperature in the low-frequency ranges and appears to merge in the high–frequency region irrespective of temperature. This result can be attributed to the release of space charge as a result of reduction in the barrier properties of the clay mineral sample as already mentioned in other works by some authors [22, 25, 26]. The same authors have emphasized that this phenomenon may be a responsible factor for the enhancement of AC conductivity of material with temperature at higher frequencies.

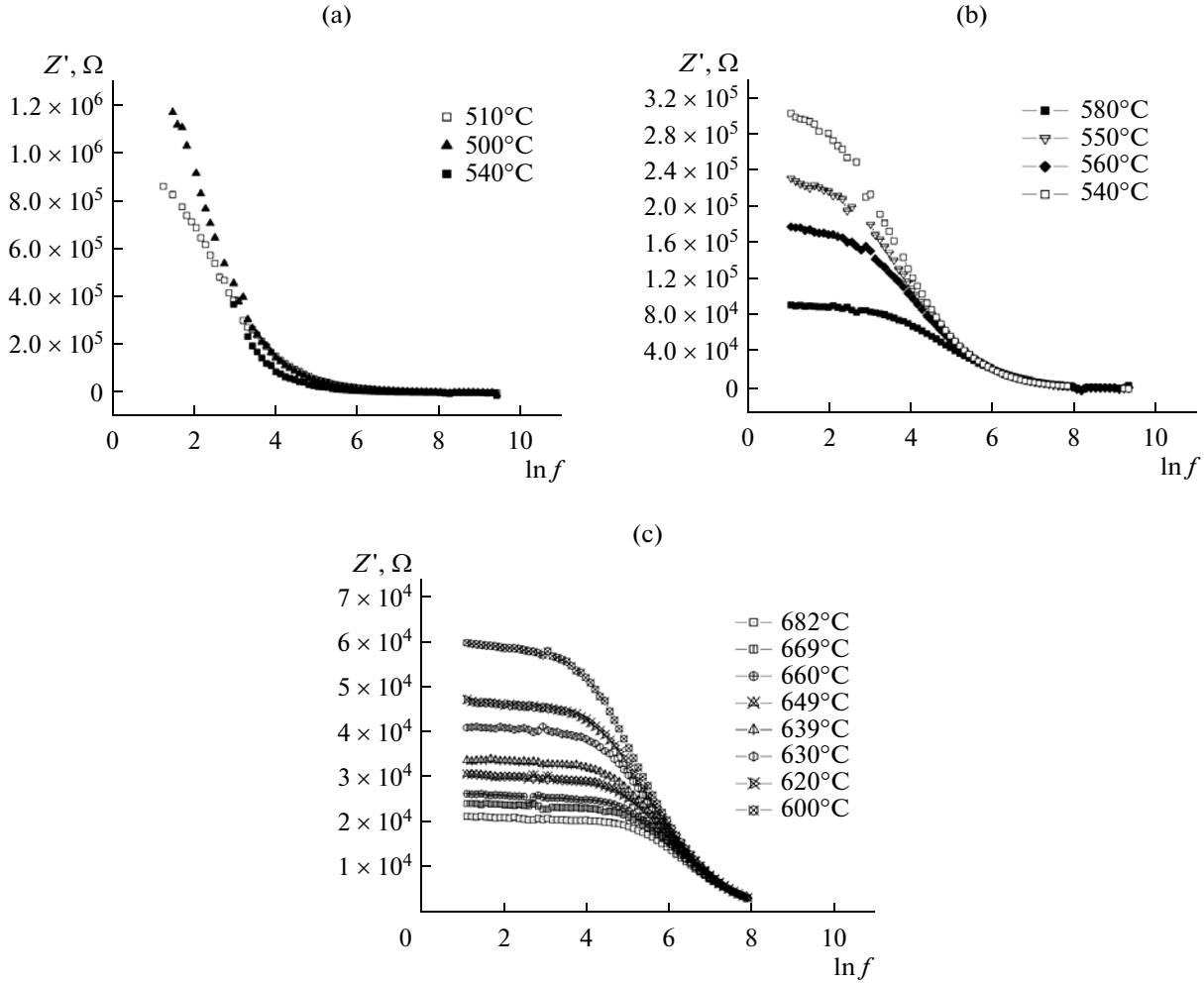

Fig. 5. Variation of real part of impedance (Z') as a function of frequency for illite It-1 sample.

Electrical Conductivity Analysis

The conductivity $\sigma(\omega)$ has been evaluated from complex impedance spectrum data. Fig. 6 shows the variation of $\sigma(\omega)$ as a function of temperature.

This plot indicates a linear increase of conductivity with rise in temperature with a typical Arrhenius-type behavior in two domains, having linear dependence of logarithm of conductivity Ln ($\sigma \times T$) on inverse of temperature $10^3/T$ K^{-1}, i.e., the electrical conductivity is a thermally process, and obeys the Arrhenius law $\sigma = (\sigma_0/T)\exp(-Ea/kT)$ where the symbols have their usual meanings. The activation energy (Ea) of the clay mineral sample can be calculated from the slope of a straight line. The increasing of conductivity with rise in temperature shows a typical characteristic of a semiconductor (i.e., negative temperature coefficient of resistance-type behavior). This curve indicates the presence of two slopes in the pattern $\sigma(\omega)$ vs. $10^3/T$ corresponding respectively to activation energy values $Ea_1 = 0.95$ eV and $Ea_2 = 2.07$ eV, situated at the temperature range between 570 and 580°C. This is attributed very likely to a change in the conduction mechanism, leading to an increase of the ionic conduction resulting either to a decrease of the barrier to ion motion or to a decrease of the number of mobile ions. Anyway, this could not be ascribed to a phase transition in the material, i.e. to a structural change since this structural change does not occur for the illite sample between 500–600°C. In fact, most of the studies described in the literature concerning the DTA curves of illitic samples show an endothermic reaction between 500–600°C which is characteristic of the nonexpendable three-layer type of clay minerals [27]. Illite could only dehydroxylate in this temperature range.

Figure 7 shows the variation of $\log\sigma$ versus $\log(f)$ at various temperatures for illite It-1. It is observed that the frequency dependence of conductivity shows two distinct regimes, within the measured frequency window: (i) the low frequency plateau region and; (ii) high frequency dispersion region. The plateau region corresponds to frequency independent conductivity (σ_{DC}) and dispersion region corresponds to the frequency–

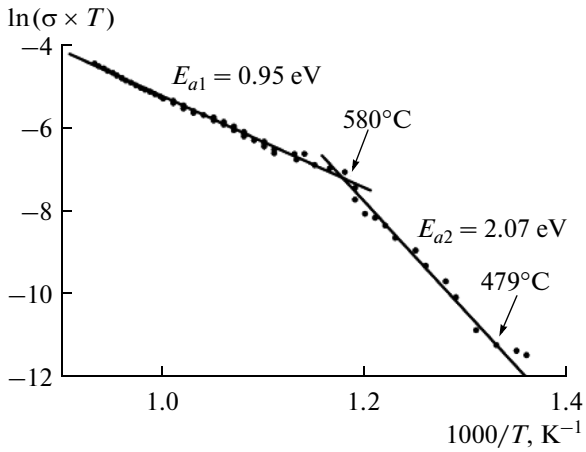

Fig. 6. Variation of σ(ω) (bulk conductivity) against $10^3/T$ K^{-1} for illite It-1.

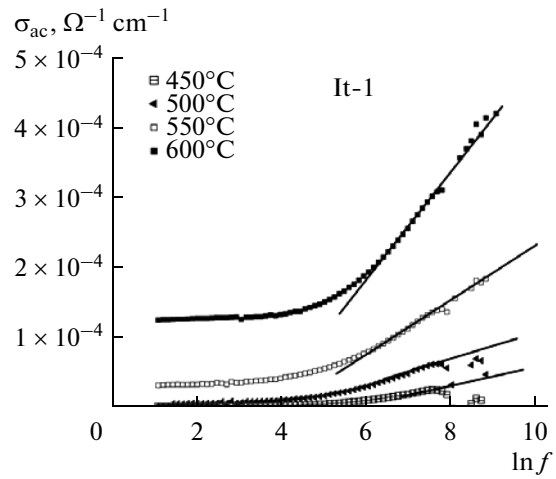

Fig. 7. logσ(ω) vs. log (*f*) plot It(Mo) at different temperatures (450–800°C) for It-1.

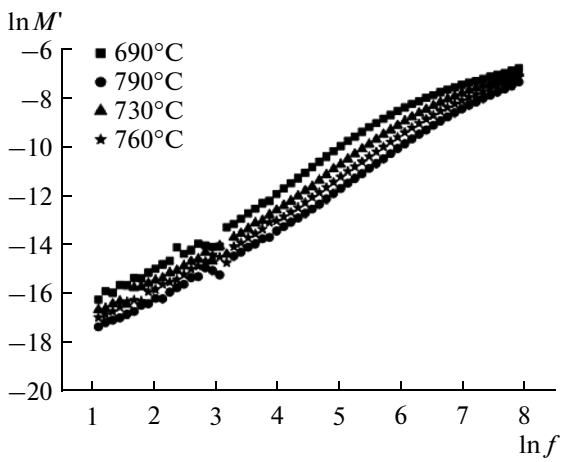

Fig. 8. Variation of real part of electrical modulus (*M*') as a function of frequency for illite It-1.

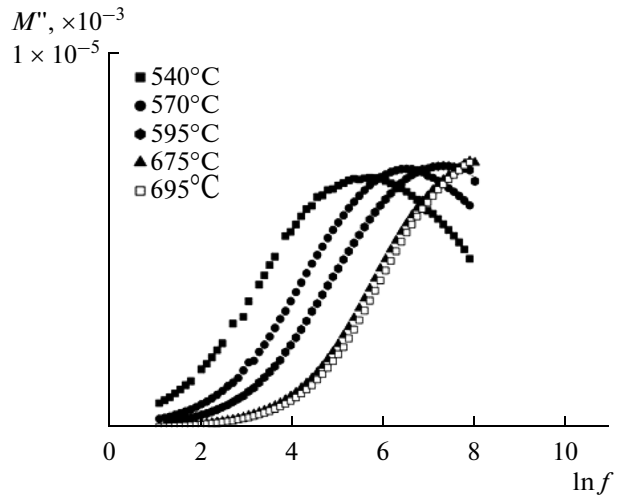

Fig. 9. Variation of imaginary part of complex modulus (*M*") as function of frequency at different temperatures for illite It-1.

dependent part (σ_{AC}). The σ_{DC} value could be obtained by extrapolating the conductivity value to the zero limit frequency.

The observed frequency dependent conductivity can be described by the equation of Jonscher (1983) [28]: $\sigma(\omega) = \sigma_{DC} + A\omega^n$, where n is the frequency exponent in the range of $0 < n < 1$, a and n are thermally activated quantities, hence electrical conduction is a thermally activated process. The *AC* conductivity (σ_{AC}) was found to obey the power law $A\omega^n$ ($n < 1$). The value of *n* was 7.65×10^{-5} at $T = 600$°C.

According to Jonscher (1977) [29], the origin of the frequency dependence of conductivity lies in the relaxation phenomena arising due to mobile charge carriers.

Figures 8 shows the variation of real part of electric modulus *M*' as a function of frequency at different temperatures. At lower frequencies, *M*' tends to be very small confirming that the electrode effects make a negligible contribution and hence may be ignored when the data are analyzed in modulus formalism [25]. In the figure *M*' reaches to constant value M_∞ at high frequencies for all temperatures and this due to relaxation processes, which are spread over a range of frequencies.

The variation of *M*" with frequency is shown in Fig. 9 at different temperatures. In the *M*" plot; the peaks are broader and asymmetric on both sides of the maxima than predicted by ideal Debye behavior. The frequency range where the peaks occur is indicative of transition from long range to short-range mobility

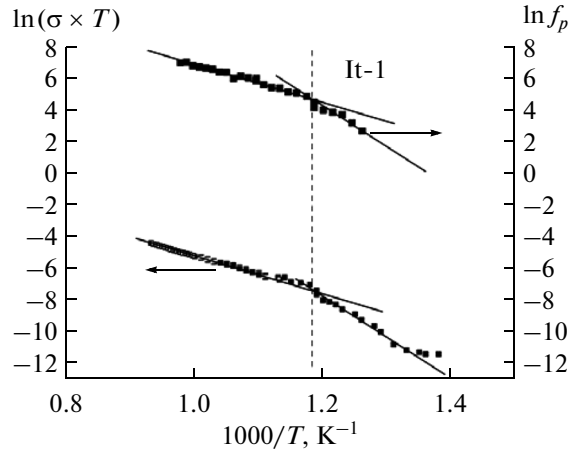

Fig. 10. Comparison of the Variation of ln σ and ln f_p as a function of temperature for the illite It-1.

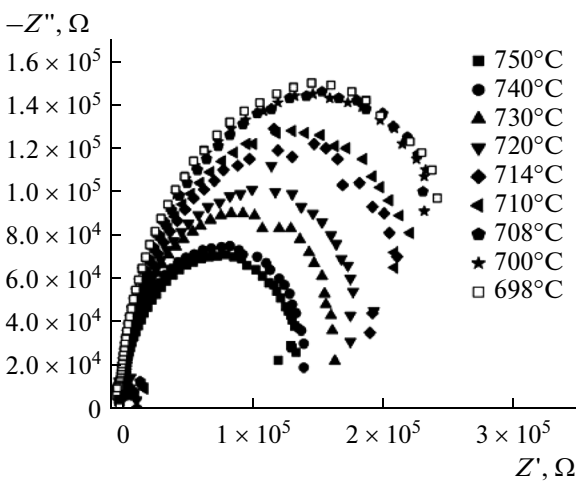

Fig. 11. Impedance spectrum of kaolinite Ha-Kass as a function of temperature.

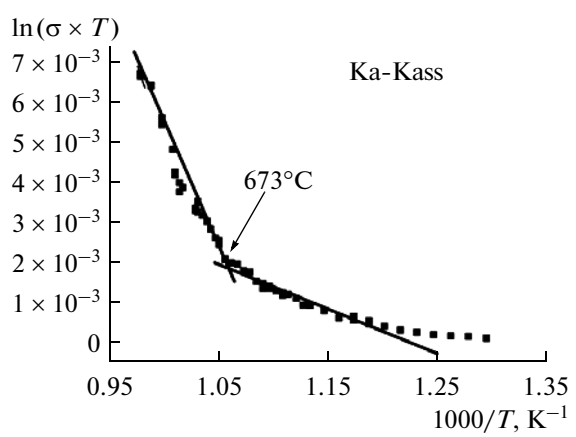

Fig. 12. Variation of σ(ω) as a function of temperature for halloysite sample (Ha-Kass).

[25, 30]. The peak in the M'' plot shifts tower higher frequencies with increase in temperature and also the peak height increases. The high frequency side of the M'' peak represents the range of frequencies in which the ions are spatially confined to their potential wells. The peak frequency of the pattern, corresponding to maximum value of M'' is called conductivity relaxation frequency, gives an estimate of conduction relaxation time (τ) in accordance with the relaxation $\omega_{max}\tau_\sigma = 1$. The value of relaxation frequency has been calculated in the temperature range (182–800°C) and its variation as a function of temperature is shown in Fig. 10.

The variation of $\ln f_{max}$ as a function of inverse absolute temperature appears to be linear satisfying the relation $f_p = f_{po}\exp(-E_f/kT)$. We can also note that experimental points representing simultaneously the variations of conductivity and frequency f_p with temperature are located on segments of parallel lines leading to the same slope values. Therefore, the activation energy values estimated from the AC conductivity pattern and modulus pattern are very similar and suggest the possibility of long-range mobility of charge carriers (ions) via hopping mechanism at higher temperature. Further, the appearance of peak in the modulus spectrum provides a clear indication of conductivity relaxation.

On the other hand, a similar study has been conducted on halloysite clay sample (Ha-Kass) in order to compare the ionic conduction mechanism in these materials of different structural properties. Impedance spectrum results indicate only the presence of a single semicircular arc whatever the temperature considered and hence the electrical processes in the material may be attributed to only intragrain phenomena (Fig. 11), which is not the case for illite It-1. The existence of a temperature-dependent electrical relaxation phenomenon in Ha-Kass sample has been also observed (variation of imaginary part of impedance (Z'') as a function of frequency). In addition, as observed in It-1 the analysis of impedance spectra in the low frequency region, show a decrease in the magnitude of Z' with rise in temperature i.e. negative temperature coefficient of resistance (NTCR)-type behavior like that of semiconductors.

The AC conductivity σ(ω) analysis shows typical Arrhenius behavior when observed as a function of temperature (Fig. 12). This curve indicates the presence of two different slopes in the pattern σ(ω) vs. $10^3/T$, located above and below 673°C, corresponding respectively to activation energy values Ea_1 = 0.94 eV and Ea_2 = 4.93 eV, which ascribe very likely to a modification of the structural material. Indeed, during this temperature 550–680°C a dehydroxylation process of the clay occurs and kaolinite forms metakaolinite by dehydroxylation [31].

On the other hand, the possibility of long-range mobility of charge carriers (ions) via hopping mecha-

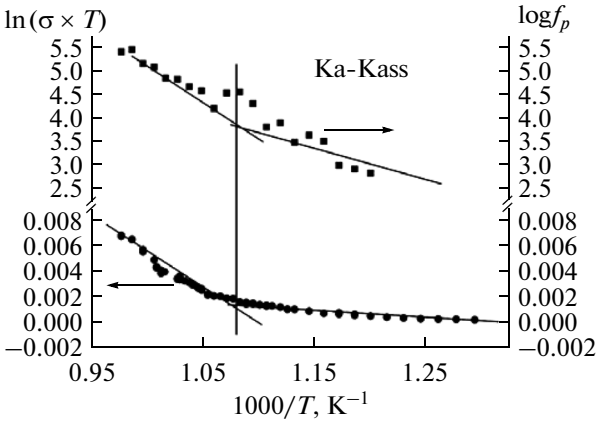

Fig. 13. Comparison of the variation of ln ($\sigma \times T$) and $\ln f_p$ as a function of temperature for halloysite sample Ha-Kass.

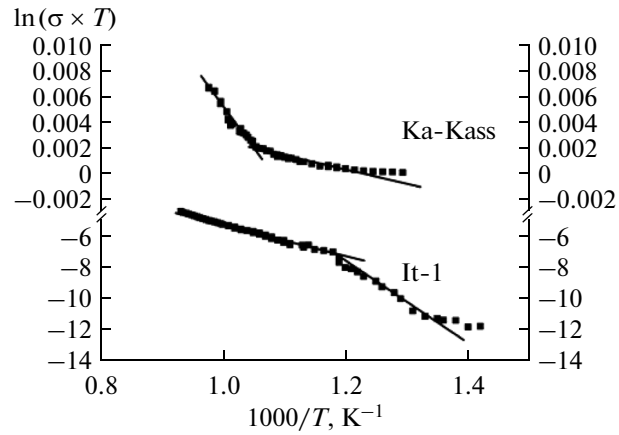

Fig. 14. Comparison of variation of $\ln(\sigma \times T)$ vs. $1000/T$ as a function of temperature for halloysite Ha-Kass and illite It-1 samples.

nism at higher temperature requires a comparison of activation energy value estimated from conductivity $\sigma(\omega)$ and modulus pattern ($\ln f_p$) as function of temperature. Indeed, the variation of $\ln \sigma T$ and $\ln f_p$ as a function of inverse of temperature is representing simultaneously as a comparison in Fig. 13. A non-similarity in the of activation energy values is evident from these plots due to the obtaining of different slope values. Consequently, this finding can confirm that the ionic conduction mechanism in the Ha-Kass is not of type hopping as in the case of the illitic clay sample. This significant difference indicates that two phenomena or a mixture of several phenomena is measured simultaneously for the material. An electrical charge transport has been demonstrated in the investigated sample and it is very likely that the charge transport is mainly of electronic nature.

Discussion Concerning the Electrical Conductivity Results of the Studied Clays

A comparative study of electrical conductivity has been conducted to better understand the electrical transport mechanism. Figure 14 shows the variation of $\ln(\sigma \times T)$ vs. $1000/T$ for the two clay mineral samples.

According to our results, it appears clearly that electrical conductivity of the 1 : 1 halloysite clay sample, has a much higher electrical conductivity value than 2 : 1 illite It-1, there is about a factor 1000 between the values of conductivity regardless of the temperature considered (example at 727°C, $\sigma_{\text{Ka-Kass}} = 10^{-3}\ \Omega^{-1}\ \text{cm}^{-1}$, $\sigma_{\text{It-1}} = 5.4 \times 10^{-6}\ \Omega^{-1}\ \text{cm}^{-1}$). This electrical conductivity is probably closely related (i) to the microstructural of the clay mineral. In all cases, the values remain below 1 which is consistent with the works of Kaya, 1999 [32]. The author noted that normalized electrical conductivity values are <1 for kaolinite of Georgia and >1 for bentonite, determined at various water contents and NaCl concentrations; (ii) to the dimensions of the cell that seem to play an important role in the mobility of the charge carriers (cations) present in the interlayer spacing of illite and kaolinite samples. From our point of view, the decrease of electrical conductivity of illite with respect to halloysite, is mainly related to the structure of this mineral. It is well known that illite is a 2 : 1 clay mineral with potassium (K) in the interlayer that restricts shrinking and swelling. Potassium ions bind to the oxygen plane of the basal tetrahedral layer of adjacent units and are not exchangeable ions. The displacement of cations (mainly Na^+ ions which are mobile than other cations in interlayer spacing is slowed by the presence of K^+ ions of greater size creating a steric blocking effect and therefore, the activation energy of the motion process increases resulting in a decrease of the ionic conductivity. Moreover, the presence of K^+ ions can alter the distribution of Na^+ in the different available sites. The conductivity may also decrease due to decrease of the number of mobile ions. About halloysite, things are otherwise, it has one layer of silicon atoms and one layer of aluminum layers in 1 : 1 structure. It is non-expanding clay mineral and different layer are held together by hydrogen bonding which occurs between the plane of basal oxygen atoms within a tetrahedral sheet and the plane of hydroxyl group within the octahedral layer. In the case of halloysite sample, the mobility of cations (essentially Na^+ ions in the interlayer) is high lea-ding to a decrease of the activation energy of the motion process and subsequently to an increase of the ionic conductivity. In any case, more studies are necessary to clarify these points and to locate the Na^+ ions in the structure of these clay minerals.

CONCLUSIONS

The electrical conductivity measurements performed on the two clay minerals show that the mobil-

ity of the cations in interlayer spacing (mainly Na^+) is mostly influenced by the structure of these materials. In illite sample, some Na^+ ions are less mobile, due to the presence of K^+ ions, leading to a decrease in the number of species participating in the conduction process which explains the decrease of ionic conductivity of this clay mineral when compared to kaolinitic sample.

REFERENCES

1. Arulanandan, K., Dielectric method for prediction of porosity of saturated soil, *J. Geotech. Eng-ASCE*, 1991, vol. 117, pp. 673–683.
2. Robinson, D.A., Bell, J.P., and Bachelor, C.H., The influence of iron minerals on the determination of soil water content using dielectric techniques, *J. Hydrol.*, 1994, vol. 161, pp. 169–180.
3. Ficai, C., Caractéristiques des matières argileuses établies en mesurant les constantes et les pertes diélectriques dans le domaine de fréquence compris entre 30 kHz et 3 MHz, *Bull. Soc. Franc. Ceram.*, 1959, vol. 42, pp. 7–16.
4. De Lima, O.A.L. and Sharm,a M.M., A generalized Maxwell-Wagner theory for membrane polarization in Shaly sands, *Geophys.*, 1992, vol. 57, pp. 431–440.
5. Knoll, M.D., *A Petrophysical Basis for Ground-Penetrating Radar and Very Early Time Electro-Magnetic, Electrical Properties of Sand-Clay Mixtures, Ph.D. Thesis*, University of British Columbia, 1996.
6. Wildenschild, D., Roberts, J.J., and Carlberg, E.D., Electrical properties of sand/clay mixtures: the effect of microstructure, *SEG Int. Exposition and 69th Annual Meeting. Houston, TX. 1999, October 31-November 5.*
7. Bona, N., Rossi, E., and Capaccioli, S., Electrical measurements in the 100 Hz–10 GHz frequency range for efficient rock wettability determination, *SPE Journ.*, 2001, vol. 6, no. 1, pp. 80–88.
8. Börner, F.D., Combined complex conductivity and dielectric measurements on core, *Proc. of the 1997 Int. Symp. of SCA in Calgary, 1997, SCA, paper No 9736,* pp. 1–10.
9. Muccillo, E.N.S. and Kleitz, M., Impedance spectroscopy of Mg-partially stabilized zirconia and cubic phase decomposition, *J. Eur. Ceram. Soc.*, 1996, vol. 16, pp. 453–465.
10. Rodrigues, C.M.S., Labrincha, J.A., and Marques, F.M.B., Monitoring of the corrosion of YSZ by impedance spectroscopy, *J. Eur. Ceram. Soc.*, 1998, vol. 18, pp. 95–104.
11. Steil, M.C., Thevenot, F., and Kleitz, M., Densification of yttria-stabilised zirconia-impedance spectroscopy analysis, *J. Electrochem. Soc.*, 1997, vol. 1, pp. 390–398.
12. McCarter, W.J., Garvin, S., and Bouzid, N., Impedance measurement on cement paste, *J. Mater. Sci. Lett.*, 1988, vol. 7, no. 10, pp. 1056–1057.
13. Christensen, B.J., Mason, T.O., and Jennings, H.M., Influence of silica fume on the early hydration of portland cements using impedance spectroscopy, *J. Am. Ceram. Soc.*, 1992, vol. 75, pp. 939–945.
14. Christensen, B.J., Coverdale, R.T., Olseon, R.A., Ford, S.J., Carboczi, E.J., Jennings, H.M., and Mason, T.O., Impedance spectroscopy of hydrating cement-based materials, *J. Am. Ceram. Soc.*, 1994, vol. 77, pp. 2789–2804.
15. Macdonald, J.R. and Barsoukov, E., *Impedance Spectroscopy. Theory. Experiment and Applications*, N.Y.: Wiley and sons, 2005, pp. 1–27.
16. Orazem, M.E. and Tribollet, B., *Electrochemical Impedance Spectroscopy*, Hoboken, New Jersey: John Wiley and Sons, 2008, Part I, Background, pp. 3–96.
17. Bergaya, F. and Vayer, M., CEC of Clays: measurement by adsorption of a copper ethylenediamine complex, *Appl. Clay Sci.*, 1997, vol. 12, pp. 275–280.
18. Brindley, G.W. and Brown, G., *Crystal Structure of Clay Minerals and their X-ray Identification*, London: Mineralogical Society, 1980.
19. Ingram, M.D., Ionic conductivity in glass, *Phys. Chem. Glasses*, 1987, vol. 28, pp. 215–234.
20. Irvine, D.C., Sinclair, A.R., and West, A.R., Electroceramics: characterization by impedance spectroscopy, *Adv. Mater.,* 1990, vol. 2, pp. 132–138.
21. Selvasekarapandian, S. and Vijaykumar, M., The AC impedance spectroscopy studies on LiD_yO_2, *Mater. Chem. Phys.*, 2003, vol. 80, pp. 29–33.
22. Brahma, S., Choudhary, R.N.P., Thakur, A.K. AC impedance analysis of $LaLiMo_2O_8$ electroceramics, *Physica B*, 2005, vol. 355, pp. 188–201.
23. Macdonald, J.R. and Johnson, W.B., *Fundamentals of Impedance Spectroscopy in Impedance Spectroscopy-Emphasizing Solid Materials and Systems*, New York: John Wiley and sons, 1987, Chap I, pp. 1–26.
24. Chatterjee, S., Mahapatra, P.K., Choudhary, R.N.P., and Takur, A.K., Complex impedance studies of sodium pyrotungstate-$Na_2W_2O_7$, *Phys. Stat. Sol. (a)*, 2004, vol. 201, pp. 588–595.
25. Sahoo, P.S., Panigrahi, A., Patri, S.K., and Choudhary, R.N.P., Impedance spectroscopy of $Ba_3Sr_2DyTi_3V_7O_{30}$ ceramic, *Bull. Mater. Sci.*, 2010, vol. 33, pp. 129–134.
26. Płocharski, J. and Wieczorek, W., Impedance spectroscopy and phase structure of PEO-NaI complexes, *Solid. State Ionics,* 1998, vols. 28–30, no. 2, pp. 979–982.
27. Grim, R.E. and Rowland, R.A., Differential thermal analysis of clay minerals and other hydrous materials, *Am. Mineralogist.*, 1942, vol. 27, pp. 746–761, 801–818.
28. Joncher, A.K., *Dielectric Relaxation in Solids*, London: Chesla Dielectric Press, 1983, pp. 56–67.
29. Jonscher, A.K., The universal dielectric response, *Nature*, 1977, vol. 267, pp. 673–679.
30. Khatri, P., Behera, B., Srinivas, V., and Choudhary, R.N.P., Complex impedance spectroscopic properties of $Ba_3V_2O_8$ ceramics, in *Research Letters in Materials Science*, 2008, Article ID 746256, 5 pages doi:10.1155/2008/746256.
31. Chakravorty, A.K., Application of TMA and DTA for study of the crystallization behaviour of SiO_2 in the thermal transformation of kaolinite, *J. Therm. Anal.*, 1993, vol. 39, pp. 289–299.
32. Kaya, A., Electrical spectroscopy of kaolin and bentonite slurries, *Turk. J. Eng. Environ. Sci.*, 2001, vol. 25, pp. 345–354.

ISSN 1068-3755, Surface Engineering and Applied Electrochemistry, 2014, Vol. 50, No. 1, pp. 95–100. © Allerton Press, Inc., 2014.
Original Russian Text © K.A. Kazdobin, K.D. Pershina, V.V. Kokhanenko, L.N. Maslyuk, A.K. Zapol'skii, 2014, published in Elektronnaya Obrabotka Materialov, 2014, No. 1, pp. 89–94.

Nature of the Conductivity of Kaolin under Hydration and Mechanochemical Activation

K. A. Kazdobin[a], K. D. Pershina[b], V. V. Kokhanenko[a], L. N. Maslyuk[c], and A. K. Zapol'skii[d]

[a]*Vernadsky Institute of General and Inorganic Chemistry, National Academy of Sciences of Ukraine, pr. Paladina 32/34, Kiev, 03142 Ukraine*

[b]*Vernadsky Taurid National University, pr. Vernadskogo 4, Simferopol, 95007 Ukraine*

[c]*Laboratoire de Physique des Solides, Université Paris Sud, Plateau de Moulon, Rue Noetzlin–Gif sur Yvette, Orsay, 91400 France*

[d]*Zhytomyr National Agroecological University, Staryi bul'v. 7, Zhytomyr, 10008 Ukraine*

e-mail: kazdobin@ionc.kiev.ua

Received December 19, 2012

Abstract—The role of hydration of kaolin and the nature of its conductivity at varying degrees of hydration have been estimated by electrochemical methods. The catalytic activity of kaolin in the generation of H_2O_2 under a mechanochemical impact has been determined. It has been shown that kaolin with a 1 : 1 close-packed structure and a monolayer of water on the surface exhibits low catalytic activity.

Keywords: kaolin, hydration, impedance, mechanochemistry

DOI: 10.3103/S1068375514010086

INTRODUCTION

A large number of studies are focused on the interaction of particles of minerals, specifically aluminosilicates, with water, in particular on their use in modern technologies, such as the production of metallurgical alumina and coagulants [1, 2] and the intensification of phase separation processes (sedimentation, flotation, filtration, centrifugation, coagulation, etc.) [3]. Slurries of aluminosilicate minerals are the most extensively used in water treatment technology and mineral dressing [4, 5].

In nature, the mineral/water interface provides a basis for self-purification of water bodies [6]. Water has a significant effect on the formation of the surface charge of aluminosilicates including kaolin.

The hydration of kaolin has been examined in [7–9]. The nucleation of ice on the surface of kaolin has been theoretically studied [7]. It has been shown that kaolin has an amphoteric surface whose properties, however, are close to hydrophobic; that is, it is capable of retaining only a monolayer of adsorbed water. Spectral studies of kaolin have shown that the activity of the surface OH groups heavily depends on their position and is determined by the degree of disordering of the surface [8]. As a consequence, the point of zero charge pH_{PZC} for kaolin minerals of different origins is in the range of 5–7 [9]. This is attributed to the mutual effect of the silicate and oxide layers of kaolin exhibiting different charges and activities with respect to hydrogen ions [9]. According to the authors, this mutual effect leads to a heterogeneous distribution of charges in the presence of water, i.e., to the formation of an electric double layer on the silicate centers to form a negative charge of the mineral surface and the complete neutralization of charges in the oxide layer [6]. This is responsible for the proton conductivity of kaolin [10] near the silicate centers and the region of the pH stability of slurries of the mineral and its partial hydrophobicity associated with the disappearance of the charge on the oxide surface centers [9].

Studies of the electrophysical properties of aqueous slurries of kaolin and bentonite by electrochemical impedance spectroscopy (EIS) have revealed their antibate behavior [11], which is characterized by an increase in the conductivity of a bentonite slurry upon dilution and, conversely, its decrease in a kaolin slurry; this suggests that the mechanisms of hydration of the surface of kaolin and bentonite are different. In fact, these minerals are assigned to different structural types: 1 : 1 and 1 : 2 for kaolinite and bentonite, respectively [12]. Accordingly, kaolin has a close-packed structure formed by hexagonal flakes, while bentonite has a loose platelike structure prone to swelling in water and electrolytes.

It was previously shown [13–16] that, upon switching from calcined to dampened natural bentonite and further to its aqueous slurries, the resistance of the systems decreases from 10^6 Ω cm in a calcined sample to 5×10^2 Ω cm in dampened bentonite and $\approx 10^2$ Ω cm in its aqueous slurries. Moreover, the presence of water leads to significant changes in the conduction mecha-

Table 1. Chemical composition of the studied kaolin (%)

LOC*	SiO_2	Al_2O_3	Fe_2O_3	MgO	CaO	TiO_2	P_2O_5	MnO
14	46.4	34.0	0.69	0.23	0.05	1.35	1.7	0.002

* Losses on calcination (1000°C).

nisms of the slurry systems, while stirring of the mineral slurries results in the mechanochemical generation of hydrogen peroxide H_2O_2 on the surface of the slurry particles. This mechanism of generation of active oxidants in water, which was first discovered by Domrachev et al. [17], was confirmed for bentonite slurries [12–13]. A surface concentration of 5×10^{-5} M H_2O_2 was obtained by stirring the slurries [16].

Based on the above features of the slurry systems, the research problem was formulated as follows: the clarification of the role of hydration of kaolin and the nature of its conductivity at varying degrees of hydration and the determination of its catalytic activity in the generation of H_2O_2 under a mechanochemical impact.

EXPERIMENTAL

The FTIR spectra of the surface of natural kaolin; the impedance spectra of calcined, dehydrated, and dampened (15 vol %) kaolin; and voltammograms of a kaolin slurry were analyzed. Enriched raw kaolin of the Glukhovtsy deposit (Ukraine) was used (State Standard GOST 21286–82). The chemical composition of the material is given in Table 1.

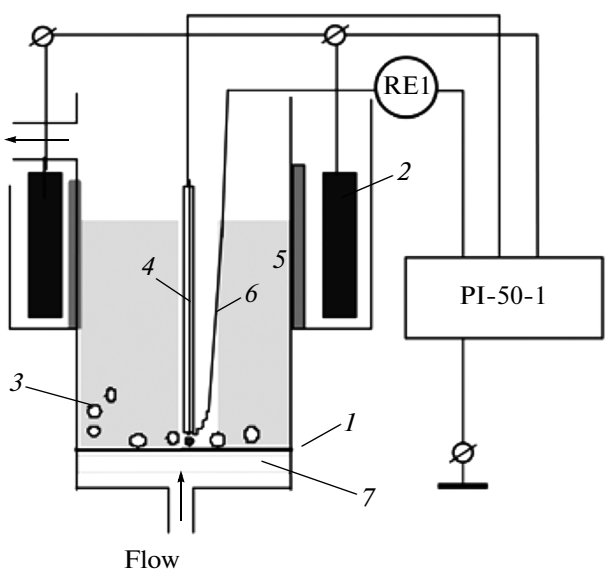

Fig. 1. Cell for voltammetric measurements: (*1*) porous base, (*2*) counter electrodes, (*3*) solution or slurry, (*4*) measuring probe electrode, (*5*) diaphragm seals, (*6*) Luggin capillary, and (*7*) flow predistributor.

It was calculated that the sample under study contains 86% kaolin: $Al_2Si_2O_5(OH)_4$.

Distilled water (GOST 2874–82) was used to prepare the solutions and process the samples. The kaolin was subjected to heat treatment at temperatures of 120, 600, and 1000°C in an SNOL 7.2/1100 oven (TermoLab, Ukraine) for 4 h.

The FTIR spectral analysis was conducted using a PerkinElmer Spectrum BX FTIR Spectrometer (serial no. 78202) with automatic recording of the spectra in a KBr medium according to a standard procedure. The samples were prepared of air-dried kaolin (14% H_2O) and kaolin additionally containing 15% water.

For the electrochemical measurements, weighed portions of aluminosilicates in the air-dry state were charged in a cell and then dampened with distilled water to 15 vol % for 2 h. The resulting kaolin was used to prepare aqueous slurries containing 1 wt % of the dispersed phase. The stability of the slurries was maintained by an IKA MS 3 basic orbital shaker (Germany).

The conductivities of the solutions, samples of the materials, and the mechanisms of the electrode reactions were studied by analyzing the electrochemical impedance (EI) spectra by constructing equivalent circuits. The EI spectra were recorded in a cell with platinum electrodes with each having an area of 2 cm^2 at a distance of 1 cm using a PGSTAT302N Metrohm Autolab-30 electrochemical module equipped with a frequency response analyzer (FRA) module in the range of 10^{-3} to 10^6 Hz. The FRA module was controlled using Autolab 4.9 software at a disturbing signal amplitude of ±5 mV with the subsequent processing using the Zview 2.0 software package.

The cyclic voltammograms of the slurries were recorded using a PI-50-1 potentiostat at a sweep rate of 10 mV/s in an electrochemical cell of a special design (Fig. 1) making it possible to adjust and average the flow rate. Owing to the design, the electrolyte was stirred at a rate of movement along the indicator sphere of 6 cm/s similar to as in [16]. The stream flowing at this rate simulated a flow-through water body. Scanning was conducted in cycles: to +1 V in the direction of the anode with respect to the stationary potential E_{st} and then to –0.6 V with respect to E_{st}. The curves were recorded with an accuracy of ±5% five times to obtain reproducibility of the measurements. The working electrode was a microprobe for scanning slurry systems in the form of a Pt sphere with a diame-

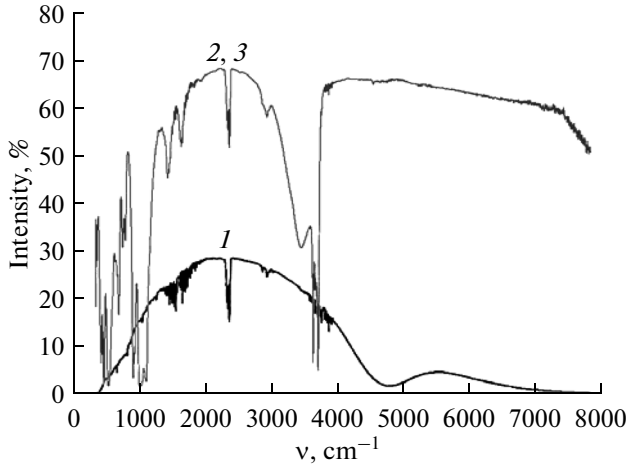

Fig. 2. FTIR spectra of (*2*) air-dried and (*3*) dampened kaolin; (*1*) KBr background.

ter of 1.1 mm on an insulated current lead with a closely located capillary of reference electrode [16].

All the experiments were conducted at 20 ± 2°C.

RESULTS AND DISCUSSION

The IR spectra of kaolin (Fig. 2) exhibit bands in the ranges characteristic of the stretching vibrations of a hydroxide anion (3620 and 3700 cm^{-1}). The detailed identification of the spectrum revealed a small peak with a maximum at 1636 cm^{-1}, which is characteristic of the vibrations of the surface water in an $M{-}OH_2$ complex. In accordance with these spectra, an increase in the amount of water should not affect the original structure of the mineral, as proved in experiments (see Fig. 2). This fact confirmed the weak binding of water to the surface of the mineral, which suggests that the presence of excess water leads to slight changes in the pattern of the charge transport and conductivity.

The EIS studies of kaolin dispersions at the different stages of heat treatment revealed that, under the experimental conditions, measurements of air-dried powders give no reproducible results, which is associated with the high irreproducible resistance of the samples. This is attributed to the enhancement of the spontaneous mutual effect of the silicate and oxide layers of the mineral with a decrease in the number of water molecules on the metal-oxide centers [10]. This behavior of the samples made it necessary to measure the impedance spectra in the presence of a trace amount of water (Fig. 3, Table 2).

Studies based on X-ray diffraction analysis [1] showed that, during drying to 120°C, kaolinite does not undergo irreversible transformations; during rehydration of the dry samples, their hydration is resumed. However, as the drying temperature increases to 450–550°C, the rehydration process occurs much more slowly. Calcination at 1000°C is accompanied by the formation of mullite $3Al_2O_3 \cdot 2SiO_2$, which is hardly hydrated at all.

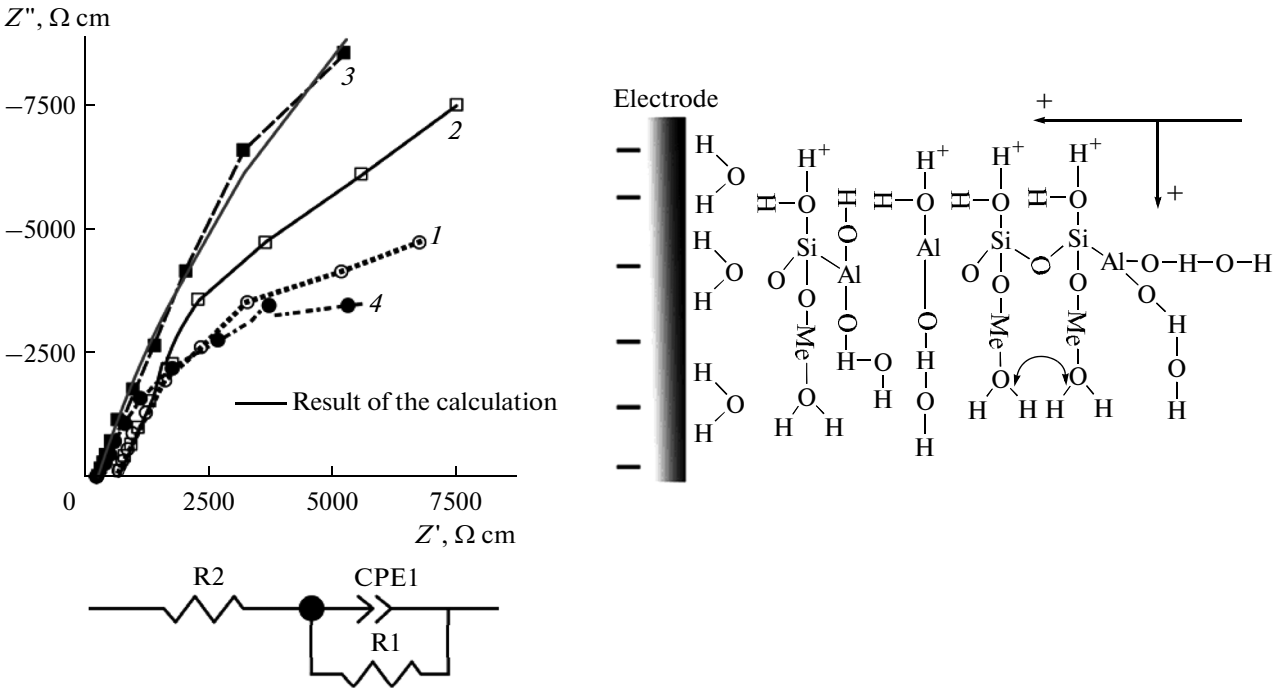

Fig. 3. Impedance spectra and equivalent circuit of the dampened kaolin (15% H_2O) after heat treatment at (*1*) 20 (initial), (*2*) 120, (*3*) 600, and (*4*) 10000°C. The structure of the dampened kaolin–water electrochemical system is shown on the right.

Table 2. Parameters of the equivalent circuit of conductivity of kaolin

Dampened sample	R_{sol}	CPE-T	CPE-P	R_2
Initial	617.1	0.00051	0.7630	13926
120°C	642	0.00044	0.7642	25977
600°C	270.5	0.00061	0.8014	47805
1000°C	349	0.00063	0.8066	93950

Table 3. Parameters of the equivalent circuit of the conductivity of 1% kaolin slurries

Slurry	L	R_1	CPE-P	CPE-T	R_2
Initial	–0.000156	1540	0.00053	0.8240	10579
120°C	–0.000223	1913	0.00053	0.80767	74028
600°C	–0.000307	2238	0.00051	0.79874	112330

The spectra measured in the Nyquist coordinates are similar to the EI spectra of an indifferent electrolyte [14] and indicate the occurrence of electrode reactions (the slope of the spectrum line is different from 90°). Despite the change in the chemical composition of the mineral associated with water loss and restructuring, an increase in the calcination temperature leads to a change only in the active component of the impedance at the electrode/solution interface.

The presence of an ice-like structure of water coordinated around the oxide centers generates steric hindrances to the charge propagation (see Fig. 3b) because of stabilization of the symmetry of the hydrogen bonds. Therefore, an increase in the water content in kaolin does not lead to a significant change in the electrochemical properties of the slurry relative to the anhydrous sample. As the amount of water in the system increases, the resistance at the electrode/solution interface increases (Table 2), which indicates the blocking of the surface of the platinum electrode by the water and oxygen molecules [15] and the occurrence of electrode reactions associated with the adsorption of dissolved oxygen:

$$O_{ads} + H_2O + 2e^- \rightarrow 2OH^-. \quad (1) \qquad (1)$$

The appearance of a hydroxide ion in the near-electrode layer must hinder the motion of the proton, which is a majority carrier in this case. Low values of the constant phase element CPE-T suggest that the proton motion scheme will have a T-shaped pattern and form the active resistance of the studied samples. The CPE-P values of about 0.8 prove the presence of a dense double layer inhibiting the proton reduction on the electrode.

To confirm the effect of oxygen on the conducting properties of kaolin, slurries containing 1 wt % of kaolin were examined. The comparative analysis of the derived spectra revealed both visual and simulative differences (Fig. 4, Table 3), which indicate the occur-

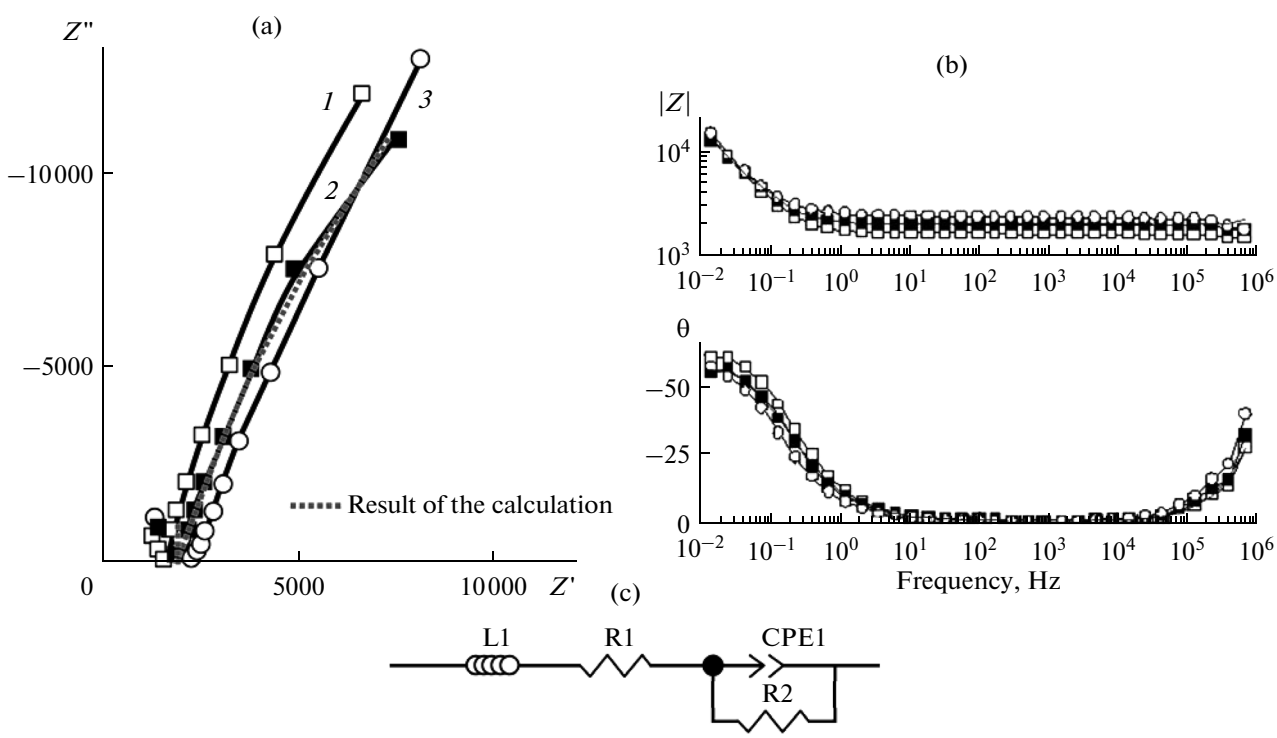

Fig. 4. Impedance spectra in (a) the Nyquist and (b) Bode coordinates and (c) the equivalent circuit of 1% kaolin slurries at heat treatment temperatures of (*1*) 20 (initial), (*2*) 120, and (*3*) 600°C.

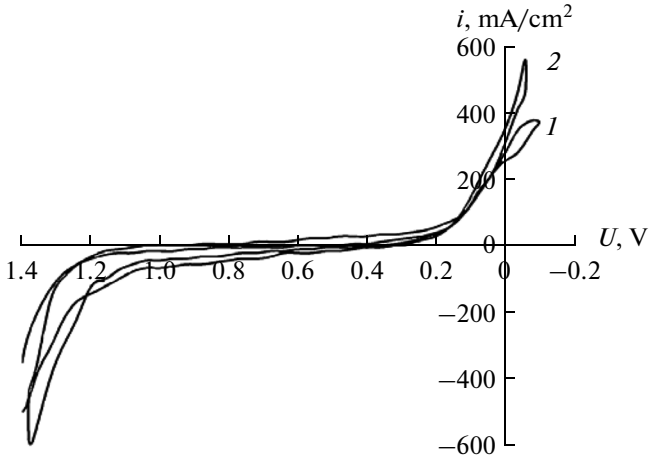

Fig. 5. Current–voltage curves of 1% kaolin slurries in distilled water: (*1*) static mode and (*2*) a flow rate of 6 cm/s.

rence of a large number of long-living paramagnetic particles (in particular, those of adsorbed oxygen) in the system. Owing to this, an inductance element can be introduced into the equivalent circuit [16]. An increase in the active resistance at the electrode/solution interface confirms the involvement of water and oxygen in the formation of a complex structure of the near-electrode layer.

This effect is significantly stronger in the samples with completely removed intrinsic water than in the water-containing samples (see Table 3). This fact confirms the involvement of water in the generation of charge carriers in the structure of the studied samples and the formation of the electrode/solution interface. Hydrated forms of iron(III) ions can also have an effect; however, their concentration in the composition of kaolin is so insignificant (less than 1 wt %) that it cannot cause the observed change in the resistance by 45%.

To explore the possibility of the electrochemical generation of active forms of oxygen, cyclic voltammograms (Fig. 5) were measured in the different modes (static and dynamic); they confirmed the cathodic generation of hydrogen peroxide [17], which increases under stirring.

The hydrogen peroxide concentration was determined from the current–voltage curves in the reaction potentials region:

$$O_2 + 2H^+ + 2e^- \rightarrow H_2O_2, \quad (2)$$

$$H_2O_2 + 2H+ + 2e^- \rightarrow 2H_2O. \quad (3)$$

The following H_2O_2 concentrations were obtained in the experiment: $C_{stat} = 2.48 \times 10^{-6}$ M for static conditions and $C_{dyn} = 3.47 \times 10^{-6}$ M for stirring conditions; these values are an order of magnitude lower than for the bentonite slurries. The kaolin material acts as a flow promotor rather than as a catalytically active surface. In this case, the features of the 1 : 1 close-packed structure of kaolin with a monolayer of water on the surface become apparent. The absence of long-range structuring of the electrolyte is responsible for the low activity of the mineral in the mechanochemical generation of H_2O_2.

Thus, the appearance of aluminosilicate containing hydrophobic centers increases the surface heterogeneity owing to the changes in the degree and conditions of the charge transport with the formation of conductivity channels involving water. The hydrophobic centers play the role of "regulators" of the motion of the proton along the hydrogen bond network that controls the number of water molecules and hence the number of protons in the channel. The low conductivity of kaolin inhibits the supply of electrons to the reaction zone. The regulated motion of protons and electrons provides conditions for the cathodic generation of "active" oxygen, including hydrogen peroxide. However, the presence of hydrophobic regions decreases the specific proton and electron transport; this effectively shields the electrode reaction from mechanical activation.

REFERENCES

1. Zapol'skii, A.K., *Sernokislotnaya pererabotka vysokokremnistogo alyuminievogo syr'ya* (Sulfuric-Acid Processing of High-Silica Aluminum Feedstocks), Kiev: Naukova dumka, 1981.
2. Tkachev, K.V., Zapol'skii, A.K., and Kisil', Yu.K., *Tekhnologiya koagulyantov* (Coagulant Technology), Leningrad: Khimiya, 1978.
3. Mel'nikov, E.Ya., Saltanova, V.P., and Naumova, A.M., *Tekhnologiya neorganicheskikh veshchestv i mineral'nykh udobrenii* (Technology of Inorganic Substances and Mineral Fertilizers), Moscow: Khimiya, 1983.
4. Zapol'skii, A.K. and Baran, A.A., *Koagulyanty i flokulyanty v protsessakh ochistki vody: Svoistva. Poluchenie. Primenenie* (Coagulants and Flocculants in Water Treatment Processes: Properties, Preparation, and Application), Leningrad: Khimiya, 1987.
5. Zapol'skii, A.K., *Ochistka vody koagulirovaniem* (Water Treatment by Coagulation), Kamenets-Podol'skii: Medobory, 2006.
6. Shtamm, E.V., Purmal', A.P., and Skurlatov, Yu.N., The role of hydrogen peroxide in a natural aqueous environment, *Usp. Khim.*, 1991, vol. 60, no. 11, pp. 2373–2411.
7. Hu, X. L. and Michaelides, A., Water on the hydroxylated (001) surface of kaolinite: From monomer adsorption to a flat 2D wetting layer, *Surf. Sci.*, 2008, vol. 602, pp. 960–974.
8. Frost, R.L., The structure of the kaolinite minerals—a FT-Raman study, *Clay Miner.*, 1997, vol. 32, pp. 65–77.
9. Herrington, T.M., Clarke, A.Q., and Watts, J.C., The surface charge of kaolin, *Colloids Surf.*, 1992, vol. 68, pp. 161–169.

10. Alberti, G. and Casciola, M., in *Proton Conductors*, Colomban, Ph., Ed., Cambridge: Cambridge Univ. Press, 1992, pp. 238–253.

11. Kaya, A., Electrical spectroscopy of kaolin and bentonite slurries, *Turk. J. Eng. Environ. Sci.*, 2001, vol. 25, pp. 345–354.

12. Berry, L., Mason, B., and Dietrich, R., *Mineralogy: Concepts, Descriptions, Determinations*, San-Francisco: Freeman, 1983.

13. Pershina, K.D., Karpushin, N.A., and Kazdobin, K.A., Aluminosilicate conductivity at the presence of water, *Surf. Eng. Appl. Electrochem.,* 2010, vol. 46, no. 4, pp. 339–347.

14. Kazdobin, K.A. and Pershina, E.D., The role of mechanochemical processes of hydrogen peroxide formation in water body ecology, *Ukr. Khim. Zh.*, 2012, vol. 78, no. 6, pp. 103–117.

15. Pershina, K.D., Kokhanenko, V.V., Masluk, L.N., and Kazdobin, K.A., Conductivity of aqueous suspensions of alumosilicates, *Surf. Eng. Appl. Electrochem.*, 2011, vol. 47, no. 5, pp. 441–445.

16. Kazdobin, K.A., Pershina, K.D., Kokhanenko, E.V., and Duma, V.Yu., Electrochemical behavior of diluted aqueous electrolytes containing oxygen after superimposition of mechanical effects, *J. Water Chem. Technol.*, 2009, vol. 31, no. 3, pp. 177–185.

17. Domrachev, G.A., Rodygin, Yu.L., and Selivanovskii, D.A., Mechanochemically activated decomposition of water in the liquid phase, *Dokl. Akad. Nauk SSSR*, 1993, vol. 329, no. 2, pp. 186–188.

18. Trasatti, S. and Kurzweil, P., Electrochemical supercapacitors as versatile energy stores, *Platinum Met. Rev.*, 1994, vol. 38, no. 2, pp. 46–56.

19. Tarasevich, M.R., Andoralov, V.M., Bogdanovskaya, V.A., Novikov, D.V., and Kapustina, N.A., Cathodic reduction of oxygen on PdCo/C catalyst synthesized based on commercial Pd/C catalyst, *Russ. J. Electrochem.*, 2010, vol. 46, no. 3, pp. 272–277.

20. Starodub, N.F., Hydrogen peroxide: Control of the content in water bodies, *Khim. Tekhnol. Vody*, 2007, vol. 29, no. 6, pp. 491–505.

Translated by M. Timoshinina